

**EPA-600/2-77-173**  
**August 1977**

**Environmental Protection Technology Series**

# **FINE PARTICLE CHARGING DEVELOPMENT**



**Industrial Environmental Research Laboratory  
Office of Research and Development  
U.S. Environmental Protection Agency  
Research Triangle Park, North Carolina 27711**

## **RESEARCH REPORTING SERIES**

Research reports of the Office of Research and Development, U.S. Environmental Protection Agency, have been grouped into nine series. These nine broad categories were established to facilitate further development and application of environmental technology. Elimination of traditional grouping was consciously planned to foster technology transfer and a maximum interface in related fields. The nine series are:

1. Environmental Health Effects Research
2. Environmental Protection Technology
3. Ecological Research
4. Environmental Monitoring
5. Socioeconomic Environmental Studies
6. Scientific and Technical Assessment Reports (STAR)
7. Interagency Energy-Environment Research and Development
8. "Special" Reports
9. Miscellaneous Reports

This report has been assigned to the ENVIRONMENTAL PROTECTION TECHNOLOGY series. This series describes research performed to develop and demonstrate instrumentation, equipment, and methodology to repair or prevent environmental degradation from point and non-point sources of pollution. This work provides the new or improved technology required for the control and treatment of pollution sources to meet environmental quality standards.

## **REVIEW NOTICE**

This report has been reviewed by the participating Federal Agencies, and approved for publication. Approval does not signify that the contents necessarily reflect the views and policies of the Government, nor does mention of trade names or commercial products constitute endorsement or recommendation for use.

This document is available to the public through the National Technical Information Service, Springfield, Virginia 22161.

**EPA-600/2-77-173**

**August 1977**

# **FINE PARTICLE CHARGING DEVELOPMENT**

by

**D.H. Pontius, L.G. Felix,  
J.R. McDonald, and W.B. Smith**

**Southern Research Institute  
2000 Ninth Avenue, South  
Birmingham, Alabama 35205**

**Contract No. 68-02-1490  
ROAP No. 21ADL-036  
Program Element No. 1AB012**

**EPA Project Officer: Leslie E. Sparks**

**Industrial Environmental Research Laboratory  
Office of Energy, Minerals, and Industry  
Research Triangle Park, N.C. 27711**

**Prepared for**

**U.S. ENVIRONMENTAL PROTECTION AGENCY  
Office of Research and Development  
Washington, D.C. 20460**

## EXECUTIVE SUMMARY

The general objectives of this research program were to develop a new theory for the process of fine particle charging by unipolar ions in an electric field, to expand the available base of fine particle charging data, and to design, construct, and evaluate a pilot scale precharging device capable of handling 600 to 1000 ft<sup>3</sup>/min of flue gas.

The existing literature was reviewed in order to establish a background for theoretical development and to compile a base of available data.

A new particle charging theory, in which the thermal motion of the ions is assumed to dominate the process, was developed. In this theory the presence of an electric field has the effect of modifying the ion distribution in the vicinity of each particle. The theory has a statistical basis, and therefore predicts the average charge per particle in a large collection of particles of the same size and material, subjected to identical charging conditions.

Experimental determinations of particle charging were made using an electrical mobility analyzer to find the end points of particle trajectories in an electric field. Charging was accomplished with a unipolar ion field derived from an electrical corona discharge. The apparatus used for the charging experiments was designed to permit independent variations in charging field strength, ion density, charging time, ion polarity, and temperature, as well as particle size and dielectric constant. Experimental charging data were obtained for particles from 0.32 to 7  $\mu\text{m}$  diameter.

The experimental results generally substantiate the theory. Agreement was usually within 20 percent. When the results of charging by positive and negative corona are compared, however, the difference is much larger than predicted by the theory. The free electron contribution to the negative ion current may be responsible for this discrepancy. A more detailed study may be required to determine an appropriate means for taking the free electron contribution into consideration in the theory. The new theory was used to model the performance of the pilot scale charging device developed under this contract, and has also been successfully incorporated into the EPA-SRI electrostatic precipitator computer model.



A pilot scale precharging device capable of treating a total gas volume of up to approximately 1000 ACFM was designed and constructed. Evaluation of charging effectiveness of the device was carried out using redispersed flyash at ambient temperature. When the precharger was installed at the inlet of a pilot scale electrostatic precipitator a significant improvement in the overall collection efficiency of the system was measured. Particle migration velocities increased by values up to 60 percent over that of the precipitator without precharger.

Analysis of the theoretical and experimental results indicates that reductions in electrostatic precipitator size by as much as a factor of three may be feasible by using a two-stage, precharger-precipitator system without sacrifice in collection efficiency or increase in energy requirements. The capital costs could be reduced by approximately one half for the estimated size reduction.

This report was submitted in fulfillment of Contract No. 68-02-1490 by Southern Research Institute under the sponsorship of the U.S. Environmental Protection Agency. This report covers a period from June 24, 1974 to August 31, 1976, and work was completed as of September 29, 1976.

## CONTENTS

Executive Summary.....	ii
Figures.....	v
Tables.....	xv
Acknowledgements.....	xvi
1. Introduction.....	1
2. Summary and Recommendations.....	3
Analysis and Conclusions.....	4
Recommendations.....	4
3. Theoretical Development.....	6
4. Laboratory Charging Experiments.....	30
Apparatus and Methodology.....	30
Experimental Results.....	47
5. Pilot Scale Experimental Work.....	73
6. Analysis and Evaluation of the Two-Stage	
Precharger-ESP Concept.....	109
Particle Charging.....	109
General Precharger Design Considerations.....	123
Cost Estimates.....	135
References.....	140
Appendices	
A. Literature Review-Theory of Particle Charging.....	143
B. Literature Review-Particle Charging Data.....	196
C. Particle Charging Programs for Portable Calculators.....	216

## FIGURES

<u>Number</u>	<u>Page</u>
1 Two dimensional physical model for developing a charging theory.....	8
2 Model for mathematical treatment of charging rate. Along $r=r_0$ and at $\theta_0$ . the radial component of the electric field is equal to zero. The values of $E_0$ , $a$ , $n$ , and $n_s$ were chosen arbitrarily for this example.....	9
3 Relationship among the charging rates in Regions I, II, and III and the total charging rate for a small particle and low electric field.....	16
4 Relationship among the charging rates in Regions I, II, and III and the total charging rate for an immediate sized particle and moderate electric field...	17
5 Relationship among the charging rates in Regions I, II, and III and the total charging rate for a larger particle and high electric field.....	18
6 Distribution of ions around the surface of a partially charged aerosol particle in the presence of an applied electric field.....	19
7 Distribution of ions around the surface of a partially charged aerosol particle in the presence of an applied electric field.....	20
8 Comparison of charging theories and Hewitt's experimental data for a $0.18 \mu\text{m}$ diameter particle. In all theories and experiment the ion mobility is $1.6 \times 10^{-4} \text{m}^2/\text{V} \cdot \text{sec}$ and the ion mean thermal speed is $500 \text{ m/sec}$ . ....	22
9 Comparison of charging theories and Hewitt's experimental data for a $0.28 \mu\text{m}$ diameter particle. $\mu=1.6 \times 10^{-4} \text{m}^2/\text{V} \cdot \text{sec}$ and $\bar{v} = 500 \text{ m/sec}$ .....	23

# FIGURES (Cont'd)

<u>Number</u>		<u>Page</u>
10	Comparison of charging theories and Hewitt's experimental data for 0.56 $\mu\text{m}$ diameter particle. $\mu=1.6 \times 10^{-4} \text{ m}^2/\text{V}\cdot\text{sec}$ and $\bar{v} = 500 \text{ m/sec}$ .....	24
11	Comparison of charging theories and Hewitt's experimental data for a 0.92 $\mu\text{m}$ diameter particle. $\mu=1.6 \times 10^{-4} \text{ m}^2/\text{V}\cdot\text{sec}$ and $\bar{v} = 500 \text{ m/sec}$ .....	25
12	The dependence of charge upon particle size for a low electric field. $N_0 t = 1 \times 10^{13} \text{ sec/m}^3$ , $\mu=1.6 \times 10^{-4} \text{ m}^2/\text{V}\cdot\text{sec}$ and $\bar{v} = 500 \text{ m/sec}$ . The experimental data are by Hewitt (1957).....	26
13	The dependence of charge upon particle size for a moderate electric field, $N_0 t = 1 \times 10^{13} \text{ sec/m}^3$ , $\mu=1.6 \times 10^{-4} \text{ m}^2/\text{V}\cdot\text{sec}$ and $\bar{v} = 500 \text{ m/sec}$ . The experimental data are by Hewitt (1957).....	27
14	The dependence of charge upon particle size for a high electric field. $N_0 t = 1 \times 10^{13} \text{ sec/m}^3$ , $\mu=1.6 \times 10^{-4} \text{ m}^2/\text{V}\cdot\text{sec}$ and $\bar{v} = 500 \text{ m/sec}$ . The experimental data are by Hewitt.....	28
15	Mobility analyzer for measuring fine particle charge.....	31
16	The Assembled SRI Mobility Analyzer.....	32
17	Schematic representation of the Vibrating Orifice Aerosol Generator.....	34
18	Ammonium fluorescein aerosol particles generated using the vibrating orifice generator. The particle diameters are 3.0 $\mu\text{m}$ .....	37
19	Cylindrical geometry particle charger, after Hewitt. Ions originating at the corona wire pass through the screen electrode into the charging region between the screen and the center plate electrode....	38
20	Fraction of time spent charging vs. charging voltage for Hewitt charger. No resistors in parallel, 100 and 200 Hz.....	40
21	Nt as a function of corona current for various values of the average fields in the charger.....	42

## FIGURES (Cont'd.)

<u>Number</u>		<u>Page</u>
22	Charger I-V characteristics for three conducting media: (A) dry air, (B) water vapor in air, and (C) methanol in air.....	44
23	Penetration of a 13 channel diffusion battery by particles of various sizes as determined by mobility analyzer measurements on singly charged particles. The continuous line is the theoretical penetration as a function of particle diameter.....	46
24	First part of sample printout of program used in analyzing the experimental data.....	48
25	Second part of sample printout of program used in analyzing the experimental data.....	49
26	Number of charges per particle as a function of ion density-residence time product, (Nt) for a 0.56 $\mu\text{m}$ diameter dioctyl phthalate (DOP) aerosol. The continuous lines represent the theoretical calculations corresponding to these charging conditions.....	50
27	Number of charges per particle as a function of the Nt product for a 1.4 $\mu\text{m}$ diameter DOP aerosol. Four different values of the charging field strength were used. The blacked-in symbols denote the theoretical curves corresponding to the data plotted with the open symbols of the same shape.....	51
28	Number of charges per particle as a function of Nt product for a 1.0 $\mu\text{m}$ diameter DOP aerosol. The solid lines represent the SRI charging theory.....	53
29	Number of charges per particle as a function of Nt product for a 1.0 $\mu\text{m}$ diameter DOP aerosol.....	54
30	Comparison of experimental and theoretical values of particle charge for a 2.0 $\mu\text{m}$ diameter DOP aerosol.....	56
31	Number of charges per particle as a function of Nt product for 4.0 $\mu\text{m}$ diameter DOP particles.....	57
32	Number of charges per particle as a function of Nt product for a 7.0 $\mu\text{m}$ diameter DOP aerosol.....	58



# FIGURES (Cont'd.)

<u>Number</u>		<u>Page</u>
33	Theoretical and experimental values of charge per particle as a function of Nt product for 2.0 $\mu\text{m}$ diameter stearic acid particles.....	59
34	Number of charges per particle as a function of Nt product for a 2.06 $\mu\text{m}$ diameter stearic acid aerosol.....	60
35	Stearic acid aerosols, calculated diameter 2.0 $\mu\text{m}$ (a) no heating, (b) heated to approximately 100 <sup>o</sup> F....	62
36	Charge per particle as a function of Nt product for a 2.0 $\mu\text{m}$ glycerol aerosol. The relative dielectric constant for this material is 42.5.....	63
37	Comparison of particle charging as a function of charging field strength for two different Hewitt-type chargers. The Nt product was held constant at $1.0 \times 10^{13}$ sec/ $\text{m}^3$ on the field was varied. Aerosols used were DOP, 1.0 $\mu\text{m}$ and 2.0 $\mu\text{m}$ in diameter....	65
38	Charge per particle as a function of Nt product for a 1.0 $\mu\text{m}$ DOP aerosol. The second Hewitt charger was used for these data.....	66
39	Charge per particle as a function of Nt product for a 1.0 $\mu\text{m}$ DOP aerosol, charged with the second Hewitt-type charger.....	67
40	Number of charges per particle for polystyrene latex particles of various sizes. The Nt product was held constant at $5 \times 10^{12}$ sec/ $\text{m}^3$ as the charging field was varied.....	68
41	Number of charges per particle as a function of charging field strength for polystyrene latex particles of four different sizes. Nt is $1.0 \times 10^{13}$ sec/ $\text{m}^2$ .....	69
42	Number of charges per particle as a function of charging field strength for polystyrene latex particles, with $\text{Nt} = 1.5 \times 10^{13}$ sec/ $\text{m}^3$ .....	70
43	Comparison of positive and negative corona charging for 0.109 $\mu\text{m}$ polystyrene latex spheres.....	72

# FIGURES (Cont'd.)

<u>Number</u>		<u>Page</u>
44	Conceptual sketch of pilot scale charging device. Only the three-wire charging section is shown. A second charging device with five corona wires and six plates is located in the opposite end of the enclosure.....	74
45	Sketch of electric field lines in (a) periodic geometry of infinite extent employed in computer program, and (b) pilot scale precharger section containing one wire and having finite plate width.....	75
46	Current-voltage characteristics of both sections of the pilot scale precharger with 0.0254 cm corona wire at positive potential.....	77
47	Current-voltage characteristics of both sections of the pilot scale precharger with 0.0254 cm corona wire at negative potential.....	78
48	Electric field profiles for both sections of the pilot scale precharger at the maximum experimental current density, positive corona. 0.0254 cm diameter corona wires were used.....	79
49	Electric field profiles for both sections of the pilot scale precharger at the maximum experimental current density, negative corona. 0.0254 cm diameter corona wires were used.....	80
50	Comparison of current-voltage characteristics of precharger with 0.0254 cm corona wire and with 0.127 cm corona wire, positive corona.....	81
51	Comparison of current-voltage characteristics of precharger with 0.0254 cm corona wire and with 0.127 cm corona wire, negative corona.....	82
52	Current-voltage characteristic for the 3-wire precharger section with no dust loading, negative corona.....	83
53	Current-voltage characteristic for the 3-wire precharger section under 6.85 grain/ft <sup>3</sup> dust loading, negative corona.....	84
54	Current-voltage characteristic for the 3-wire precharger section under 11.8 grains/ft <sup>3</sup> dust loading, negative corona.....	85

# FIGURES (Cont'd.)

<u>Number</u>		<u>Page</u>
55	Comparison of the theoretical curves corresponding to Figures 76 through 78 for the 3-wire precharger section.....	86
56	Electric field profiles along a line from wire to plate, normal to the plate, for the maximum values of current and voltage plotted in Figure 79.....	87
57	Current-voltage characteristics of 5-wire precharger section under various conditions, negative corona....	88
58	Charge/mass ratio as a function of voltage applied to precharger, negative corona.....	90
59	Charge/mass ratio as a function of precharger voltage, positive corona.....	91
60	Size distributions of flyash at inlet, as measured with Brink impactor and at outlet using Andersen impactor.....	92
61	Collection efficiency of pilot scale dry wall precipitator with 3-wire precharger section turned on compared with efficiency obtained with the precharger off.....	94
62	Charge/mass ratio as a function of precharger voltage for various particle sizes in the 3-wire precharger section, negative corona.....	95
63	Charge/mass ratio as a function of precharger voltage for various particulate sizes in the 3-wire precharger section, positive corona.....	96
64	Charge/mass ratio as a function of precharger voltage for various particle sizes in the 5-wire precharger section, negative corona.....	97
65	Charge/mass ratio as a function of precharger voltage for various particle sizes in the 5-wire precharger section, positive corona.....	98
66	Comparison of experiment with theory for overall charge/mass ratio of flyash sample in 3-wire precharger section, negative corona.....	99

## FIGURES (Cont'd.)

<u>Number</u>	<u>Page</u>
67 Comparison of experiment with theory for overall charge/mass ratio of flyash sample in 3-wire pre-charger section, positive corona.....	100
68 Comparison of experiment with theory for overall charge-mass ratio of flyash sample in 5-wire pre-charger section, negative corona.....	101
69 Comparison of experiment with theory for overall charge/mass ratio of flyash sample in 5-wire pre-charger section, positive corona.....	102
70 Collection efficiency of the pilot scale electrostatic precipitator for various particle sizes.....	104
71 Collection efficiency of the pilot scale electrostatic precipitator as a function of the voltage on the 5-wire precharger section.....	105
72 Collection efficiency and migration velocity as a function of precharger current density for various particle sizes, using the 3-wire precharger.....	106
73 Collection efficiency and migration velocity as a function of precharger current density for various particle sizes, using the 5-wire precharger.....	107
74 Collection efficiency of pilot scale electrostatic precipitator as main voltage is varied while maintaining the 3-wire precharger voltage constant at approximately 20 kV.....	108
75 Charge per particle as a function of electric field for three particle sizes and two values of $N_0 t$ .....	110
76 Charge per particle as a function of ion concentration-residence time product for three particle sizes and two values of electric field.....	111
77 Current-voltage characteristics of a wire-plate corona system for various sizes of corona wire, holding all other parameters constant. $S_x$ is wire-plate spacing, $S_y$ is wire-to-wire spacing, $b_x$ is ion mobility, and $a_y$ is corona wire diameter.....	113

## FIGURES (Cont'd)

<u>Number</u>	<u>Page</u>
78 Electric field at the plate electrode, $E_p$ , and average electric field, $E_a$ , as a function of current density at the plate for various wire sizes in a wire-plate corona system.....	114
79 Current-voltage characteristics for a wire-plate corona system for several values of wire-plate separation, holding all other parameters constant.....	115
80 Maximum permissible current density before breakdown as a function of resistivity for an assumed breakdown strength of $10^4$ V/cm. Back corona and loss of particle charging effectiveness occurs for particle resistivity and corona current density corresponding to points above the diagonal line.....	117
81 Electric field profile in a duct geometry device for various values of equivalent mobility, while holding the average current density constant at the plate electrode.....	122
82 Theoretical electric field profiles for various electrode geometries, all normalized to a field of 5 kV/cm at the passive electrode.....	124
83 Probability charging field as a function of distance from corona electrode, calculated from the field profiles shown in Figure 82.....	127
84 Experimental I-V characteristics for four corona system geometries.....	129
85 Theoretical collection efficiencies for the Gorgas full-scale precipitator compared to a precharger-E.S.P. system.....	134
86 Particle mobility as a function of diameter for shellac aerosol particles charged in a positive ion field (After Cochet and Trillat <sup>18</sup> ).....	198
87 Charge per particle for a mineral oil aerosol charged in a negative ion field (after Fuchs et al <sup>2</sup> ). $Nt = 3.27 \times 10^{11}$ sec/m .....	199
88 Charge per particle for a mineral oil aerosol charged in a negative ion field (after Fuchs et al <sup>2</sup> ). $Nt = 4.64 \times 10^{11}$ sec/m .....	199



# FIGURES (Cont'd.)

<u>Number</u>		<u>Page</u>
89	Charge per particle for a mineral oil aerosol charge by negative ions (after Fuchs et al <sup>2</sup> ). Nt = $5.10 \times 10^{11}$ sec/m <sup>3</sup> .....	200
90	Electrical mobility of dioctyl phthalate droplets as a function of particle diameter (after Hewitt <sup>8</sup> ). Positive corona charging.....	201
91	Particle mobility as a function of charging field strength for a dioctyl phthalate aerosol under positive corona charging (after Hewitt <sup>8</sup> ).....	202
92	Charge per particle as a function of particle diameter for a dioctyl phthalate aerosol under positive corona charging (after Hewitt <sup>8</sup> ).....	203
93	Charge per particle as a function of ion density-residence time product, Nt in a positive corona (after Hewitt <sup>8</sup> ) for 0.18 $\mu$ m diameter dioctyl phthalate particles.....	204
94	Charge per particle as a function of ion density-residence time product, Nt in a positive corona for 0.28 $\mu$ m diameter dioctyl phthalate particles (after Hewitt <sup>8</sup> ).....	205
95	Particle charge as a function of charging field strength for 0.28 $\mu$ m diameter dioctyl phthalate particles (after Hewitt <sup>8</sup> ).....	206
96	Particle charge as a function of ion density-residence time product for 0.56 $\mu$ m diameter dioctyl phthalate particles (after Hewitt <sup>8</sup> ).....	207
97	Particle charge as a function of ion density-residence time product for 0.92 $\mu$ m diameter dioctyl phthalate aerosol particles (after Hewitt <sup>8</sup> ).....	208
98	The spread of the mobility analyzer response curve for fixed values of Nt, particle size and charging field strength (after Hewitt <sup>8</sup> ).....	209
99	Particle charge as a function of particle diameter for a dioctyl phthalate aerosol (after Penney and Lynch <sup>7</sup> ).....	210

## FIGURES (Cont'd.)

<u>Number</u>		<u>Page</u>
100	Particle charge as a function of charging field strength for 0.30 $\mu\text{m}$ diameter dioctyl phthalate particles in a positive corona (after Penney and Lynch <sup>7</sup> ).....	211
101	Particle charge as a function of charging field strength and ion density-time product for a 0.30 $\mu\text{m}$ diameter dioctyl phthalate aerosol in a negative ion field (after Penney and Lynch <sup>7</sup> ).....	212
102	Comparison of particle charging for negative and positive corona acting on 0.30 $\mu\text{m}$ diameter dioctyl phthalate particles (after Penney and Lynch <sup>7</sup> ).....	213
103	Average charge per particle as a function of particle diameter. The curve derived from the calculator program is the simple sum of the field charging and diffusion charging results.....	223

## TABLES

<u>Number</u>	<u>Page</u>
1	Effect of Changing Particle Size On The "Goodness of Fit" Between Experiment and Theory. The Calculated Diameter was 1.0 $\mu\text{m}$ DOP..... 55
2	Electrical Operating Characteristics For Several Plate-Wire-Plate Charger Geometries..... 131
3	Calculated Charge and Fractional Efficiency of the Precharger-ESP System. The ESP Has An SCA of 28 $\text{ft}^2/1000$ ACFM..... 133
4	Flange to Flange Cost Estimates of Particulate Collection Systems (No Installation Costs Included)... 137
5	Estimated Cost Benefit Ratios For Precharger Collector Systems..... 138
6	Comparison of Primary Power Requirements In Kilowatts - 900,000 ACFM..... 139
7	Summary of the Published Experimental Data On Particle Charging..... 197
8	Comparison of Experimental Data. Number of Elementary Charges as a Function of Nt..... 215

#### ACKNOWLEDGMENTS

Dr. H. J. White provided essential background information and insight regarding this charging project. We also consulted with Dr. George Hewitt, who made several helpful suggestions concerning the design of the aerosol charger used in this work.

Particle mobility measurements were carried out by Mr. David Hussey, and assistance in high voltage electronic design work was furnished by Mr. Preston Rice. The continuing encouragement and assistance of Dr. Leslie Sparks is gratefully acknowledged.

## SECTION 1

### INTRODUCTION

The process of charging airborne particles in a unipolar ion field is fundamental to electrostatic precipitation. Once charged, the particles can be forced toward a collecting surface by an electric field. The overall efficiency of any electrostatic precipitator is thus intimately related to the effectiveness of particle charging in the system. A thorough understanding of the mechanisms related to particle charging is important to the search for improvements in electrostatic precipitator technology. This report presents the results of the research efforts undertaken pursuant to Environmental Protection Agency Contract No. 68-02-1490, which covers a joint theoretical-experimental study of fine particle charging. The principal objectives of this study were: to develop an adequate theory for the charging of fine particles in a unipolar ion field with an applied electric field, to extend existing experimental data on fine particle charging, and to design and construct a pilot scale charging device in order to investigate the technical and economic feasibility of improved collection of high resistivity particulate matter by using a precharging section in conjunction with a high field, low current density electrostatic precipitator.

A new charging theory developed as part of this work, provides improvements over existing theories in accuracy and flexibility of application. Comparisons made between this new theory and data drawn from the literature show better agreement, in general, than was achieved with previous charging theories.

In order to expand the base of particle charging data for comparison with the theory, an experimental program was carried out. Specially generated monodisperse aerosols were charged under various controlled conditions of ion density and electric field strength. The average charge per particle was determined in each case by means of a mobility analyzer, a device in which the trajectory of a charged particle under the combined influences of a laminar gas flow and an electric field can be measured. Airborne particle charging in a unipolar ion field depends upon ion density, electric field strength, particle residence time in the ion field, particle diameter, and electrical characteristics of the particulate material. Experimental tests to verify the charging theory were done, varying each of these parameters. The charging experiments were generally successful and consistent with the theory, although some additional work is needed in the regime of ultrafine particles, negative corona, and elevated temperatures and pressure.



This new theory was used to model the performance of the pilot scale precharger developed under this contract, and was also incorporated into the EPA-SRI electrostatic precipitator computer model, thus allowing more accurate predictions of E.S.P. performance.

The particle charging theory and the two-stage electrostatic precipitator concept were tested with a pilot scale device capable of handling up to 1000 ft<sup>3</sup>/min of flue gas. The two-stage electrostatic precipitator concept is based on separation of the particle charging and collection functions. In the first stage, or precharger, a high ion density and high electric field strength are maintained to provide optimum charging effectiveness. Particle collection in the precharger should be minimized, since an accumulated dust layer affects the electrical characteristics of a corona system, particularly if the electrical resistivity of the dust layer is very high. Particle collection is reserved for the second stage, which operates with a high electric field strength and low current density. In practice, however, some particle collection in the precharger section is virtually inevitable.

Calculations based on the results of the pilot scale precharger study show that precharger-ESP systems can be reduced in size to limits determined by mechanical, rather than electrical considerations. Theoretically, an ESP located downstream from a precharger could be reduced in size by almost a factor of 10. Because of ash handling problems and reentrainment we estimate that a factor of 3 might be more realistic.

Basically, a precharger would work best where an ESP works best; i.e., with moderate particulate loadings and low resistivity ashes. The chief advantage, excluding size and cost, is the potential for alleviating the high resistivity problem by means which are too expensive or complicated to be applied to full scale ESP installations. This is primarily because the small precharger units can be more carefully aligned, can be of more complex design, and extraordinary means can be used to overcome the high resistivity problem. In addition, the precharger could be utilized to improve the performance of scrubbers, existing ESP's, and perhaps baghouses or novel collection devices.

## SECTION 2

### SUMMARY AND RECOMMENDATIONS

A study of particle charging in a unipolar ion field was carried out using a combined program of theoretical and experimental investigations. An extensive literature review, presented in the Appendix, provided the necessary background information for both the theoretical development and the experimental design.

A new charging theory based on kinetic theory was developed. In the new theory the charging rate is calculated in terms of the probability of collisions between aerosol particles and ions. In order to simplify the mathematics the surface of the particle is considered as being divided into three charging regions and separate charging rates are calculated for each region. The total charging rate is the sum of these three individual rates. For large particles and high electric fields this theory predicts essentially the same charging rate as the classical field charging equations of Rohmann<sup>5</sup> and Pauthenier<sup>17</sup>. For low electric fields the theory reduces to White's<sup>27</sup> diffusional charging equation. In this new theory the charging process is considered to be dominated by the thermal motion of the ions. The principal effect of the field is to modify the ion distribution in the vicinity of the particle.

Experimental verification of the theory was undertaken using apparatus and methodology similar to that employed by Hewitt.<sup>8</sup> Three different charging devices were constructed in the course of the experimental work. The basic requirements of charger design included separate control of charging field strength and ion density in the charging region.

Particle charge measurements were made with a mobility analyzer which was designed and constructed for this project. In this device, described in Section 5, the trajectories of charged particles in an electric field were determined. The particle mobility was then calculated, and, using the particle diameter, the charge per particle was calculated using Stokes' law.

Among the variables investigated in the charging experiments were the charging field strength, ion density-residence time product, particle diameter and dielectric constant and ion polarity in the charging region.

The results of the charging experiments agreed, in general, within approximately 20 percent of the theoretical charging results. Detailed comparisons between theory and experiment are presented in Section 5.

A particle charging device designed for installation at the inlet of a pilot scale electrostatic precipitator was tested and evaluated in terms of charging effectiveness and relative improvement of overall precipitator collection efficiency. The charger consists of two electrically independent sections, each containing a multiple wire-plate corona electrode system. Redispersed flyash at ambient temperature was used for particulate loading up to  $27 \text{ g/m}^3$ , at a gas velocity of about  $1.3 \text{ m/sec}$ . The charging performance of the device was measured by catching particulate samples on a silver mesh filter connected to an electrometer. The samples were weighed and the charge to mass ratio,  $Q/M$  was computed. Values of  $Q/M$  up to  $1.2 \times 10^{-5} \text{ coul/g}$  were found. A theoretical calculation of  $Q/M$  as a function of charger voltage was in good agreement with the experimental results. The charger-precipitator combination was operated as a two-stage system, and measurements of performance were compared with those for the precipitator alone. The migration velocities of the particles were found to be up to 60 percent larger for the two-stage system than for the single-stage precipitator.

## ANALYSIS AND CONCLUSIONS

An analysis of the two stage precharger-ESP concept was carried out on the basis of the experimental and theoretical results obtained in this project. The effects of corona electrode geometry, applications to high resistivity particulate, and space charge resulting from large concentrations of fine particles in the gas stream were taken into consideration. The conclusions detailed in Section 7 indicate that size reduction by a factor of approximately three in overall size of an industrial electrostatic precipitator may be achieved by using a high current density precharger stage operated upstream from a conventional, low current density ESP. No sacrifice in collection efficiency or increased energy expenditures would be required for such a system.

## RECOMMENDATIONS

Although the particle charging experiments and theoretical development were generally successful; additional work is needed to investigate the effects of certain parameters more intensively, and to apply the results to full scale precipitators where non-ideal conditions exist. The specific topics which need further work are:

1. Further experiments need to be done and modelled which relate the charging theory to precipitator geometries when the electric field, ion density, and charging time are non-uniform.
2. Further experiments need to be done and modelled to isolate the effects of free electrons on particle charging.
3. Further experiments need to be done and modelled to investigate the effects of elevated temperature on particle charging.
4. Further experiments need to be done to study the effect of larger variations in particle dielectric constant on particle charging.
5. Further experiments need to be done which allow us to interpret the theoretical predictions of fractional unit charges on ultrafine particles.
6. Further work to modify the theory to include any significant effects found in the experimental work which are not already included needs to be done.

Because of the possible improvements in electrostatic precipitator performance with the addition of a precharger stage, further work in precharger design should be pursued. Of particular importance is the control or elimination of back corona, which limits the current density in any corona system where high resistivity particulate material is present.

Finally, the two stage precharger-ESP concept should be subjected to tests involving actual industrial emissions for comparison with conventional control devices and systems.

## SECTION 3

### THEORETICAL DEVELOPMENT

#### BACKGROUND

The processes resulting in attachment of ions to airborne particles in a unipolar ion field include effects caused by the thermal motion of the ions as well as those related to the presence of an electric field. Previous theories, discussed in detail in the Appendix, have dealt with both the diffusion charging mechanism and the field charging process. In general, those theories which attempt to include both charging mechanisms have produced results which are either a linear combination of the two effects<sup>1,0</sup>, or have given rise to mathematical expressions difficult to evaluate<sup>1,2</sup>. Theories which treat the two charging processes separately are too limited for general application<sup>3,4</sup>. It is apparent, then, that further theoretical development is required to provide an accurate and useful model for particle charging.

The basic mechanism for our charging theory is similar to that described by Murphy et al<sup>1</sup> where charging is largely attributed to the thermal motion of the ions, and the electric field acts as a perturbation on the thermal charging process. As Murphy et al pointed out, the field can influence the charging rate in two ways: (1) the ions can gain kinetic energy from the applied field which will help overcome the repulsive force of the charged particle, and (2) the ion distribution near the particle may be altered. Although in practical situations the kinetic energy of the ions due to their random thermal velocity is always much greater than the kinetic energy gained from the external electric field, experiments show that the charging rate is greatly enhanced by the application of an electric field. This is due mainly to item (2) above.

#### Formulation of the Theory

Our theory predicts the charging rate of particles in an ion field on a statistical basis. For given charging conditions, the instantaneous charge depends upon the ion density-time product or "exposure" to the ions ( $N_0 t$ ). In experimental charging studies the time  $t$  is equal to the residence time in the charging



region. The ion density is determined experimentally by measuring the current density  $j$  and the electric field  $E$  in the charging region and then using the relationship

$$N_0 = \frac{j}{e\mu E} ,$$

where  $\mu$  is the ion mobility and  $e$  is the electronic charge.

Figure 1 shows a two-dimensional diagram of the physical model which is used as the basis for the development of the theory described in the following paragraphs. The particle shown in this sketch, and its environment, are considered to be representative of the average of a large number of similar systems which make up the aerosol under investigation. Because the ion concentration may only be 10-100 times as large as the particle concentration and because of the screening effect of neighboring charged particles, macroscopic theories based on diffusion due to ion concentration gradients are not applicable. It is possible, however, to apply some ideas from kinetic theory of gases in order to calculate the charging rate in terms of the probability of collisions between ions and the particle of interest.

The nomenclature used in the development of the theory is defined in Figure 2. The physical description, however, will be based on the conceptual representation shown in Figure 1 where the particle of interest is surrounded by gas molecules, ions, and other charged particles. The particle is assumed to be spherical and only components of the electric field due to charge on the particle and the applied field are considered. The external electric field is taken to be uniform and directed along the negative  $z$  axis. The dashed line in Figure 2, labeled  $r_0$ , corresponds to points in space where the radial component of the total electric field is equal to zero. The angle  $\theta_0$  corresponds to the azimuthal angle at which  $r_0$  is equal to the particle radius,  $a$ . The point of intersection between  $r_0$  and the particle surface will always lie on the hemisphere defined by  $\theta_0 \leq \pi/2$ . As the charge on the particle increases,  $\theta_0$  will go to zero and  $r_0$  will exceed the particle radius for all angles.

If the space charge in the region outside the volume of interest is homogeneous, we can write down an expression for the radial component of the electric field very near the particle as follows:

$$E_r = E_0 \cos\theta \left( 1 + 2\frac{K-1}{K+2} \frac{a^3}{r^3} \right) - \frac{ne}{4\pi\epsilon_0 r^2} , \quad (1)$$

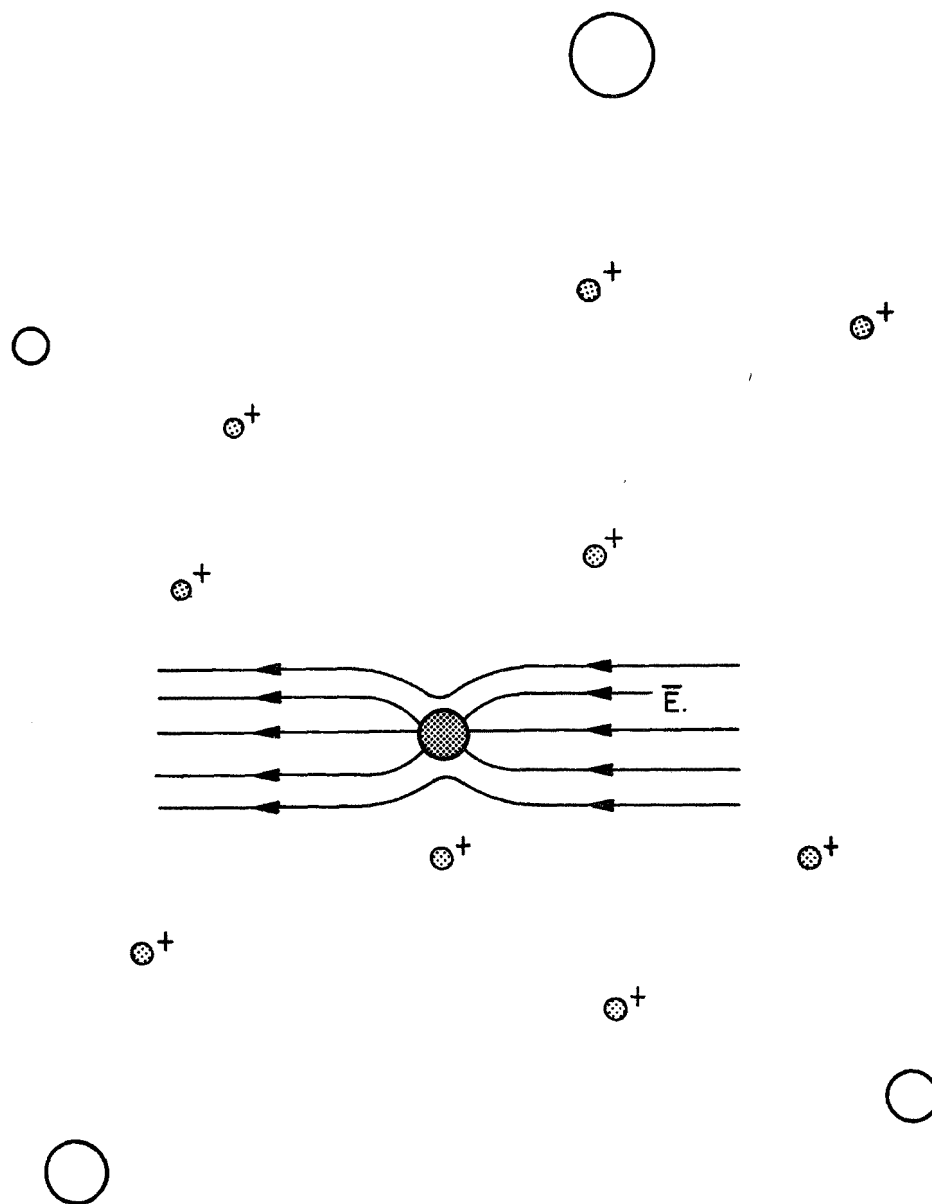


Figure 1. Two dimensional physical model for developing a charging theory.

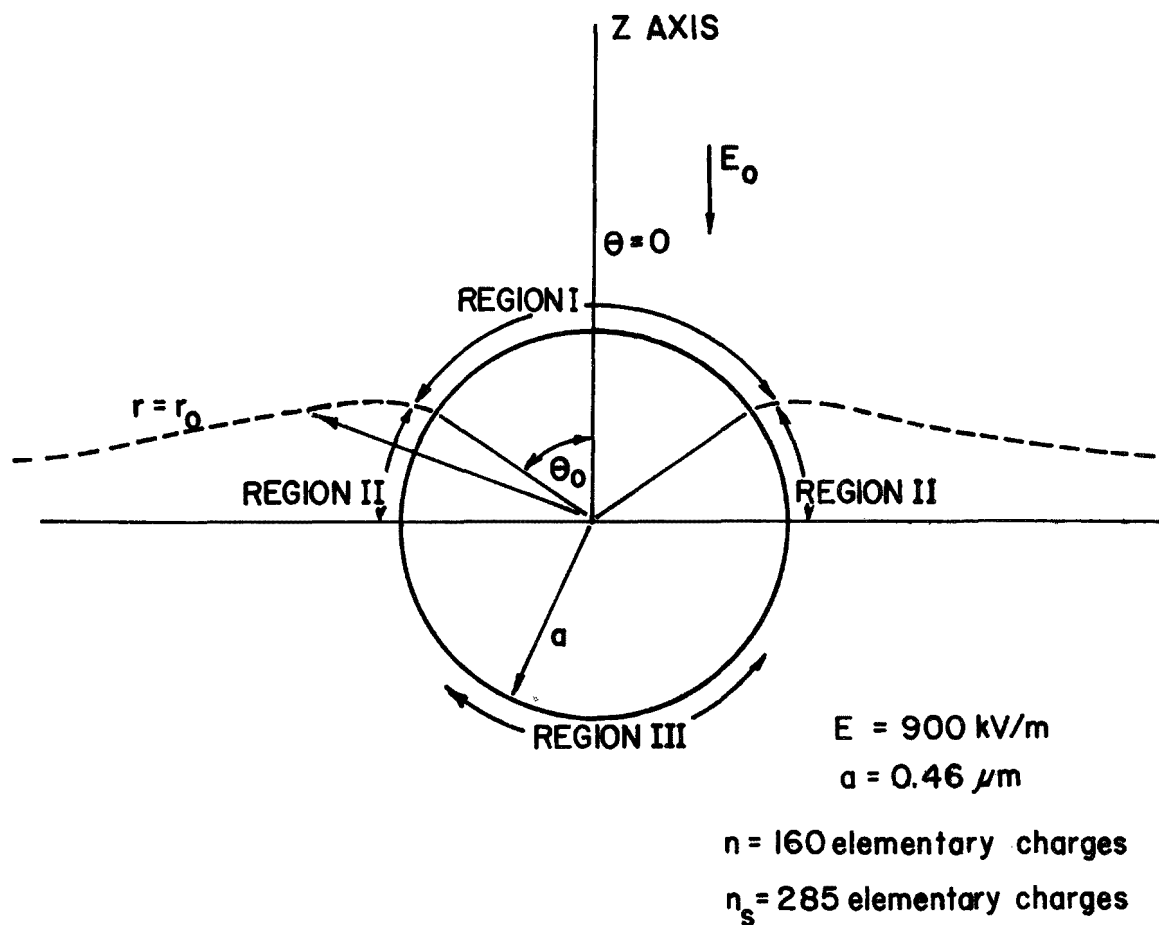


Figure 2. Model for mathematical treatment of charging rate. Along  $r=r_0$  and at  $\theta_0$ , the radial component of the electric field is equal to zero. The values of  $E_0$ ,  $a$ ,  $n$ , and  $n_s$  were chosen arbitrarily for this example.

where  $E_r$  = radial component of electric field (V/m),

$E_0$  = external field (V/m),

$K$  = particle dielectric constant,

$r$  = radial distance to point of interest (m), and

$\theta$  = the azimuthal angle measured from the  $z$  axis,  
and the other symbols have been previously defined.

For the purpose of discussion we will define three areas of interest on the particle surface. One area, designated by Region I, is that bounded by  $\theta = 0$  and  $\theta = \theta_0$ ; a second region, Region II, is bounded by  $\theta = \theta_0$  and  $\theta = \pi/2$ ; and the third region of interest, Region III, is the "dark side" of the particle where  $\theta > \pi/2$ . Our approach to arriving at an equation for the charging rate,  $dq/dt$ , is to estimate the probability that ions can reach the particle surface in each of these three regions.

The rate at which ions reach the particle surface is

$$\frac{dn}{dt} = \frac{1}{e} \frac{dq}{dt} = P \cdot N_s(E_0, a, \theta), \quad (2)$$

where

$P$  = the probability that a given ion will move in a direction to impact with the particle. From kinetic theory,  $P = \frac{1}{4} \bar{v} A$ . (Here  $\bar{v}$  is mean thermal speed of the ions and  $A$  is the surface area of the particle on which the ions may impinge), and

$N_s(E_0, a, \theta)$  = the ion concentration near the particle surface.

Again, from classical kinetic theory,  $N_s(E_0, a, \theta)$  can be related to the average ion concentration,  $N_0$ , by the expression

$$N_s(E_0, a, \theta) = N_0 e^{-\Delta V(E_0, a, \theta)/kT},$$

where  $\Delta V(E_0, a, \theta)$  is the energy difference between the particle surface ( $r=a$ ) and some point in space where the average ion distribution is undisturbed ( $r=r'$ ).

Thus, for diffusion to the entire surface of a spherical particle, we write

$$\frac{dq}{dt} = N_0 e \pi a^2 \bar{v} e^{-\Delta V(E_0, a, \theta)/kT}. \quad (3)$$

Up to this point the derivation is similar to that given by White for the classical diffusional charging rate. For classical diffusional charging,  $\Delta V$  is set equal to  $ne^2/4\pi\epsilon_0 a$ , the potential energy at the particle surface, and the influence of the applied field is not taken into account (in this case,  $r' = \infty$ ).

Because of collisions with neutral molecules, the energy of the ions is not conserved and hence, there is no potential energy function associated with the electric field given by equation (1). We can say, however, that a minimum amount of work must be done in moving an ion from some point in space (defined by  $r=r'$ ) to the particle surface. This minimum work is given by

$$\Delta V(E_0, a, \theta) = \int_{r'}^a \vec{F} \cdot \overline{dr} = \int_{r'}^a eE_r dr = \left\{ \frac{ne^2}{4\pi\epsilon_0 r} + eE_0 r \cos \theta \left[ 1 - \frac{K-1}{K+2} \frac{a^3}{r^3} \right] \right\}_{r=r'}^{r=a}.$$

If this expression is used for  $\Delta V$ ,  $N_S(E_0, a, \theta)$  becomes

$$N_S(E_0, a, \theta) = N_0 \exp - \left\{ \frac{ne^2(r'-a)}{4\pi\epsilon_0 kT a r'} + \frac{[3ar'^2 - r'^3(K+2) + a^3(K-1)] eE_0 \cos \theta}{kT(r')^2(K+2)} \right\}. \quad (4)$$

If  $\theta$  is set equal to zero and this equation is used for  $N_S$ , equation (3) becomes identical to that given by Liu and Yeh<sup>5</sup> as a solution to the diffusional equation. Our approach to the solution of this differential equation for the charging rate is quite different, however, and yields a smaller charging rate for larger particles.

Ideally, we would like to apply equation (4) to the entire particle surface by averaging over the angle  $\theta$ . To do this, it is necessary to choose some radial distance  $r'(\theta)$  where the ion density is undisturbed. If we choose the point at which the radial component of the electric field ( $E_r$ ) is equal to zero ( $r_0$ ), as did Liu and Yeh<sup>13</sup>, we can only apply equation (3) in its present form to Region II as defined in Figure 19. In Region I,  $r_0 < a$ , and the argument of the exponential becomes positive. From energy considerations, this can be interpreted as meaning that any ion which is near the particle surface in Region I and moving toward the particle has a 100% probability of impinging on the particle surface. In Region III no finite  $r_0$  exists. Thus,

different approximations are used to calculate the charging rate in each region and the rates are then added to yield the total charging rate:

$$\frac{dq}{dt} \rightarrow \left(\frac{dq}{dt}\right)_I + \left(\frac{dq}{dt}\right)_{II} + \left(\frac{dq}{dt}\right)_{III} . \quad (5)$$

Equation (3) was developed using expressions from kinetic theory which, in turn, are based on the assumption that the system is in equilibrium. In solving equation (3) for the charge as a function of time we will assume that the charging dynamics can be approximated by a series of steady states so that these expressions may be applied. Nevertheless, in reaching the ultimate expression for  $q(N_0t)$ , we will consider the motion of the ions due to the applied field.

### Calculation of the Particle Charging Rate

#### Region I--

In Region I the argument of the exponential in equation (4) becomes positive. In this case, equation (2) predicts charging rates which are too large to be approximated by steady state solutions because of the finite source of ions. In fact, the charging rate is limited to the rate at which ions are brought into the system by the external field. This rate is given by the product of the current density and the surface area ( $A_I$ ) of Region I:

$$\left(\frac{dq}{dt}\right)_I = \int_{A_I} \vec{j} \cdot d\vec{A}_I = \mu e N_0 \int_{A_I} E_r dA_I \quad (6)$$

This is identical to the charging equation developed by Pauthenier which we refer to as the classical field charging equation. We may write this equation in a more conventional and useful form as

$$\left(\frac{dq}{dt}\right)_I = \frac{N_0 \mu \pi n_s}{4\pi \epsilon_0} e^2 \left(1 - \frac{n}{n_s}\right)^2 \quad (7)$$

where

$$n_s = \left[ \left(1 + 2\frac{K-1}{K+2}\right) E_0 a^2 / e \right] 4\pi \epsilon_0 , \quad (8)$$

$$\theta_0 = \arccos (n/n_s), \quad (9)$$

and the other symbols are as previously defined.

When  $n > n_s$ ,  $r_0$  is greater than the particle radius for all values of the angle  $\theta$ ,  $(dq/dt)_I$  is zero. That is, field charging ceases.

## Region II--

In Region II, charge is acquired by the particle due to ion diffusion which is enhanced by the presence of the applied electric field. In this case equations (2) and (4) apply and the charging rate is

$$\left(\frac{dq}{dt}\right)_{II} = \frac{e\tilde{v}}{4} \int_{A_{II}} N_S dA_{II},$$

where  $N_S(E_0, a, \theta)$  is given by equation (5). Using this expression for  $N_S$  and writing  $A_{II}$  in terms of  $a$  and  $\theta$ , we find

$$\left(\frac{dq}{dt}\right)_{II} = \frac{e\tilde{v}}{4} \int_{\theta_0}^{\pi/2} N_S (2\pi a^2 \sin\theta) d\theta,$$

or

$$\begin{aligned} \left(\frac{dq}{dt}\right)_{II} = & \frac{e\pi a^2 N_0 \tilde{v}}{2} \int_{\theta_0}^{\pi/2} \exp \left[ -\frac{ne^2 (r_0 - a)}{4\pi\epsilon_0 kT a r_0} \right. \\ & \left. + \frac{[3ar_0^2 - r_0^3 (K+2) + a^3 (K-1)] eE_0 \cos\theta}{kT r_0^2 (K+2)} \right] \sin\theta d\theta. \end{aligned} \quad (10)$$

For each value of the particle charge  $ne$ , a value of  $\theta_0$  is calculated using equation (9) and the integration of equation (10) is performed. The integration is complicated by the dependence of  $r_0$  on the angle  $\theta$ . Thus for each value of  $\theta$ , a value of  $r_0$  must be calculated. The magnitude of  $r_0$  is found from the condition that for  $r=r_0$ ,  $E_r(E_0, a, \theta) = 0$ .

## Region III--

In Region III (the particle surface between the angles  $\theta = \pi/2$  and  $\theta = \pi$ ), the electric fields due to the particle charge and the external field are in the same direction and there is no radial point  $r_0$  for which the total electric field is equal to zero. In this case, equations (2 and 4) would predict that no charging could occur on this side of the particle. This is a result of our application of equilibrium thermodynamics to a dynamic problem. Physically this means that the ions move in the direction of the electric force and are swept from the system. In reality, additional ions are swept into the system by the same electric field, effectively creating a steady state charge density. As Murphy et al<sup>1</sup> and Liu and Yeh<sup>5</sup> have pointed out the change in the ion density (and hence, charging rate) near

the particle surface is much greater for small values of  $\theta$  than for the region  $\theta > \pi/2$  when an electric field is applied. Since the change in ion density in Region III is relatively small, the effects of the applied field are neglected and the classical diffusional equation is used as an approximation to calculate the charging rate:

$$\left(\frac{dq}{dt}\right)_{III} = \frac{\pi a^2 \bar{v} n_0}{2} \exp(-ne^2/4\pi\epsilon_0 akT) .$$

In the preceding paragraphs we have developed charging theories for each of three charging regions on the surface of the particle. The charging rate of the particle is the sum of these rates:

$$\frac{dq}{dt} = \left(\frac{dq}{dt}\right)_I + \left(\frac{dq}{dt}\right)_{II} + \left(\frac{dq}{dt}\right)_{III}$$

or

$$\begin{aligned} \frac{dq}{dt} = & (N_0 \mu n_s e^2 / 4\epsilon_0) \left(1 - \frac{n}{n_s}\right)^2 + \frac{e\pi a^2 \bar{v} n_0}{2} \int_{\theta_0}^{\pi/2} \exp\left[-\left\{\frac{ne^2(r_0-a)}{4\pi\epsilon_0 kT a r_0}\right.\right. \\ & \left. + \frac{[3ar_0^2 - r_0^3(K+2) + a^3(K-1)] eE_0 \cos\theta}{kT r_0^2 (K+2)}\right\}] \sin\theta d\theta \\ & + \frac{e\pi a^2 \bar{v} n_0}{2} \exp(-ne^2/4\pi\epsilon_0 akT) . \end{aligned} \quad (11)$$

Equation (11) is integrated numerically using the quartic Runge-Kutta method in the following procedure:

- (a) The initial conditions are taken to be  $n = 0$  at  $t = 0$ .
- (b)  $n_s$  is calculated using equation (8).
- (c) For each increment in the Runge-Kutta scheme, a value of  $\theta_0$  is calculated from equation (9).
- (d) The integral over  $\theta$  in equation (11) is performed using Simpson's Rule, and for each value of  $\theta$  which is chosen for this integration,  $r_0$  is calculated.
- (e) The three individual charging rates are calculated and then added to give the total instantaneous charging rate for a particular value of  $n$ .
- (f) Procedures (b) through (e) are repeated for each increment of time until the integration is completed.



## Theoretical Results

Figures 3-5 show how the charging mechanisms in each region contribute to the overall charging rate. Figure 3 shows data for a small particle and low electric field. (See also Figure 8). In this extreme case, charging is dominated by the diffusional mechanisms in Regions II and III. Figure 4 shows a small particle with a moderate applied field (also Figure 9). For values of  $N_0 t$  larger than about  $10^{12}$  sec/m<sup>3</sup>, charging is dominated by the field enhanced diffusion in Region II. Figure 5 shows data for the largest particle size tested by Hewitt (also Figure 11). The charging rate is again higher in Region II, for large  $N_0 t$ , but field charging in Region I does contribute significantly for low values of  $N_0 t$ . The deviation from a smooth decreasing curve for the total charging rate in Figures 4 and 5 appears because we have used a macroscopic description of charging in Region I which does not consider the thermal motion of the ions. Because of this approximation the charging rates in Regions I and II near  $\theta = \theta_0$  are different. However, this does not significantly affect the integrated charge.

Figures 6 and 7 show the ion distribution at the surface of a 0.28 diameter particle in an applied electric field for two values of particle charge as predicted by the new theory and the solutions to the quasi-steady diffusion equation obtained by Liu and Yeh<sup>6</sup>. Since the results obtained with the new theory are based on a microscopic kinetic theory approach and those given by Liu and Yeh include a macroscopic diffusional process, it is difficult to make a quantitative comparison. Figures 6 and 7 show that both formalisms yield ion distributions over the particle surface which are very non-uniform, with ion concentration at  $\theta = 0$  being three or more orders of magnitude higher than the ion concentration at  $\theta = 180^\circ$ . The two formalisms differ in that the new theory predicts higher ion concentrations at smaller values of  $\theta$  and lower ion concentrations at larger values. However, the quantity of interest is the area under the curves since, in effect, this represents the number of ions at the particle surface and hence, the number of ions available for charging. The areas predicted by the two formalisms are in reasonable agreement.

## Comparison With Hewitt's Data

There has been a wide range of values reported in the literature for the mobility of ions created in a corona discharge. Liu et al<sup>7</sup> measured ion mobilities of  $1.1 \times 10^{-4}$  m<sup>2</sup>/V·sec in their experimental arrangement. Hewitt<sup>8</sup> used a value of  $1.6 \times 10^{-4}$  m<sup>2</sup>/V·sec to calculate  $N_0$  from the measured values of current density and electric field in his aerosol charger. Also, the mobility of ions in laboratory air has been shown to decrease

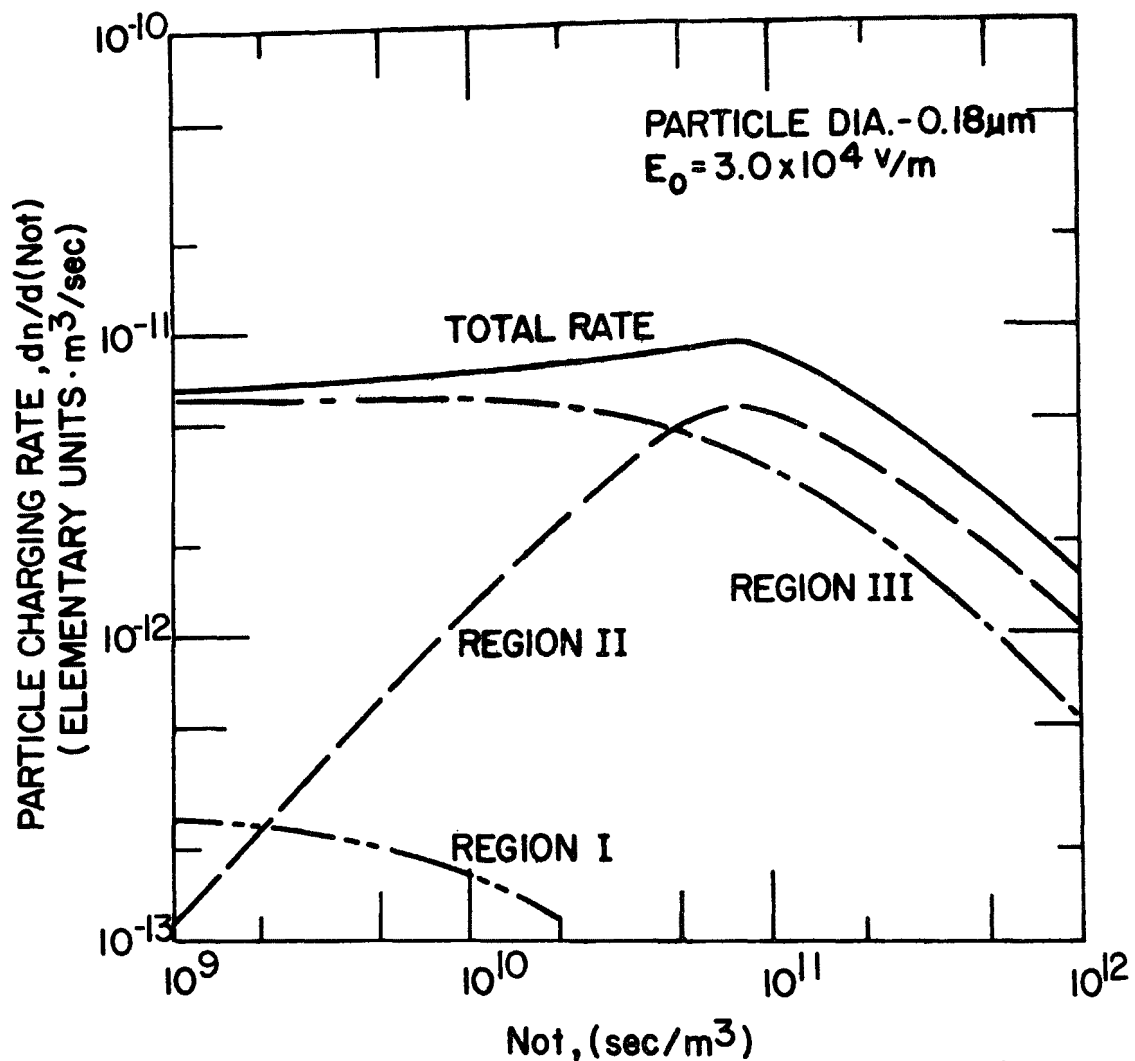


Figure 3. Relationship among the charging rates in Regions I, II, and III and the total charging rate for a small particle and low electric field.

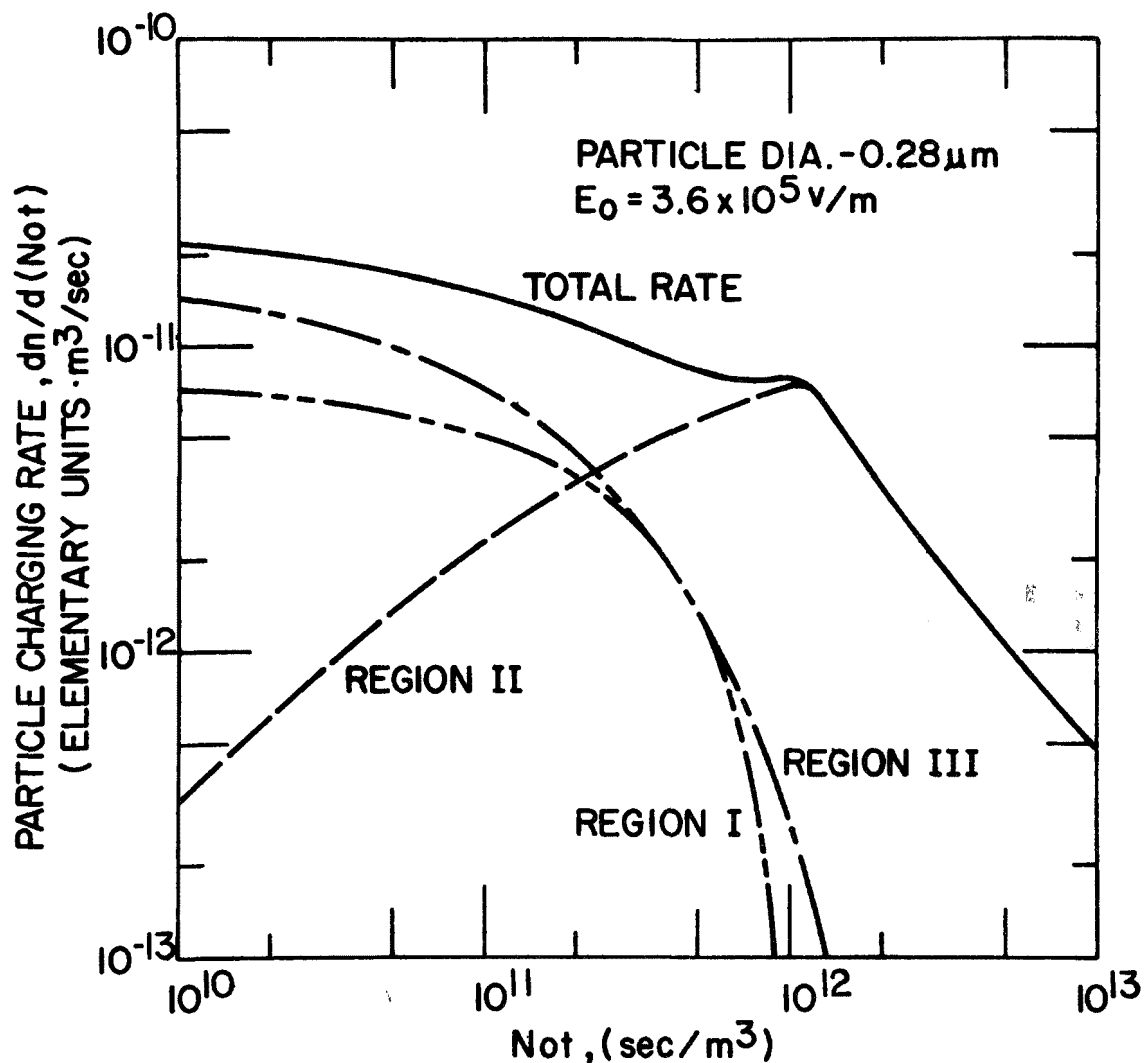


Figure 4. Relationship among the charging rates in Regions I, II, and III and the total charging rate for an immediate sized particle and moderate electric field.

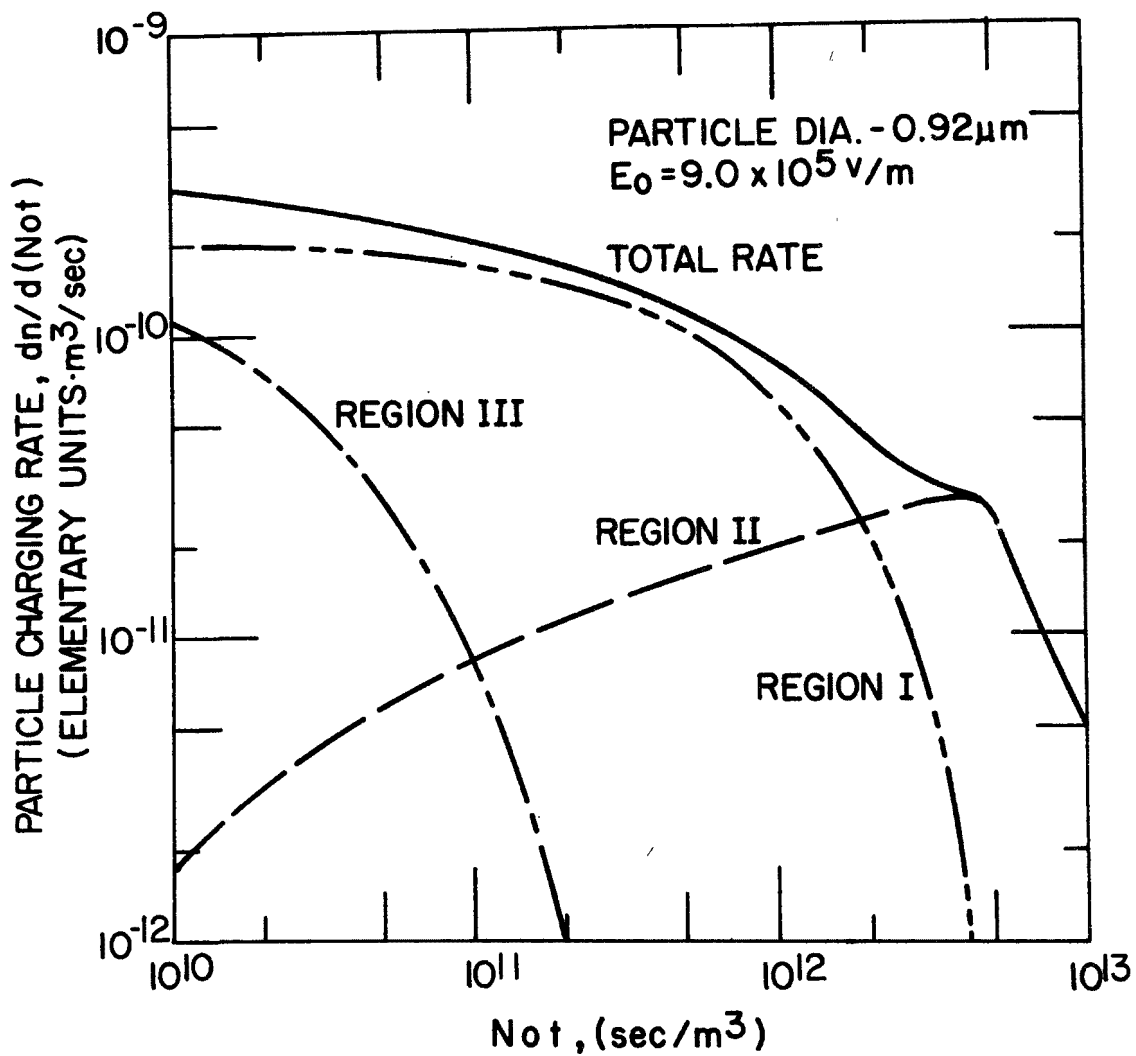


Figure 5. Relationship among the charging rates in Regions I, II, and III and the total charging rate for a larger particle and high electric field.

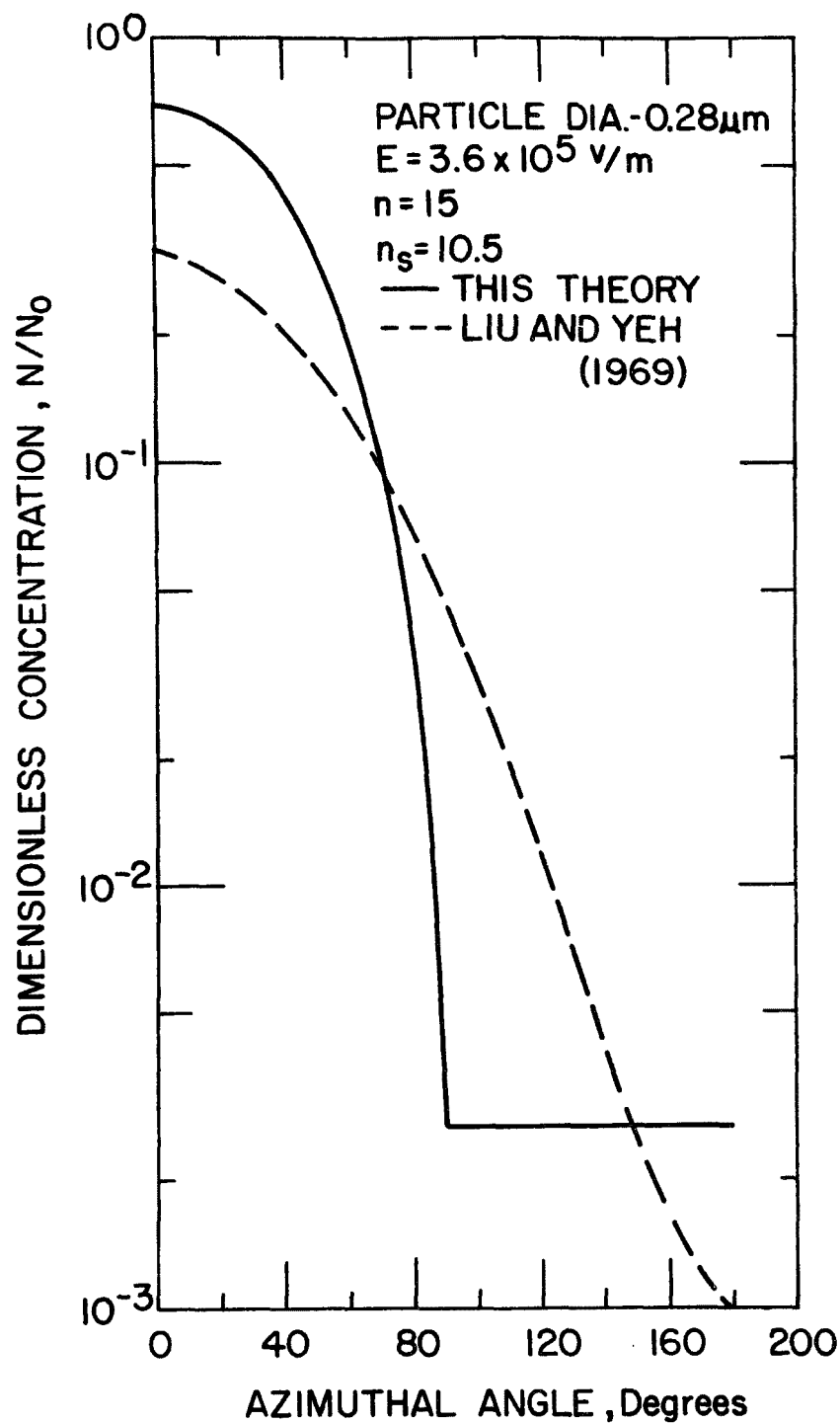


Figure 6. Distribution of ions around the surface of a partially charged aerosol particle in the presence of an applied electric field.

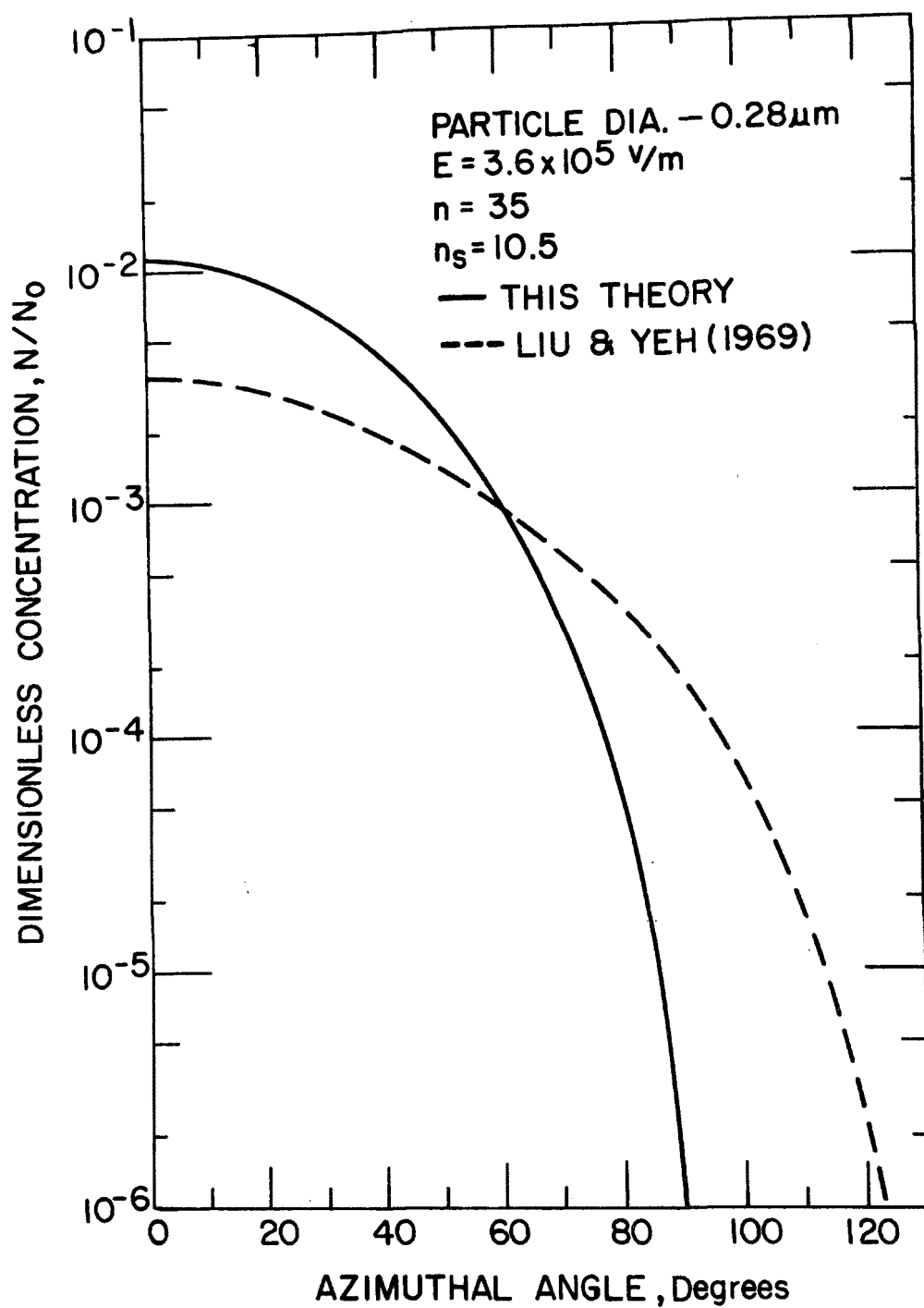


Figure 7. Distribution of ions around the surface of a partially charged aerosol particle in the presence of an applied electric field.

with time and to depend upon the gas constituency. For ion transport times on the order of 1 msec, the range in mobilities (due to different species) was reported by Bricard *et al*<sup>9</sup> to be from  $2.1 \times 10^{-4} \text{ m}^2/\text{V}\cdot\text{sec}$  to  $1.35 \times 10^{-4} \text{ m}^2/\text{V}\cdot\text{sec}$ . Research conducted by Löeb and his students<sup>10</sup> indicates that a value of  $2\text{--}2.2 \times 10^{-4} \text{ m}^2/\text{V}\cdot\text{sec}$  is representative of both positive and negative corona in laboratory air. Thus, because of the uncertainty in ion mobility, it is difficult to select a value which is characteristic of corona discharge in general.

In order to make valid comparisons of theoretical results with the experimental data reported by Hewitt, two methods are possible. One approach is to choose a representative value for the ion mobility  $\mu$  and then normalize both the experimental data ( $N_0t$ ) and the theoretical results to this particular value. The other approach is to use Hewitt's value in the theory. Since Hewitt's value is well within the range reported by Bricard *et al*<sup>9</sup> the latter approach has been used in making comparisons presented in this report and the value of  $1.6 \times 10^{-4} \text{ m}^2/\text{V}\cdot\text{sec}$  has been used for the ion mobility to obtain the theoretical results. Also, Hewitt's value of 500 m/sec has been used for the mean thermal speed  $\bar{v}$  of the ions in order to be consistent with the choice of ion mobility. This causes much less agreement between the theory of Liu and Yeh and Hewitt's experimental results than is observed if low values for  $\mu$  and  $\bar{v}$  are used in the theory and high values in the experiment, as was done by the individual workers. Nevertheless, the same values for  $\mu$  and  $\bar{v}$  must be used in both the theory and experiment for meaningful comparisons to be made.

Figures 8-14 compare the predictions of this new theory with Hewitt's experimental data and with the theory of Liu and Yeh for DOP particles with a dielectric constant of 5.1. Figures 8-11 show the charge accumulated by particles for different values of particle radius, applied electric field, and  $N_0t$  product. Figures 12-14 show the dependence of charge upon particle size for fixed values of the electric field where  $N_0t = 1 \times 10^{13} \text{ sec}/\text{m}^3$ . In Figures 12-14, results obtained from the classical field equations are shown for comparison.

The curves predicted by the new theory in Figures 8-11, in most cases, follow the shape of the experimental data very closely. That is, they rise with a very steep slope until  $N_0t$  is  $1 \times 10^{13} \text{ sec}/\text{m}^3$  and then for larger values of  $N_0t$  the slope decreases smoothly and not too fast so that the curves do not flatten out quickly (as is the case in other approximate theories). The close agreement in the predicted curves and the experimental data for small values of  $N_0t$  indicates that this new theory gives an adequate description of the charging process during the time when both field and diffusional charging are

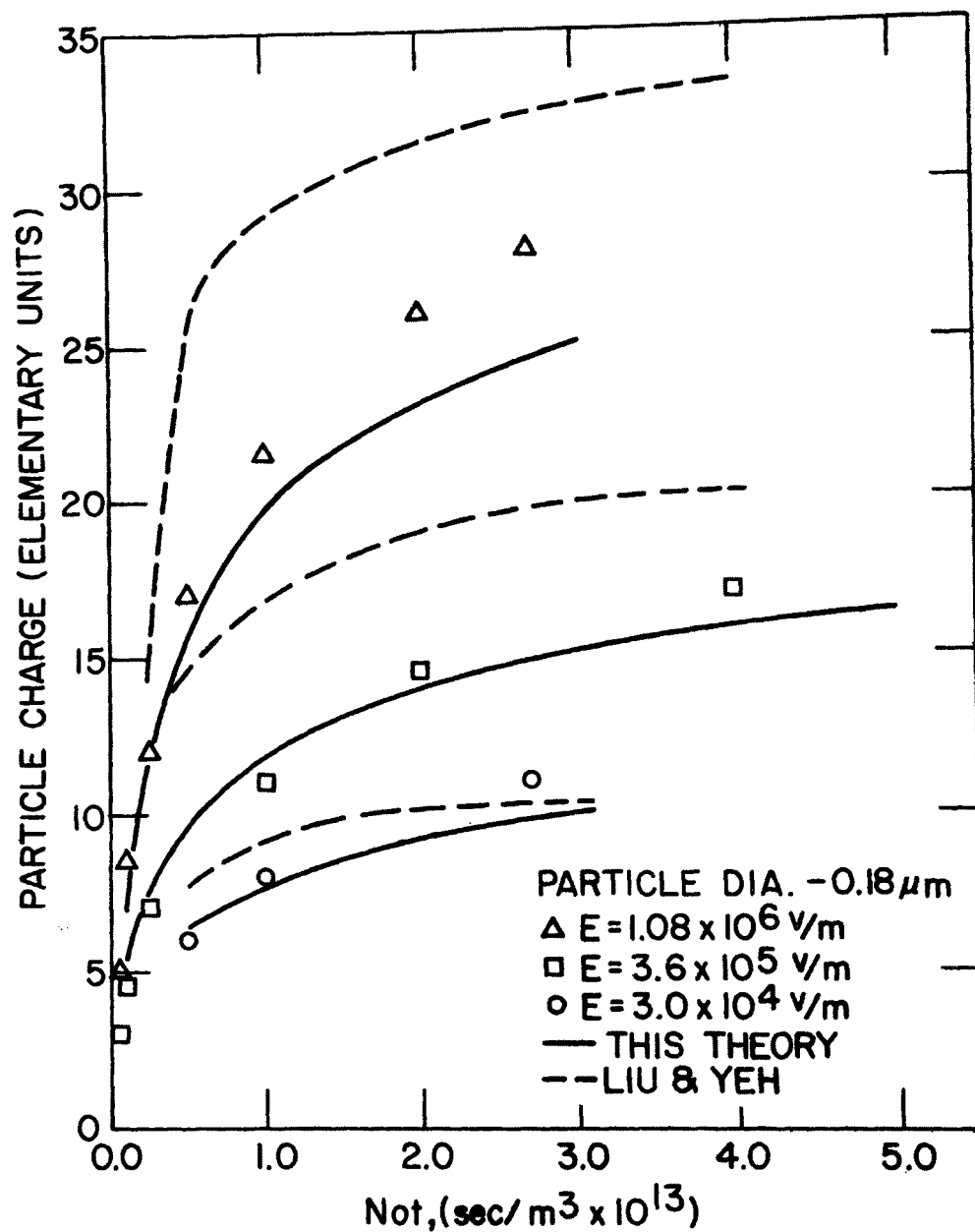


Figure 8. Comparison of charging theories and Hewitt's experimental data for a 0.18 μm diameter particle. In all theories and experiment the ion mobility is  $1.6 \times 10^{-4} \text{ m}^2/\text{V}\cdot\text{sec}$  and the ion mean thermal speed is 500 m/sec.



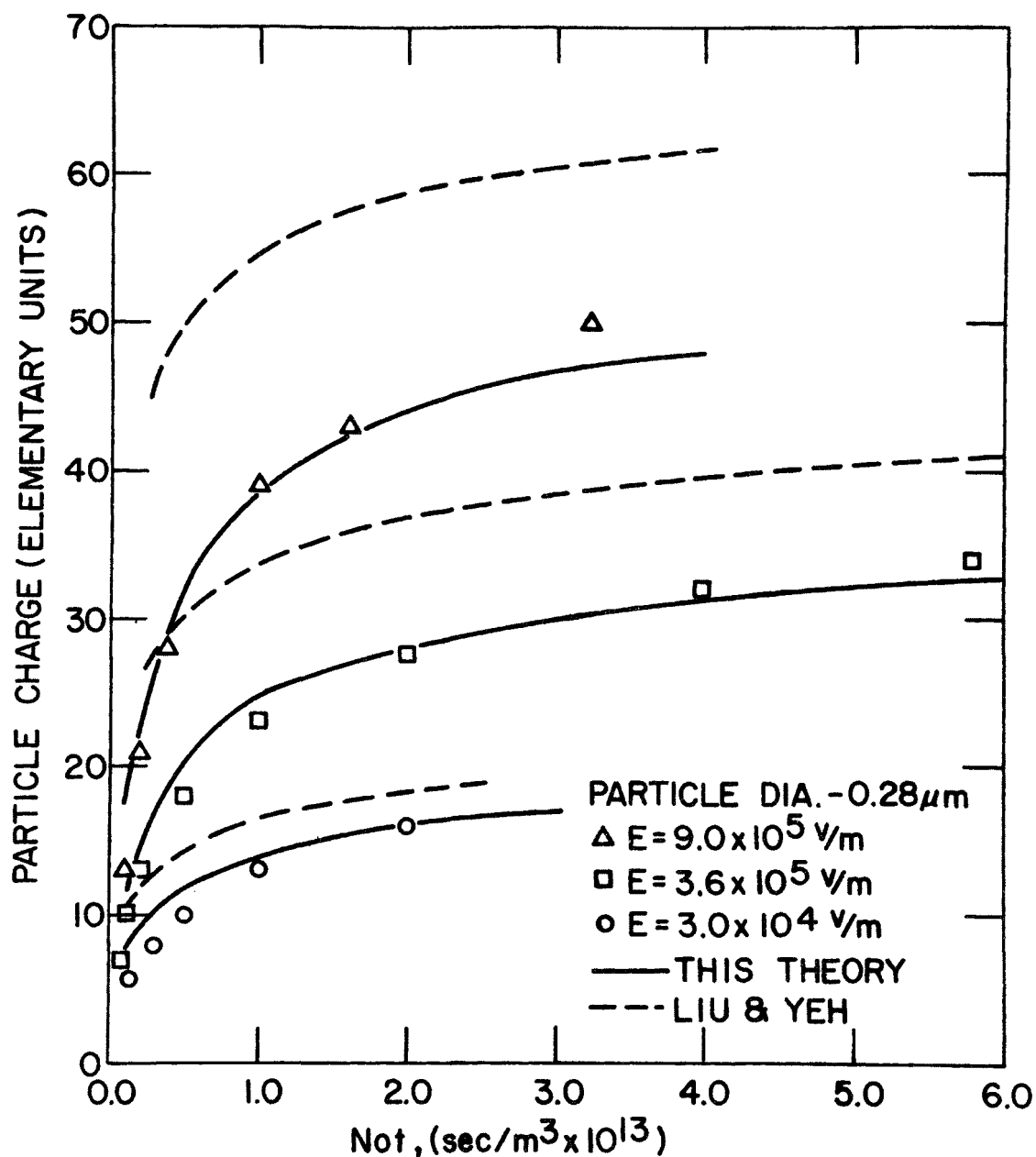


Figure 9. Comparison of charging theories and Hewitt's experimental data for a 0.28 μm diameter particle.  $\mu = 1.6 \times 10^{-4} \text{ m}^2/\text{V} \cdot \text{sec}$  and  $\bar{v} = 500 \text{ m/sec}$ .

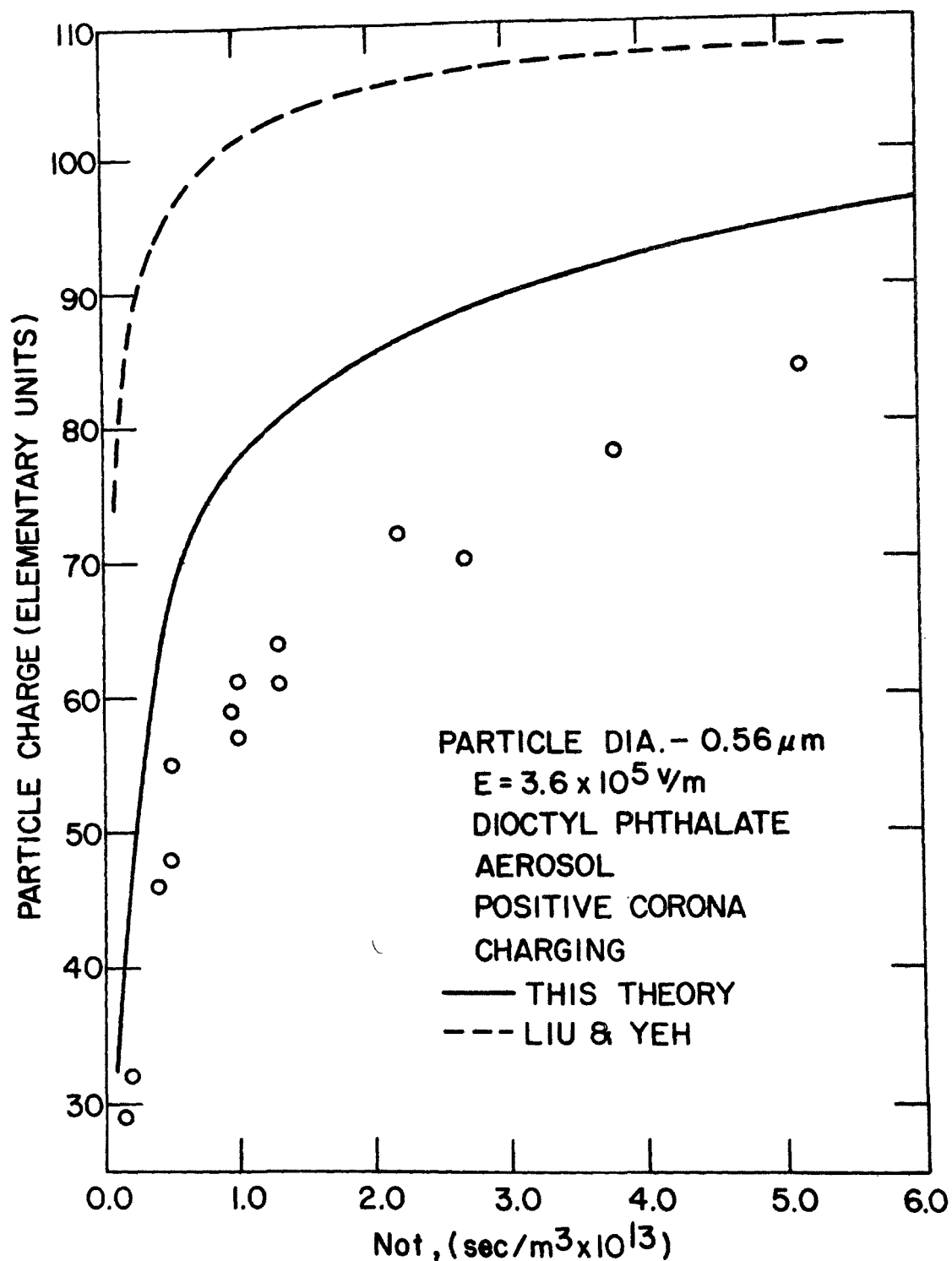


Figure 10. Comparison of charging theories and Hewitt's experimental data for  $0.56 \mu\text{m}$  diameter particle.  
 $\mu = 1.6 \times 10^{-4} \text{ m}^2/\text{V}\cdot\text{sec}$  and  $\bar{v} = 500 \text{ m/sec}$ .

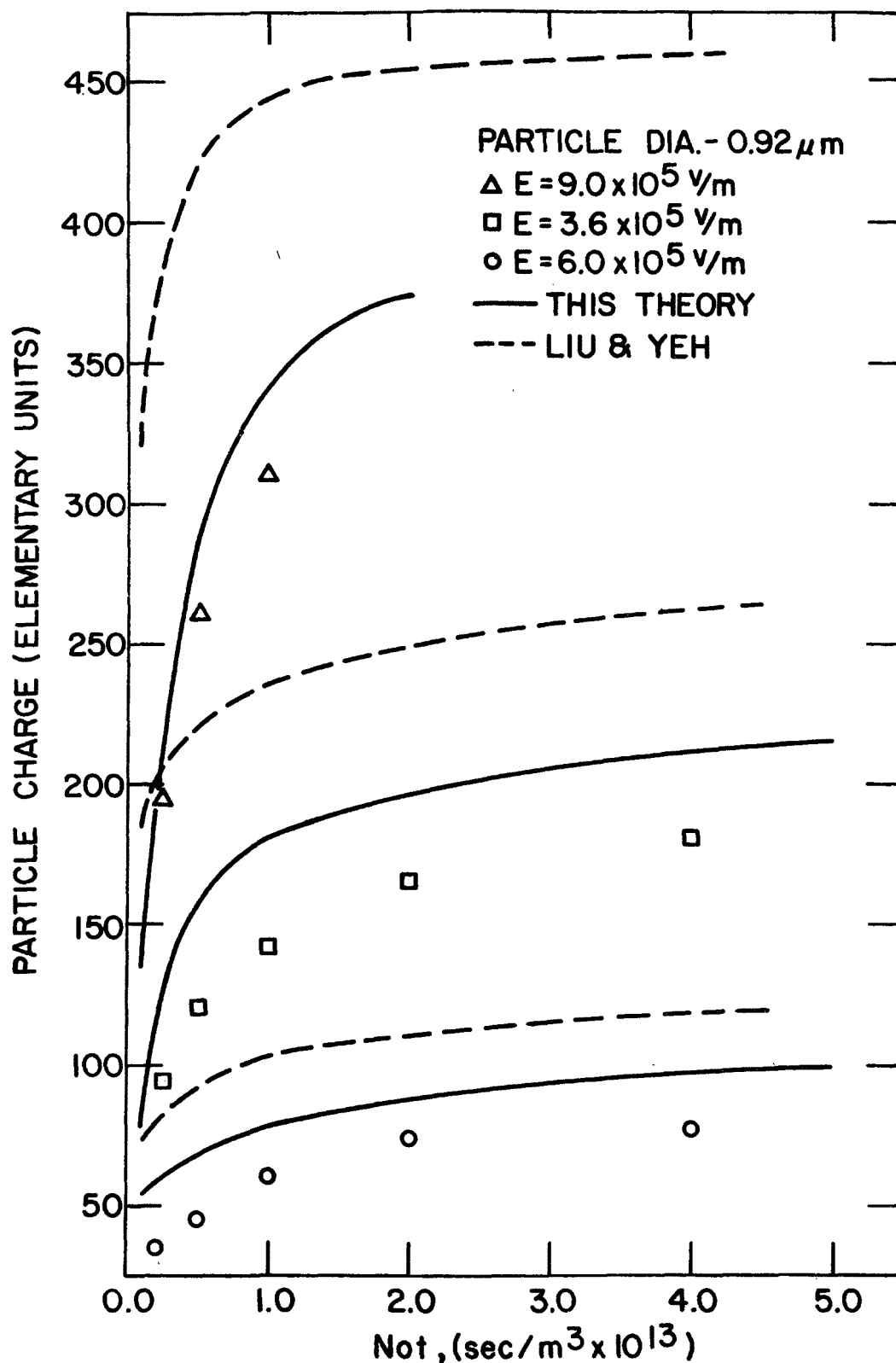


Figure 11. Comparison of charging theories and Hewitt's experimental data for a  $0.92 \mu\text{m}$  diameter particle.  $\mu = 1.6 \times 10^{-4} \text{ m}^2/\text{V}\cdot\text{sec}$  and  $\bar{v} = 500 \text{ m/sec}$ .

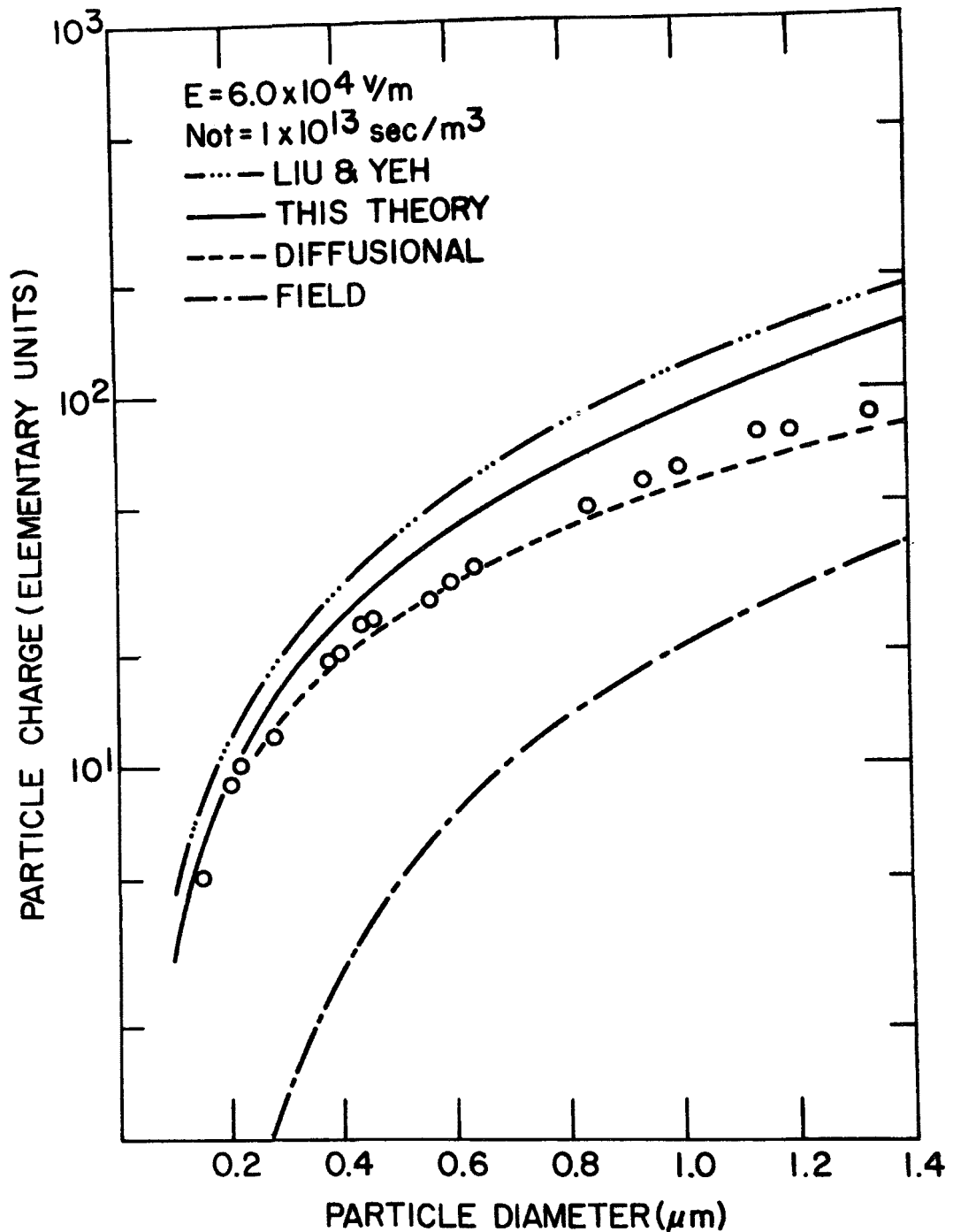


Figure 12. The dependence of charge upon particle size for a low electric field.  $N_0 t = 1 \times 10^{13} \text{ sec/m}^3$ ,  $\mu = 1.6 \times 10^{-4} \text{ m}^2/\text{V} \cdot \text{sec}$  and  $\bar{v} = 500 \text{ m/sec}$ . The experimental data are by Hewitt

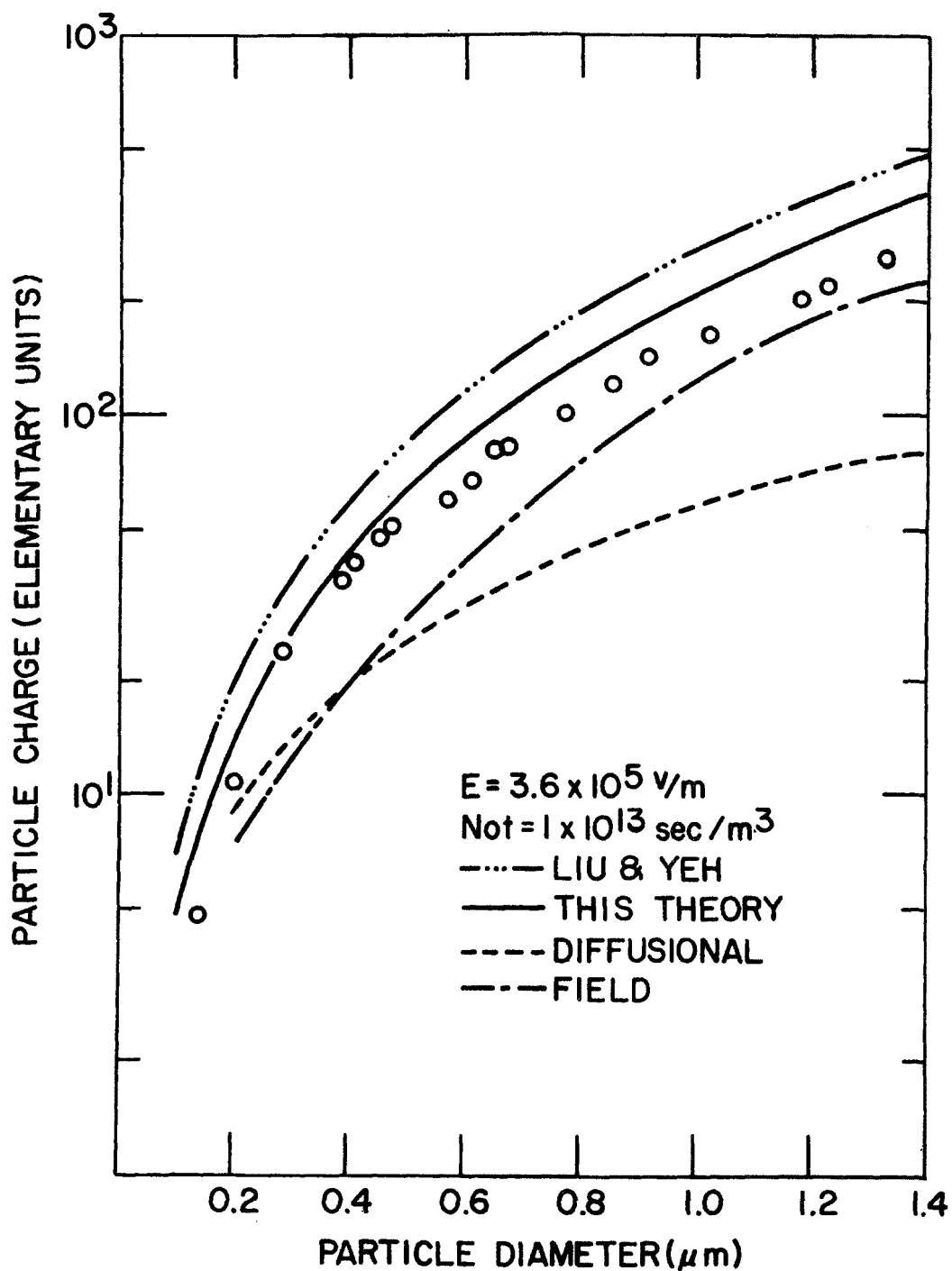


Figure 13. The dependence of charge upon particle size for a moderate electric field.  $N_0 t = 1 \times 10^{13} \text{ sec/m}^3$ ,  $\mu = 1.6 \times 10^{-4} \text{ m}^2/\text{V} \cdot \text{sec}$  and  $v = 500 \text{ m/sec}$ . The experimental data are by Hewitt

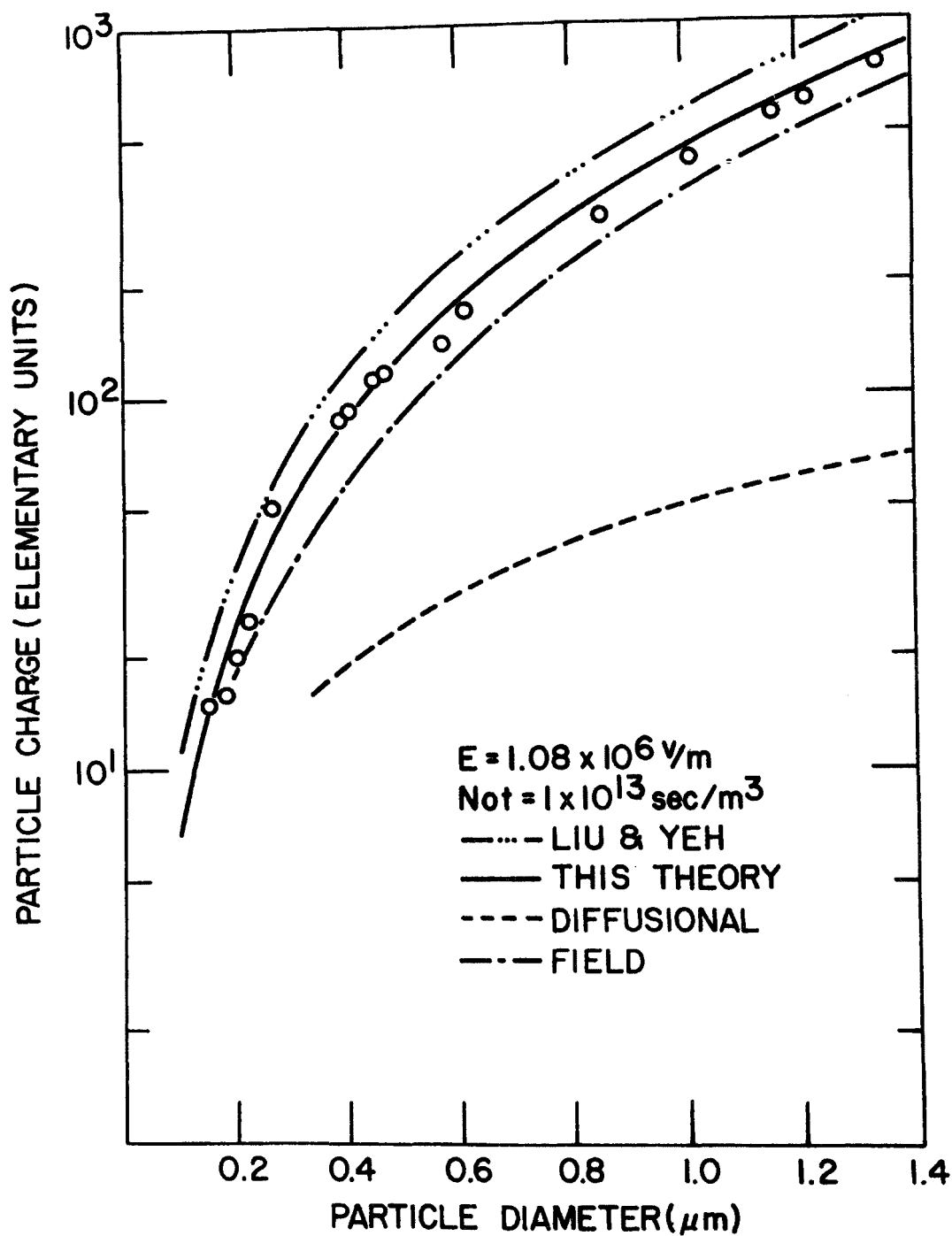


Figure 14. The dependence of charge upon particle size for a high electric field.  $N_0 t = 1 \times 10^{13} \text{ sec/m}^3$ ,  $\mu = 1.6 \times 10^{-4} \text{ m}^2/\text{V} \cdot \text{sec}$  and  $\bar{v} = 500 \text{ m/sec}$ . The experimental data are by Hewitt.

active. Also, the agreement with experiment for values of  $N_0t$  larger than  $1 \times 10^{13}$  sec/m<sup>3</sup> indicates that the effect of the external electric field on particle charging has been closely approximated in the diffusion processes which occur on Regions II and III of the particle's surface.

The curves of charge versus particle size given in Figures 12-14, indicate that the new theory gives good agreement with experimental data over a wide range of particle sizes and electric field strengths. Agreement for particle sizes up to 0.5  $\mu$ m diameter is excellent for low, medium, and high fields. The agreement between theory and experiment for particles larger than 0.5  $\mu$ m diameter improves as the electric field strength is increased. For the high electric field strength the agreement is excellent for all the particle sizes given. For the low electric field strength the classical diffusional charging theory gives good agreement with the experimental data for all particle sizes given. Such agreement is reasonable because the effect of an external electric field is not included in the classical diffusional charging equation. Thus, it is to be expected that agreement with the results predicted by the diffusion equation should improve as the applied field strength is reduced.

The charging rate predicted by the new theory is in excellent agreement with Hewitt's data for the 0.28  $\mu$ m particle in an applied field of  $3.6 \times 10^5$  V/m, whereas the charging rate given by Liu and Yeh using the ion distributions obtained from the quasi-static diffusion equation yields a curve that lies below Hewitt's data with considerable disagreement at certain practical values of  $N_0t$ .

The agreement between the new theory and Hewitt's experimental data is within 25% over the entire range of data that is available and is within 15% for practical charging times in electrostatic precipitators. Although the theory involves certain approximations in describing the charging process, the agreement with existing experimental data indicates that it can be used in its present form to describe particle charging with an accuracy comparable to the experimental accuracy of charge measurements.

## SECTION 4

### LABORATORY CHARGING EXPERIMENTS

#### APPARATUS AND METHODOLOGY

Because of the scope of measurements undertaken it was necessary to use various techniques for generating aerosols and for detecting them. The charge measurements were made, in general, by determining the electrical mobility of aerosol samples after subjecting them to controlled charging conditions. The laboratory setup for a given set of measurements thus consisted of an aerosol source, a charging apparatus, a mobility-selective device and a particle detector.

#### Mobility Analyzer

Measurements of electrical mobility of charged particles were made by determining particle trajectories in an electric field. Figure 15 is an assembly drawing of the mobility analyzer, and Figure 16 is a photograph of the assembled device. The design is based on a concentric cylinder geometry, and is similar to that used by Hewitt<sup>8</sup> in performing his experiments. Filtered air flows the length of the mobility analyzer under laminar flow conditions. Charged particles enter through a narrow annular passage, and experience a radial force toward the central cylinder due to the applied field between the inner and outer cylinder. By moving the scanning slit axially, the mobility of the charged particles can be measured. Since the particle mobility bears a well defined relationship to the charge on the particle, a measurement of mobility is sufficient to determine the charge. The overall dimensions of the instrument are dictated by the resolution that is desired, and the requirement that laminar flow be maintained between the concentric cylinders.

The relationship between particle trajectory length  $L$ , and mobility  $M$  in the mobility analyzer is<sup>8</sup>

$$M = \frac{Q}{2\pi LV} \ln \frac{r_2}{r_1} \quad (12)$$

where  $V$  = the applied voltage between inner and outer cylinder,

$Q$  = the volume rate of air flow between cylinders, and



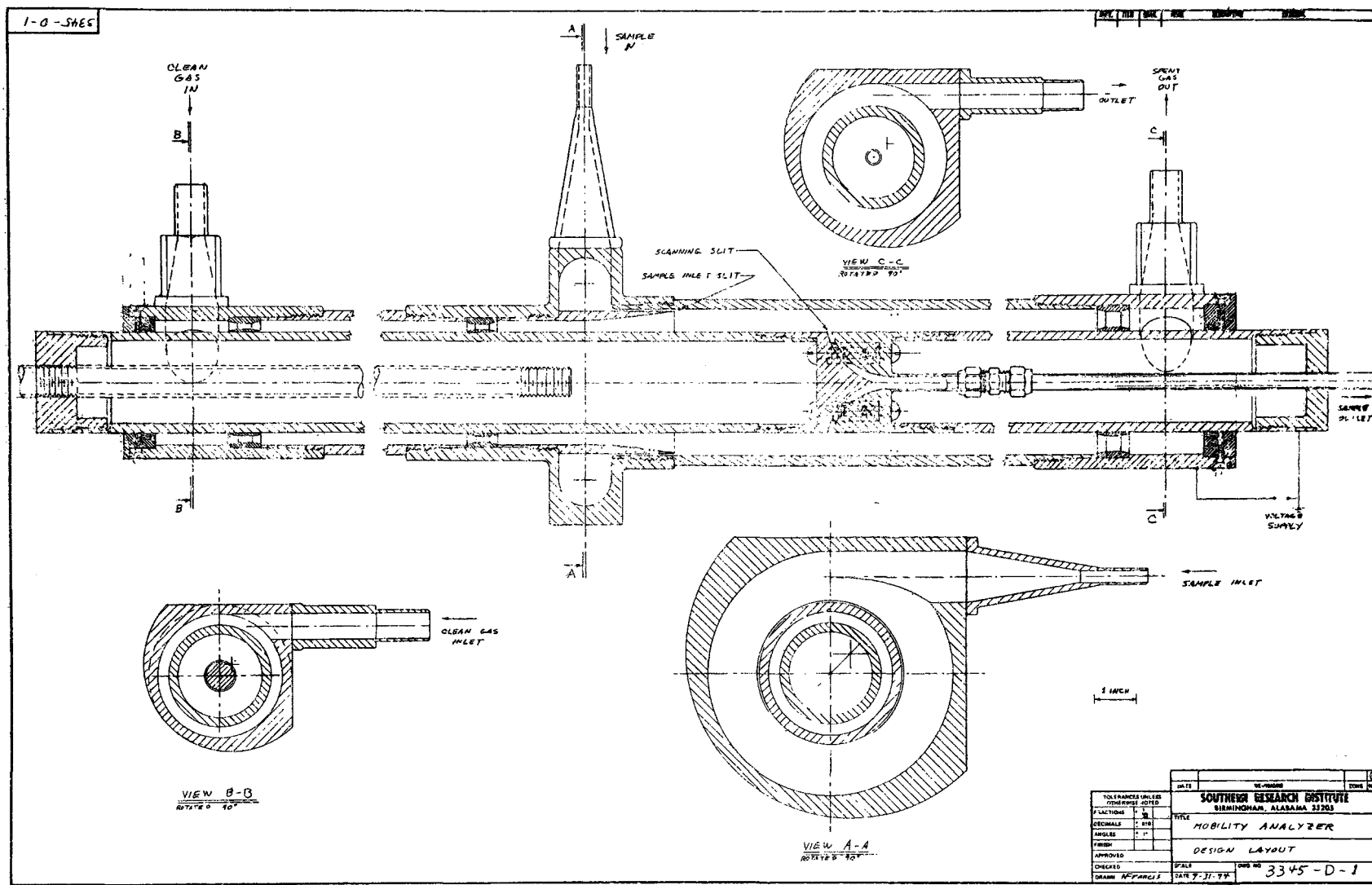


Figure 15. Mobility analyzer for measuring fine particle charge.

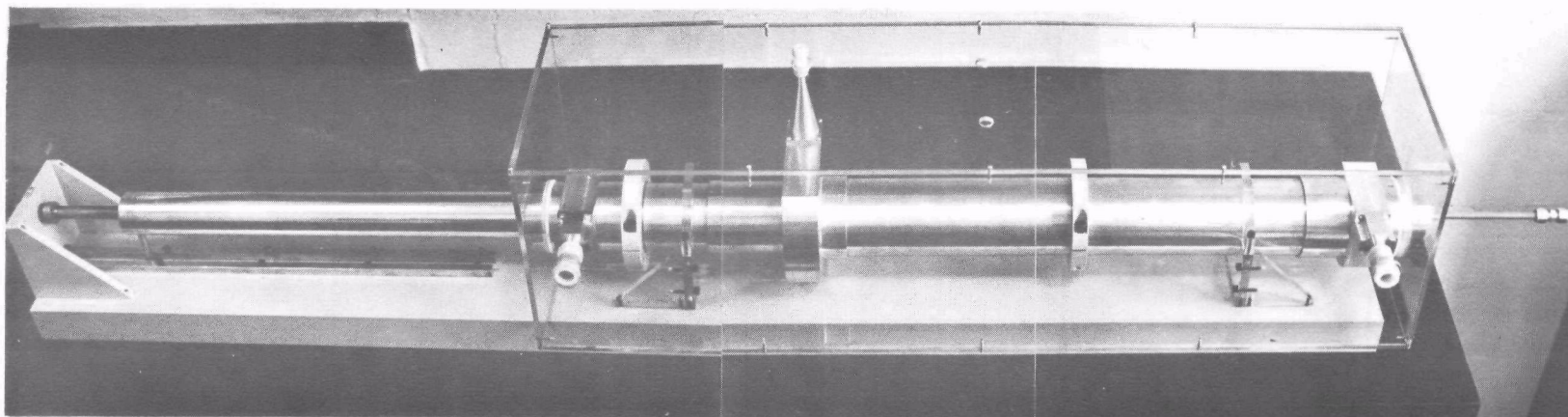


Figure 16. The Assembled SRI Mobility Analyzer

$r_1$  and  $r_2$  = the radii of the inner and outer cylinders, respectively.

Stokes' Law gives the mobility of a particle of radius  $a$ , carrying  $n$  elementary charges as

$$M = \frac{Cne}{6\pi\eta a} , \quad (13)$$

where  $\eta$  = the viscosity of the air,

$e$  = the electron charge, and

$C$  = the Cunningham slip correction factor.

Setting the above two expressions for the mobility equal to each other, we obtain

$$n = \frac{3Q\eta a}{CLVe} \ln \frac{r_2}{r_1}$$

for the charge on a particle in terms of measurable quantities. The factor  $C$  (Cunningham Correction factor) is dependent upon particle radius, and may be expressed as

$$C = 1 + \frac{\lambda}{a} \left\{ 1.2 + 0.4 \exp [(-0.88a)/\lambda] \right\} , \quad (14)$$

where  $\lambda$  is the mean free path of the air molecules.

### Aerosol Generators

In order to cover the range of particle diameters required in the charging experiments two different aerosol generators were used. For particles greater than about  $1 \mu\text{m}$  in diameter a vibrating orifice aerosol generator was used, and a Collison Nebulizer was used to produce particles less than  $2 \mu\text{m}$  in diameter.

#### Vibrating Orifice Aerosol Generator (VOAG)--

Figure 17 is a schematic diagram of the vibrating orifice aerosol generator (VOAG) which has been constructed for use on this project. This particular device was designed and built at Southern Research Institute, although similar devices have been reported by several authors previously.<sup>11,12,13</sup> A solution of known concentration is forced through a small orifice (5, 10, 15, or  $20 \mu\text{m}$  diameter). The orifice is attached to a piezoelectric ceramic which, under oscillatory electrical stimulation, will vibrate at a known frequency. This vibration imposes periodic perturbations on the liquid jet causing it to break up into uniformly-sized droplets. If the liquid flow rate and the

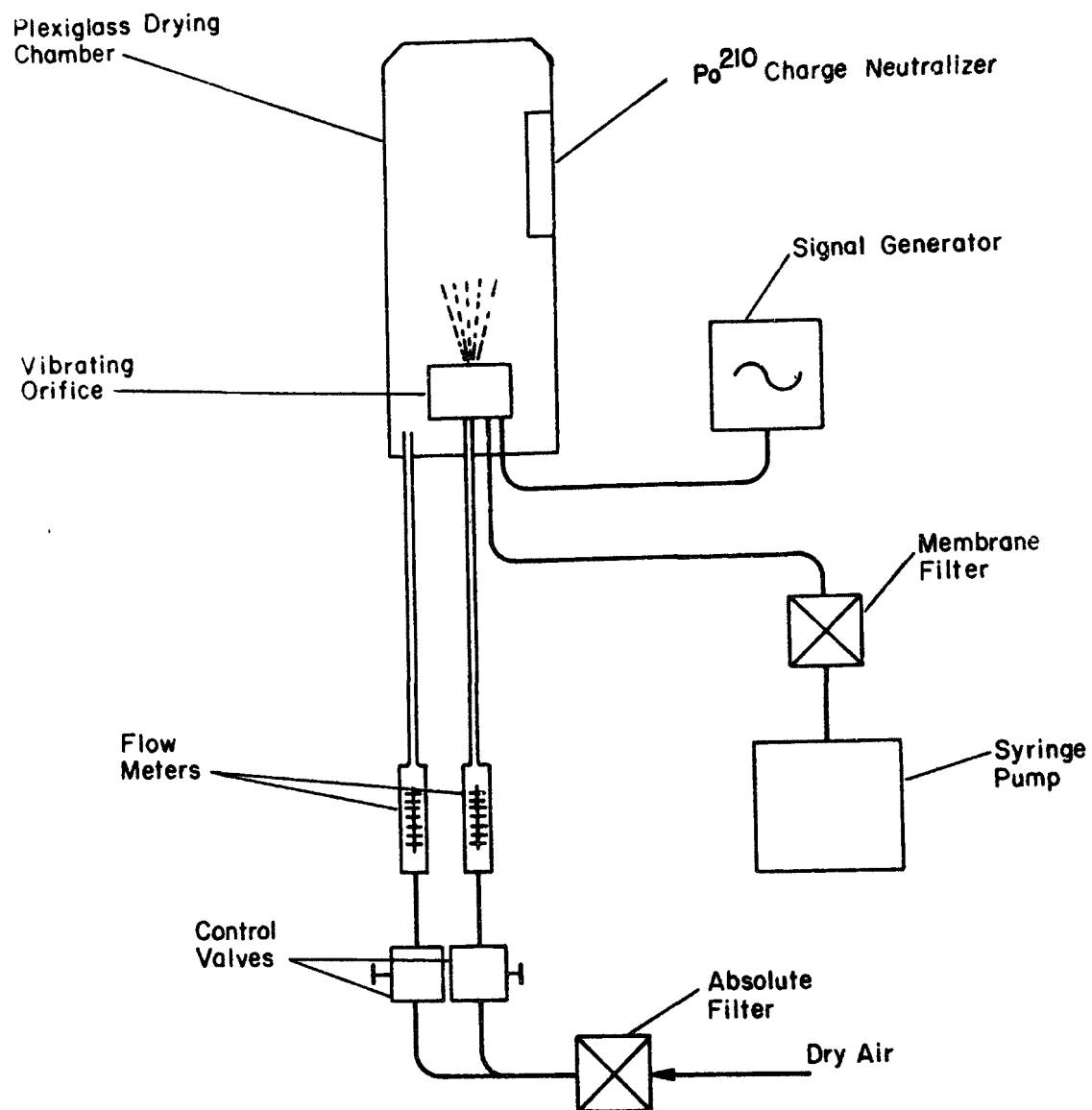


Figure 17. Schematic representation of the Vibrating Orifice Aerosol Generator

perturbation frequency are known, the droplet diameter can be readily calculated. The solvent evaporates from the droplets leaving the nonvolatile solute as a spherical residue. The ultimate dry particle diameter is calculated from the droplet diameter and the known concentration of the liquid solution.

To calculate the dry particle diameter, the expression

$$d_p = \left[ \frac{6QC}{60\pi f} \left( 1 + \frac{I}{C} \right) \right]^{1/3} \quad (15)$$

is used,<sup>14</sup>

where C = the solution concentration or volume of solute/volume of solution,

Q = the solution flow rate (cm<sup>3</sup>/min),

f - the perturbation frequency (Hz), and

I = the volumetric fraction of nonvolatile impurities.

The solution flow rate and the perturbation frequency cannot be varied independently without disturbing the monodispersity of the aerosol. For a given orifice and solution flow rate the perturbation frequency must be adjusted so that one and only one droplet breaks off the stream passing through the orifice in each oscillation. If the frequency is set too low, droplets may break off prematurely at random, and if the frequency is too high, not enough solution will be available to produce a well-formed droplet for each cycle. The system must, therefore, be tuned to provide a monodisperse aerosol.

Monodispersity can be tested by blowing a well-defined jet of air across the aerosol stream. Since the particle aerodynamics are strongly dependent upon particle diameter a uniform deflection of the particle stream indicates monodispersity. If the particles are polydisperse, deflection by a transverse air jet will break the stream up into two or more separate streams. By observing the stream deflection and adjusting the perturbation frequency one can produce a very monodisperse aerosol. The technique described above was employed each time the VOAG was set up to produce an aerosol. During system operation the particle monodispersity was also checked by drawing off filter samples for microscopic examination and measurement.

Because clogging was a severe problem with the smaller orifices the 20  $\mu$ m diameter orifice was used almost exclusively in this work. In order to avoid clogging the orifices were washed

with ultrasonic agitation and rinsed in the solvent to be used in aerosol generation. The liquid handling system was also flushed with the solvent.

The VOAG orifice was operated at the bottom of a plenum chamber made of a clear plastic cylinder six inches in diameter and three feet high. Air was introduced at the bottom of the cylinder to loft and disperse the particles. Sampling ports at the top of the chamber were used to extract the airborne particles. Figure 18 shows a 3.0  $\mu\text{m}$  diameter test aerosol generated from a solution of fluorescein in 0.1 N  $\text{NH}_4\text{OH}$ .

#### Collison Nebulizer--

A spray of liquid droplets is produced by atomizer action in the Collison nebulizer. As in the VOAG, the primary droplets, made up of a dilute solution of the desired aerosol material, are evaporated to leave a residue of much smaller size than the primary droplets. The diameter of the residual particles is a function of the solution concentration. Because the atomizer action produces a spray of polydisperse particles the use of the Collison Nebulizer was limited principally to dispersing suspensions of pre-sized insoluble particles, such as polystyrene latex.

#### Particle Charging Devices

Requirements for a particle charger for these experiments included independent control of the electric field strength and the ion density in the charging region. Three chargers were constructed and used in the course of this project. The first device was based on a wire-plate electrode geometry, and both of the other two were designed in a cylindrical configuration similar to Hewitt's device.<sup>6</sup> Of the three charging devices constructed the most satisfactory performance was achieved with the second "Hewitt-type" charger, illustrated in Figure 19.

In a simple corona system consisting of a corona electrode and a passive electrode the ion density and electric field strength cannot be varied independently of each other. For this reason, the particle charging devices were designed with a screen electrode between the discharge and passive electrodes. The space between the screen and the passive electrode was then used as the particle charging region.

In the Hewitt charger the screen and plate electrodes lie on concentric cylinders, and a corona wire is located along the cylinder axis. At first a shutter assembly was included to mask part of the screen area so that the aerosol residence time could be varied without adjusting the flow rate. The shutter had to be removed, however, because it contributed to sparking.

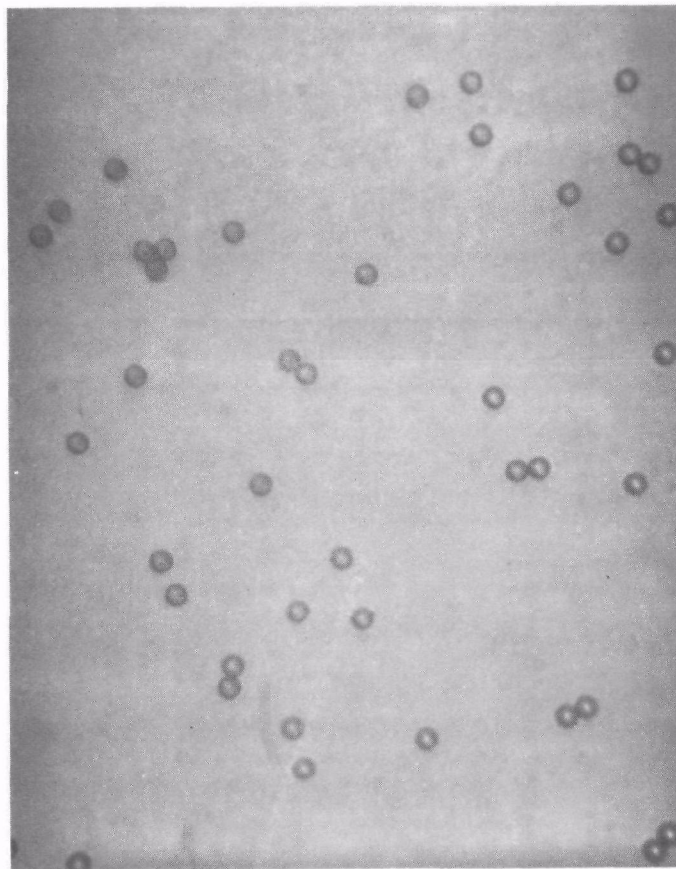


Figure 18. Ammonium fluorescein aerosol particles generated using the vibrating orifice generator. The particle diameters are  $3.0\text{ }\mu\text{m}$ .

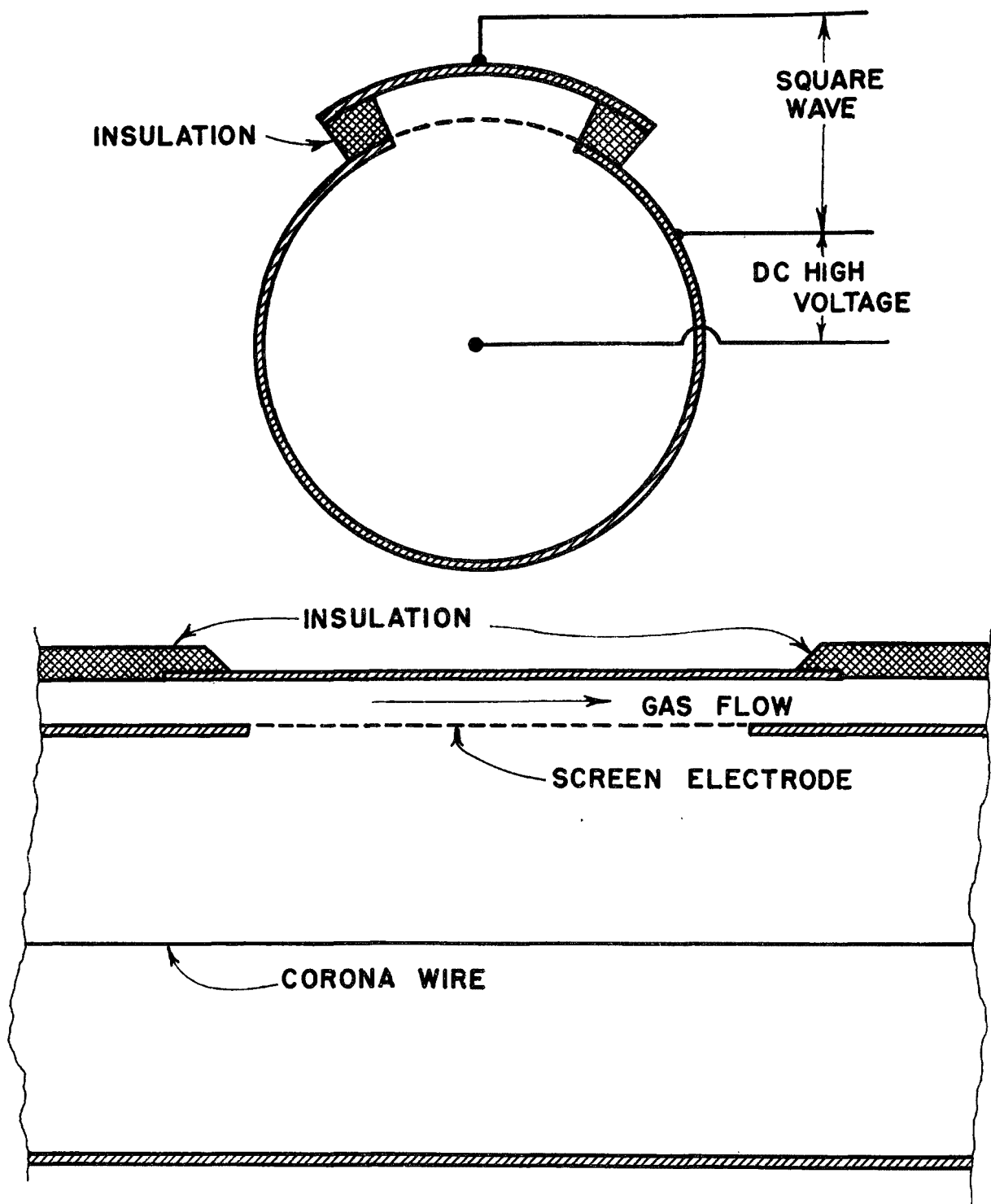


Figure 19. Cylindrical geometry particle charger, after Hewitt.<sup>8</sup> Ions originating at the corona wire pass through the screen electrode into the charging region between the screen and the center plate electrode.



Ions created in the corona region pass through the screen into the charging volume where they may become attached to test aerosol particles. In order to apply a charging field, a voltage is applied between the screen and plate. A dc voltage in this region would result in the precipitation of a large fraction of the particles on the plate. To avoid this, a square wave ac voltage was applied. This creates a uniform field and ion concentration during one half cycle, for charging, but reversing polarity limits the transverse motion of the charged particles to small amplitudes, thus minimizing the losses by precipitation. The ion density-time product ( $N_0 t$ ) can be varied by changing the gas flow rate or the corona current, either independently or simultaneously.

Because the electric field in the charging region is applied as a square wave the ion density-time product for particle charging must be multiplied by the fraction of time  $f_c$  in each cycle that the charging field is on. The corrected ion density-time product  $Nt$  is therefore

$$Nt = f_c N_0 t \quad . \quad (16)$$

The value of  $f_c$  was determined for various values of switching frequency and voltage by measurement on oscillograms. The period of time between the points at 90% of the maximum voltage on the leading and trailing edges of the waveform divided by the entire period of the wave was taken to be the value for  $f_c$ . Figure 20 shows the fraction  $f_c$  as a function of applied voltage between the screen and plate electrodes for switching frequencies of 100 and 200 Hz.

The ion density,  $N_0$ , during the charging period is determined from the applied electric field,  $E$ , across the charging region and the ion current,  $i$ , between the screen and plate electrodes. The ion density, electric field and current density,  $j$ , are related by the expression

$$j = N_0 e \mu E, \quad (17)$$

where  $e$  is the electronic charge, and  $\mu$  is the ion mobility. If we let  $A$  be the area of the plate electrode, then

$$i = jA,$$

and, substituting into equation (17), we obtain

$$N_0 = \frac{i}{e \mu A E} \quad .$$

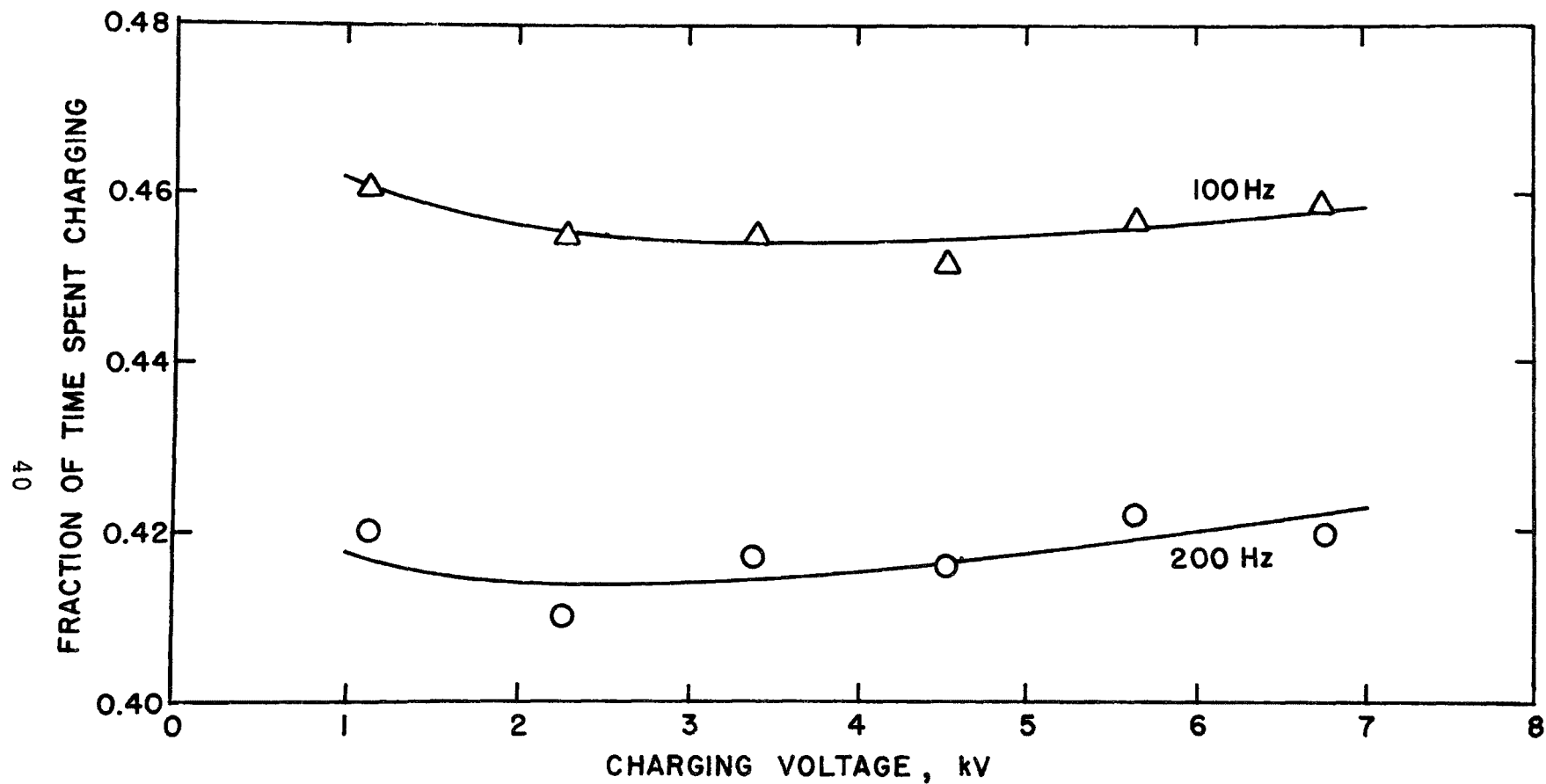


Figure 20. Fraction of time spent charging vs. charging voltage for Hewitt charger. No resistors in parallel, 100 and 200 Hz.

Correcting for ac excitation with the fraction  $f_c$ , we may write

$$Nt = \frac{if_c t}{e\mu AE},$$

where  $t$  is the transit time of an aerosol particle through the charging region.

Because various values for the ion mobility were found in the literature it was ultimately necessary to make separate determinations of ion mobility for the particular charger system geometry used, the ion polarity and the gas constitution. The method used to determine ion mobility will be discussed in greater detail later in this section.

Figure 21 displays  $Nt$  as a function of corona current for various values of average field in the charging region.

### Ion Mobility Measurements

The aerosols used in the charging experiments are derived by evaporation of solvent from solutions containing the desired aerosol material. Solvent molecules are thus present in the charger and will affect the ion mobility. The solvents most frequently used were  $H_2O$  and methanol.

In order to determine the ion mobility, I-V characteristics of the charger were measured with a solvent vapor present in the concentration normally resulting from aerosol generation. A non-linear curve fit was then applied, using the following theoretical expression relating the current and voltage in a cylindrical corona system:

$$V = \frac{V_0}{\ln b/a} \left\{ \left( \ln \frac{b}{a} \right) - 1 + \sqrt{1 + \frac{b^2 I}{2\pi\epsilon_0 \mu L} \left( \frac{\ln b/a}{V_0} \right)^2} \right. \\ \left. - \ln \left[ \frac{1}{2} + \frac{1}{2} \sqrt{1 + \frac{b^2 I}{2\pi\epsilon_0 \mu L} \left( \frac{\ln b/a}{V_0} \right)^2} \right] \right\} \quad (18)$$

where  $b$  = cylinder radius,

$a$  = corona wire radius,

$L$  = length of corona wire,

$V_0$  = corona inception voltage, and

$\mu$  = ion mobility.

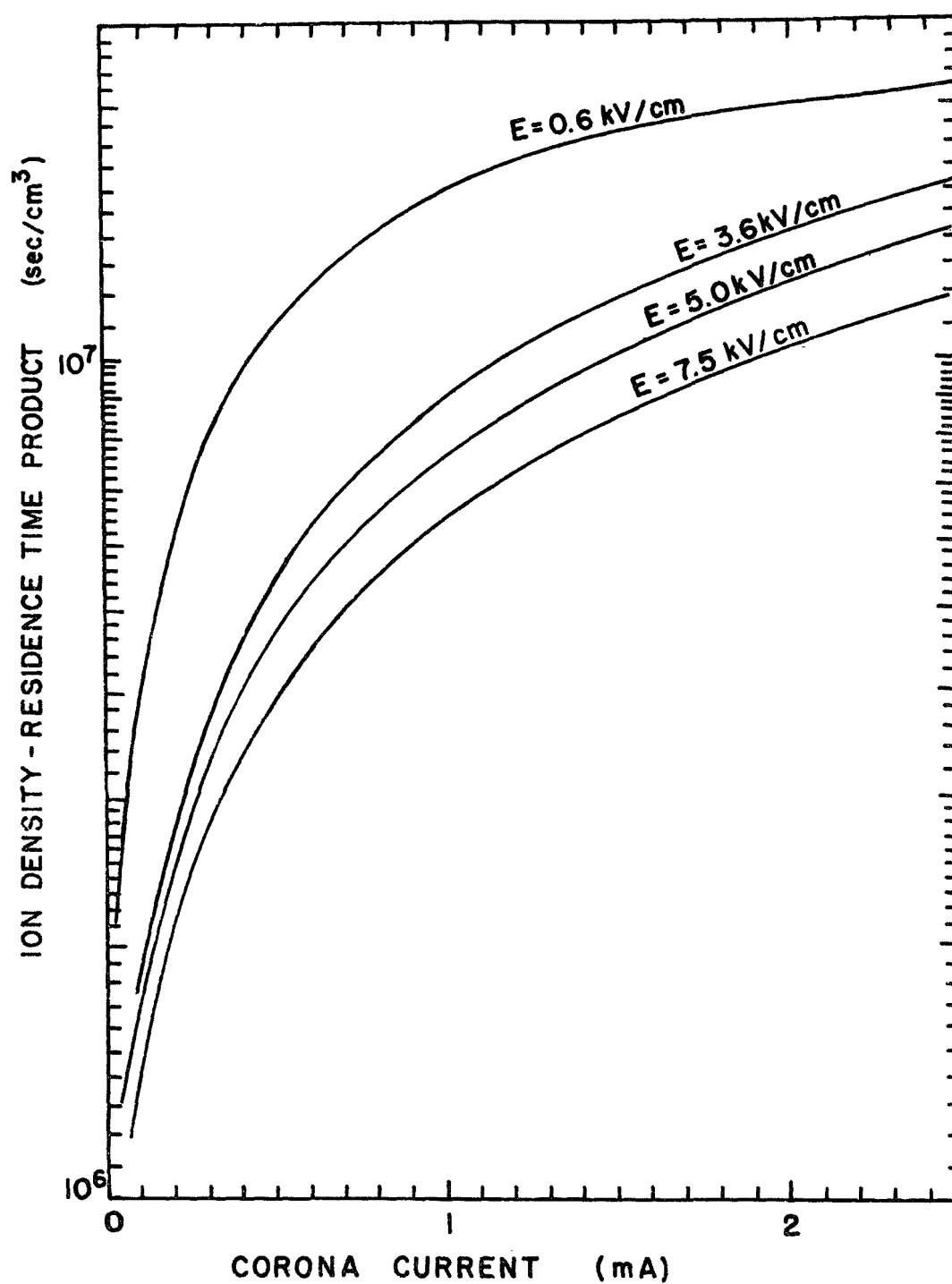


Figure 21.  $Nt$  as a function of corona current for various values of the average field in the charger.

The measured I-V characteristics of the Hewitt-type charger are presented in Figure 22 for three media: dry air, H<sub>2</sub>O in air, and methanol in air. The curve for dry air exhibits a discontinuity at approximately 21 kV. This effect may be a back corona resulting from a thin oxide layer on the inside surface of the cylinder, but in any case it is of no consequence in the charging experiments since a liquid solvent is invariably used in aerosol generation for this work. The behavior of the curves for methanol and H<sub>2</sub>O is stable up to current densities of about  $4 \times 10^{-6}$  A/cm<sup>2</sup>.

The curve fitting was applied to the lower part of each of the curves (current less than 2 mA) where anomalous behavior, such as inhomogeneous current, thermal effects, etc., are least likely to occur. The resulting mobility values were  $2.38 \times 10^{-4}$  m<sup>2</sup>/V·sec for H<sub>2</sub>O in air, and  $2.03 \times 10^{-4}$  m<sup>2</sup>/V·sec for methanol. For dry air the best fit also produced a calculated value of  $2.38 \times 10^{-4}$  m<sup>2</sup>/V·sec.

Bricard<sup>9</sup> has reported results of mobility measurements which indicate effects of ion aging. When the ion lifetime is increased, by decreasing the applied voltage or increasing the electrode separation, the measured mobility decreases. Apparently the more mobile ion species are quickly depleted from the conducting medium. For ion lifetimes less than 1 msec, as in our charging device, Bricard reports a mobility of  $2.3 \times 10^{-4}$  m<sup>2</sup>/V·sec for positive corona in dry air, which is within 5% of our determination.

#### Calibration of the Mobility Analyzer

A direct measurement of the ratio of charge to mass in a monodisperse aerosol taken from the outlet of the charger would provide data necessary for calculating a particle's electrical mobility which would allow a calibration of the SRI mobility analyzer.

Attempts to measure charge and mass directly, using a monodisperse polystyrene latex aerosol, yielded poor results due to particle leakage through (or around) the silver filter used to collect the aerosol sample.

A second series of experiments was undertaken using a monodisperse fluorescein aerosol. The sampling was again accomplished using a silver filter in an insulating plastic holder. Accumulated charge was measured with an electrometer.

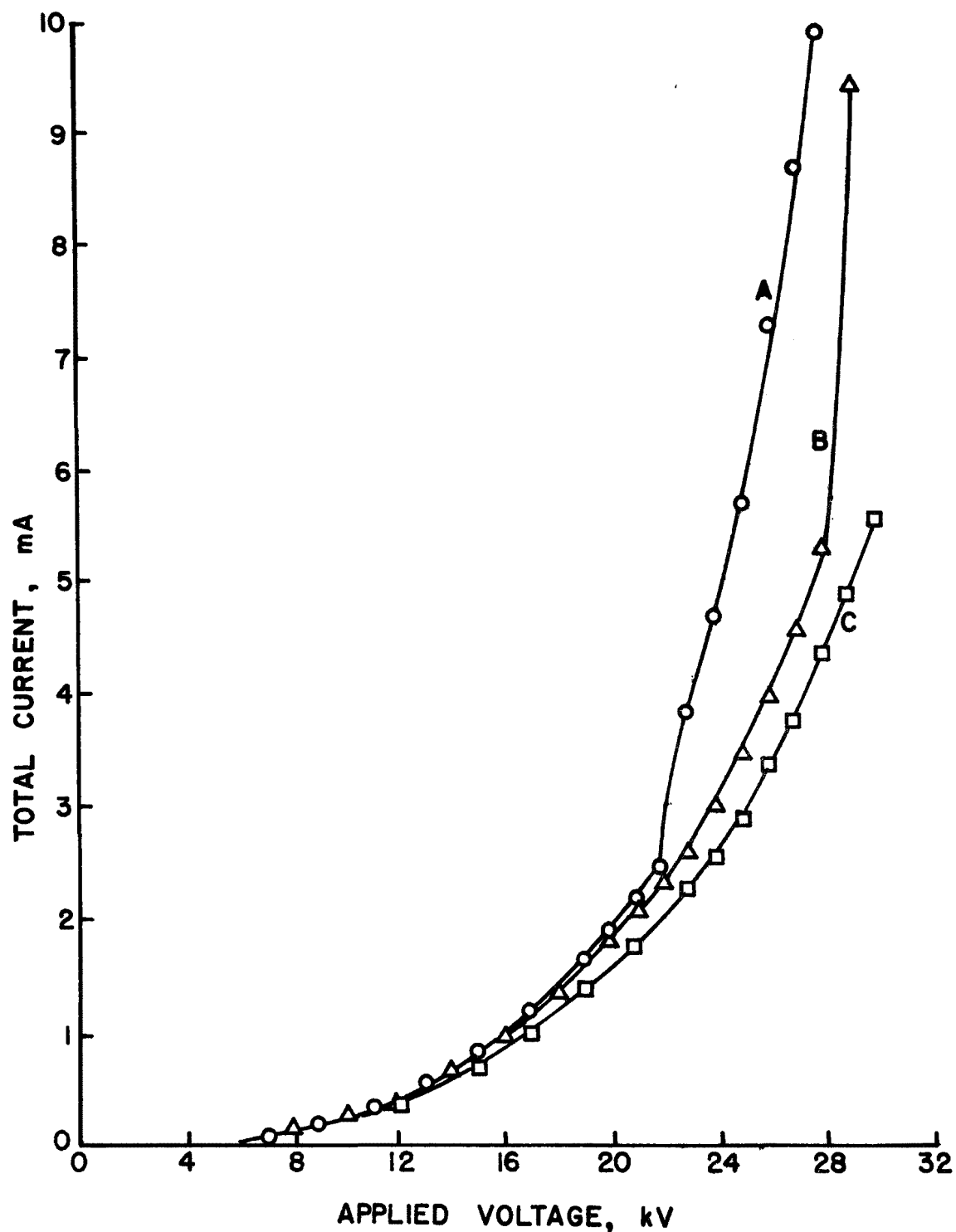


Figure 22. Charger I-V characteristics for three conducting media: (A) dry air, (B) water vapor in air, and (C) methanol in air.

Approximately two hours run time was required to collect a 0.5 milligram sample with a corresponding charge accumulation of about  $5.4 \times 10^{-9}$  coul. This corresponds to a collection rate of only  $7.5 \times 10^{-13}$  coulomb/sec. By turning off the aerosol generator and leaving all other apparatus energized, a background current of about  $2 \times 10^{-13}$  coul/sec was established. Fluctuations in the background current could therefore introduce substantial error in the measured charge. The Q/M measurements were thus not sufficiently consistent to provide the degree of accuracy required for system calibration.

A comparison of measurements of singly-charged particle diameters as determined by the mobility analyzer and by a diffusion battery has provided the best verification of mobility analyzer performance. The method of comparison is described in the following:

In the range of particle diameters between 0.02 and 0.06  $\mu\text{m}$ , a Collison nebulizer was used to produce an aerosol which was passed through a bipolar ionizing region produced by a  $\text{Kr}^{85}$  radiation source. In the resulting equilibrium condition, all except a negligibly small portion of the particles were, at most, singly charged. These particles were then introduced into the mobility analyzer.

For any fixed values of voltage and trajectory length in the mobility analyzer, only those particles with the mobility thus defined can pass through the analyzer. Since the particles are, at most, singly charged, and those with zero charge are eliminated by the mobility selection, the aerosol at the mobility analyzer output is essentially monodisperse. The diameter of the aerosol can be calculated from Stokes' law, using the value of electrical mobility defined by the voltage and trajectory length in the mobility analyzer.

By using various values for the voltage and trajectory length in the mobility analyzer a number of different monodisperse aerosols were generated, with diameters between 0.02 and 0.06  $\mu\text{m}$ . For each case the penetration through a 13 channel diffusion battery was determined by measuring the diffusion battery inlet and outlet concentrations with a condensation nuclei counter (Environment One, Model Rich 100). The data points shown in Figure 23 indicate the measured values of diffusion battery penetration as a function of the particle diameter, as determined from the mobility analyzer parameters, and with the assumption that the particles are singly charged. The solid line is the theoretical diffusion battery penetration as a function of particle diameter. There is considerable scatter in these data, particularly for small values of diffusion battery penetration. Aerosol source fluctuations are probably responsible for at least some of the scatter, and for the smaller values of penetration the condensation nuclei counter was operating in a less sensitive range than for the larger values.

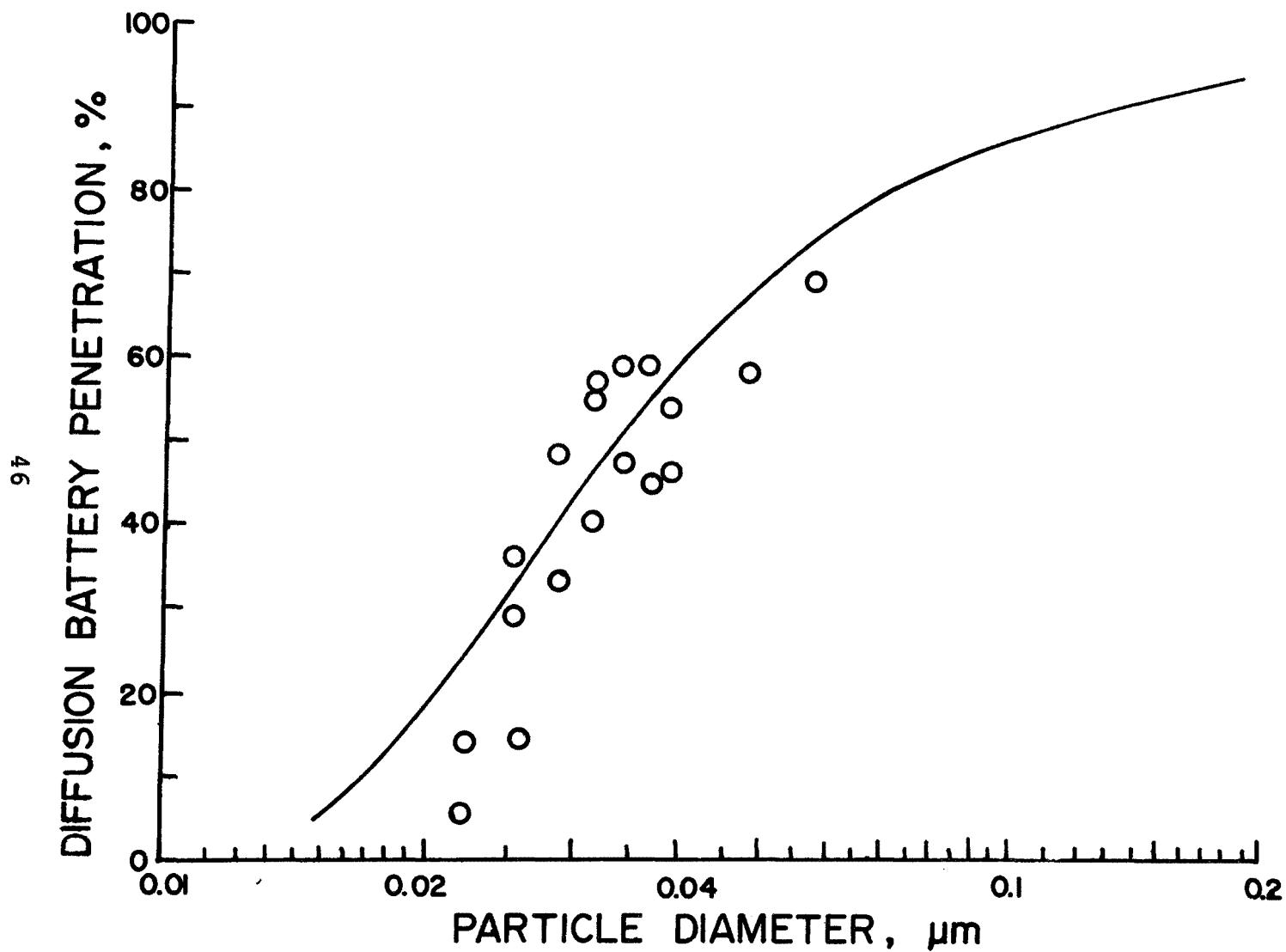


Figure 23. Penetration of a 13 channel diffusion battery by particles of various sizes as determined by mobility analyzer measurements on singly charged particles. The continuous line is the theoretical penetration as a function of particle diameter.



## Computer Program

A FORTRAN IV computer program was written which takes raw experimental data as input, computes the mobility and charge corresponding to each data point, averages the data taken for each value of  $Nt$ , calculates standard deviations, determines the charge predicted at that value of  $Nt$  by the SRI theory, and calculates a percentage difference between the average charge and predicted charge. Sample printouts, showing a tabulation of the input data and the resulting statistical summary are presented in Figures 24 and 25.

## EXPERIMENTAL RESULTS

### Rectangular Geometry Charger

The first measurements of particle mobility were made on monodisperse aerosols of dioctyl phthalate (DOP), generated by a VOAG, and charged by use of the rectangular charging system. Values of ion density-residence time product ( $Nt$ ) between  $1.0 \times 10^{12}$  and  $1.0 \times 10^{13}$  sec/m<sup>3</sup> were used, with charging field strength values of  $6.0 \times 10^4$  to  $5.0 \times 10^5$  V/m. The number of charges per particle as a function of  $Nt$  product for two values of charging field strength are presented in Figure 26 for a 0.56  $\mu$ m diameter DOP aerosol. The theoretical charging curves are also illustrated for comparison. For this particle size the theory predicts a larger number of charges per particle for a field strength of  $6.0 \times 10^4$  V/m, than the measured values. But for a charging field strength of  $2.0 \times 10^5$  V/m the theoretical values are lower than those measured in the experiments.

Similar results are found for a 1.4  $\mu$ m DOP aerosol, as shown in Figure 27. Fairly good agreement between theory and experiment occurs for intermediate values of the charging field. But the theoretical values are below experiment for a high charging field and above the measured values for a low charging field.

It was found that severe turbulence effects occur in this charging device for large values of  $Nt$ , thus limiting the effective operating range of the charger. For this reason the rectangular charger was replaced by a device of cylindrical geometry, similar in design to those used by Hewitt<sup>8</sup> in his charging experiments.

### First Hewitt Charger

Mobility measurements were made on charged monodisperse DOP aerosols ranging from 1.0 to 7.0  $\mu$ m in diameter. Charging field strengths were between  $8.0 \times 10^3$  to  $8.0 \times 10^5$  V/m. The ion concentration-residence time product ( $Nt$ ) ranged from  $2 \times 10^{12}$  sec/m<sup>3</sup> to a maximum of  $4 \times 10^{13}$  sec/m<sup>3</sup>. Figures 28 through 31 show the results of these experiments. The graphs are ordered by particle

1.000E+00 MICRON DIAMETER  
5.100E+00 DIELECTRIC CONSTANT

4.000E+03 CHARGING FIELD STRENGTH, V/CM  
1.356E+04 VOLTS PEAK TO PEAK, OBSERVED  
1.530E+04 VOLTS PEAK TO PEAK ACTUAL  
4.000E+02 VOLTS ON MOBILITY ANALYZER  
5.600E+01 SCFM FLOW IN MOBILITY ANALYZER

POSITIVE ION CHARGING  
2.200E+00 CM\*\*2/(VOLT-SEC) ION MOBILITY  
500.0 M/S MEAN THERMAL SPEED  
298.0 DEGREES K TEMPERATURE

CORONA CURRENT (MILLIAMPERES)	NT (SEC/M**3)	LENGTH (CM)	MOBILITY (M**2/VOLT-SEC)	CHARGE (ELEMENTARY UNITS)
1.350E-01	2.000E+12	2.450E+01	2.667E-07	2.493E+02
1.350E-01	2.000E+12	2.200E+01	2.970E-07	2.776E+02
1.400E-01	2.000E+12	1.980E+01	3.300E-07	3.085E+02
1.400E-01	2.000E+12	1.920E+01	3.403E-07	3.181E+02
2.500E-01	3.000E+12	2.060E+01	3.172E-07	2.965E+02
2.500E-01	3.000E+12	1.960E+01	3.334E-07	3.116E+02
2.590E-01	3.000E+12	1.670E+01	3.913E-07	3.658E+02
2.590E-01	3.000E+12	1.600E+01	4.084E-07	3.818E+02
3.750E-01	4.000E+12	1.910E+01	3.421E-07	3.198E+02
3.750E-01	4.000E+12	1.800E+01	3.630E-07	3.393E+02
3.820E-01	4.000E+12	1.500E+01	4.356E-07	4.072E+02
3.820E-01	4.000E+12	1.440E+01	4.537E-07	4.242E+02
5.250E-01	5.000E+12	1.750E+01	3.734E-07	3.490E+02
5.250E-01	5.000E+12	1.690E+01	3.866E-07	3.614E+02
5.380E-01	5.000E+12	1.460E+01	4.475E-07	4.184E+02
5.380E-01	5.000E+12	1.440E+01	4.537E-07	4.242E+02
6.800E-01	6.000E+12	1.670E+01	3.913E-07	3.658E+02
6.800E-01	6.000E+12	1.640E+01	3.984E-07	3.724E+02
6.820E-01	6.000E+12	1.350E+01	4.840E-07	4.525E+02
6.820E-01	6.000E+12	1.280E+01	5.105E-07	4.772E+02
7.820E-01	7.000E+12	1.640E+01	3.984E-07	3.724E+02
7.820E-01	7.000E+12	1.600E+01	4.084E-07	3.818E+02
8.520E-01	7.000E+12	1.300E+01	5.026E-07	4.699E+02
8.520E-01	7.000E+12	1.260E+01	5.186E-07	4.848E+02
1.020E+00	8.000E+12	1.590E+01	4.109E-07	3.842E+02
1.020E+00	8.000E+12	1.480E+01	4.415E-07	4.127E+02
1.050E+00	8.000E+12	1.260E+01	5.186E-07	4.848E+02
1.050E+00	8.000E+12	1.200E+01	5.445E-07	5.090E+02
1.210E+00	9.000E+12	1.530E+01	4.271E-07	3.992E+02
1.210E+00	9.000E+12	1.460E+01	4.475E-07	4.184E+02
1.280E+00	9.000E+12	1.230E+01	5.312E-07	4.966E+02
1.280E+00	9.000E+12	1.140E+01	5.732E-07	5.358E+02
1.420E+00	1.000E+13	1.480E+01	4.415E-07	4.127E+02
1.420E+00	1.000E+13	1.420E+01	4.601E-07	4.302E+02
1.550E+00	1.000E+13	1.220E+01	5.356E-07	5.007E+02
1.550E+00	1.000E+13	1.110E+01	5.886E-07	5.503E+02

Figure 24. First part of sample printout of program used in analyzing the experimental data.

1.000E+00 MICRON DIAMETER PARTICLE  
 8.000E+03 CHARGING FIELD STRENGTH, VOLTS/CM  
 5.100E+00 DIELECTRIC CONSTANT

2.200E+00 CM\*\*2/(VOLT-SEC) ION MOBILITY  
 500.0 M/S MEAN THERMAL SPEED  
 298.0 DEGRFES K TEMPERATURE

POSITIVE ION CHARGING FOR DOP  
 2.991E+02 SATURATION CHARGE

NT (SEC/M**3)	AVERAGE MOBILITY (M**2/V*SEC)	MOBILITY STD-DEV. (M**2/V*SEC)	AVERAGE CHARGE (ELEM UNITS)	CHARGE STD-DEV. (ELEM UNITS)	SRI THEORY CHARGE (ELEM UNITS)	EXPT.-THEORY CHARGE (ELEM UNITS)	PERCENT DIFF. CHARGE
2.000E+12	3.085E-07	3.344E-08	2.884E+02	3.126E+01	2.261E+02	6.234F+01	2.423E+01
3.000E+12	3.625E-07	4.410E-08	3.389E+02	4.122E+01	3.174E+02	1.955F+01	5.938E+00
4.000E+12	3.986E-07	5.438E-08	3.726E+02	5.083E+01	3.366E+02	3.604E+01	1.016E+01
5.000E+12	4.153E-07	4.122E-08	3.883E+02	3.853E+01	3.482E+02	4.006F+01	1.088E+01
6.000E+12	4.460E-07	6.017E-08	4.170E+02	5.625E+01	3.568E+02	6.020E+01	1.556E+01
7.000E+12	4.570E-07	6.237E-08	4.272E+02	5.830E+01	3.635E+02	6.372F+01	1.612E+01
8.000E+12	4.789E-07	6.297E-08	4.477E+02	5.886E+01	3.690E+02	7.868E+01	1.927E+01
9.000E+12	4.947E-07	6.901E-08	4.625E+02	6.452E+01	3.736E+02	8.888E+01	2.126E+01
1.000E+13	5.026E-07	6.219E-08	4.698E+02	5.814E+01	3.776E+02	9.223F+01	2.177E+01

Figure 25. Second part of sample printout of program used in analyzing the experimental data.

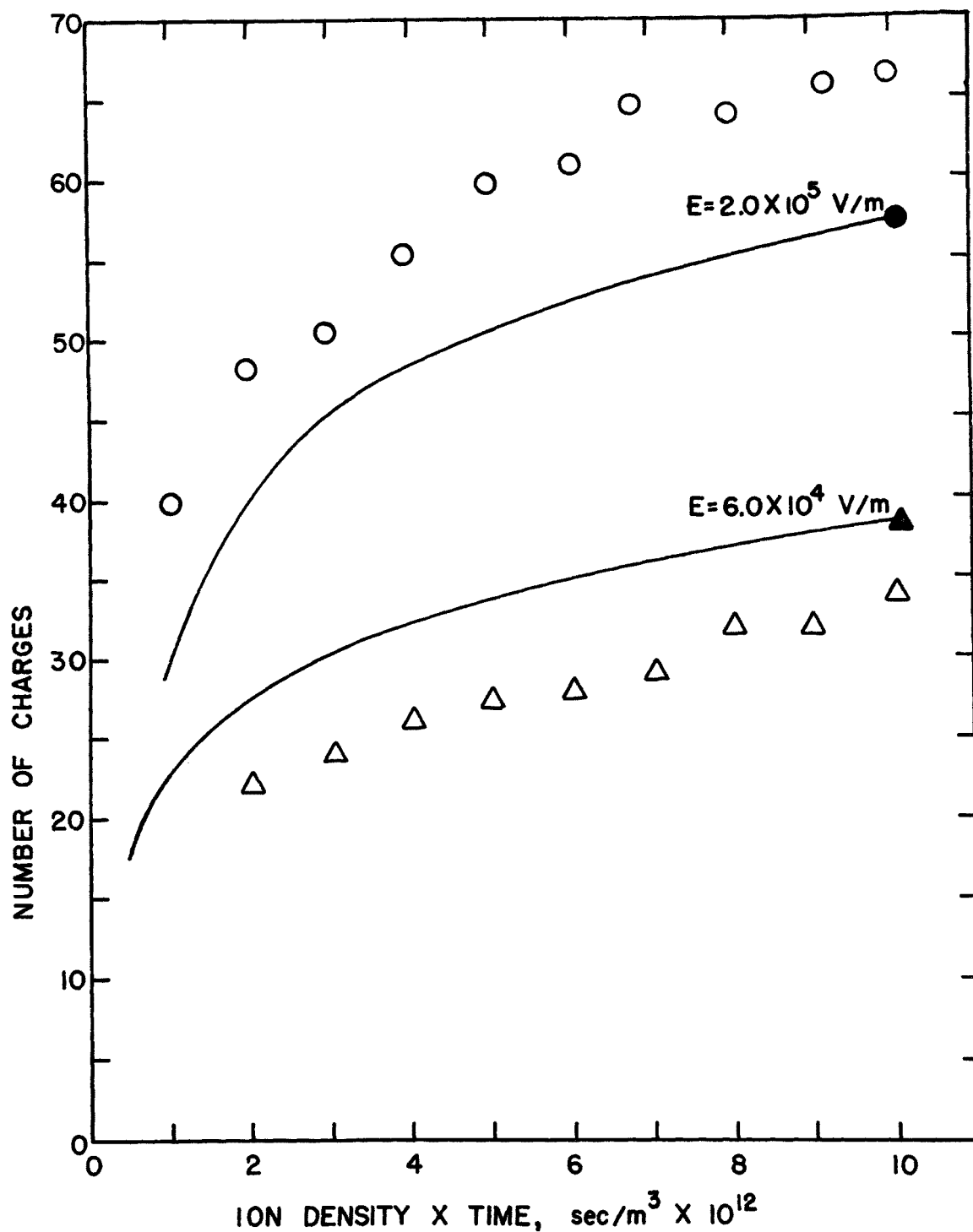


Figure 26. Number of charges per particle as a function of ion density-residence time product,  $(Nt)$  for a  $0.56 \mu\text{m}$  diameter dioctyl phthalate (DOP) aerosol. The continuous lines represent the theoretical calculations corresponding to these charging conditions.

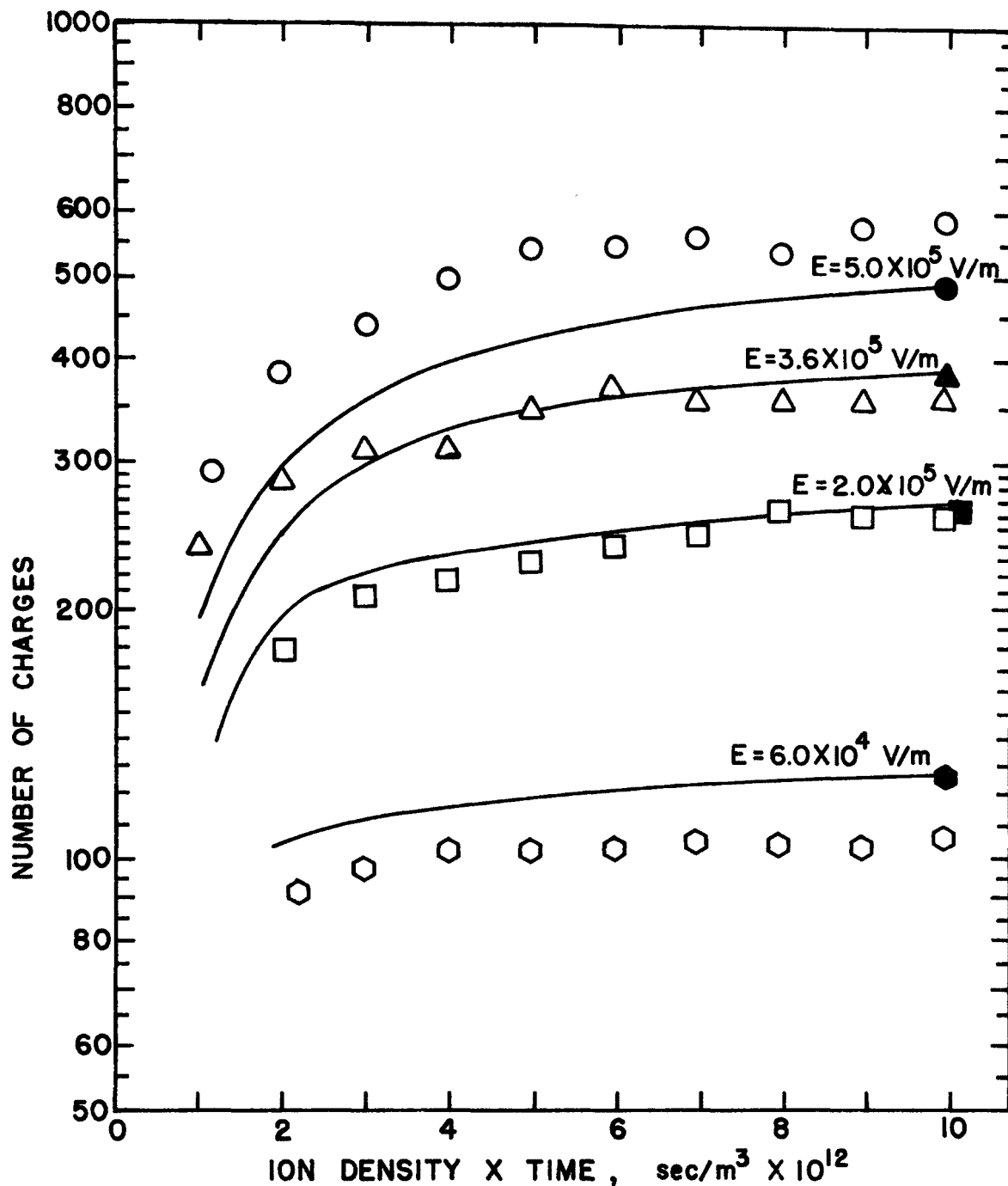


Figure 27. Number of charges per particle as a function of the  $Nt$  product for a  $1.4 \mu\text{m}$  diameter DOP aerosol. Four different values of the charging field strength were used. The blacked-in symbols denote the theoretical curves corresponding to the data plotted with the open symbols of the same shape.

diameter. Each graph shows the experimentally determined values of charge per particle along with the values predicted by the theory described in section 3.

Figures 28 and 29 present the results for a 1.0  $\mu\text{m}$  DOP aerosol. As in our previous results the theoretical predictions of charge are lower than those found in the experiments for large values of the charging field, and higher than the experimental values in the lowest range of charging fields.

Calculations were made to investigate the significance of possible errors in particle size. Particle diameters from 0.8  $\mu\text{m}$  to 1.2  $\mu\text{m}$  were used in the charging theory and compared with data from a 1.0  $\mu\text{m}$  diameter particle. It was found that for a charging field strength of  $6.0 \times 10^4$  V/m a 0.8  $\mu\text{m}$  diameter particle produces a lower percentage difference between theory and experiment, whereas at higher field strengths a 1.2  $\mu\text{m}$  particle gives a better fit. Table 1 summarizes this comparison. The concentration of DOP in methanol required to produce a 1.2  $\mu\text{m}$  diameter DOP aerosol is approximately 2.7 times that required to produce a 1.0  $\mu\text{m}$  diameter DOP aerosol particle. Thus it is unlikely the particle diameter was as large as 1.2  $\mu\text{m}$ . Also, as particle diameter increases the uncertainty of concentration decreases. We conclude from this exercise that any lack of agreement between theory and experiment is not due primarily to errors in particle diameter. The source of the discrepancies may be related to a dependence of ion mobility on the electric field strength.<sup>9</sup> Since the calculation of the ion density depends upon the value determined for the mobility of the ions, any uncertainty in the mobility will be reflected in the  $Nt$  product, which will, in turn, affect the particle charging calculations.

Figure 30 shows the results for 2.0  $\mu\text{m}$  diameter DOP particles. In this case the tendency continues for experiment to rise from below to above theory as the charging field strength is increased from 0.6 kV/cm to 7.5 kV/cm. However, the effect is not as marked as with the 1.0  $\mu\text{m}$  diameter aerosol.

The experimental results for 4.0  $\mu\text{m}$  and 7.0  $\mu\text{m}$  diameter DOP particles are compared with theoretical charge calculations in Figures 31 and 32, respectively. In both of these cases the theory predicts larger values of particle charging than are found experimentally for all values of charging field strength.

Particle charging experiments were carried out with aerosols made from stearic acid and glycerol. Figures 33 and 34 show the results for stearic acid aerosols 2.0  $\mu\text{m}$  and 2.06  $\mu\text{m}$  in diameter, respectively. Agreement between theory and experiment for this aerosol material was generally quite poor.

The source of the poor agreement between experiment and theory is believed to be incomplete drying on the part of the stearic

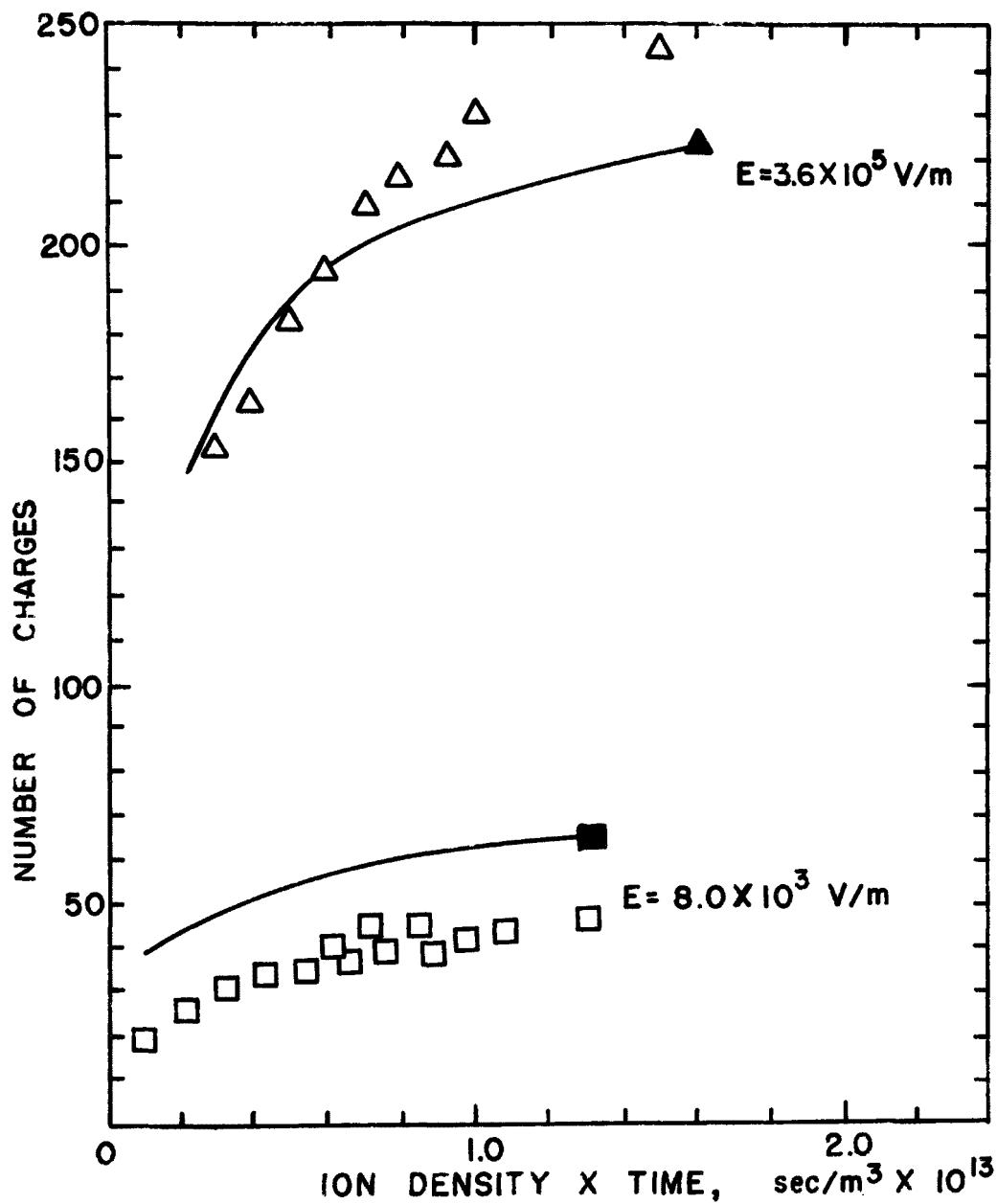


Figure 28. Number of charges per particle as a function of  $Nt$  product for a  $1.0 \mu\text{m}$  diameter DOP aerosol. The solid lines represent the SRI charging theory.

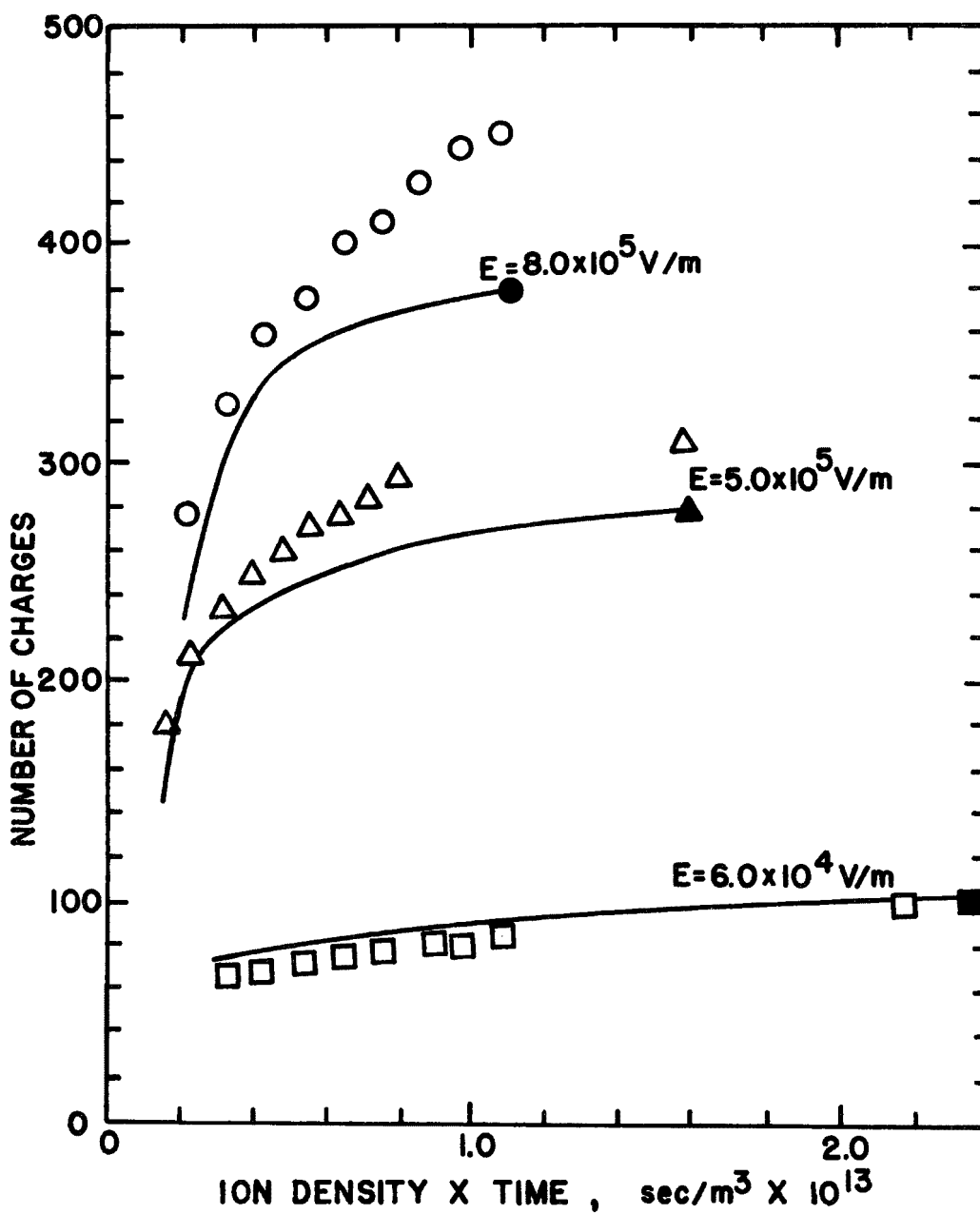


Figure 29. Number of charges per particle as a function of  $Nt$  product for a  $1.0 \mu\text{m}$  diameter DOP aerosol.



TABLE 1. EFFECT OF A CHANGING PARTICLE SIZE ON THE "GOODNESS OF FIT"  
BETWEEN EXPERIMENT AND THEORY. THE CALCULATED DIAMETER WAS  
1.0  $\mu\text{m}$  DOP

	Particle Size (microns)	Charging Field Strength				
		80 V/cm	600 V/cm	3.6 kV/cm	5.0kV/cm	7.5 kV/cm
55	0.8	Best Fit				
	0.9					
	1.0	Best Fit				
	1.1					
	1.2			Best Fit	Best Fit	Best Fit

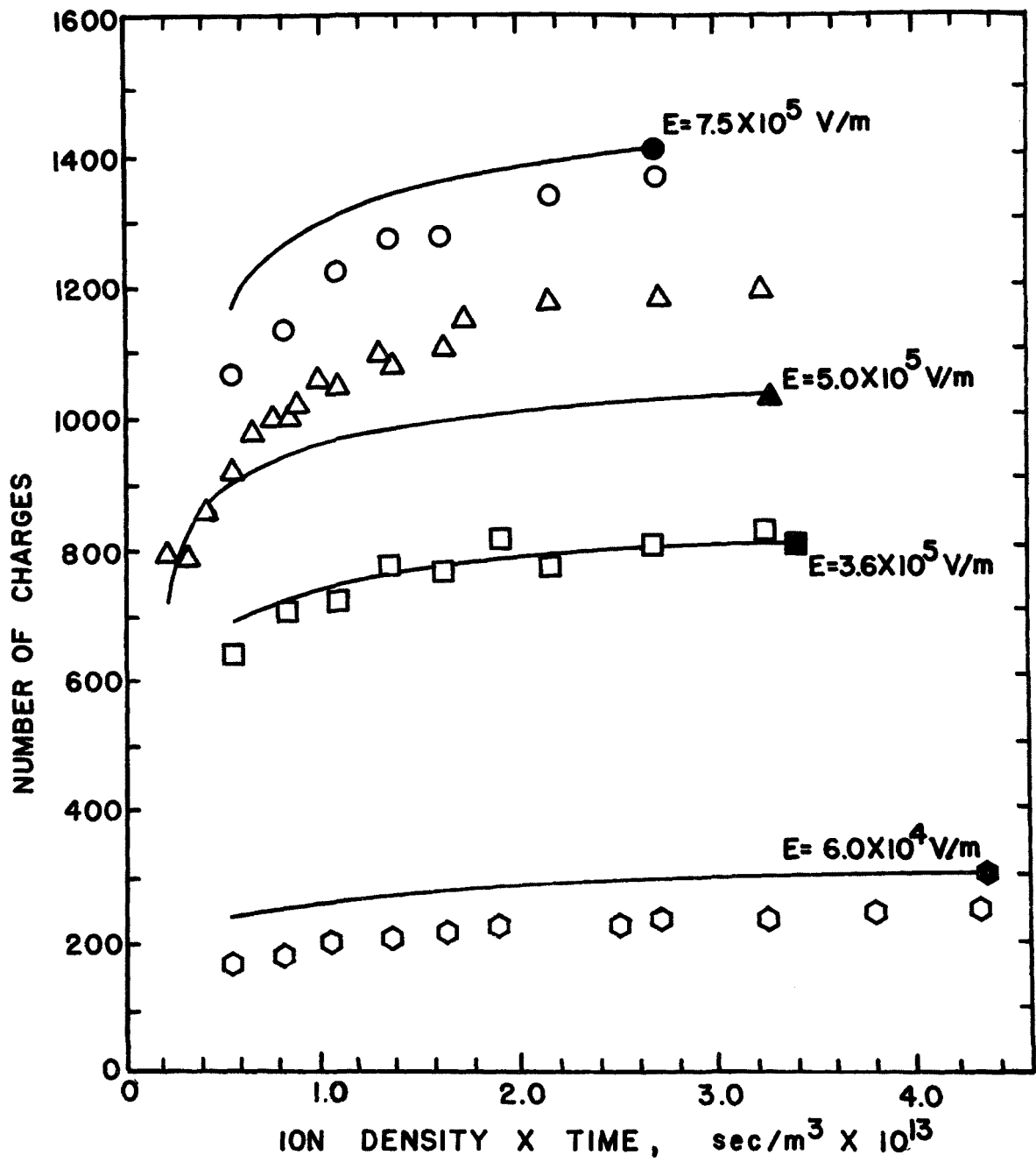


Figure 30. Comparison of experimental and theoretical values of particle charge for a 2.0  $\mu\text{m}$  diameter DOP aerosol.

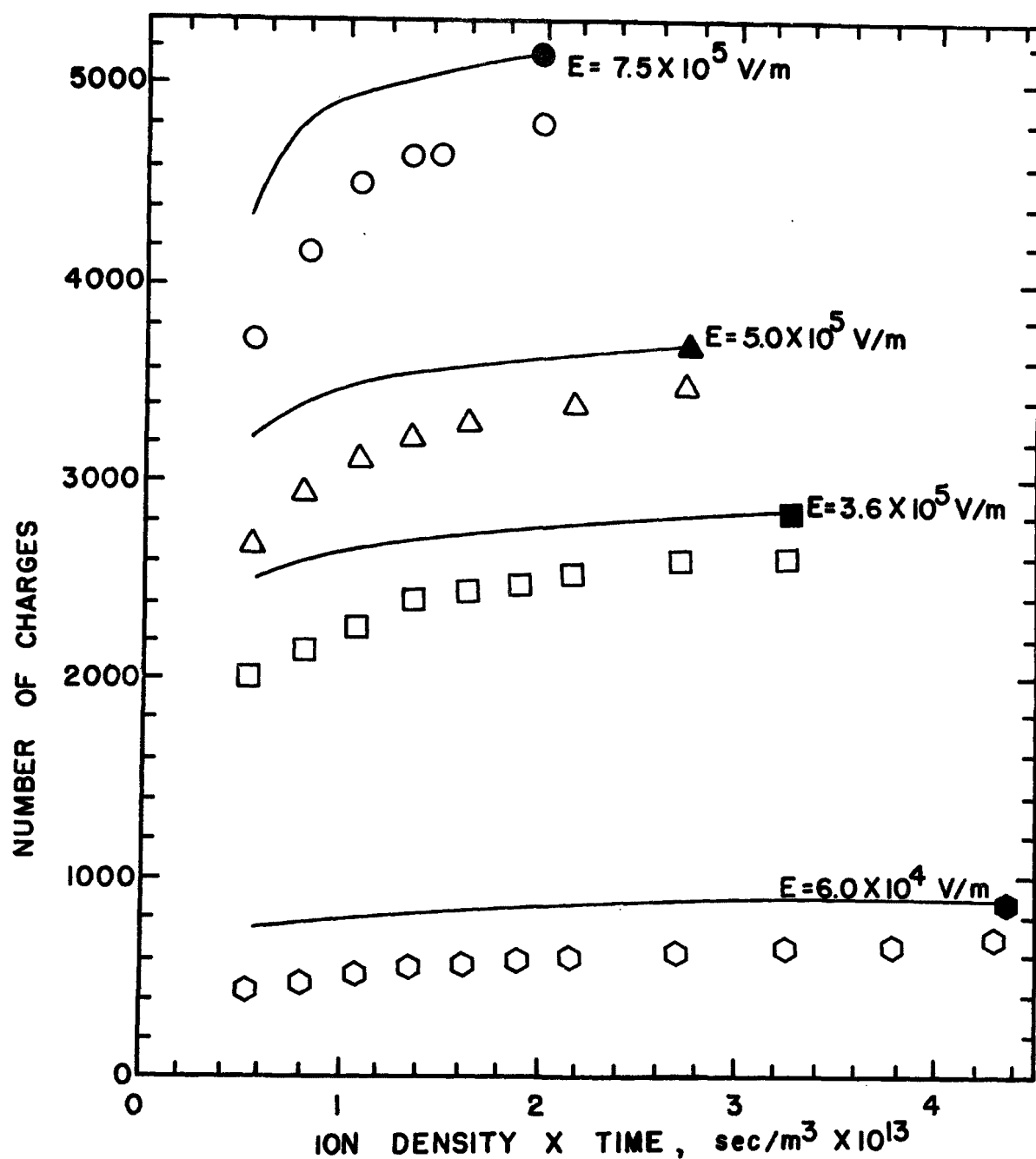


Figure 31. Number of charges per particle as a function of  $Nt$  product for 4.0  $\mu$ m diameter DOP particles.

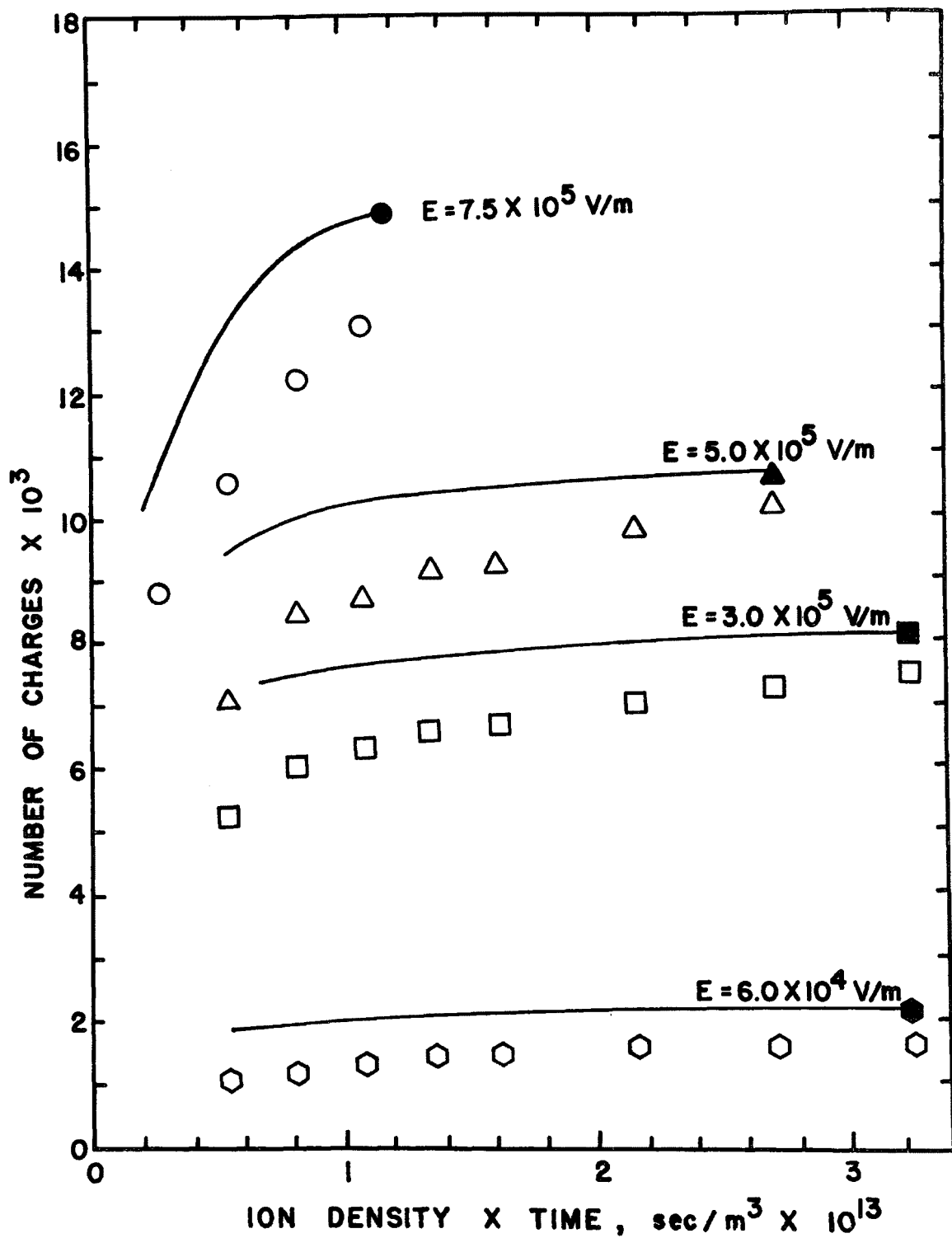


Figure 32. Number of charges per particle as a function of  $Nt$  product for a  $7.0 \mu\text{m}$  diameter DOP aerosol.

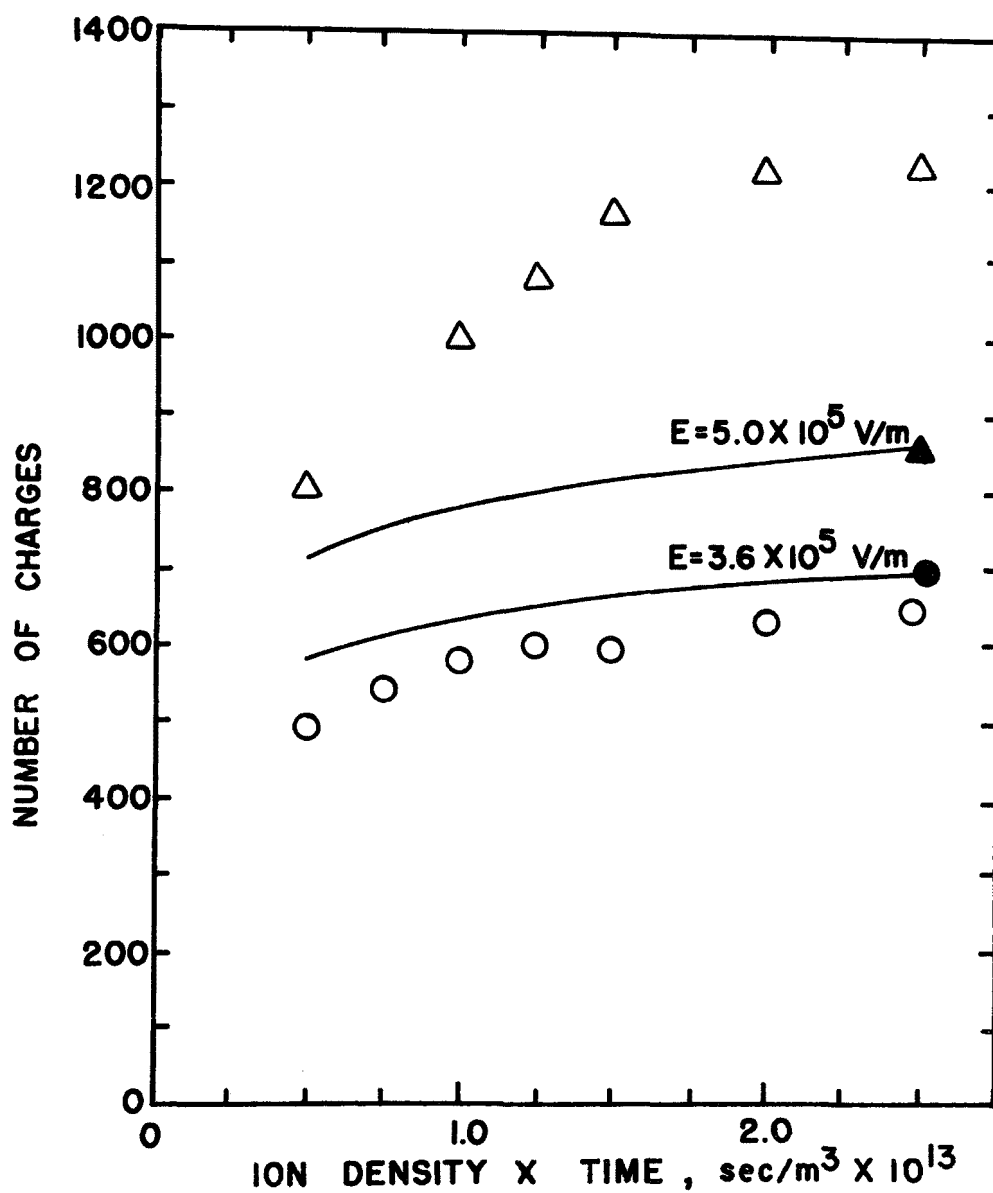


Figure 33. Theoretical and experimental values of charge per particle as a function of  $Nt$  product for 2.0  $\mu\text{m}$  diameter stearic acid particles.

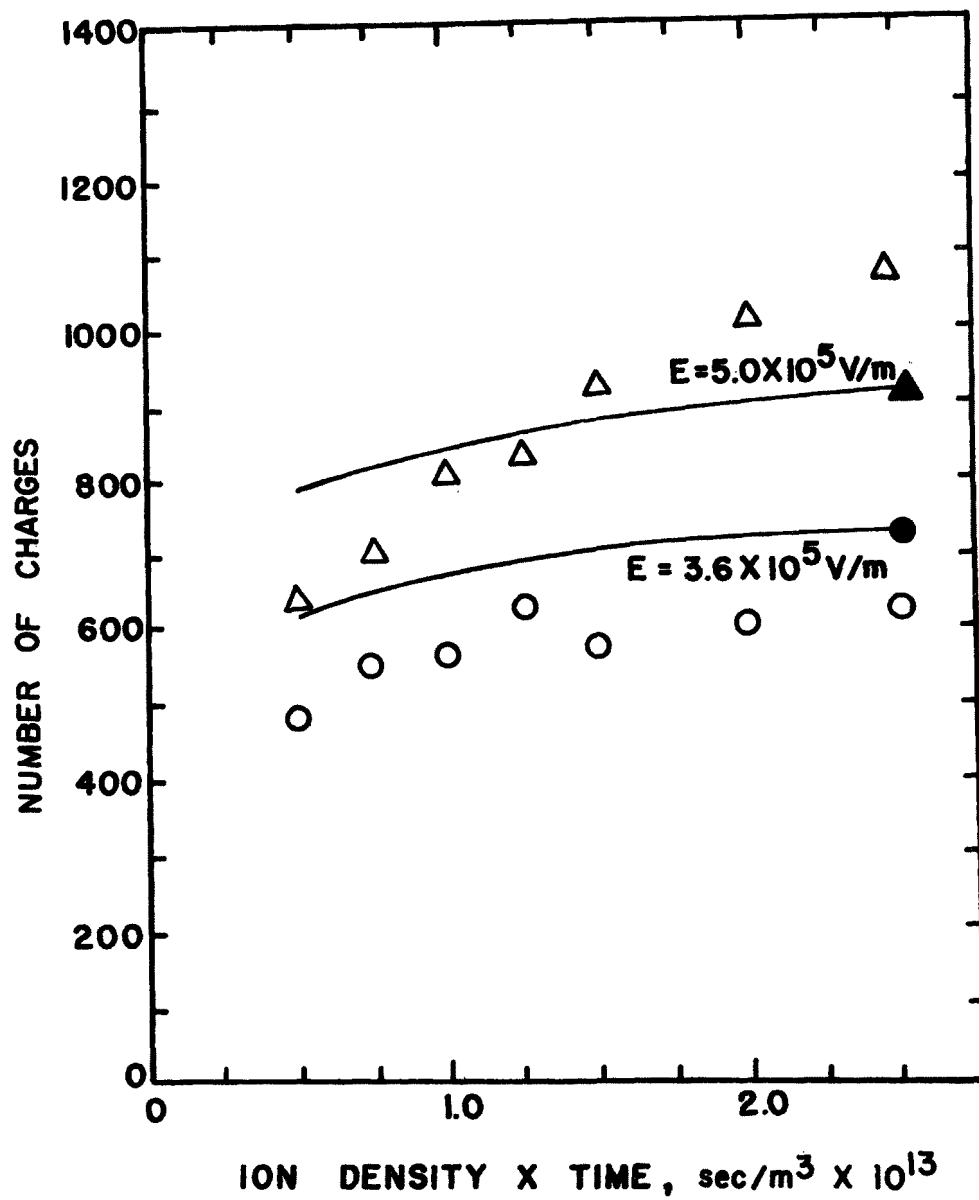


Figure 34. Number of charges per particle as a function of  $Nt$  product for a 2.06  $\mu\text{m}$  diameter stearic acid aerosol.

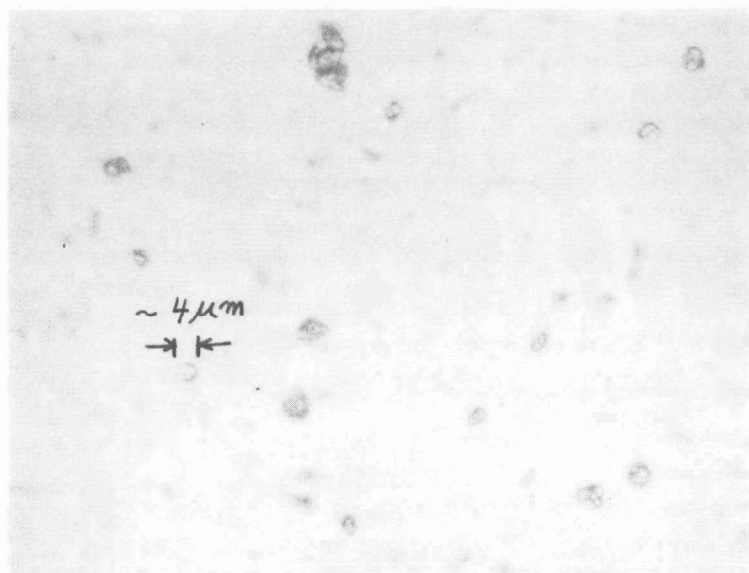
acid aerosol. This was indicated by samples of stearic acid aerosol particles which were observed after impaction on microscope cover glasses. The more usual technique of sampling a solid aerosol by catching it on a filter then coating the filter with immersion oil to aid in observing the particles will not work in this case, because the index of refraction of stearic acid and immersion oil are very nearly the same. It was found that the particles were nonspherical and much larger than their calculated diameters.<sup>11</sup> Figure 35(a) shows a photomicrograph of these particles. Other photomicrographs show that clumping and splattering on impact also occurs. It was therefore concluded that the aerosol was not sufficiently dried. Heating the aerosol does not appear to solve the problem although spherical particles can be produced. Figure 35(b) shows a photomicrograph of the same aerosol after being passed through a heated pyrex tube approximately 70 cm long and 1.8 cm in diameter. Temperature inside the tube was approximately 41°C. Best results were obtained at this temperature, with the aerosol becoming plastic and splattering on impaction at higher temperatures.

The majority of aerosol particles are spherical, but some nonspherical particles remain and evidence of impact splattering and clustering still exist. These particles should be approximately 2.0  $\mu\text{m}$  in diameter according to Berglund's<sup>11</sup> equations; however, 3.5  $\mu\text{m}$  to 4.0  $\mu\text{m}$  are more typical of what is seen.

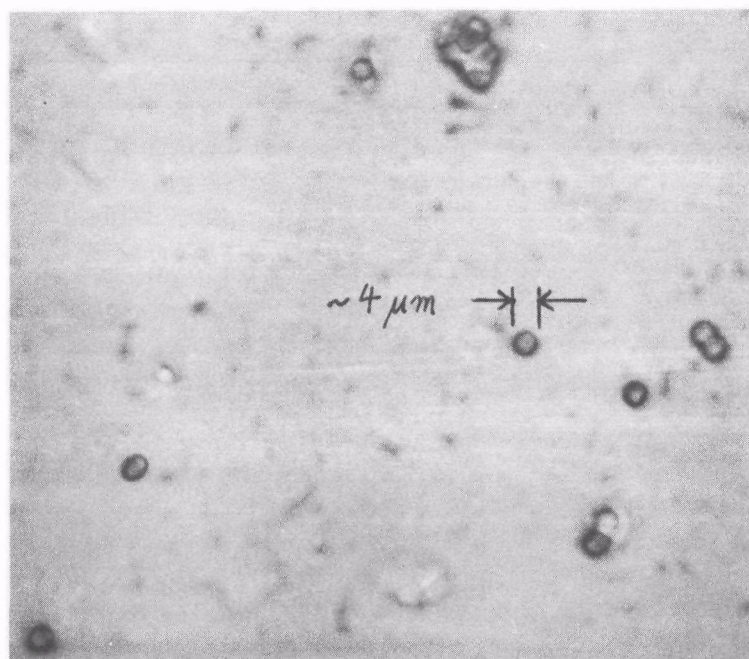
Figure 36 presents the results of charging experiments performed with aerosols of glycerol. This material has a relative dielectric constant of 42.5, much higher than any of the other materials used. The experimentally determined values of charge are much lower than the theoretical values. This result may occur because of an uncertainty in the determination of particle size. Glycerol tends to wet almost any surface it contacts; therefore, direct observation of glycerol aerosol particles is difficult. Optical measurements of the sizes of the glycerol particles used in these charging experiments indicated a size below the 2.0  $\mu\text{m}$  calculated from Berglund's equations. Because of this it was suspected that some of the glycerol itself was evaporating along with the solvent, methanol. Although glycerol has a low vapor pressure (1 mm Hg at 125°C)<sup>15</sup> it is significantly higher than that of DOP (0.028 mm Hg at 125°C).<sup>14</sup> A diameter of 1.8  $\mu\text{m}$  for the aerosol provides the best theoretical fit to the data shown in Figure 36, which indicates that as much as 25 percent of the glycerol may have evaporated before charging took place. Because of the apparent evaporation problem the use of glycerol as an aerosol material was not pursued further.

#### Second Hewitt Charger

It became apparent during experiments with the first Hewitt-type charger that certain modifications in the design could be



(a)



(b)

Figure 35. Stearic acid aerosols, calculated diameter  $2.0\ \mu\text{m}$  (a) no heating, (b) heated to approximately  $100^{\circ}\text{F}$ .



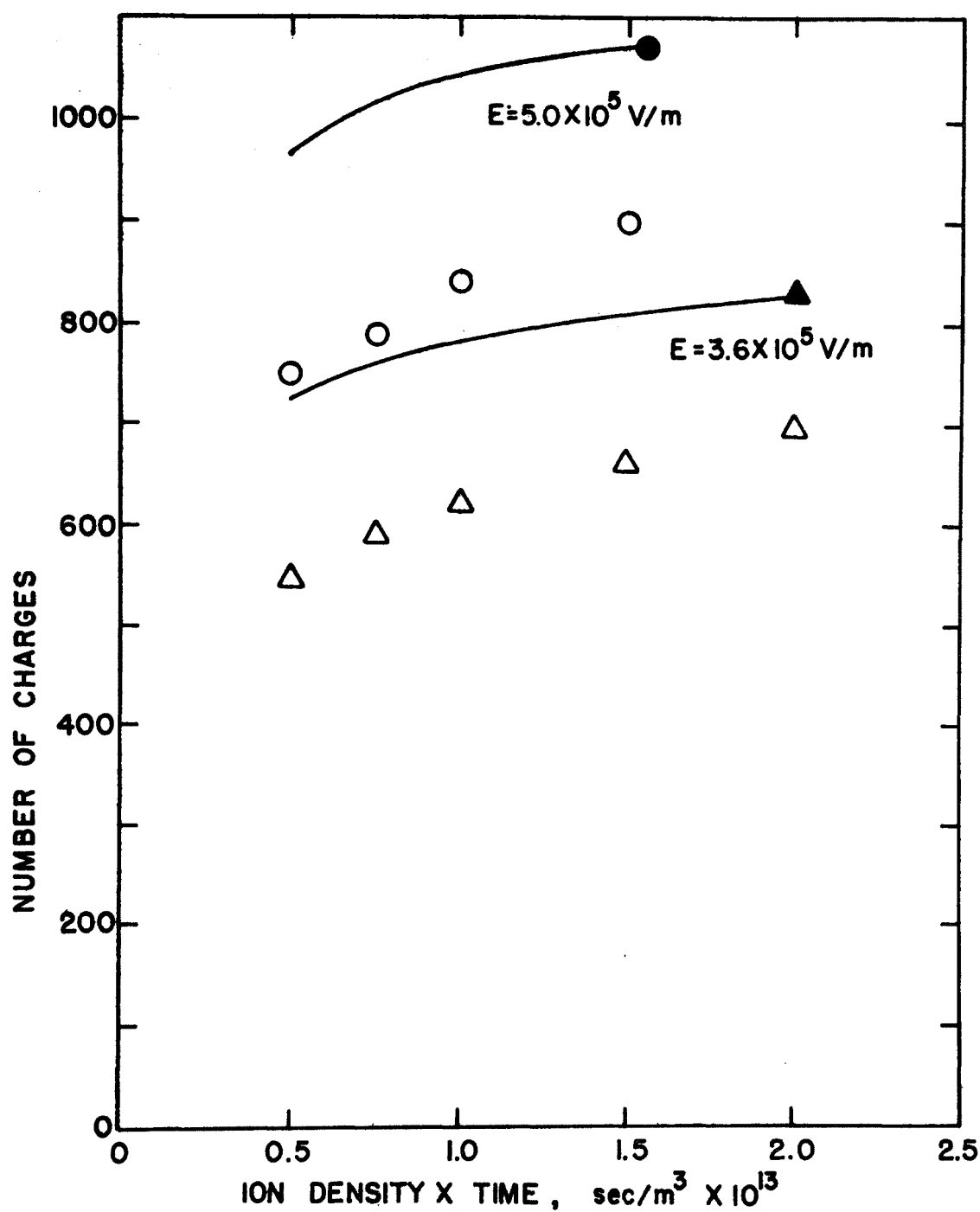


Figure 36. Charge per particle as a function of  $Nt$  product for a  $2.0 \mu\text{m}$  glycerol aerosol. The relative dielectric constant for this material is 42.5.

made to improve the electrical behavior and the gas flow characteristics. A second Hewitt charger was designed, with special attention given to the elimination of sharp edges and corners which might contribute to sparking. Smooth transition pieces, cast in RTV 106 silicone rubber (General Electric), were made in order to provide for reduced turbulence in the aerosol stream entering and leaving the charging region.

When the first Hewitt charger was replaced by the second one a number of measurements were repeated to compare the two devices. Figure 37 shows the theoretical and experimental behavior of particle charging for DOP particles 1.0  $\mu\text{m}$  and 2.0  $\mu\text{m}$  in diameter as the electric field strength in the charging region is varied while holding the  $Nt$  product fixed at  $1.0 \times 10^{13}$  sec/ $\text{m}^3$ . Data taken with both Hewitt-type chargers is in reasonably good agreement with theory for charging field strengths up to about  $8 \times 10^5$  V/m. At low field strengths the measured value of the charge falls below the theory, and at high field strengths experimental values are above the theoretical values. There are two possible sources for this effect. First, there may be sufficient turbulence related to the corona wind at high field strengths to cause a substantial increase in the average particle residence time in the charging region. Secondly, in view of Bricard's study<sup>9</sup> concerning the effects of aging on ion mobility, the enhancement of charging above the theoretical predictions at high charging field strengths may be at least partly due to an effective increase in ion mobility.

Figures 38 and 39 show charge per particle for a 1.0  $\mu\text{m}$  DOP aerosol as a function of  $Nt$  for various values of the charging field strength. The data taken with the two Hewitt chargers is generally in good agreement (compare with Figures 28 and 29) with the exception of the case for which the charging field strength is  $3.6 \times 10^5$  V/m, where the data taken using the second charger lies much closer to the theory.

The results of charging experiments using polystyrene latex (PSL) aerosols in the second Hewitt charger are presented, with the theoretical charge predictions, in Figures 40, 41, and 42. Four different particle sizes were used, ranging from 0.109  $\mu\text{m}$  to 1.099  $\mu\text{m}$  in diameter. The dielectric constant of this material was taken to be 2.5, the value for bulk polystyrene.<sup>16</sup> The theory agrees well with experimentally determined charge for the 0.109  $\mu\text{m}$  and 0.312  $\mu\text{m}$  particles. For the larger particles the agreement is not quite as good, but still falls within about 30 percent.

### Negative Corona Charging

The ion mobility associated with a negative corona is generally slightly higher than that found for a positive corona. With

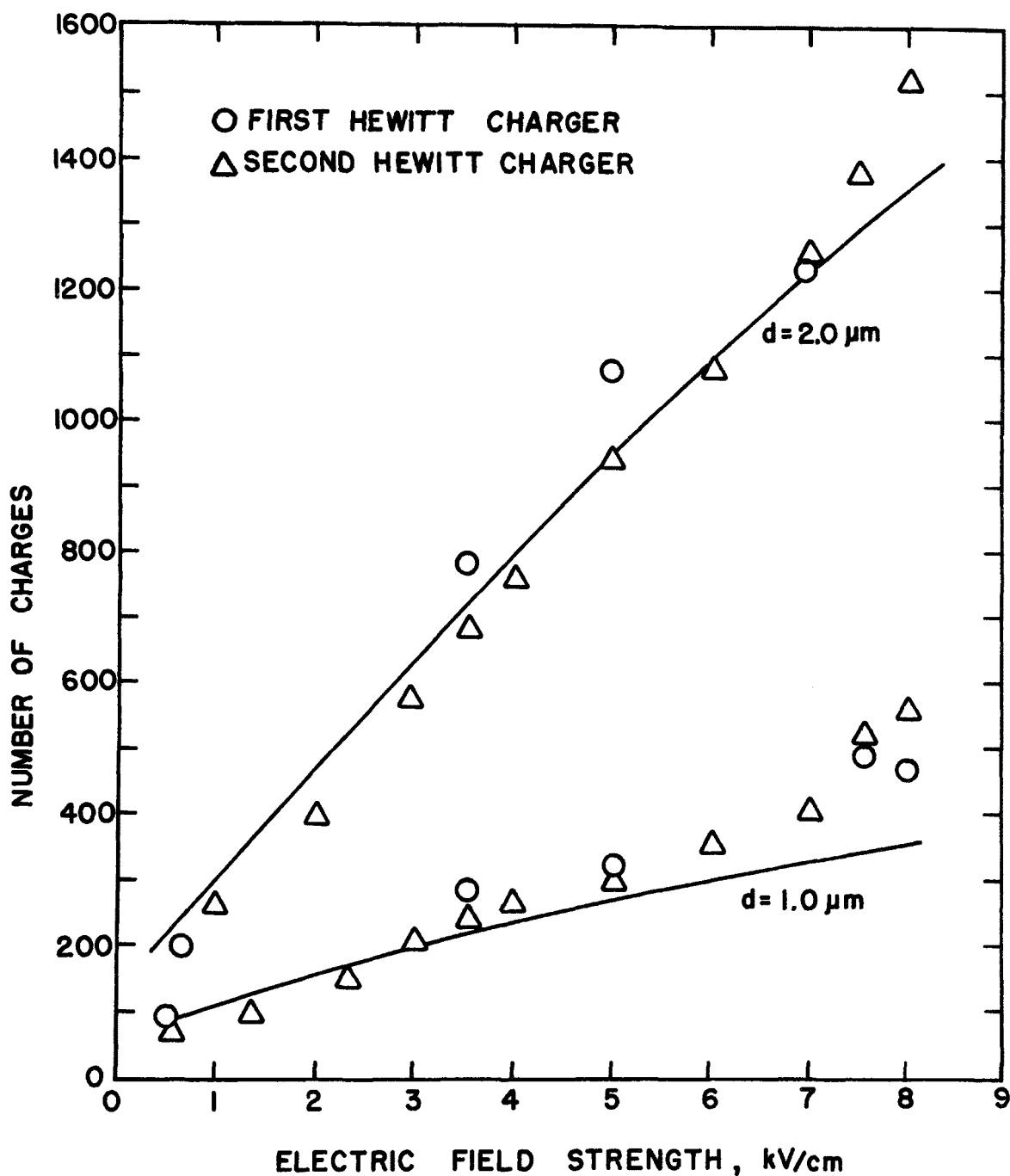


Figure 37. Comparison of particle charging as a function of charging field strength for two different Hewitt-type chargers. The Nt product was held constant at  $1.0 \times 10^{13}$  sec/m<sup>3</sup> on the field was varied. Aerosols used were DOP, 1.0 μm and 2.0 μm in diameter.

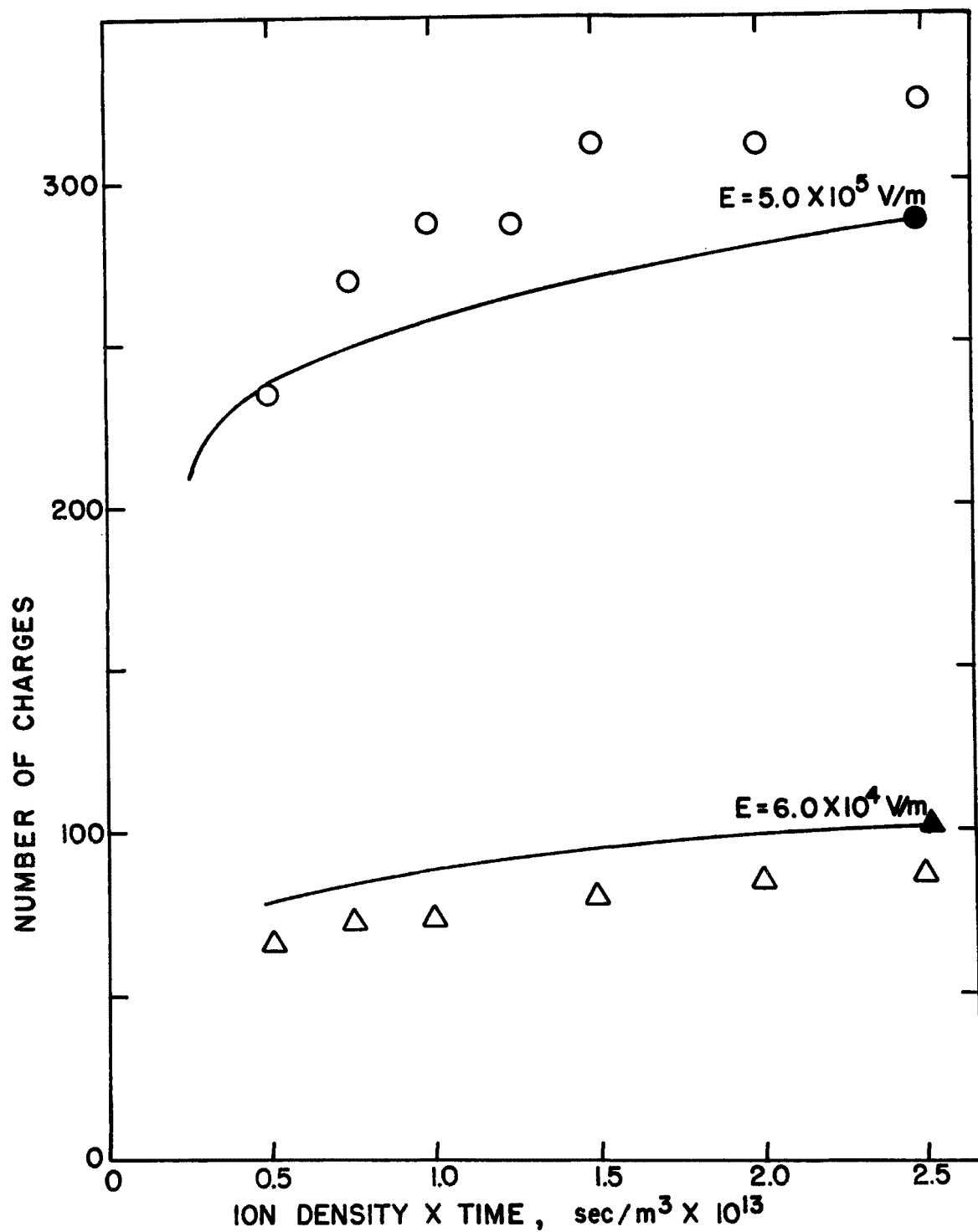


Figure 38. Charge per particle as a function of  $Nt$  product for a  $1.0 \mu\text{m}$  DOP aerosol. The second Hewitt charger was used for these data.

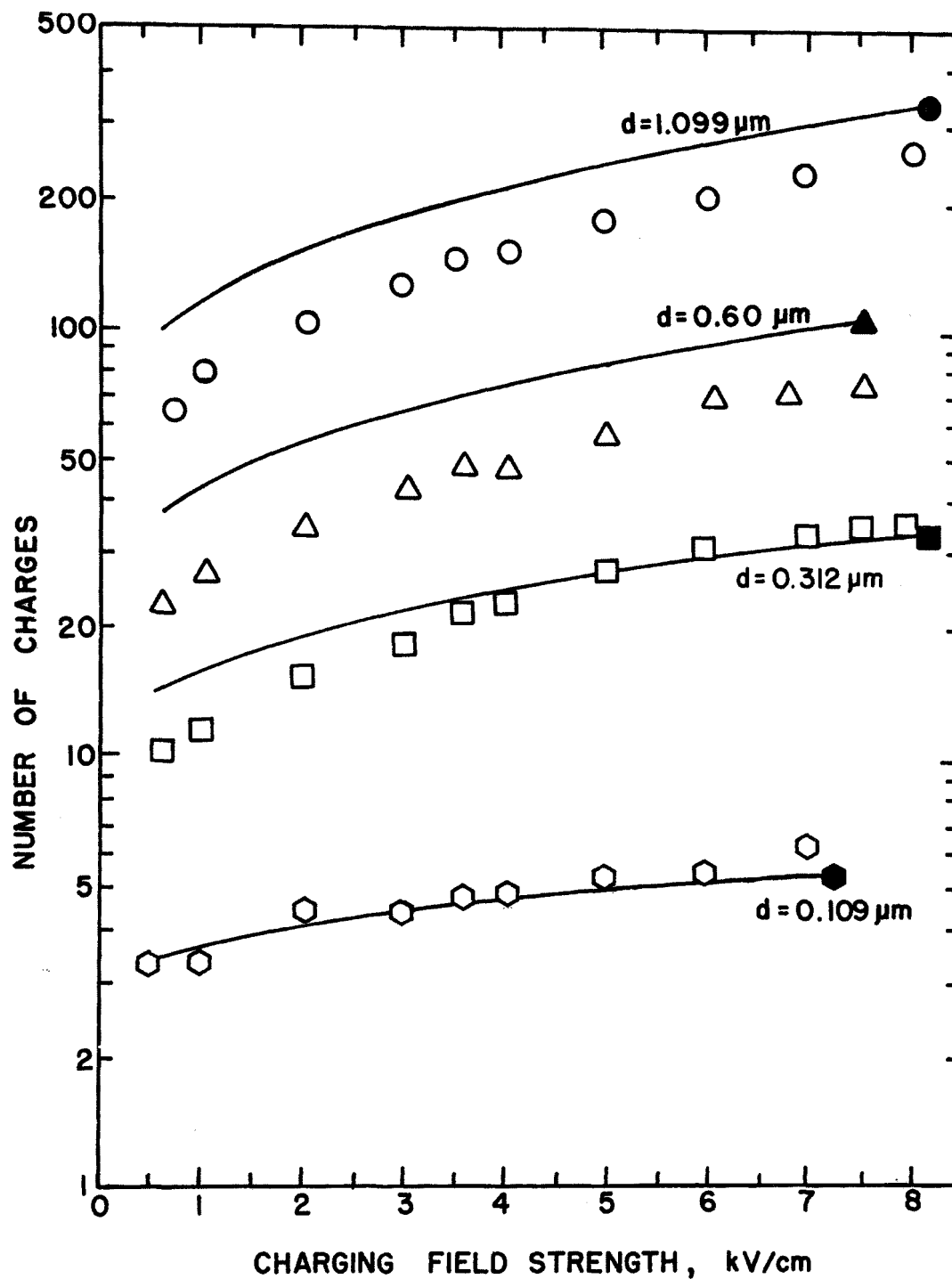


Figure 40. Number of charges per particle for polystyrene latex particles of various sizes. The  $Nt$  product was held constant at  $5 \times 10^{12}$  sec/m<sup>3</sup> as the charging field was varied.

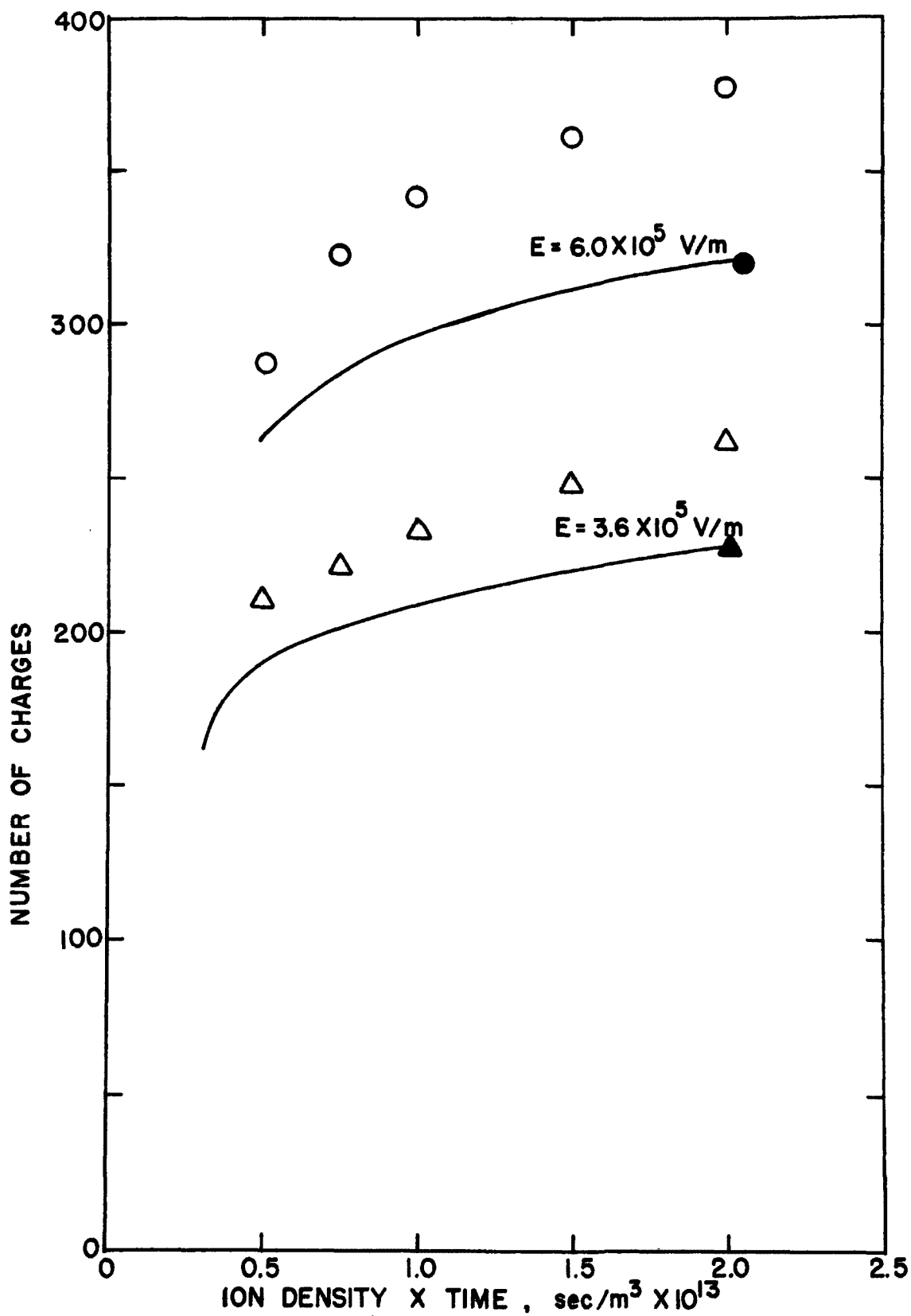


Figure 39. Charge per particle as a function of  $Nt$  product for a  $1.0 \mu\text{m}$  DOP aerosol, charged with the second Hewitt-type charger.

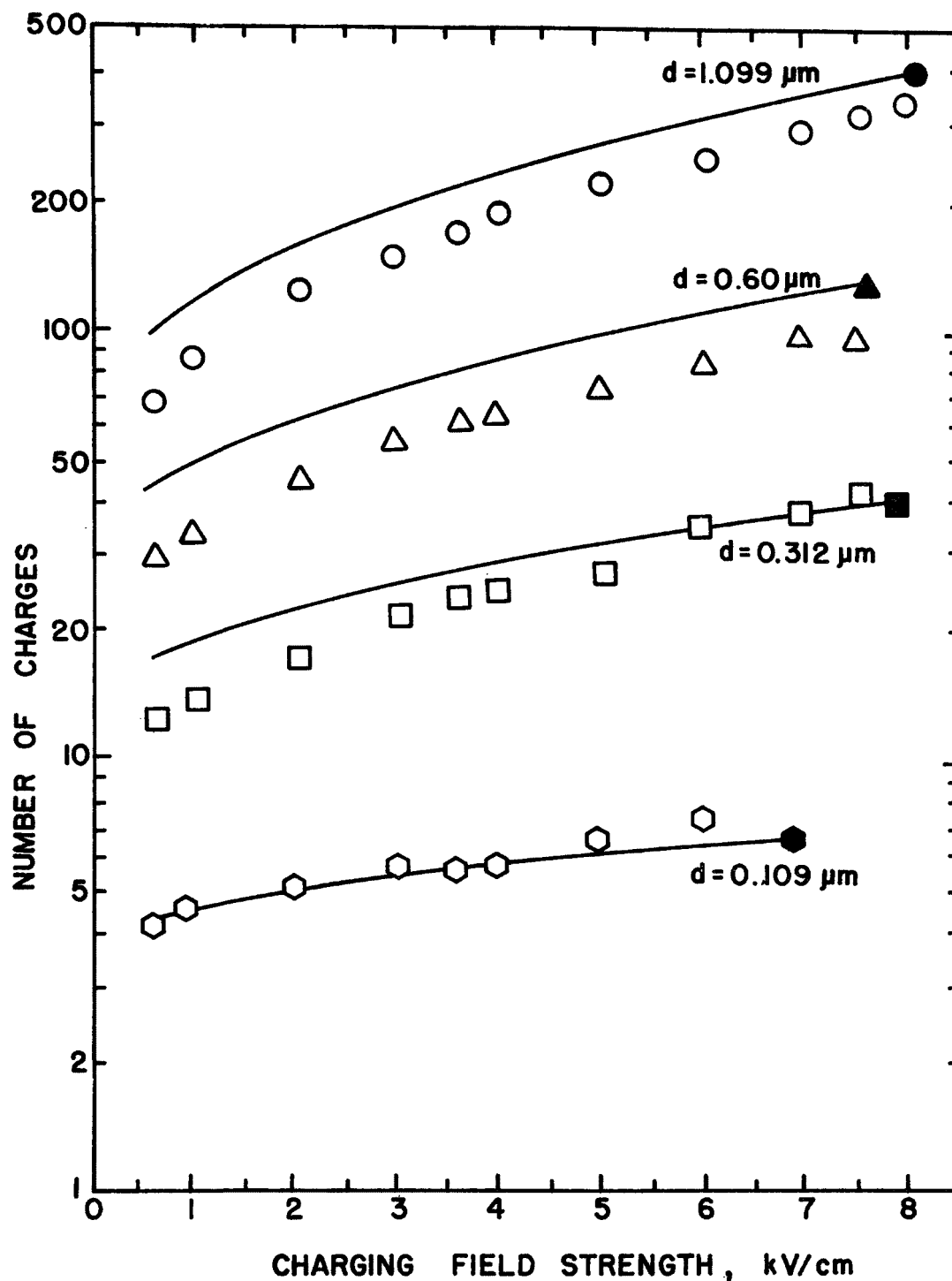


Figure 41. Number of charges per particle as a function of charging field strength for polystyrene latex particles of four different sizes.  $Nt$  is  $1.0 \times 10^{13}$  sec/m<sup>2</sup>.

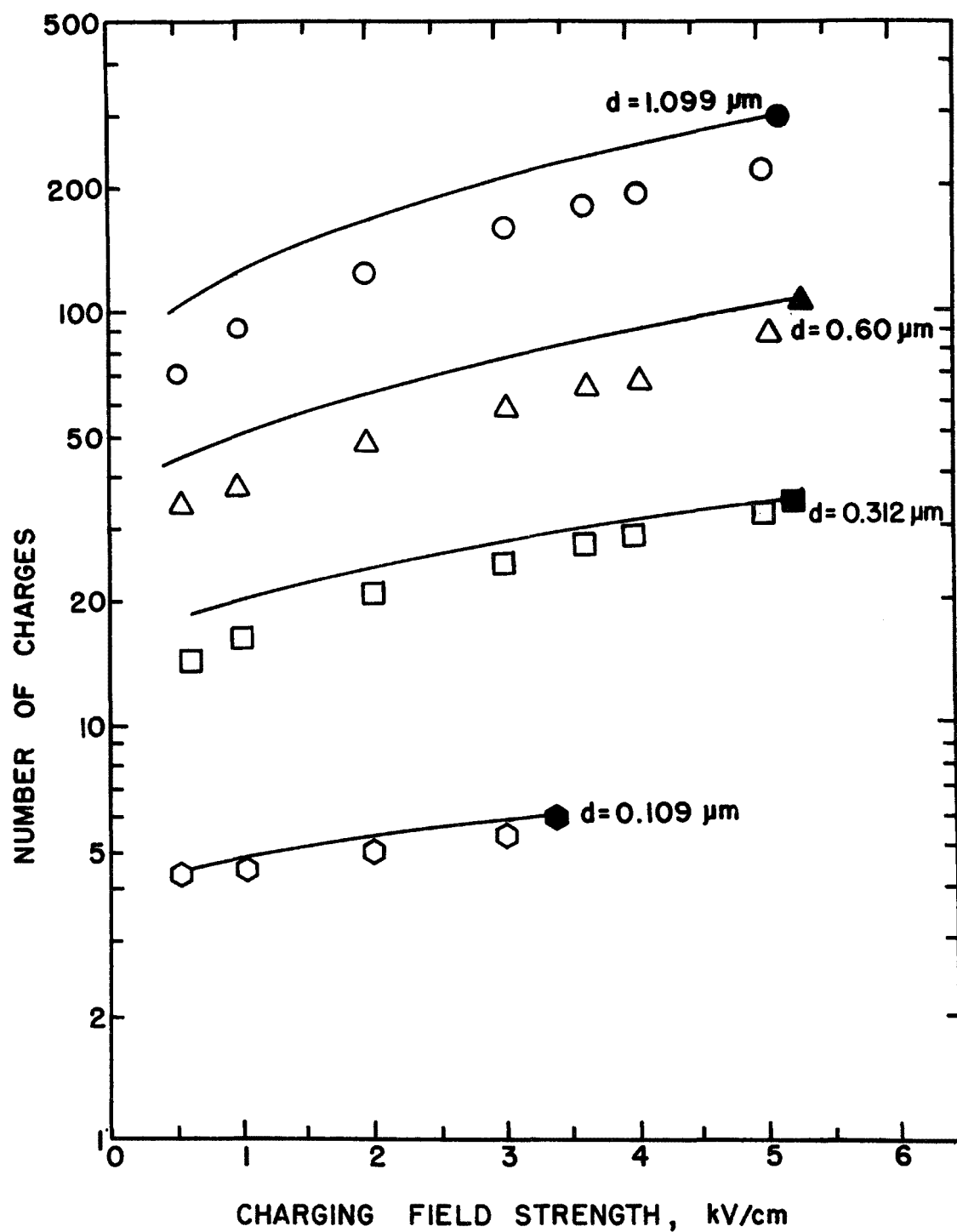


Figure 42. Number of charges per particle as a function of charging field strength for polystyrene latex particles, with  $Nt = 1.5 \times 10^{13} \text{ sec/m}^3$ .



the curve fitting technique employing Equation (18) a value of  $2.70 \times 10^{-4} \text{ m}^2/\text{V}\cdot\text{sec}$  has been determined for negative corona charging, as compared with  $2.38 \times 10^{-4} \text{ m}^2/\text{V}\cdot\text{sec}$  for positive corona under like conditions.

Figure 43 shows a comparison between the results of positive and negative corona charging for  $0.109 \text{ }\mu\text{m}$  diameter PSL particles, with the  $Nt$  product held at  $5.0 \times 10^{12} \text{ sec}/\text{m}^3$  for both cases.

The charging theory predicts results which differ by less than one percent for positive and negative corona charging under the experimental conditions associated with Figure 43. But the measured values of charge for negative corona charging average approximately 1.5 times the values measures for positive charging. The disparity increases as the charging field strength is increased.

It is not immediately apparent why the charge per particle should be so much greater for negative corona than for the positive case. The principal difference between the two is that there may be free electrons included with the negative ions. And since the electron mass is extremely small in comparison with that of a gas ion there is a very large difference in the mobilities of current carrier species. It may not be appropriate, therefore to treat the system as though a single "average" mobility is sufficient to describe the combined effects of the carrier species. It is concluded that the charging mechanisms described by the theory are sound; however, further studies related to mobility measurement and proper application of such measurements to the theory may lead to a more complete understanding of the charging process.

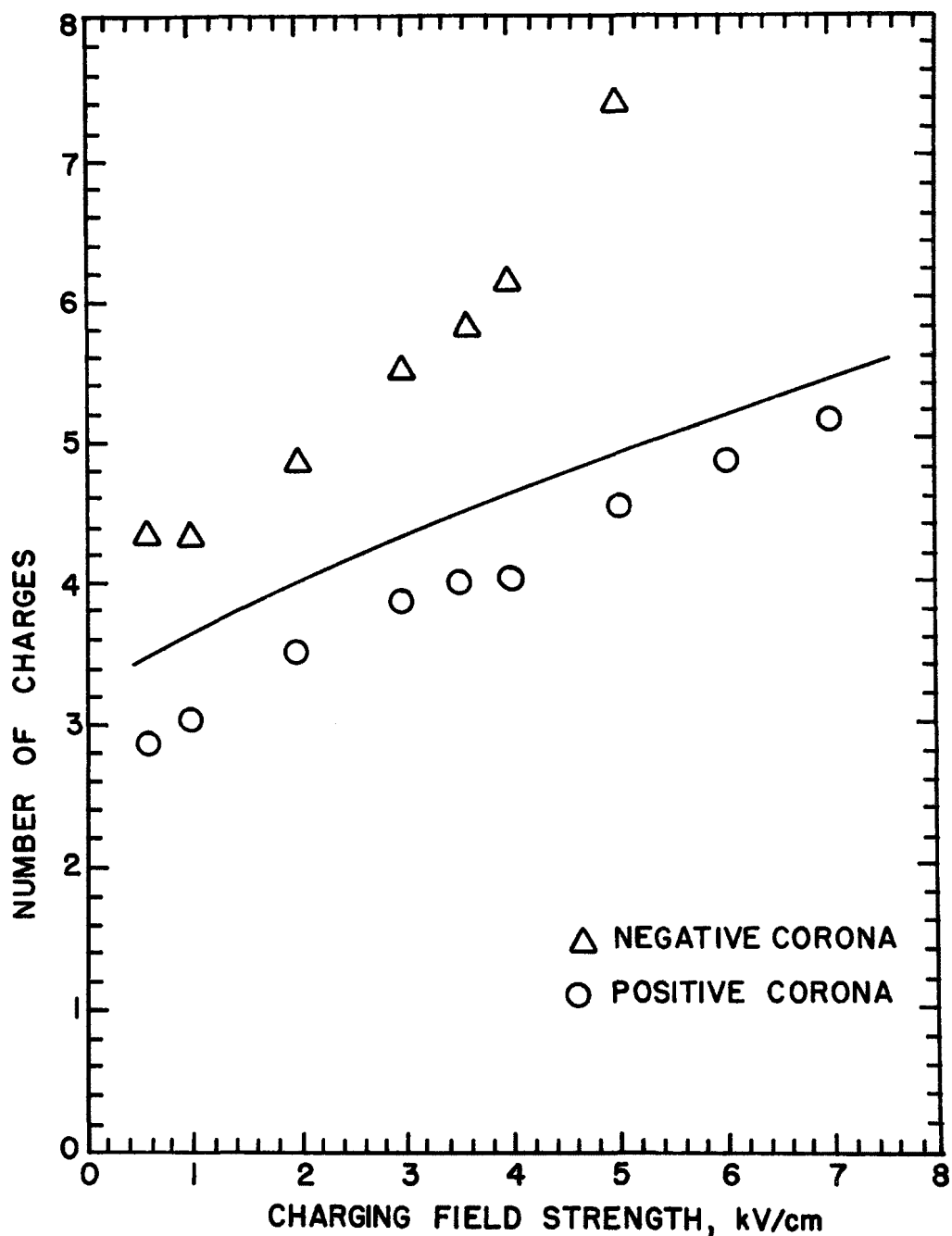


Figure 43. Comparison of positive and negative corona charging for 0.109  $\mu\text{m}$  polystyrene latex spheres. For both sets of data  $Nt$  is  $5.0 \times 10^{12} \text{ sec/m}^3$ . The theoretical curves for positive and negative corona, represented by the solid line, are indistinguishable on this scale.

## SECTION 5

### PILOT SCALE EXPERIMENTAL WORK

In order to test the charging theory and to demonstrate the feasibility of particle charging in a high current density system under various dust loading conditions a pilot scale charging device was designed and constructed for installation at the inlet of an existing 600 - 1000 ACFM pilot scale electrostatic precipitator. A multiple wire-plate electrode configuration was used, with narrow electrode separation. An assembly drawing of the precharger is presented in Figure 44. There are two separate precharging sections, both of wire-plate geometry. The first section has four 11.4 cm wide grounded plates and three corona wires while the second section has six 6.9 cm wide grounded plates and five corona wires. The grounded plates are constructed of 0.32 cm thick stainless steel with smoothed corners. The precharger is specifically designed to eliminate sneakage. A teflon enclosure holds the two precharging sections and was designed to interface with the dry-wall pilot scale precipitator mentioned above.

For each of the two separate charging sections, current-voltage characteristics were measured with 0.0254 cm and 0.127 cm corona wires. The results were compared with those of an electric field computer simulation.

The computer simulation is based on an electrode geometry consisting of a pair of infinitely long parallel plates with evenly spaced parallel wires lying in the plane midway between the plates. The precharger, on the other hand, has only a single wire between each pair of narrow parallel plates. By representing the precharger section with one segment of the periodic geometry simulated by the computer program a useful approximation can be made. In Figure 45 sketches of the electric field lines in the two configurations are compared. The correspondence is not exact because of the edge effects in the precharger geometry. Compensation for the edge effects was achieved by using a simulated duct segment length ( $L$  in Figure 45) larger than the precharger plate width. Since no precise information on the edge effects is available the width in the simulation was treated as an adjustable parameter until a good approximation to the experimental result was found for each of the two sections. This "effective plate width" was then held constant for further calculations.

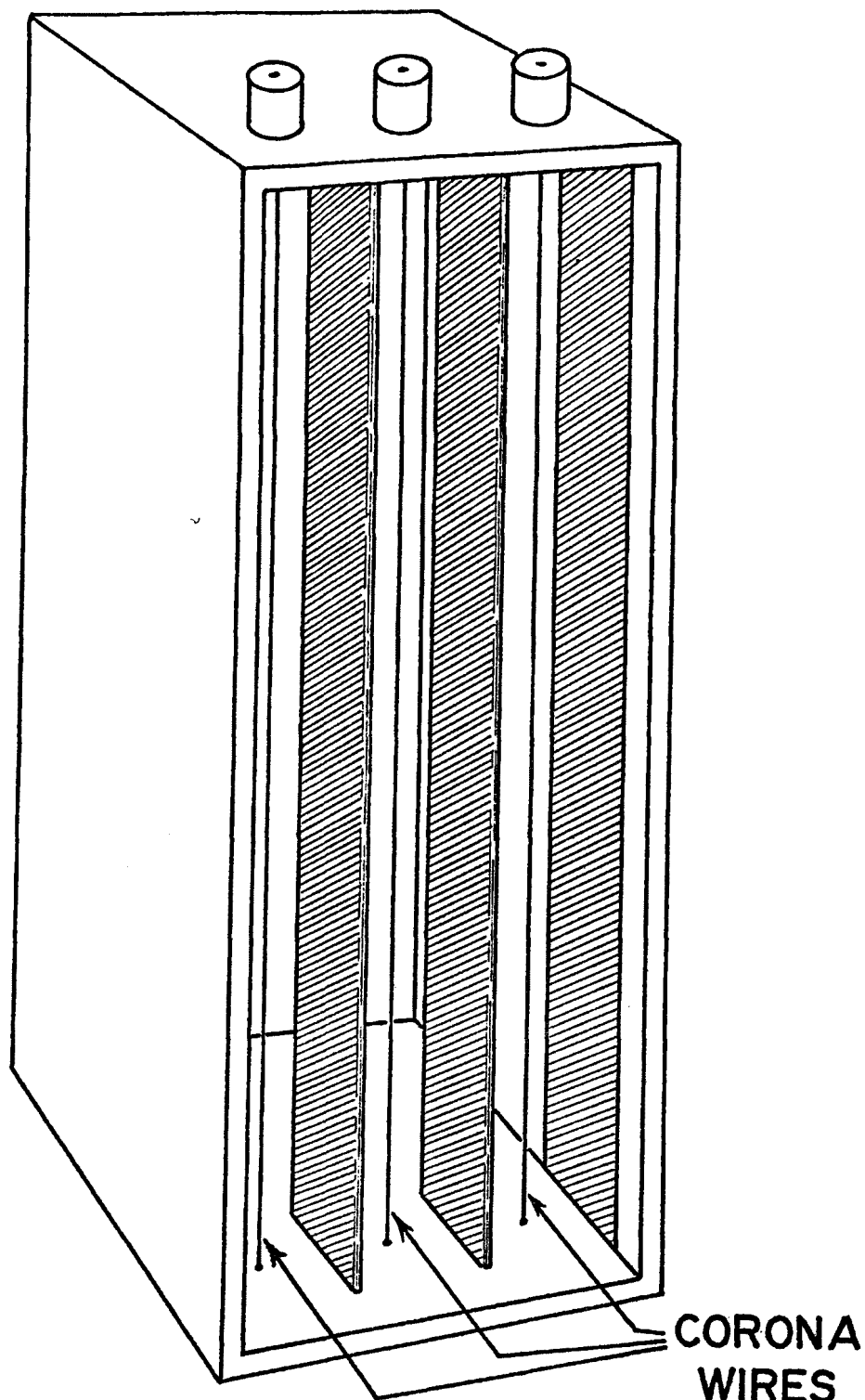
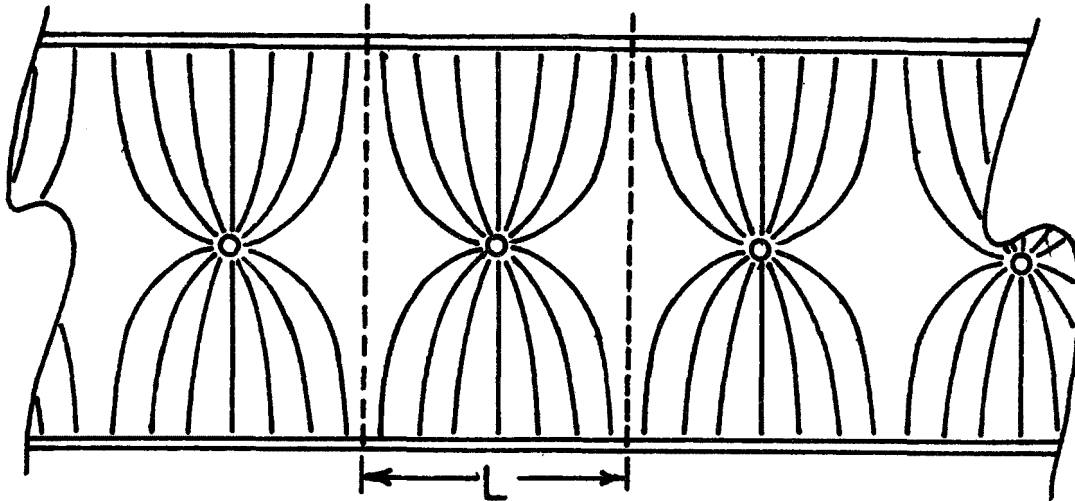
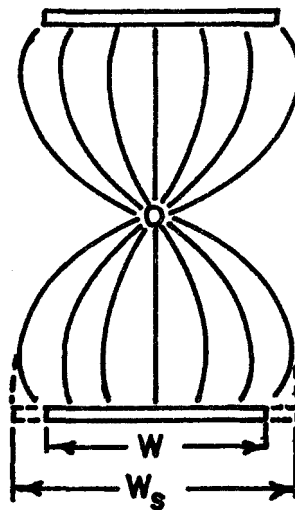


Figure 44. Conceptual sketch of pilot scale charging device. Only the three-wire charging section is shown. A second charging device with five corona wires and six plates is located in the opposite end of the enclosure.



(A) Periodic duct geometry used in computer simulation



$W$  = actual width  
 $W_s$  = simulation width

(B) Precharger section

Figure 45. Sketch of electric field lines in (a) periodic geometry of infinite extent employed in computer program, and (b) pilot scale precharger section containing one wire and having finite plate width.

Figures 46 and 47 show the experimental and theoretical results obtained with a 0.0254 cm corona wire, for positive and negative corona, respectively. For the smaller precharger section the actual plate width was 6.86 cm, and the width used in the computer simulation was 9.4 cm. The larger section plate width was 11.4 cm; the simulated width was 20.96 cm. The shapes of the curves are dominated by the mobility of the ions, which was taken to be  $2.2 \times 10^{-4} \text{ m}^2/\text{V}\cdot\text{sec}$  for positive corona in air, and  $3.0 \times 10^{-4} \text{ m}^2/\text{V}\cdot\text{sec}$  for negative corona to achieve good fits.

Figures 48 and 49 show the variation in electric field along the perpendicular line connecting the wire and plate. These theoretical curves are plotted for the maximum values of current density achieved experimentally. The precharger section with the smaller plates and spacing shows a more uniform electric field and a much higher value of maximum current density than the larger section.

Figures 50 and 51 show comparison of experimental determination of current-voltage characteristics for two different corona wire sizes. Average current density for the smaller corona wire consistently exceeds that for the larger wire in both precharger sections for both polarities and at all values of applied voltage. Next, the pilot scale precharging device, fitted with 0.0254 cm diameter corona wires, was installed in the dry wall pilot scale electrostatic precipitator. Current-voltage characteristics were measured for both precharger sections under various dust loading conditions.

In Figures 52, 53, and 54 the electrical characteristics of the three wire precharger section (1.46 in. wire-to-plate spacing) are shown along with the corresponding theoretical curves. Increases in dust loading cause a decrease in mobility and a concomitant reduction in current for a given value of applied voltage. Mobilities in the theoretical model were chosen to provide the best approximation to the experimental results. The theoretical curves are repeated together in Figure 55 for comparison. Electric field profiles at the maximum current density for each of the three cases are shown in Figure 56.

The behavior of the 5-wire precharger section (0.85 in. wire-to-plate spacing) was somewhat erratic in comparison with the 3-wire-section as may be seen in Figure 57. The current was higher at every value of voltage in the presence of dust loading than in the "clean" system. It appears that an accumulation of dust on the bottom of the precharger may be responsible for this sort of aberration. After running the system long enough to accumulate a dust layer about  $\frac{1}{4}$  in. deep on the bottom of the precharger, the dust blower was turned off and another measurement of the current-voltage characteristic was made. The presence of the dust layer provides an additional current path between the corona wire and the plate, thus producing a greater apparent average current

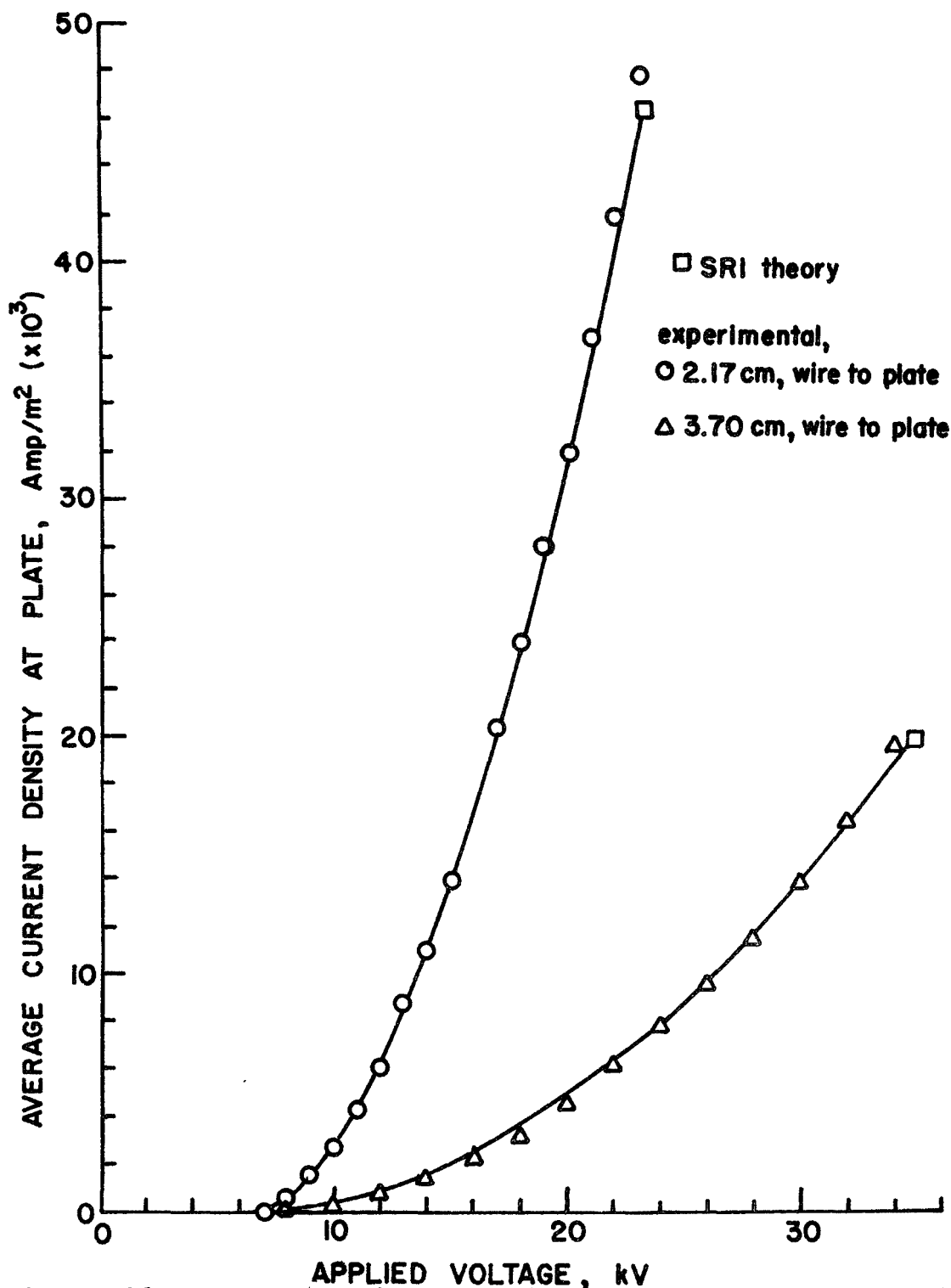


Figure 46. Current-voltage characteristics of both sections of the pilot scale precharger with 0.0254 cm corona wire at positive potential. Curves derived from computer simulation are included for comparison with the experimental results.

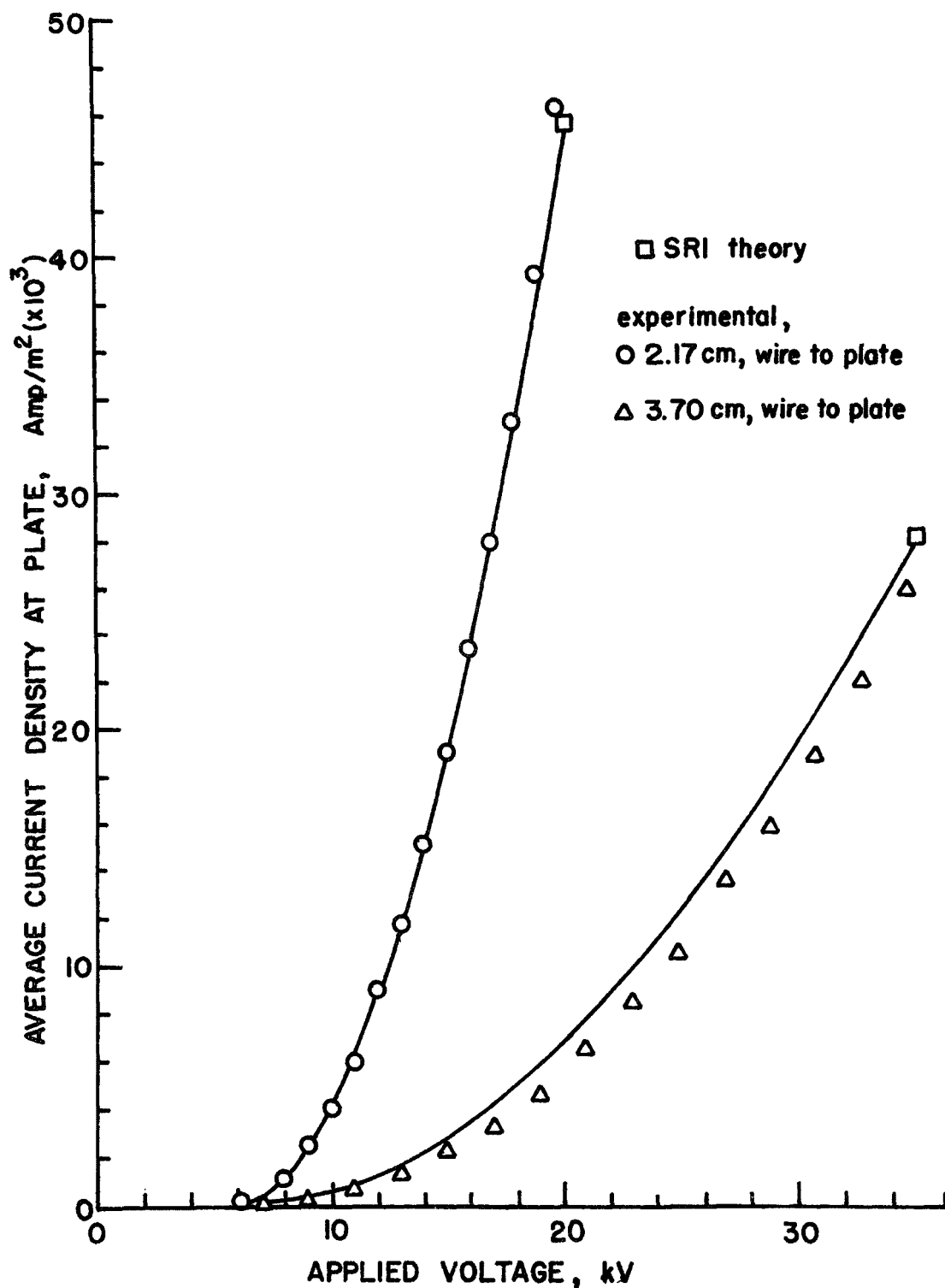


Figure 47. Current-voltage characteristics of both sections of the pilot scale precharger with 0.0254 cm corona wire at negative potential. Solid lines are computer generated curves.



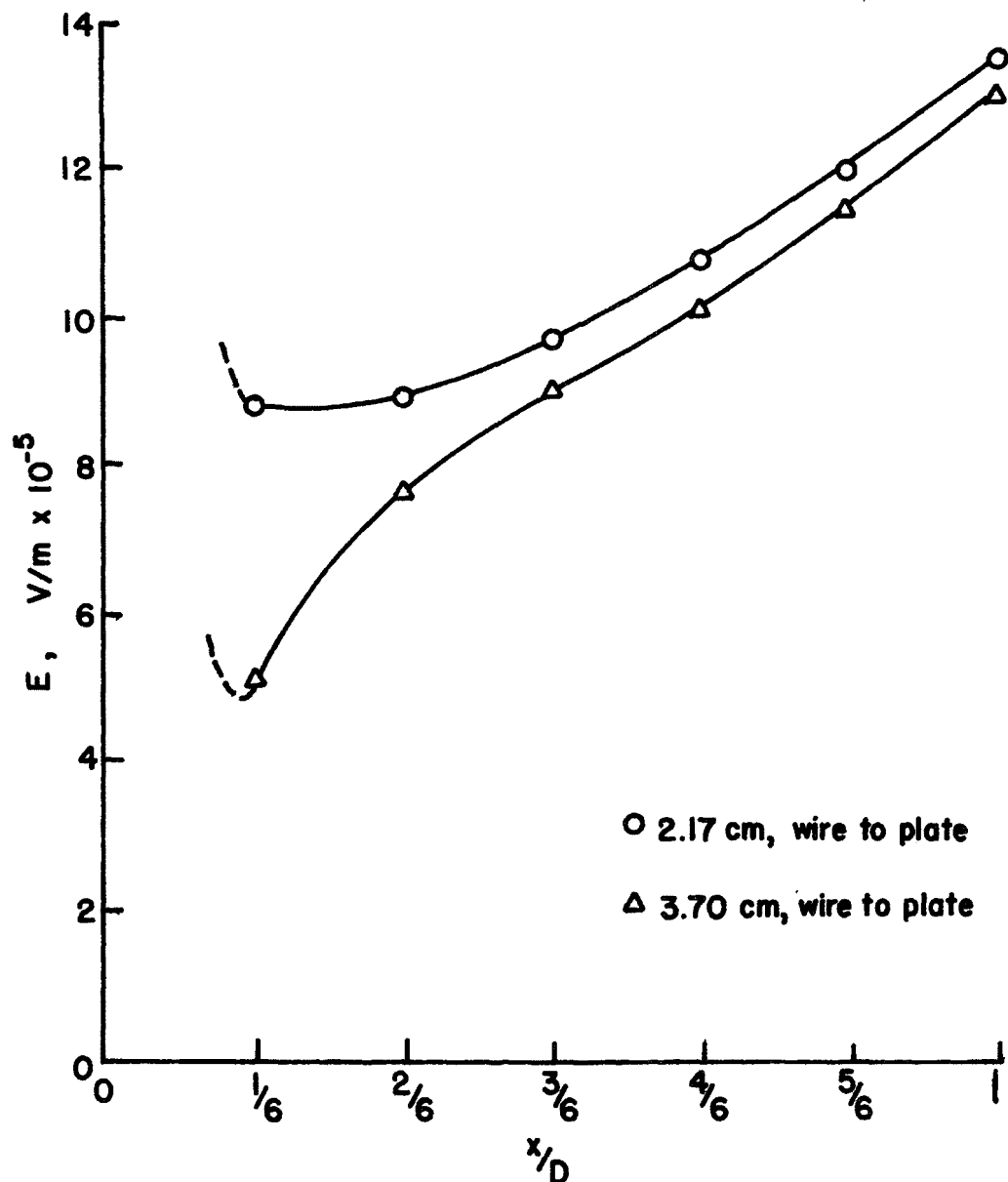


Figure 48. Electric field profiles for both sections of the pilot scale precharger at the maximum experimental current density, positive corona. 0.0254 cm diameter corona wires were used.

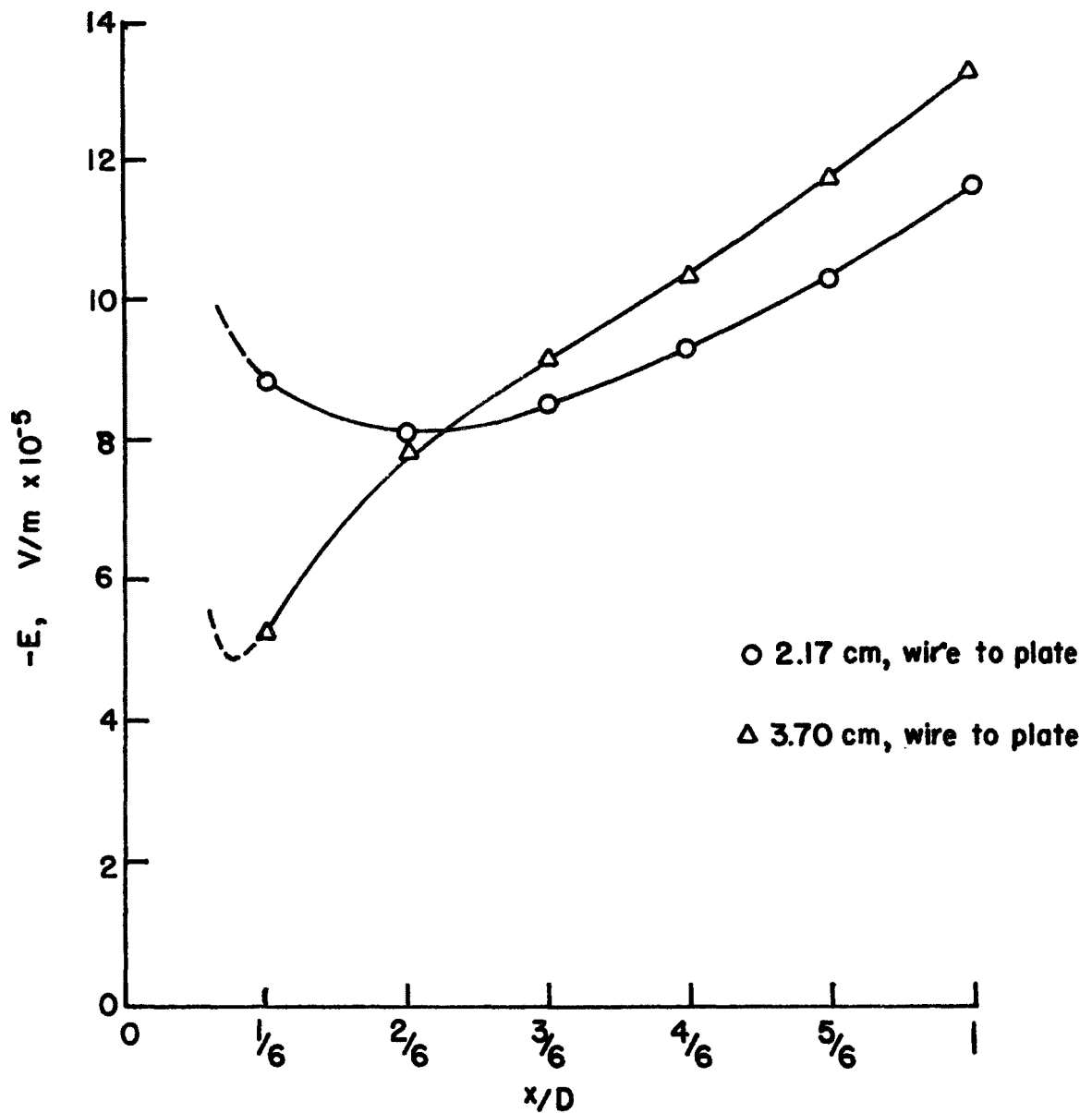


Figure 49. Electric field profiles for both sections of the pilot scale precharger at the maximum experimental current density, negative corona. 0.0254 cm diameter corona wires were used.

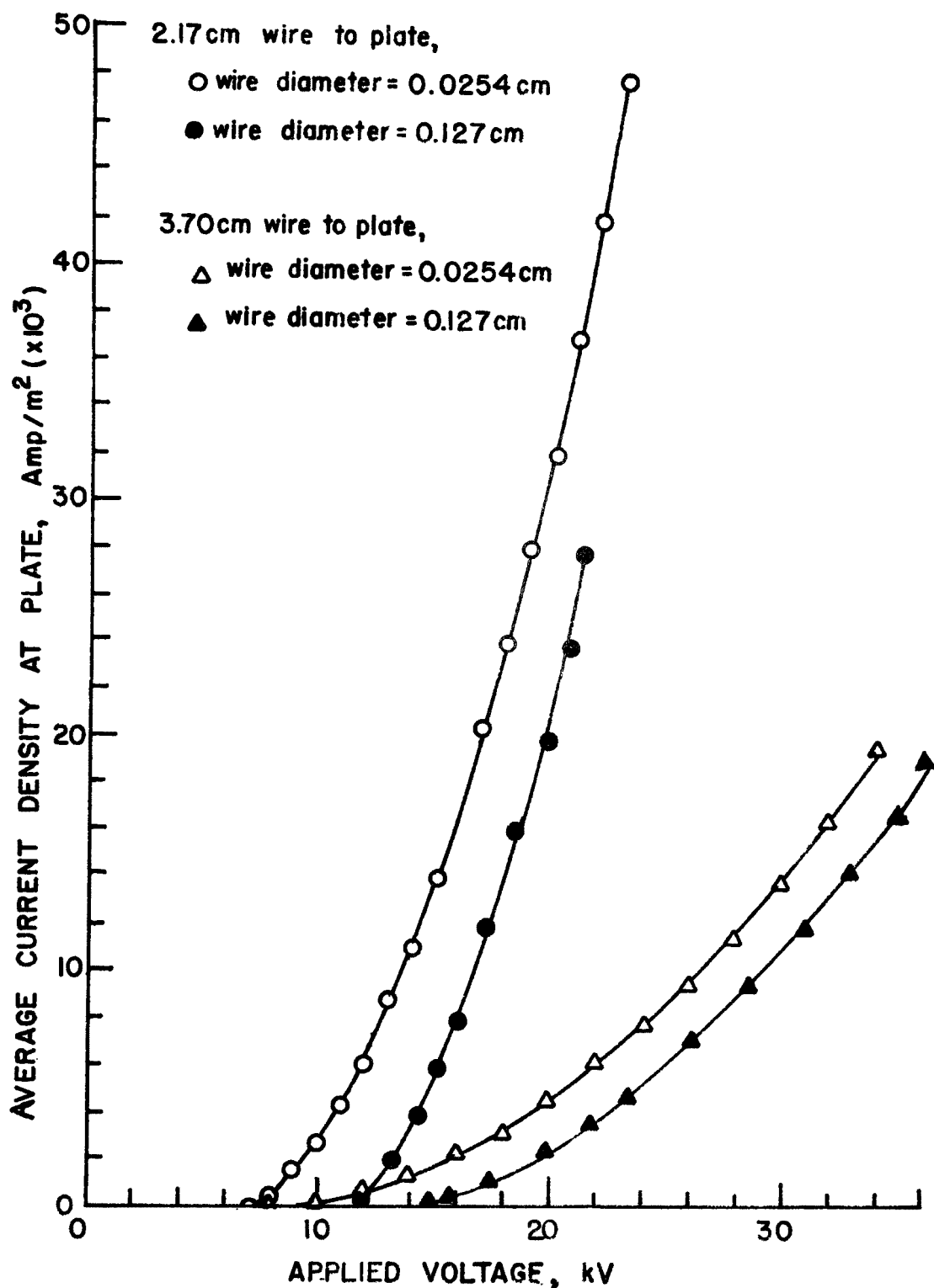


Figure 50. Comparison of current-voltage characteristics of precharger with 0.0254 cm corona wire and with 0.127 cm corona wire, positive corona.

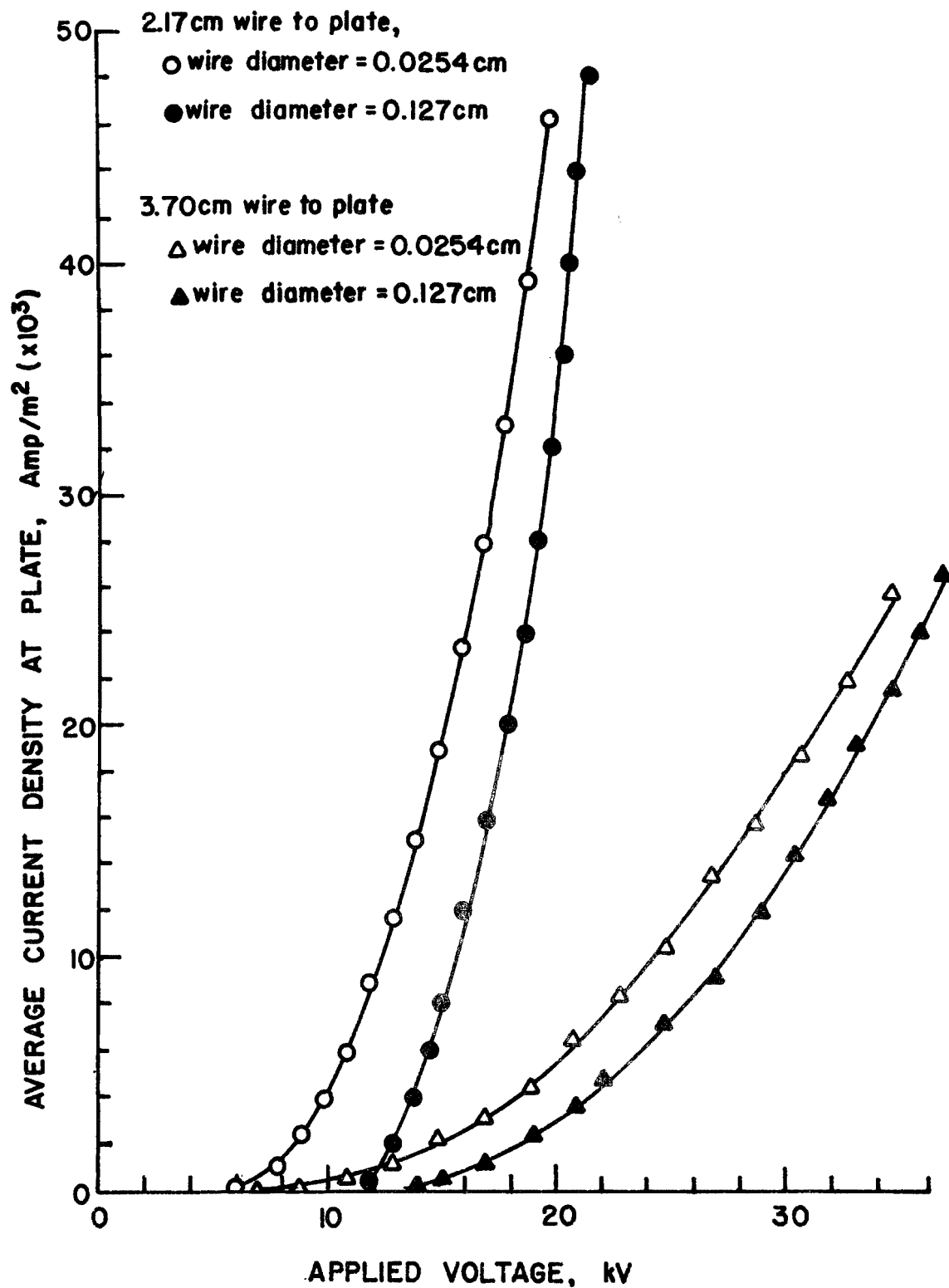


Figure 51. Comparison of current-voltage characteristics of pre-charger with 0.0254 cm corona wire and with 0.127 cm corona wire, negative corona.

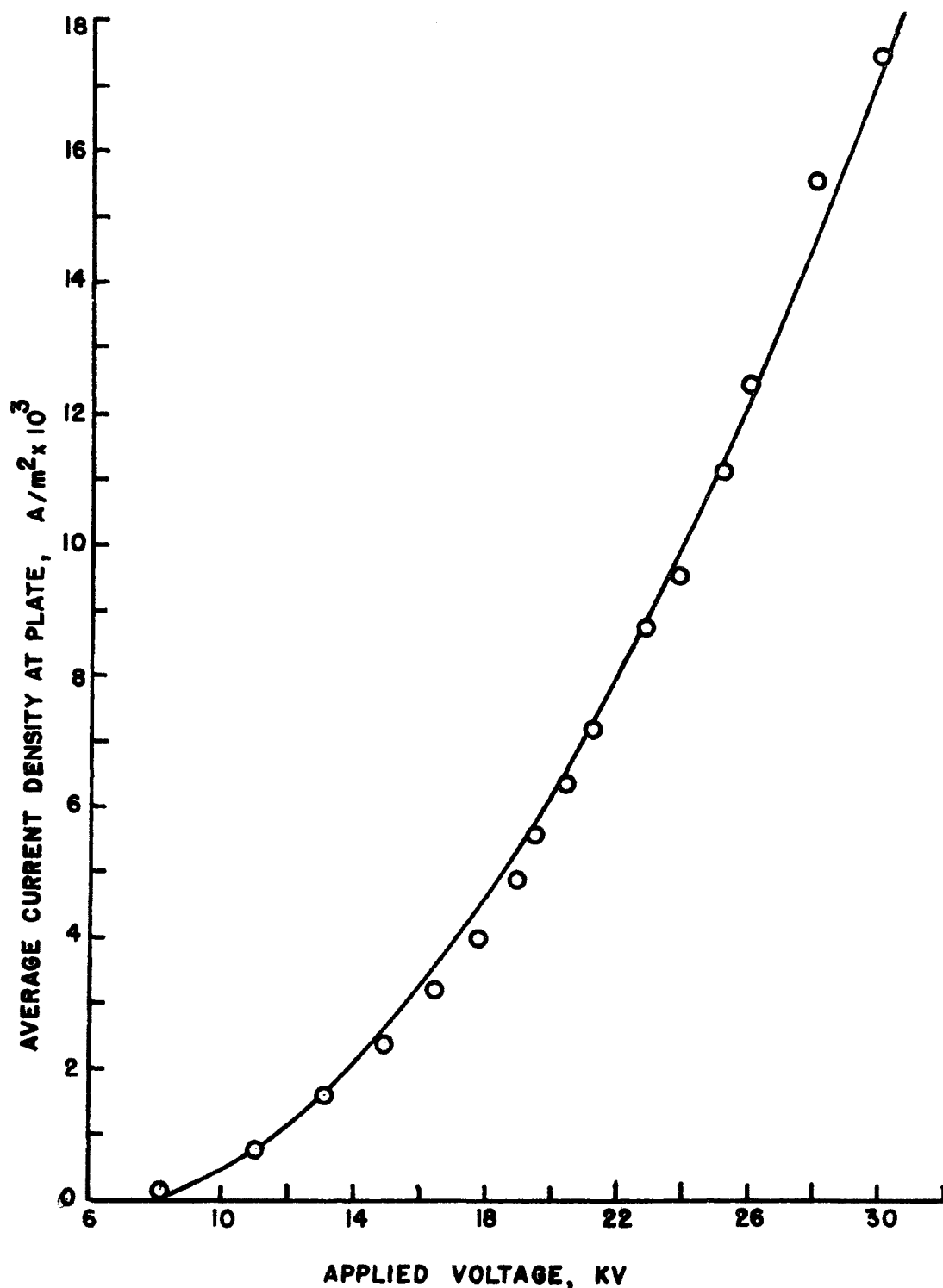


Figure 52. Current-voltage characteristic for the 3-wire pre-charger section with no dust loading, negative corona. The smooth curve is the SRI theory with mobility of  $2.7 \times 10^{-4} \text{ m}^2/\text{V}\cdot\text{sec}$ .

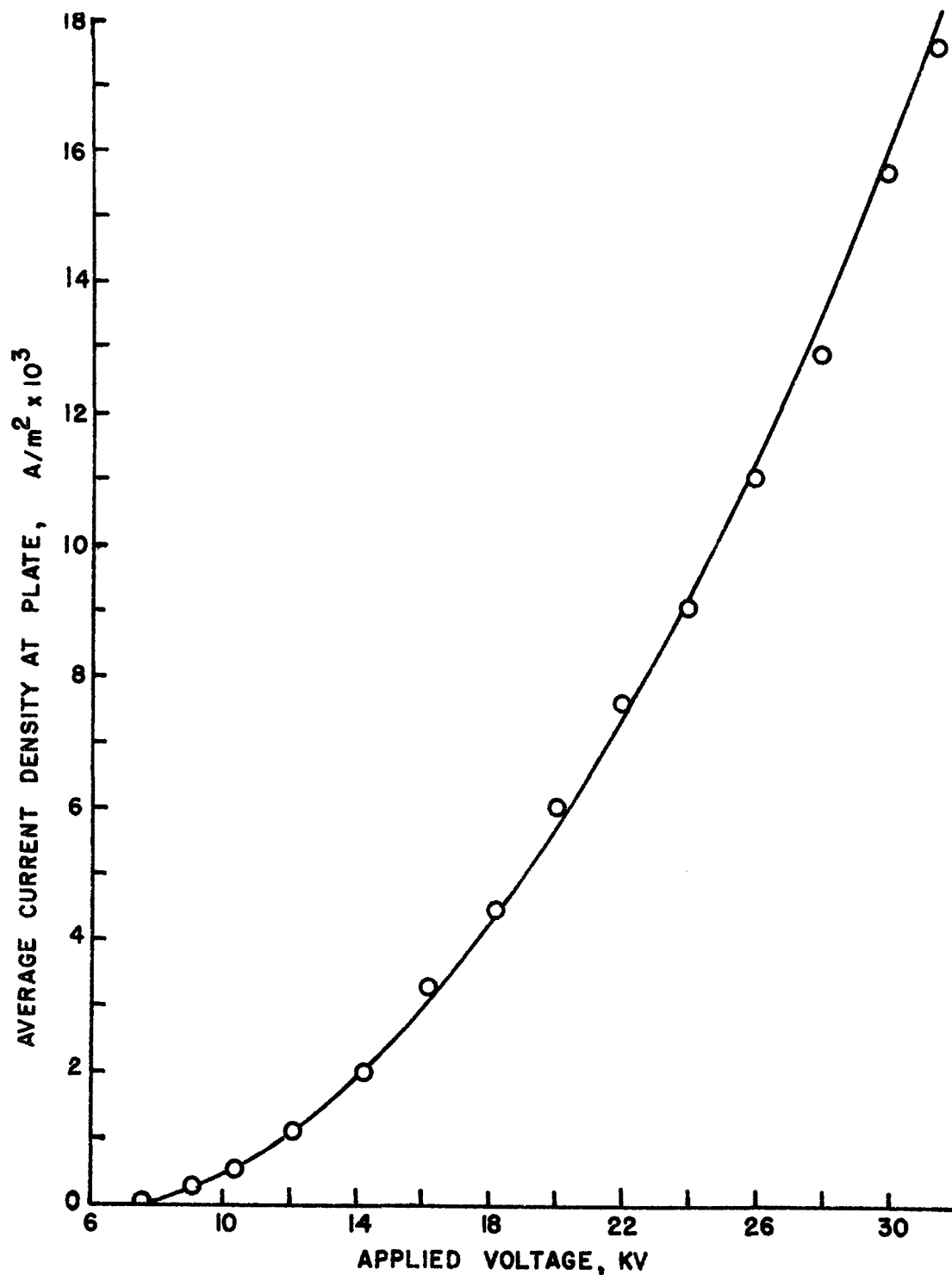


Figure 53. Current-voltage characteristic for the 3-wire pre-charger section under  $6.85 \text{ grain/ft}^3$  dust loading, negative corona. Theoretical curve for mobility of  $2.5 \times 10^{-4} \text{ m}^2/\text{V}\cdot\text{sec}$ .

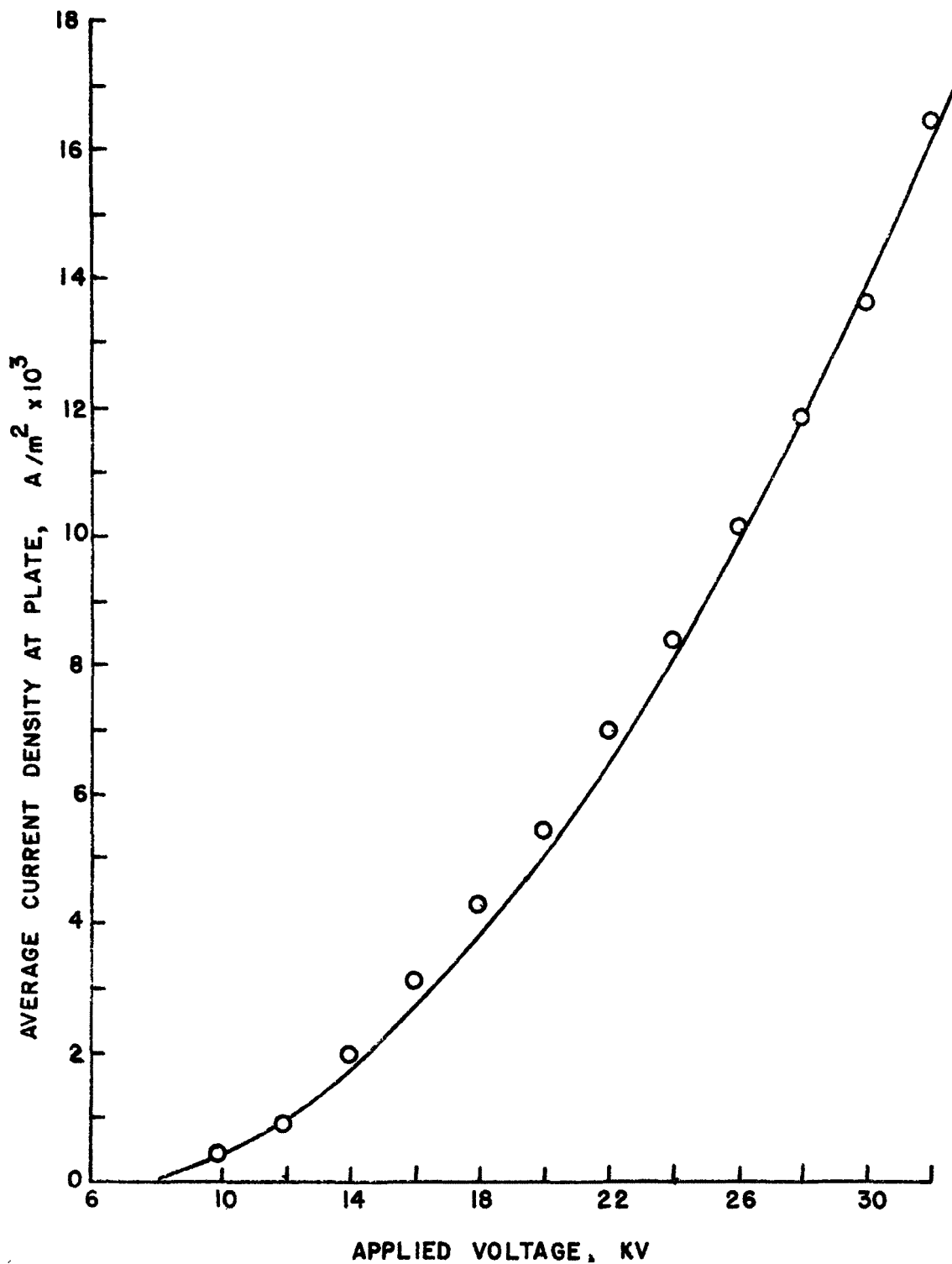


Figure 54. Current-voltage characteristic for the 3-wire pre-charger section under 11.8 grains/ft<sup>3</sup> dust loading, negative corona. Theoretical curve for mobility of  $2.2 \times 10^{-4}$  m<sup>2</sup>/V·sec.

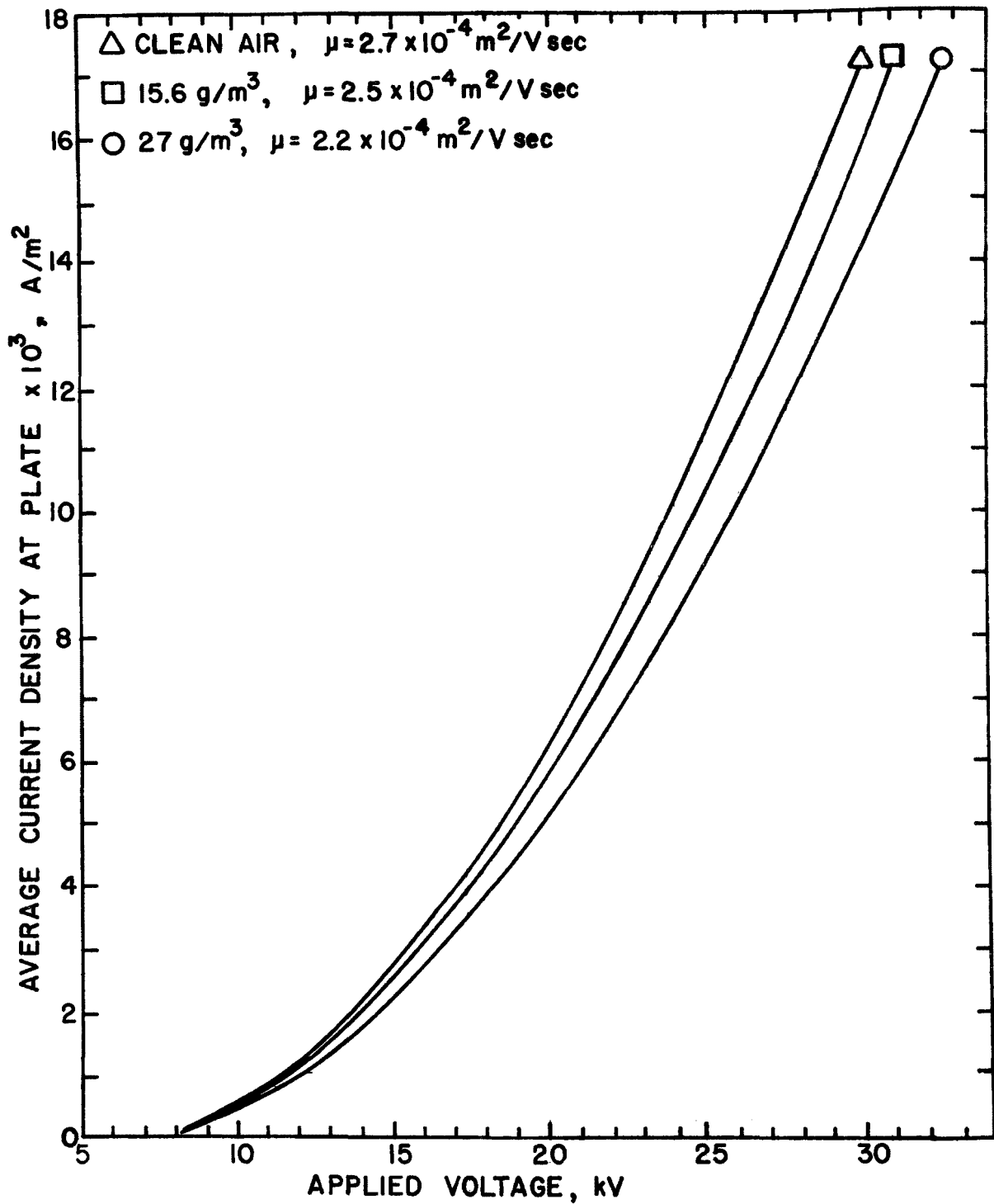


Figure 55. Comparison of the theoretical curves corresponding to Figures 52 through 54 for the 3-wire precharger section.



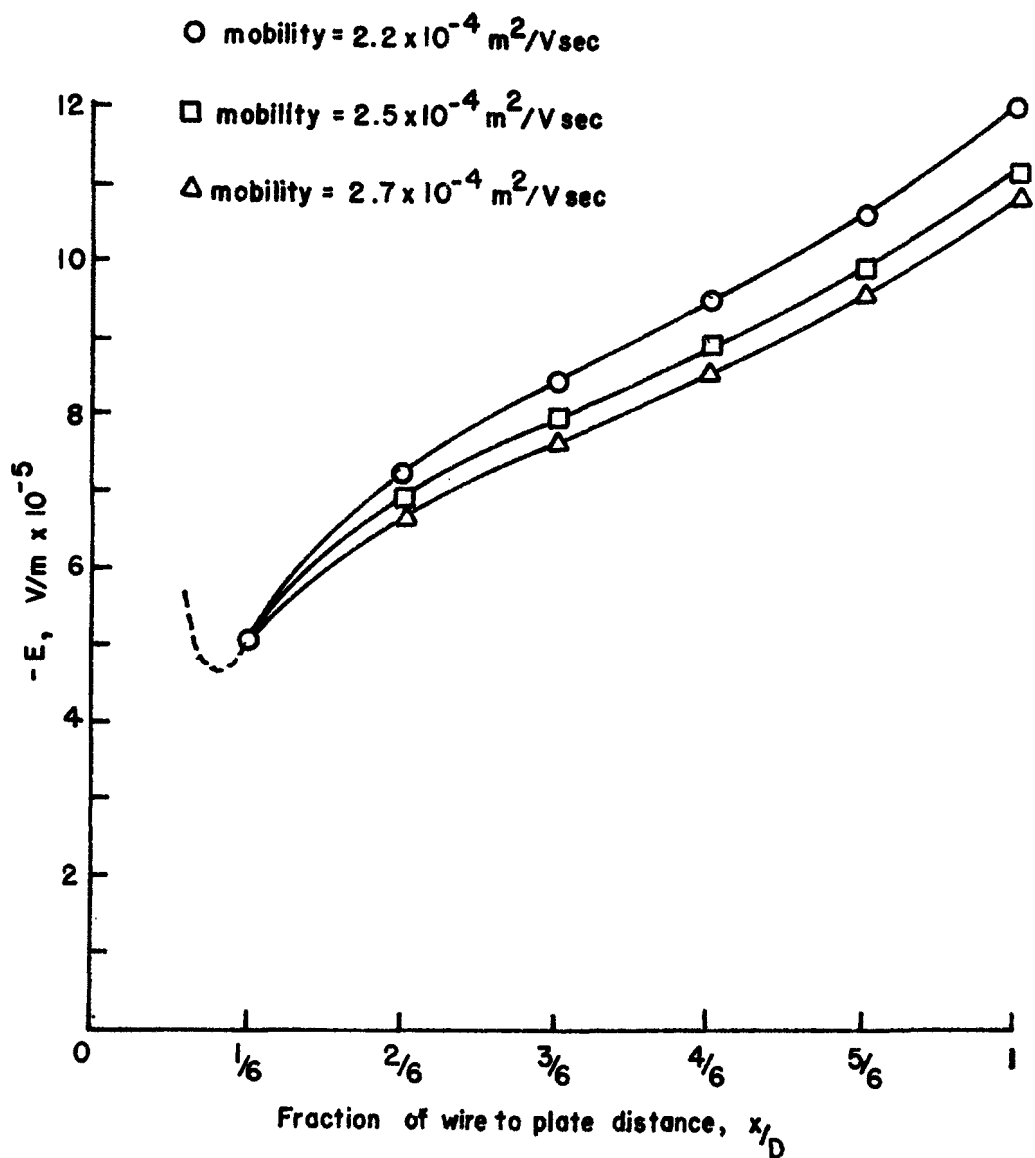


Figure 56. Electric field profiles along a line from wire to plate, normal to the plate, for the maximum values of current and voltage plotted in Figure 55.

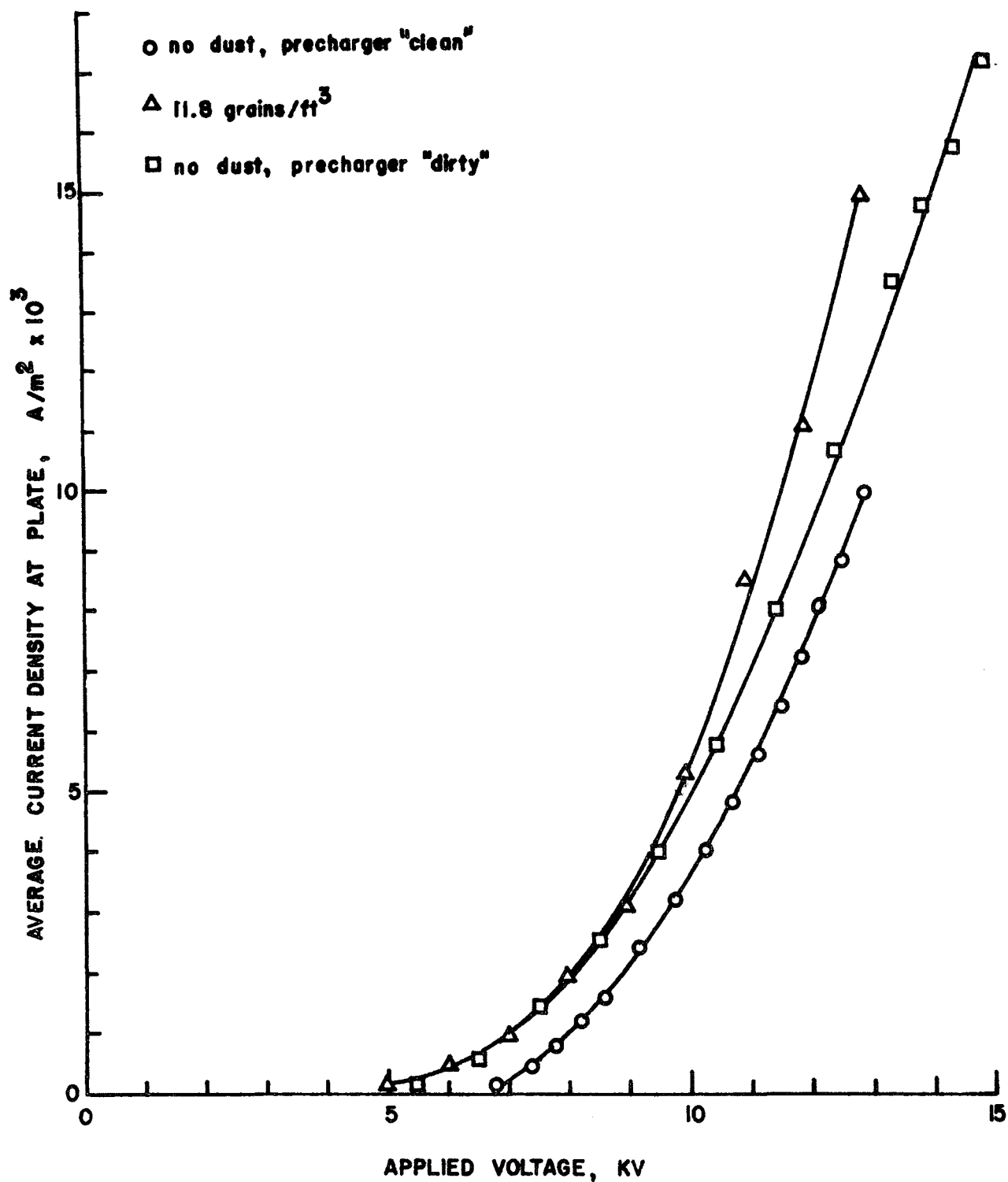


Figure 57. Current-voltage characteristics of 5-wire precharger section under various conditions, negative corona.

density than occurs in the "clean" precharger.

The three-wire precharger section is much less affected by dust accumulation. Part of the reason for this may be found by examining the dust layer after operating both precharger sections. A relatively clear area surrounds the corona wires in the 3-wire section, reaching almost to the plates. Apparently the corona wind in that area tends to blow the dust away, providing a sort of self-clearing effect. In the 5-wire section the maximum applied voltage is lower, and hence the corona wind effect is smaller.

A simple test of the charging effectiveness of the precharger was made by collecting flyash on an isolated metal filter. The filter was connected to an electrometer so that the integrated charge could be monitored for a sample of flyash which had passed through the precharger.

A plastic filter holder, fitted with a nozzle for isokinetic sampling, and containing a silver filter was placed in the duct immediately downstream from the precharger. Preliminary tests showed that when the precharger was turned on and no flyash was being blown through the system, charge accumulation on the filter was of the order of  $10^{-11}$  coul/sec or less. Approximately the same order of charge accumulation occurred with the precharger turned off and with flyash blown through the duct. When the precharger and flyash blower were both turned on the rate of charge accumulation rose abruptly to more than  $10^{-9}$  coul/sec. For each test point measured the precharger was set at a particular voltage and then the flyash feed and blower were turned on until a total charge of approximately  $5 \times 10^{-8}$  coul was accumulated on the filter. The collected flyash was then weighed and the charge/mass ratio was calculated. Figure 58 shows the results of these measurements for negative corona and Figure 59 shows the positive corona results.

A measurement of charge/mass ratio was also made at elevated temperature. The precipitator system was heated to approximately  $105^{\circ}\text{C}$  and the negative corona charging test was repeated. The results, shown in Figure 58 show a much reduced charging effectiveness. Heating the flyash produced an increase in resistivity, and apparently back corona occurred at a voltage only very slightly above the corona inception voltage.

Impactor data were taken to provide size distribution information as well as to verify the effectiveness of the precharger in improving the performance of the pilot scale precipitator. Figure 60 shows inlet data for two Brink impactor runs made on different days. An Andersen impactor was used to measure the outlet size distribution. The data points for the smaller particle sizes at the outlet with the precharger on must be considered less reliable because the samples collected by the impactor were

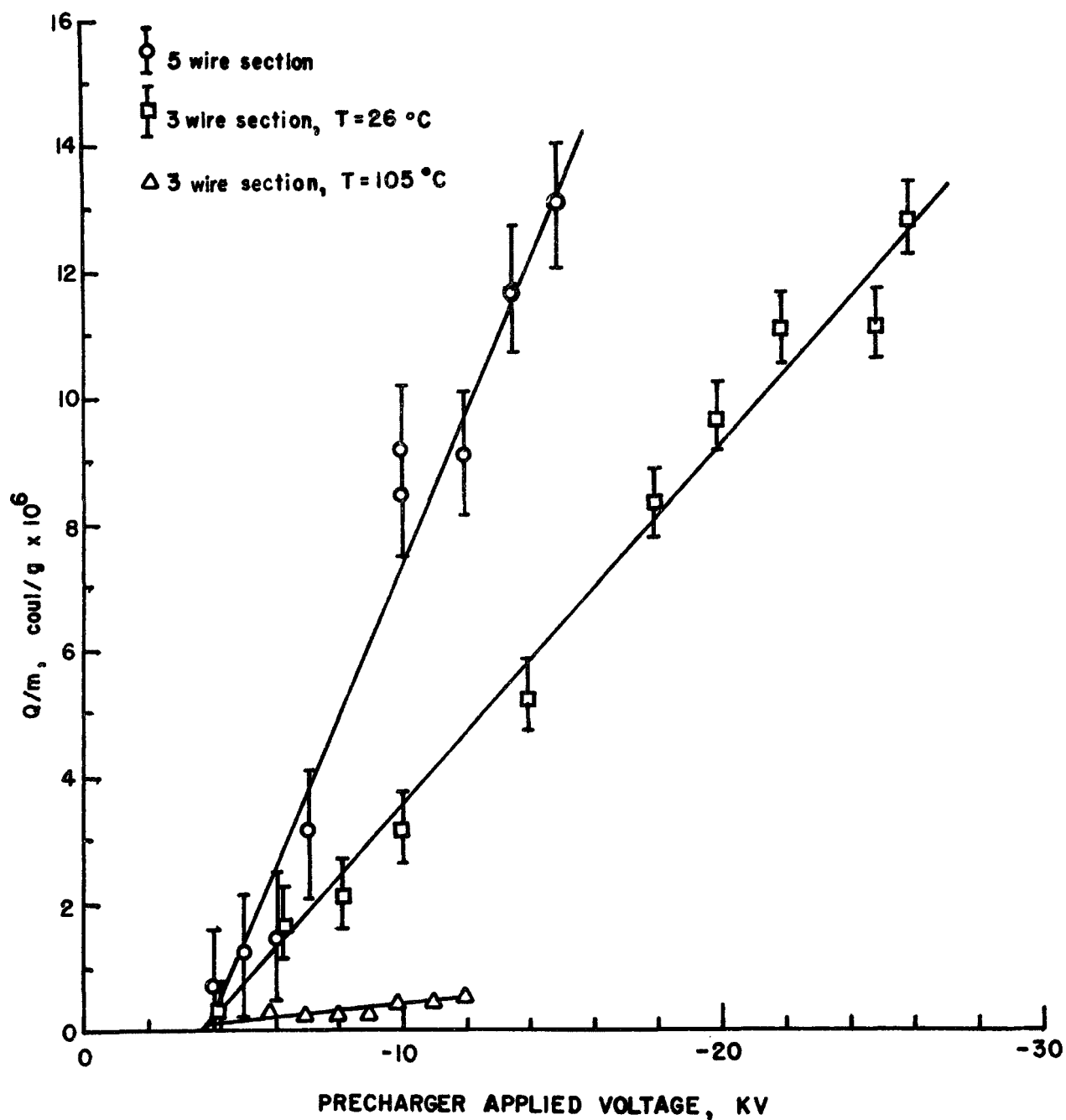


Figure 58. Charge/mass ratio as a function of voltage applied to precharger; negative corona.

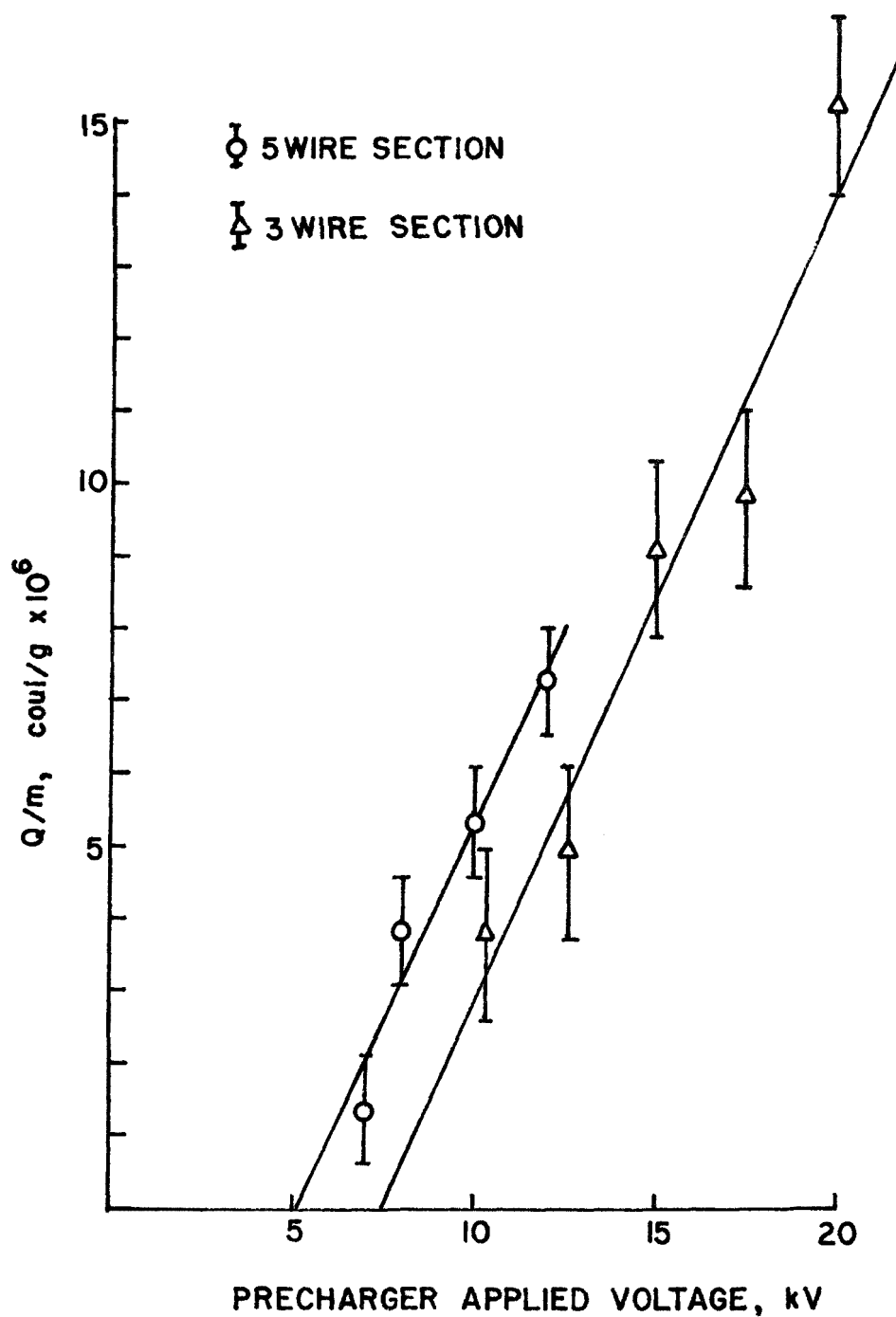


Figure 59. Charge/mass ratio as a function of precharger voltage, positive corona.

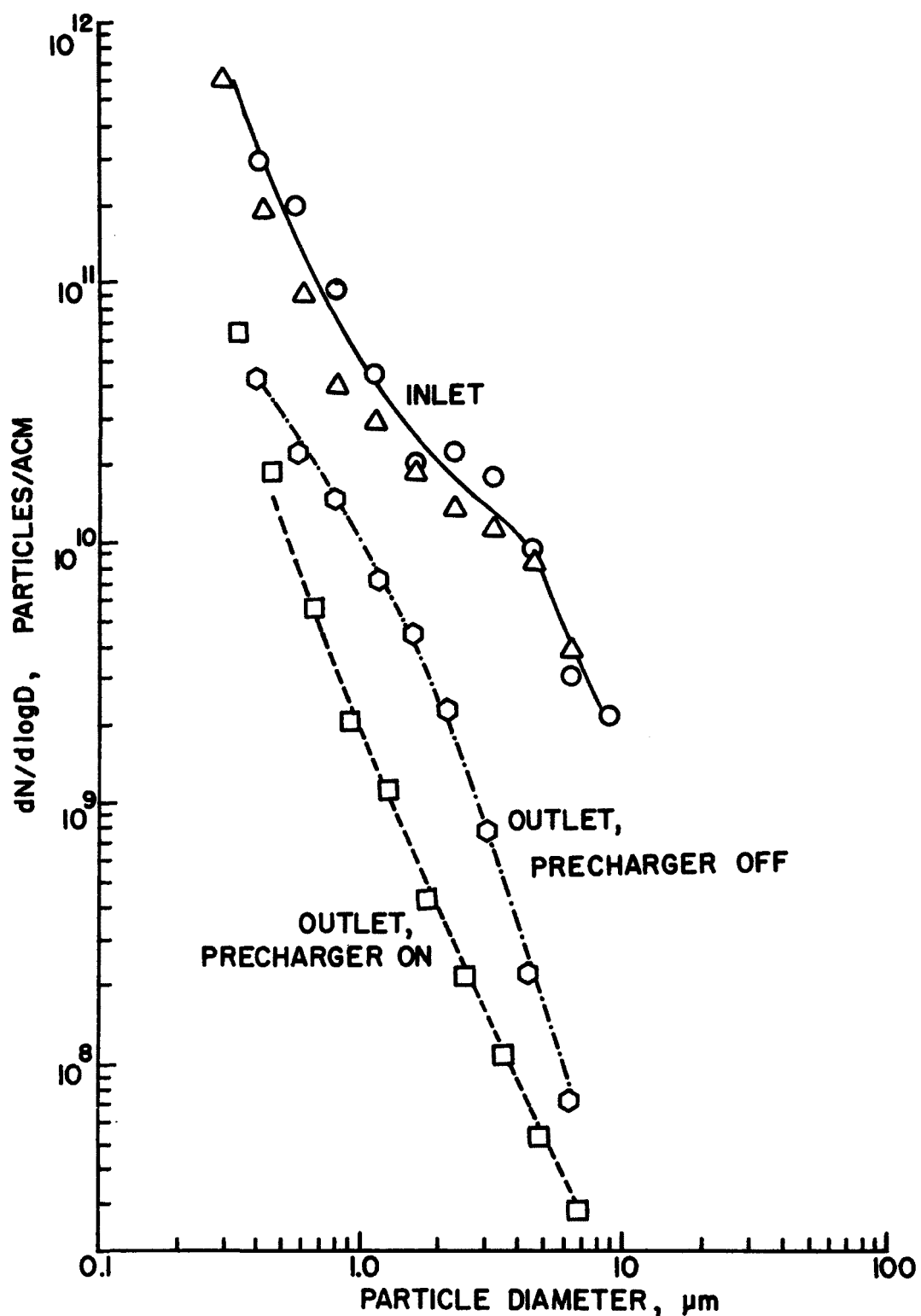


Figure 60. Size distributions of flyash at inlet, as measured with Brink impactor and at outlet using Andersen impactor.

very small. A broken corona wire in the precharger required that the sampling time be cut short.

The collection efficiency curves presented in Figure 61 were derived from the information in Figure 60. The pilot scale precipitator was operating at a current density of approximately  $270 \mu\text{A}/\text{m}^2$ . The three-wire precharger section was set at approximately  $8 \text{ mA}/\text{m}^2$ . An inlet mass loading of approximately  $3.4 \text{ g}/\text{m}^3$  was used for these measurements.

The SRI charging theory was used to compute the charge/mass ratio obtained with the precharger for comparison with the measured results. The computer program calculates the total charge per particle of a specified diameter. Input information includes average charging field, ion density, and residence time in the charging region. These quantities were derived directly from the measured current-voltage characteristics of the precharger and the flow rate through the charging region. Using a density of  $2.25 \text{ g}/\text{cm}^3$ , the charge/mass ratio was computed for eight particle sizes in the range  $0.25 \mu\text{m}$  to  $32 \mu\text{m}$  diameter, with various voltages applied. The results of these calculations are shown in Figures 62, 63, 64 and 65. The four cases include each of the precharger sections under both positive and negative corona conditions. In the range of particle sizes considered, field charging dominates over the diffusion charging process. Since the charging rate depends on the square of the radius and the mass increases as the cube of the radius the charge/mass is inversely proportional to the particle radius.

In order to compare the theoretical results with experimental measurements a sum was taken over the range of particle sizes, weighted in accordance with the measured particle size distribution. Thus, for a particulate sample having mass  $M$  and a size distribution such that there are  $N_i$  particles per gram in the  $i$ th size range, with average charge  $q_i$  per particle,

$$\frac{Q}{M} = \sum_i N_i q_i. \quad (19)$$

The theoretical values of charge/mass ratio are shown in Figures 66, 67, 68, and 69 along with the experimentally determined values. The scatter in the theoretical points arises from the fact that empirically derived input information was used in the charging theory. In nearly all cases the theoretical values are somewhat higher than those determined experimentally. But, considering the magnitude of statistical errors involved, the agreement between theory and experiment appears to be reasonable.

The effects of the precharger on overall precipitator performance were investigated under various voltage conditions by making outlet particulate load measurements with a Climet

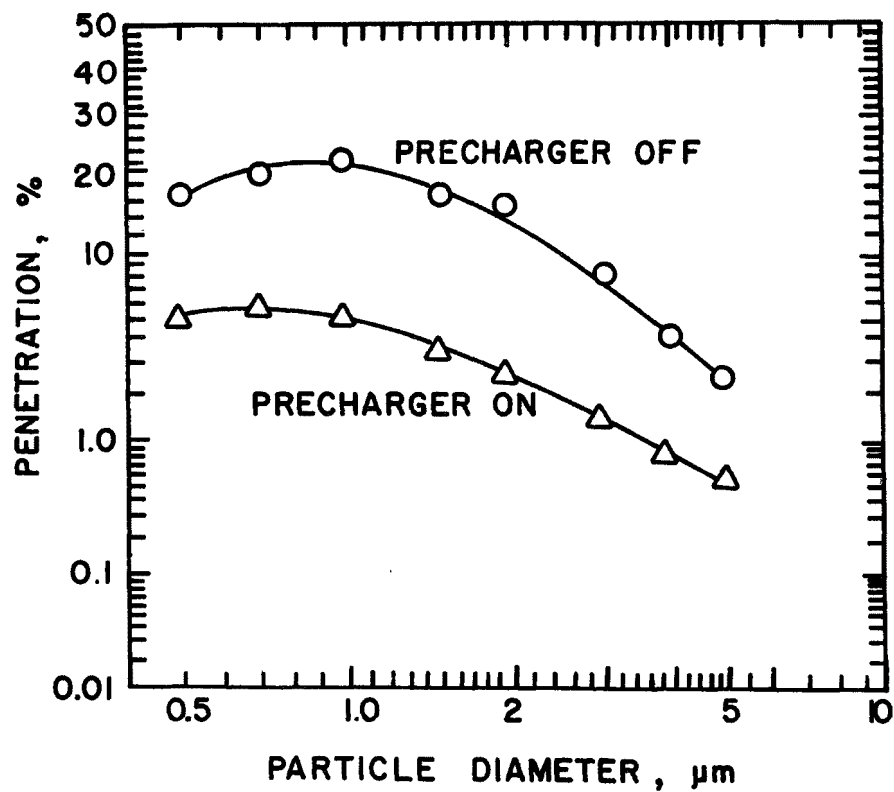


Figure 61. Penetration of pilot scale dry wall precipitator with 3-wire precharger section turned on compared with efficiency obtained with the precharger off. Precipitator current density was held at  $270 \mu\text{A}/\text{m}^2$  throughout these measurements.



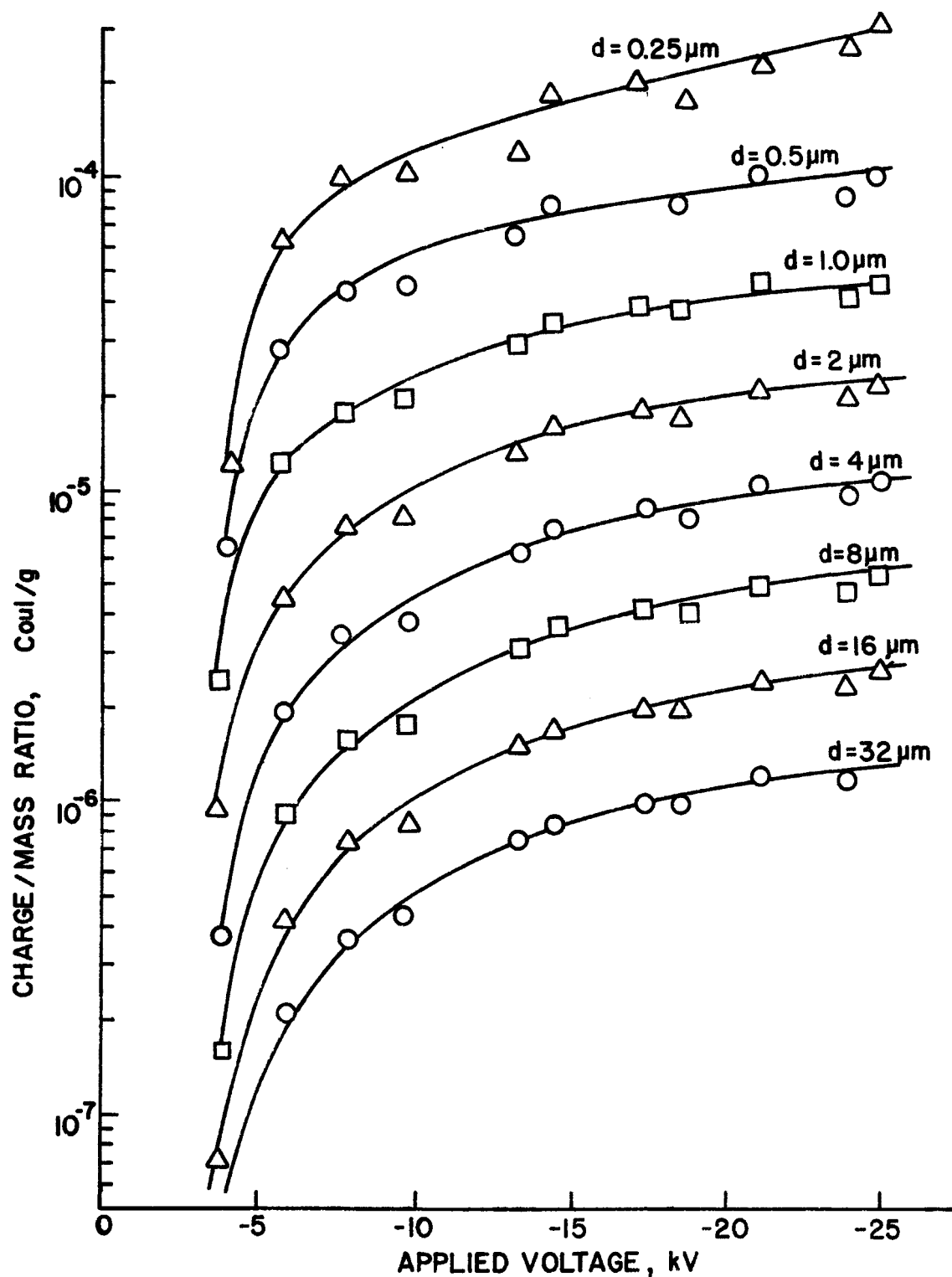


Figure 62. Charge/mass ratio as a function of precharger voltage for various particle sizes in the 3-wire precharger section, negative corona. Low resistivity flyash.

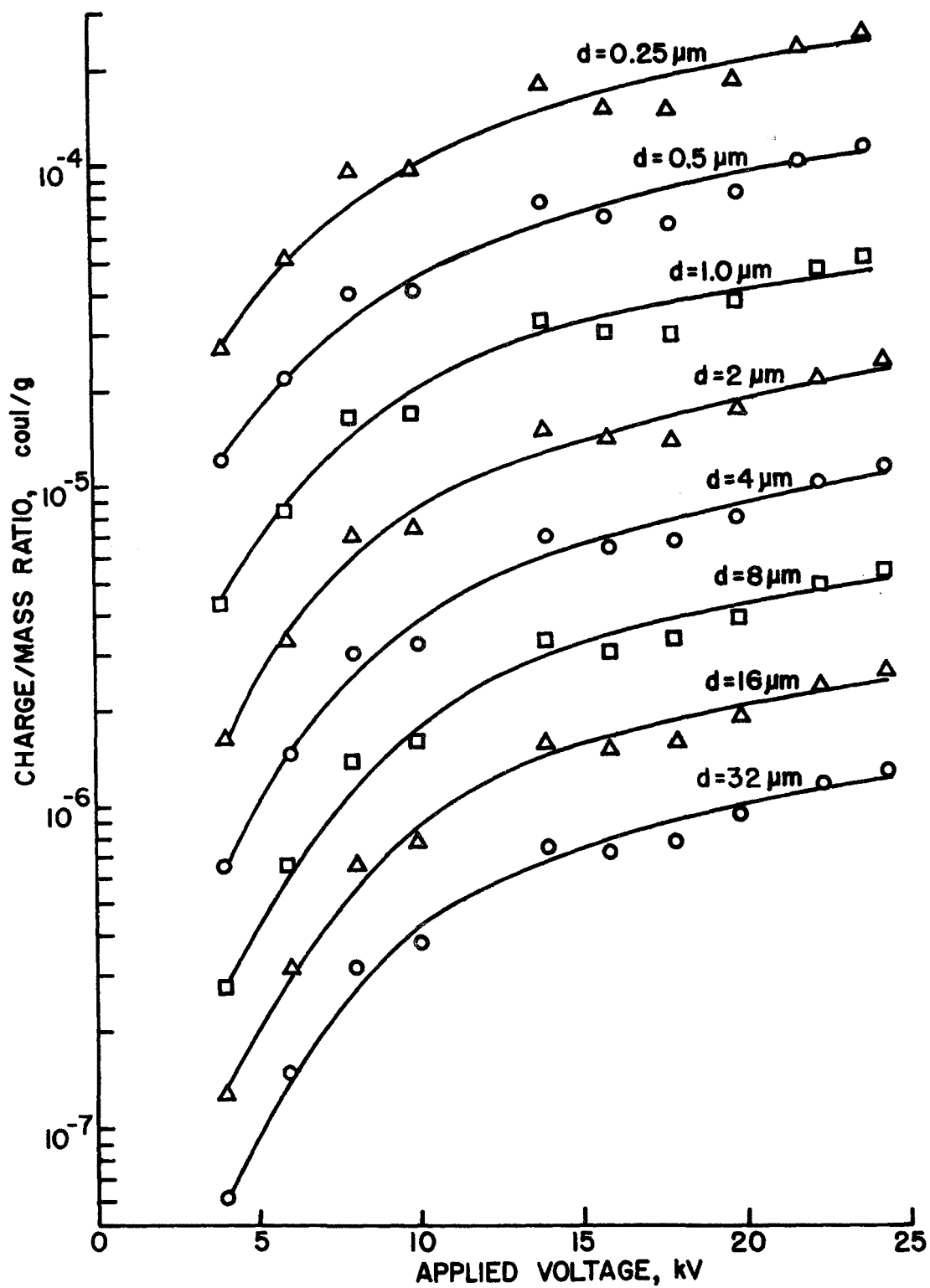


Figure 63. Charge/mass ratio as a function of precharger voltage for various particulate sizes in the 3-wire precharger section, positive corona.

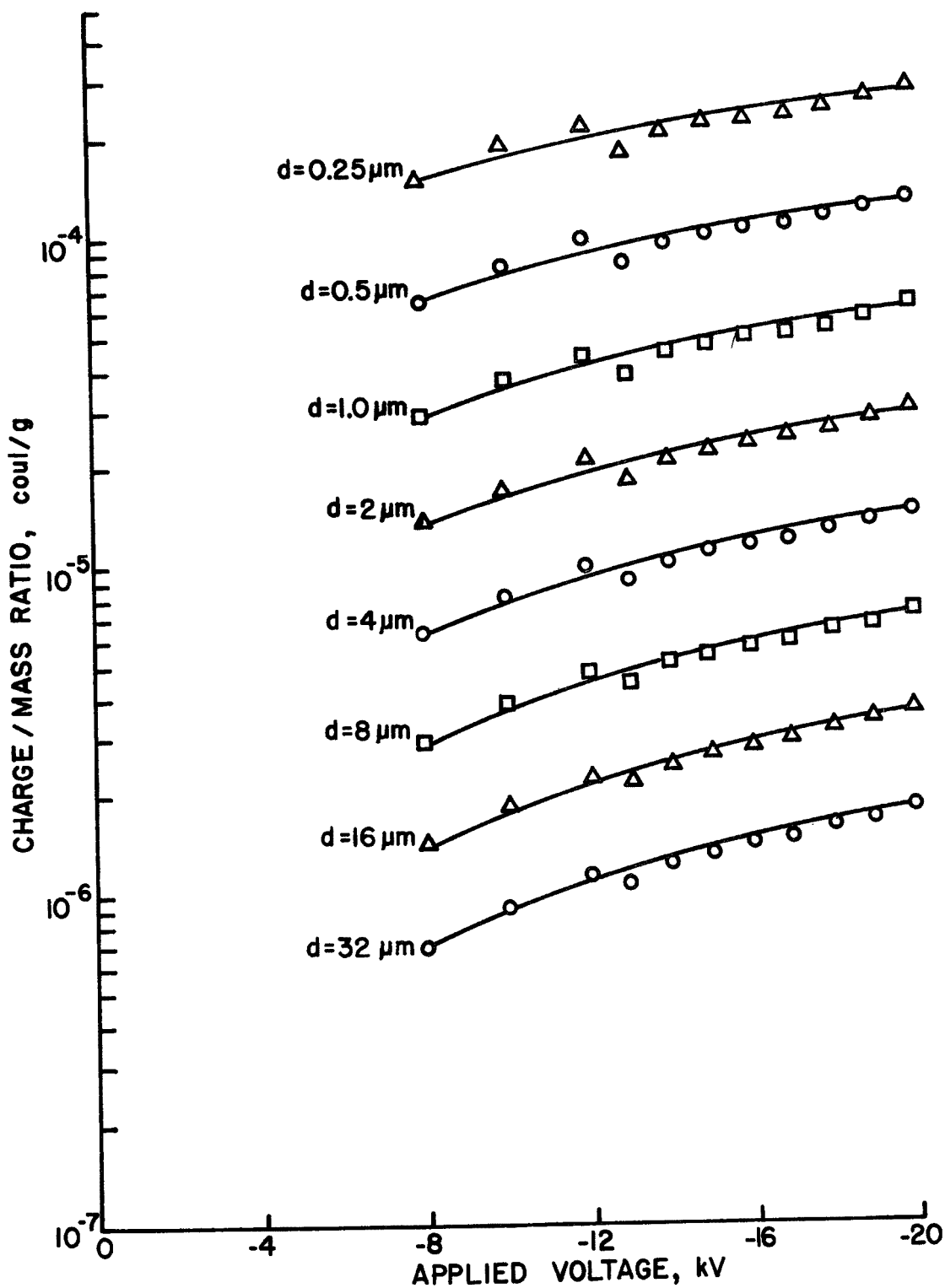


Figure 64. Charge/mass ratio as a function of precharger voltage for various particle sizes in the 5-wire precharger section, negative corona.

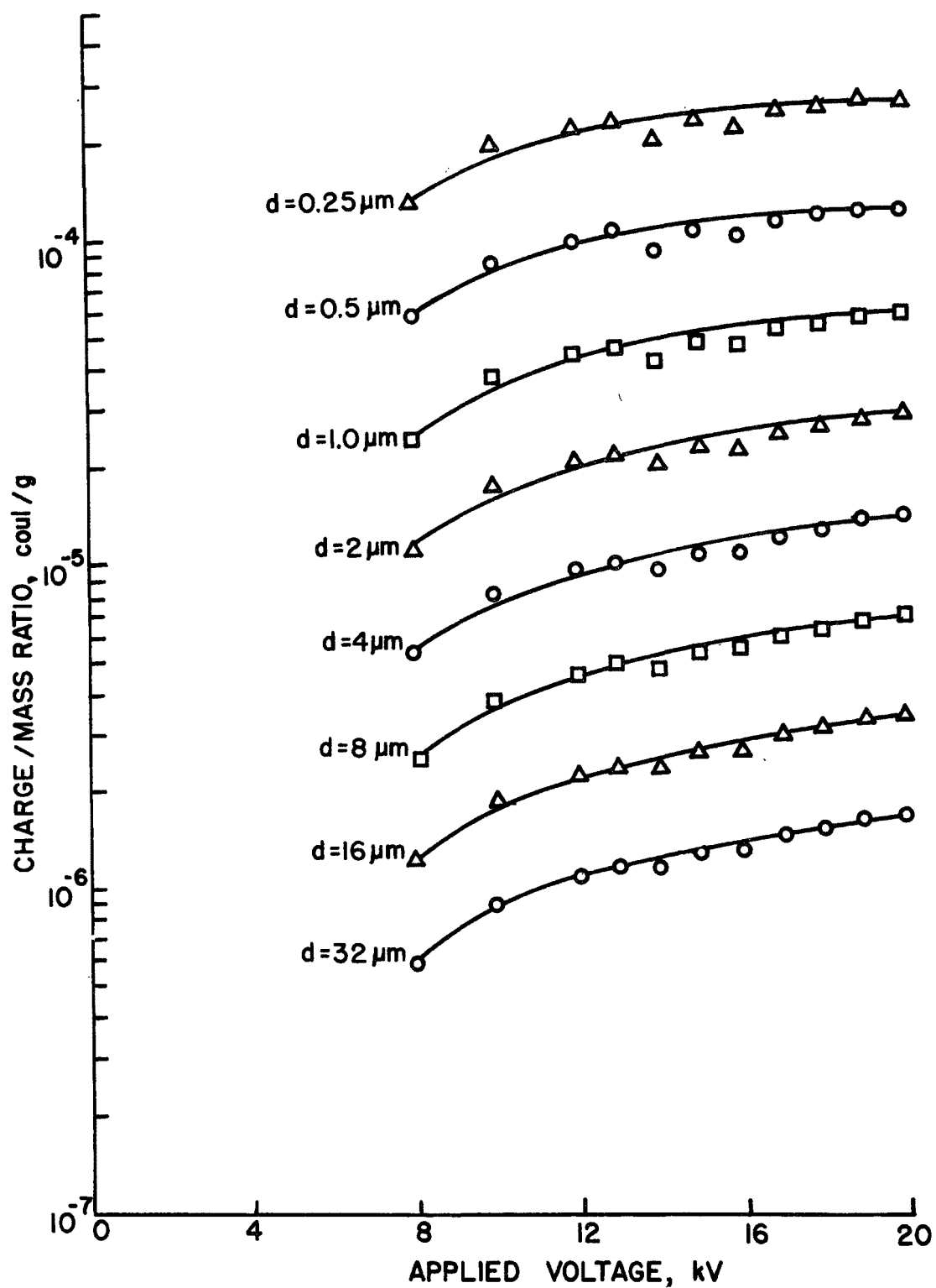


Figure 65. Charge/mass ratio as a function of precharger voltage for various particle sizes in the 5-wire precharger section, positive corona.

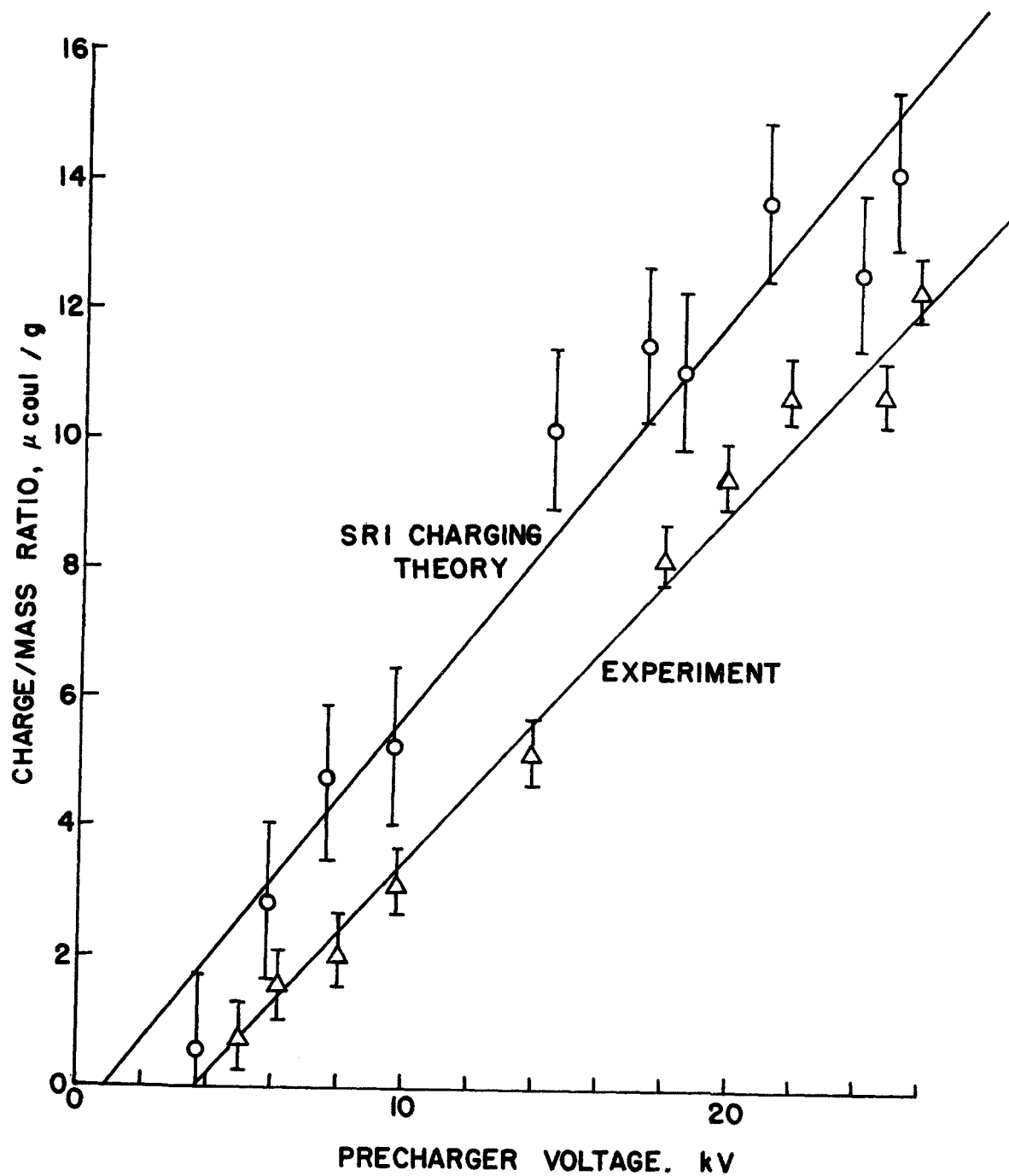


Figure 66. Comparison of experiment with theory for overall charge/mass ratio of flyash sample in 3-wire pre-charger section, negative corona.

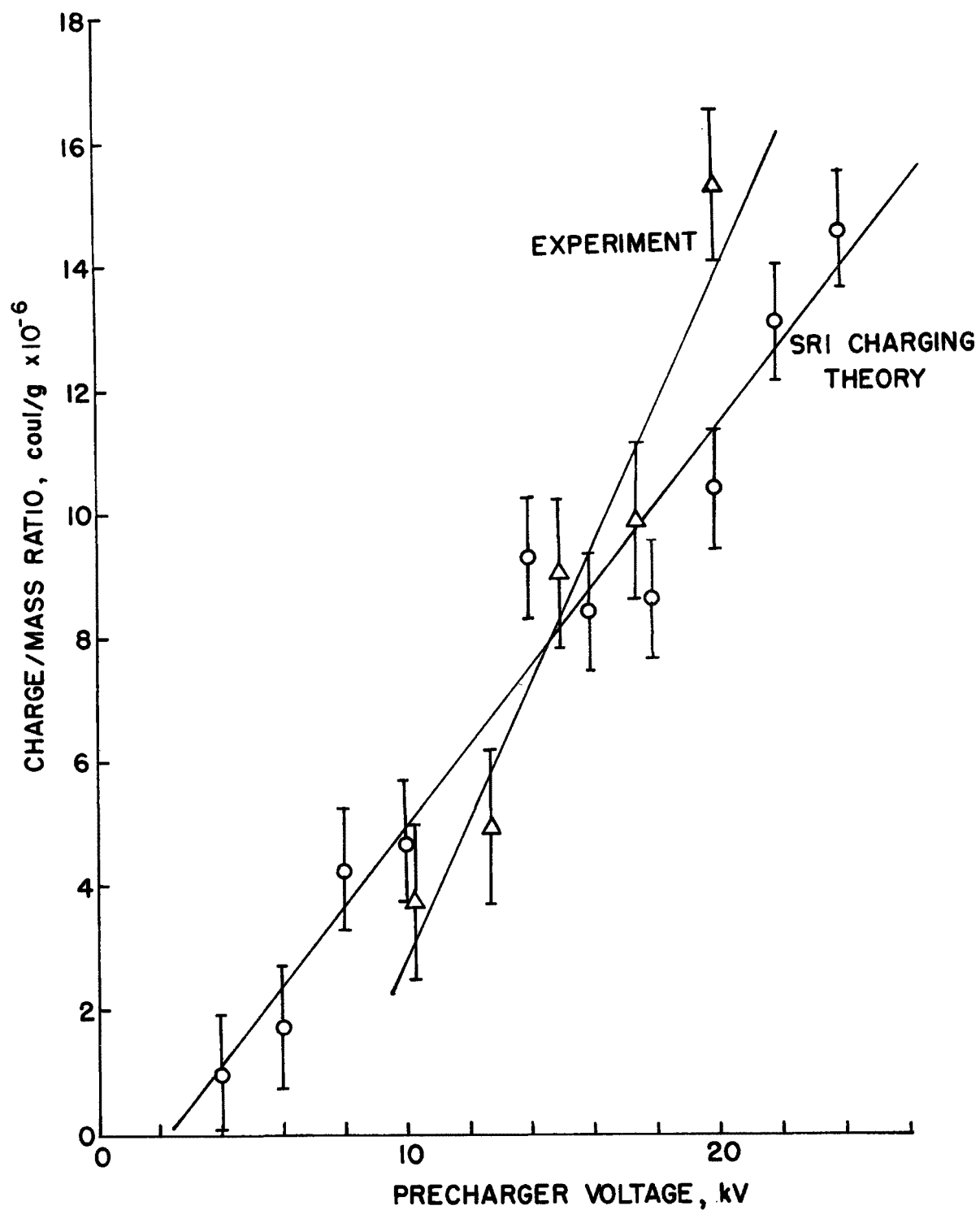


Figure 67. Comparison of experiment with theory for overall charge/mass ratio of flyash sample in 3-wire precharger section, positive corona.

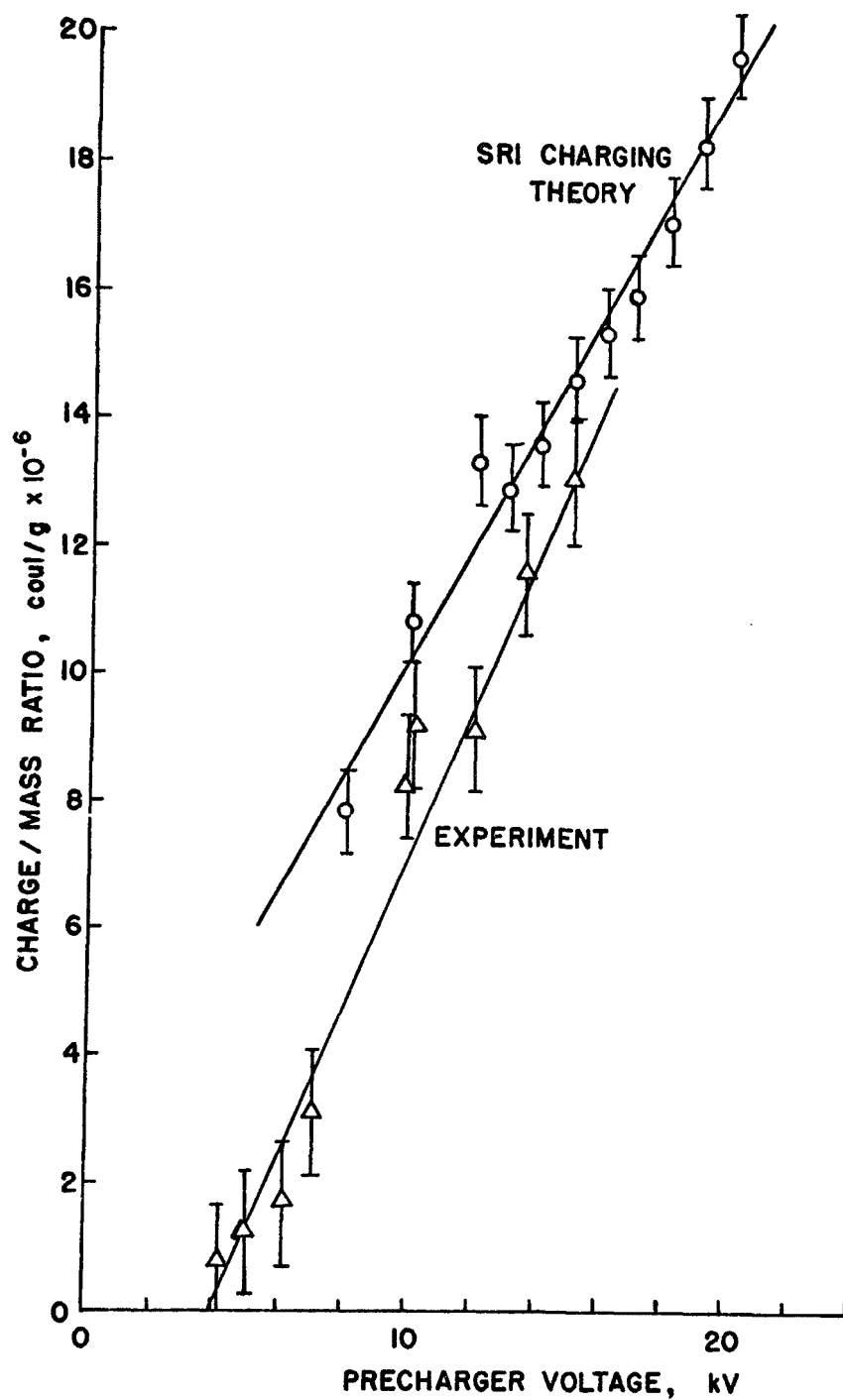


Figure 68. Comparison of experiment with theory for overall charge/mass ratio of flyash sample in 5-wire precharger section, negative corona.

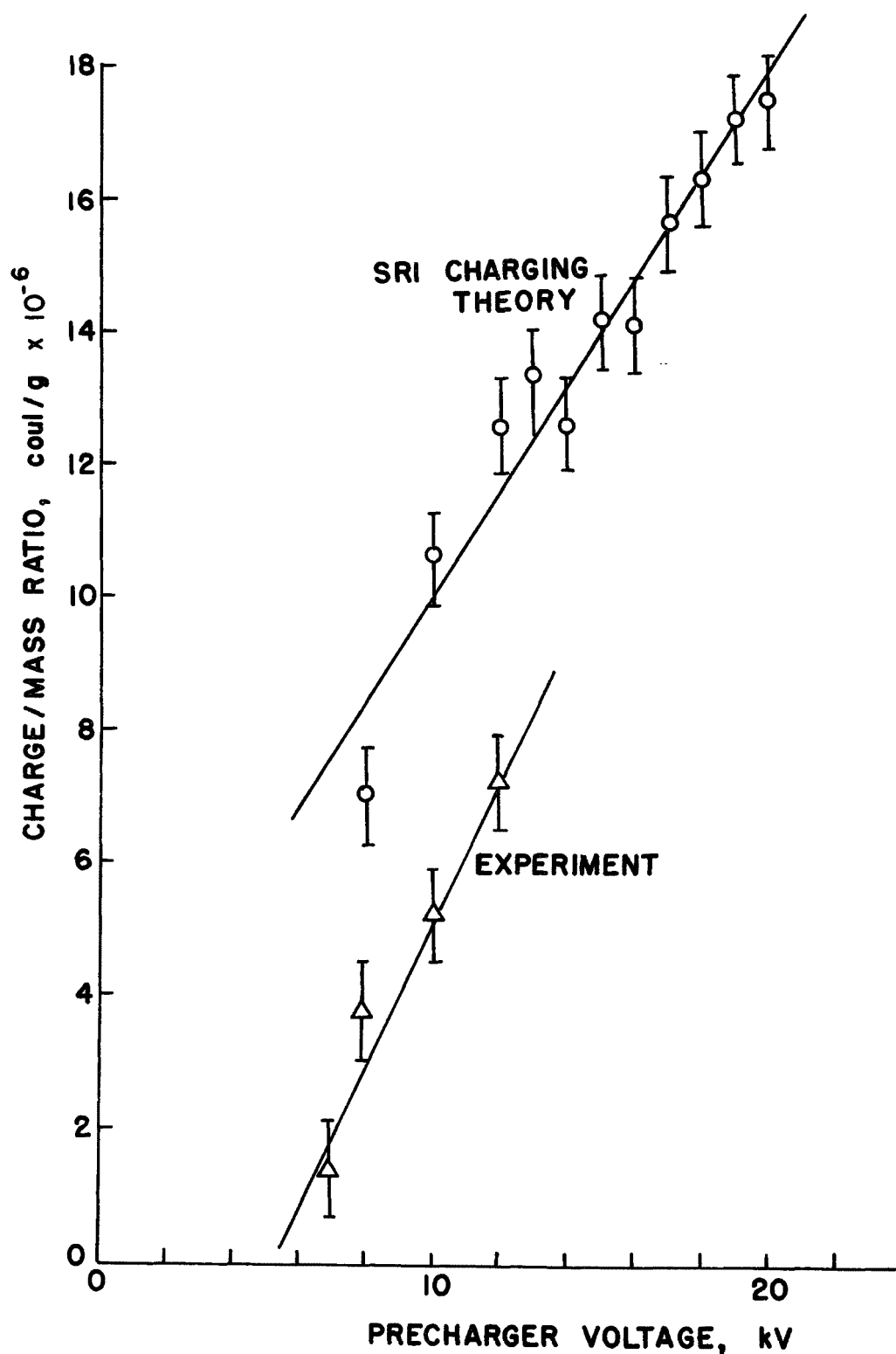


Figure 69. Comparison of experiment with theory for overall charge/mass ratio of flyash sample in 5-wire precharger section, positive corona.



Instruments Model 208 optical particle counter. A significant increase in collection efficiency was observed for all particle sizes as the precharger voltage was increased while holding the precipitator voltage constant. Figure 70 shows the results for the 3-wire precharger section and Figure 71 shows the 5-wire section results. In both cases the pilot scale precipitator was operated near the maximum voltage which could be applied without excessive sparkover; approximately 40 kV. Both precharger sections were capable of producing improved collection efficiency, but the 3-wire geometry was clearly the more effective of the two.

Figures 72 and 73 present the same data shown in the previous two graphs, except that the collection efficiency is given as a function of the current density in the precharger. The migration velocity is also shown as a function of precharger current density in these plots.

In Figure 74 the performance of the precharger - precipitator combination is indicated for various values of precipitator voltage with the precharger voltage held at approximately 20 kV. When the precipitator voltage was removed completely some particle collection was achieved. The efficiency increased as the field in the precipitator was increased, but much greater increase in efficiency occurred as the corona current in the precipitator became substantial.

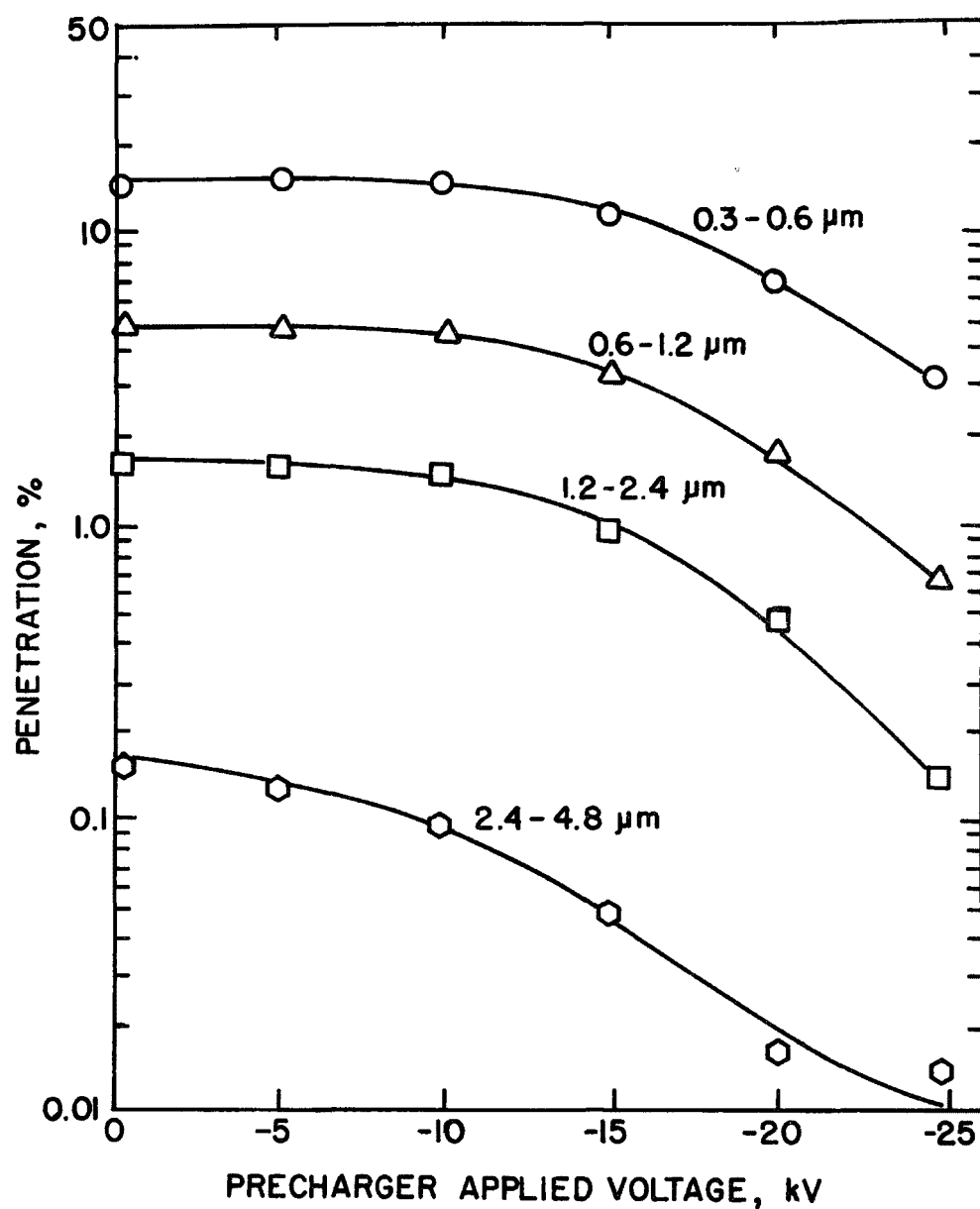


Figure 70. Penetration of the pilot scale electrostatic precipitator for various particle sizes. The precipitator voltage was held constant while the voltage on the 3-wire precharger section was varied.

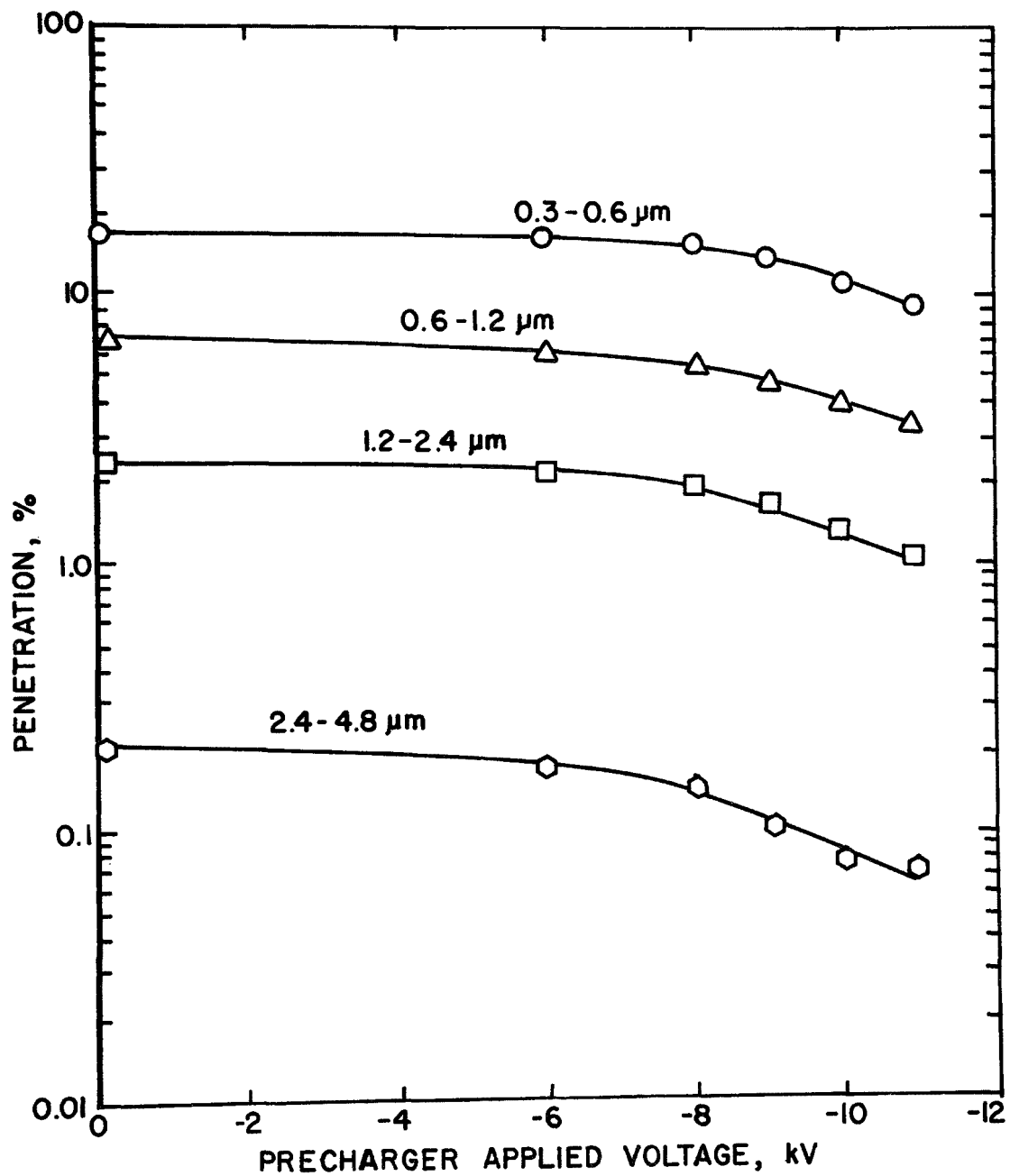


Figure 71. Penetration of the pilot scale electrostatic precipitator as a function of the voltage on the 5-wire precharger section.

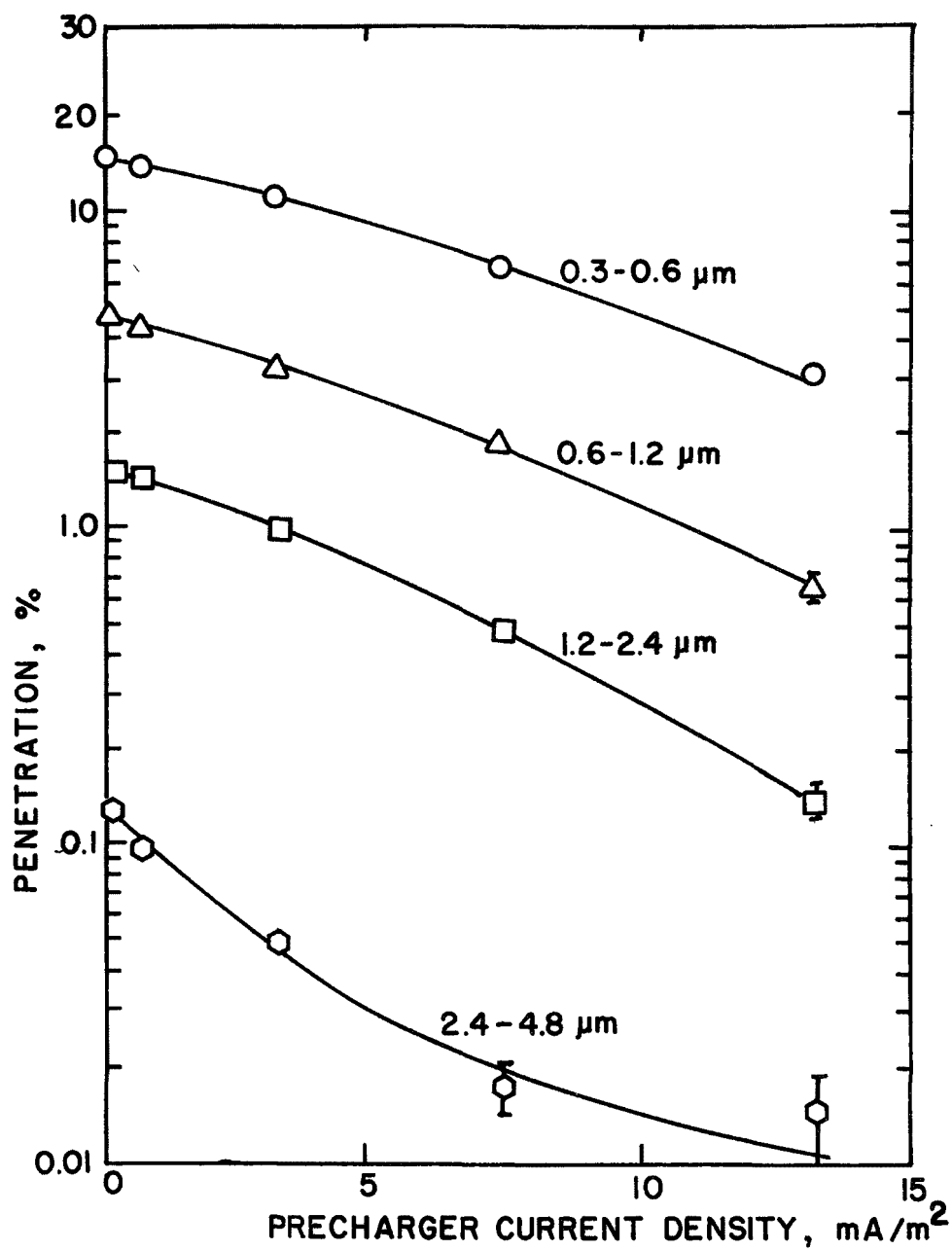


Figure 72. Penetration as a function of precharger current density for various particle sizes, using the 3-wire precharger.

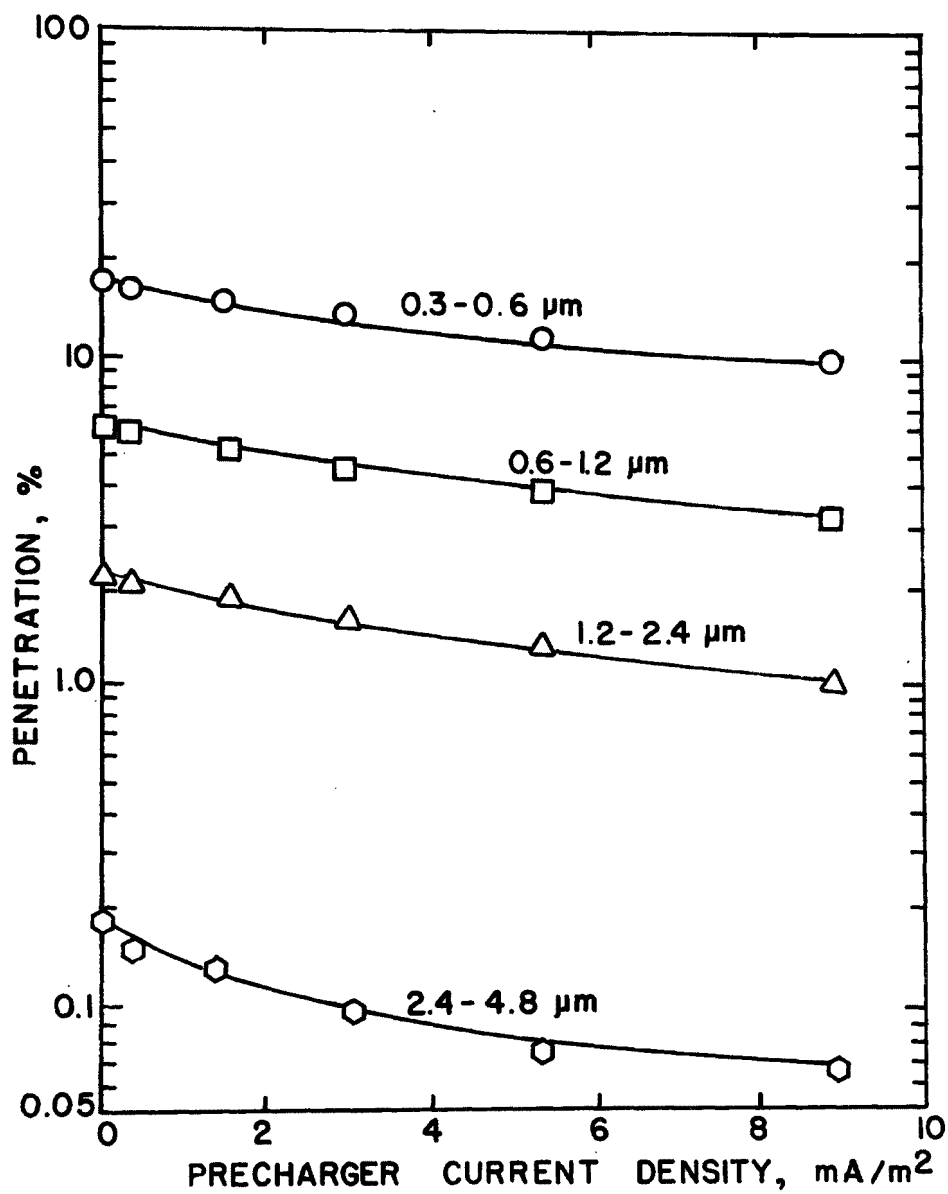


Figure 73. Penetration as a function of precharger current density for various particle sizes, using the 5-wire precharger.

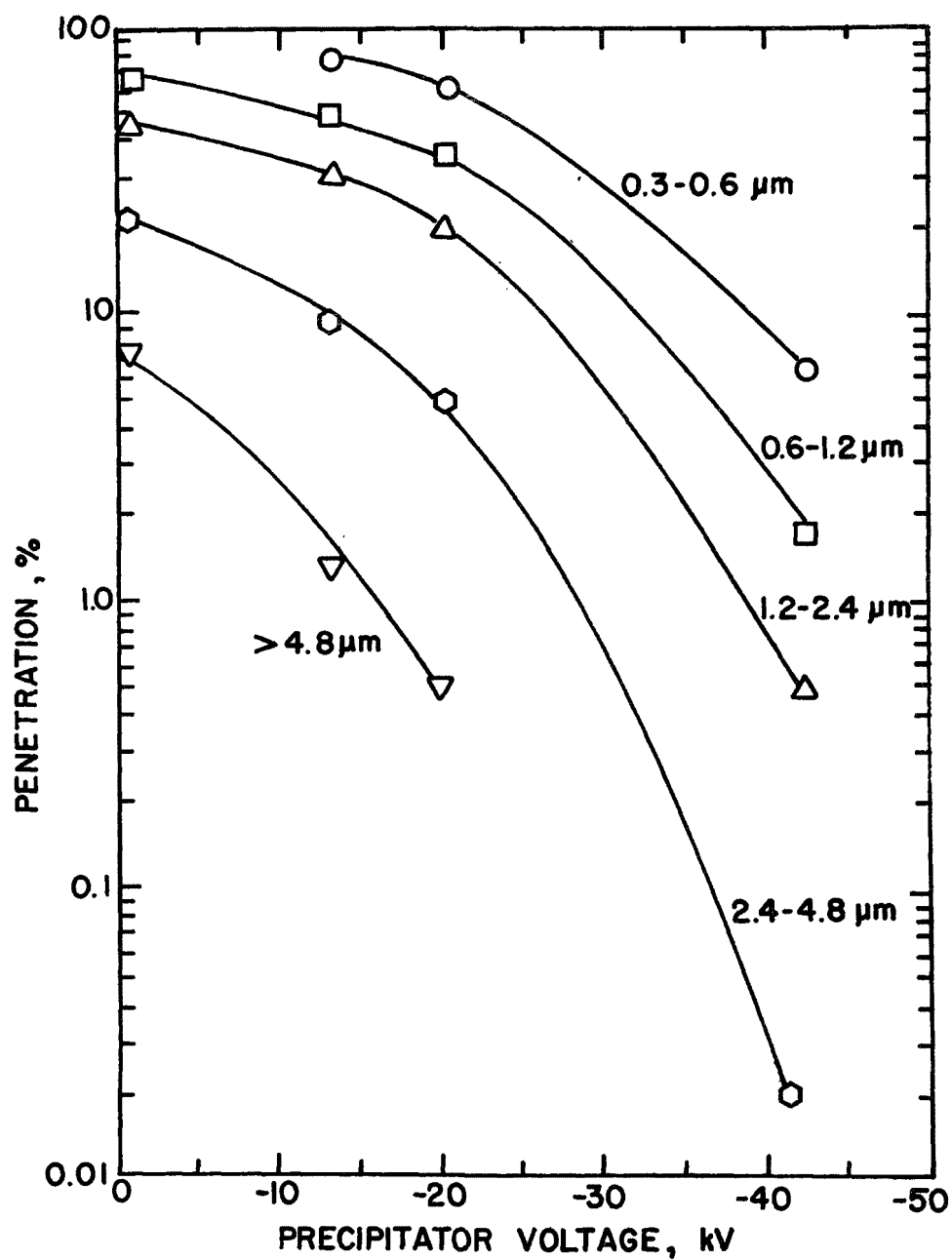


Figure 74. Penetration of pilot scale electrostatic precipitator as main voltage is varied while maintaining the 3-wire precharger voltage constant at approximately 20 kV.

## SECTION 6

### ANALYSIS AND EVALUATION OF THE TWO-STAGE, PRECHARGER-ESP CONCEPT

#### PARTICLE CHARGING

In a two-stage precharger-ESP the particle charging and collection functions are carried out separately. An important factor in the operation of a two-stage system is effective particle charging in the precharger stage. The theory shows that large values of both electric field strength and ion density-residence time product are required to provide a suitable level of particle charging effectiveness in a precharger. Practical limitations on the performance of a precharger may arise from two principal sources: (1) the presence of particulate material having high electrical resistivity, and (2) the effects of space charge on the electrical characteristics of the system. The importance of the various factors related to particle charging are discussed in the following paragraphs.

#### Electrical Parameters

The results of the charging theory may be used to examine the effects of variation of charging parameters. In the following discussion the effects of the electric field strength, the ion density-residence time product, and the corona geometry for a wire-plate system are examined.

The graph shown in Figure 75 presents the charge per particle as a function of the average field for two values of ion density-time product and for various particle sizes. The effect of varying  $Nt$  is more pronounced for small particles than for the larger ones. The effect of field charging with increasing particle size is evident from the difference in the shape of the curves for the different particle sizes.

Figure 76 indicates the charging behavior as a function of the ion density-residence time product,  $Nt$ , for fields of 5 kV/cm and 10 kV/cm for three particle sizes. It can be seen that increasing  $Nt$  above approximately  $10^{13}$  sec/cm<sup>3</sup> will produce little increase in the charge accumulated, particularly for the larger particles, where field charging dominates.

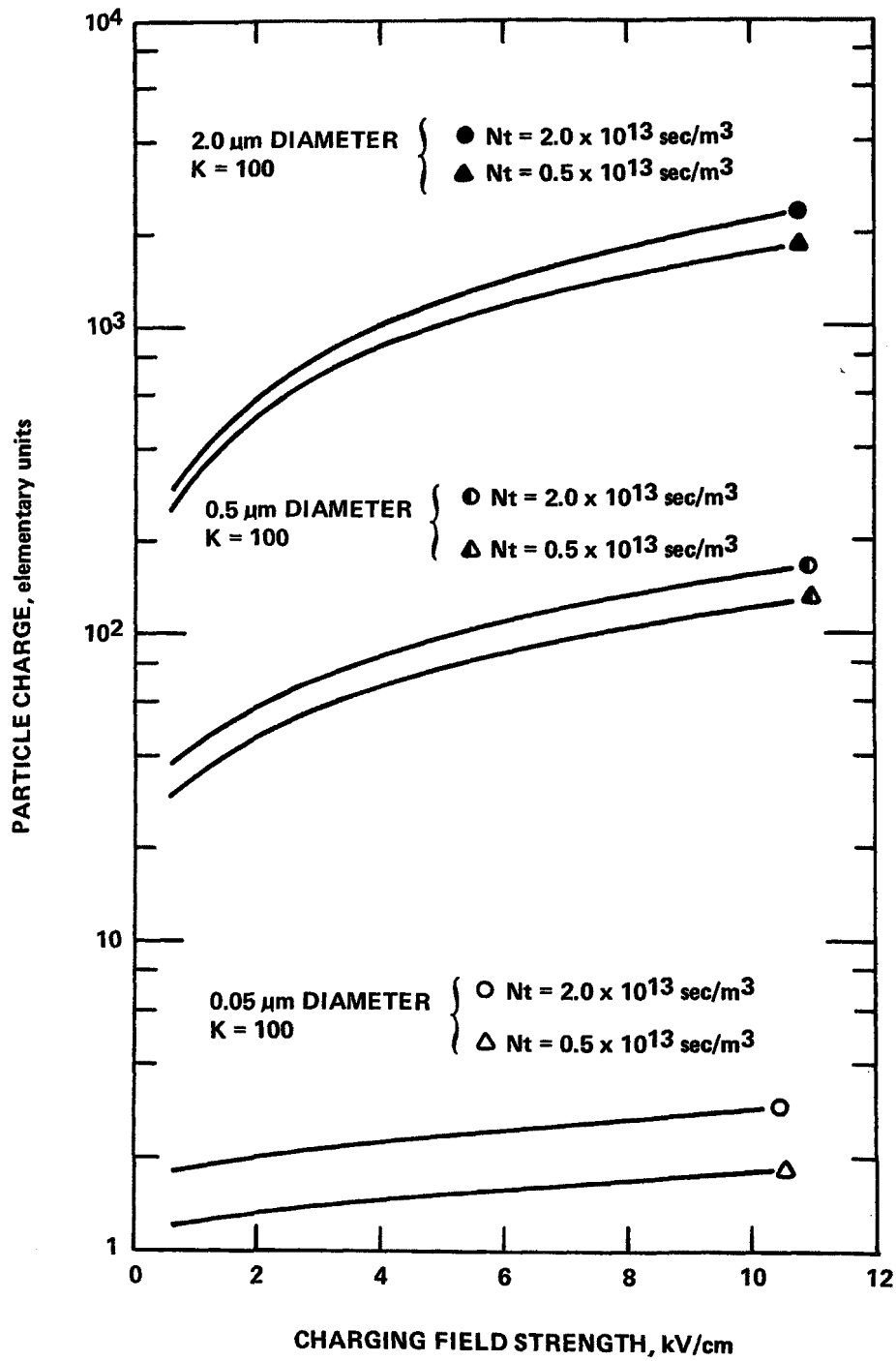


Figure 75. Charge per particle as a function of electric field for three particle sizes and two values of  $Nt$ .



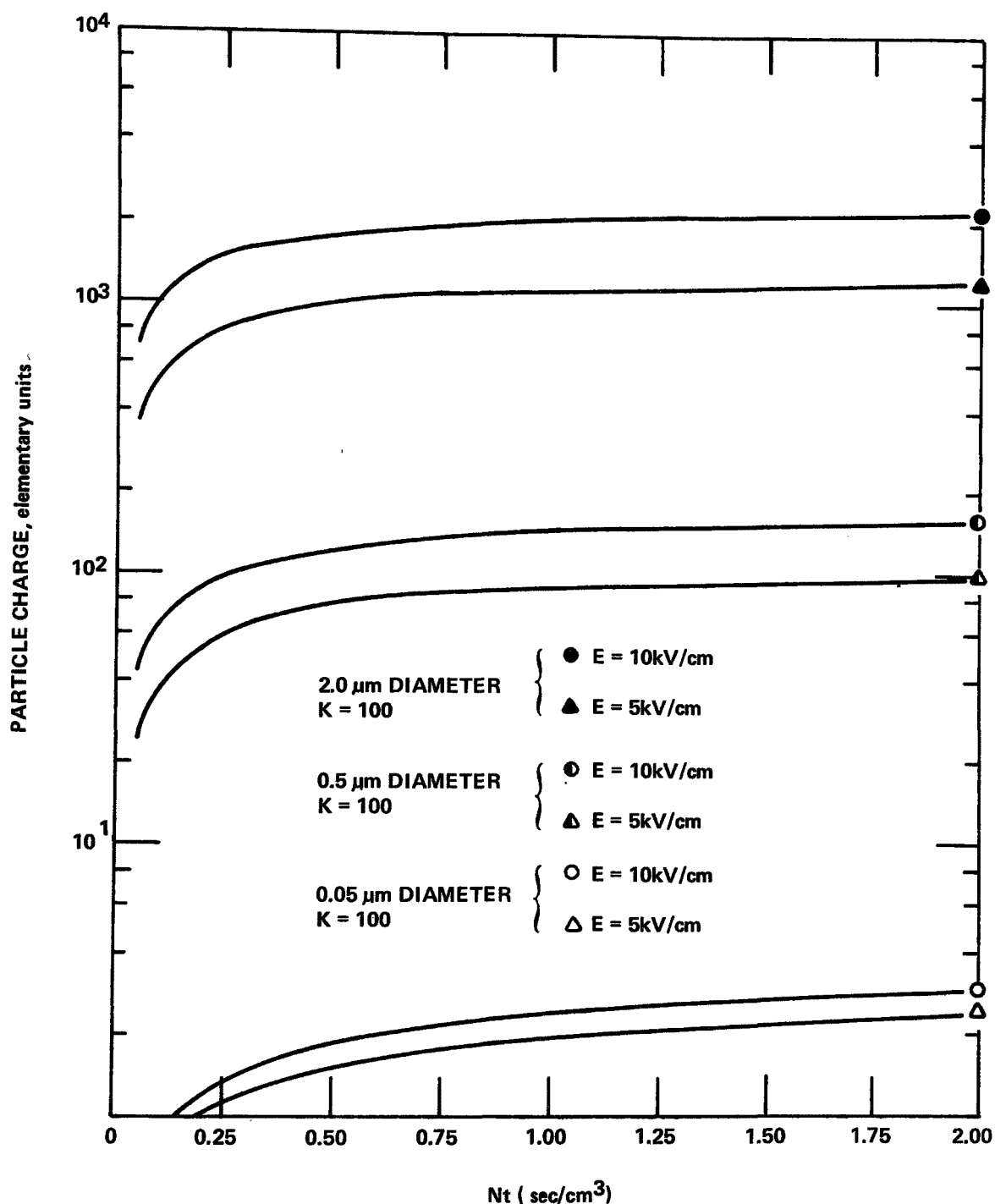


Figure 76. Charge per particle as a function of ion concentration-residence time product for three particle sizes and two values of electric field.

Figures 77-79 show calculated effects of variations in wire diameter and wire-plate spacing in a duct-type charging geometry. Increasing the wire diameter increases the corona inception voltage (see Figure 77). The slope of the current voltage curve also increases slightly for larger wire sizes. In Figure 78 the average field and the field strength at the plate are plotted as a function of wire diameter. For a given current density the average field increases much more than the field at the plate as the wire size is decreased.

Variations in the wire-plate spacing produce changes in the current-voltage characteristic as illustrated in Figure 79. In this case there is only a slight change in corona inception voltage and a large change in the slope of the I-V characteristic as the wire-plate spacing varies. This may be contrasted with Figure 77. The average field and the field at the plate are shown as functions of the current density in Figure 78. It is interesting to note that increasing the wire-plate spacing increases the field at the plate but decreases the average field. We may choose, for example, a narrow wire-plate spacing and moderate wire diameter in order to achieve high charging fields and high current density.

#### High Resistivity Particulate Material

The difficulties in electrostatic precipitation of high resistivity particles arises principally from the behavior of the corona system when the passive electrode becomes coated with the material. The effectiveness of the particle charging process becomes reduced, and the corona current tends to behave erratically. The result is a reduction in overall efficiency of the precipitator. The problem of dealing with high resistivity particulate materials and some possible approaches to the solution of the problem are discussed in the following paragraphs.

Electrical conduction through a dust layer on an electrode may be described by Ohm's law:

$$E = j\rho$$

The resistivity,  $\rho$ , depends upon the type of particulate material, temperature, humidity and other factors such as the presence of conditioning agents. A layer of high resistivity material behaves as a resistor in series with the corona system, which causes a reduction in current for a given applied voltage. But, more importantly, the field in even a thin particulate layer may become great enough to cause breakdown to occur. Localized high field regions at breakdown sites may then produce ionization, resulting in back corona.

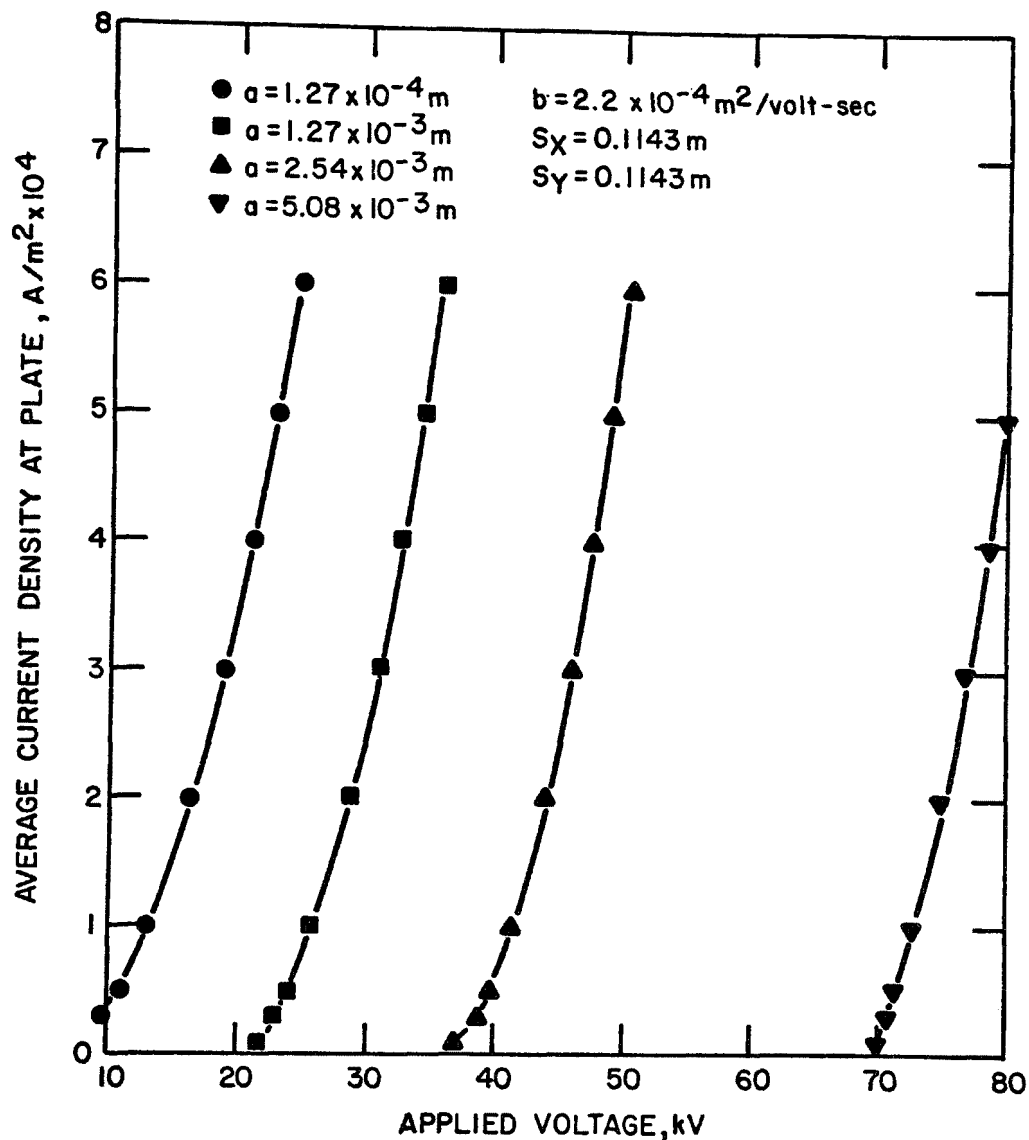


Figure 77. Current-voltage characteristics of a wire-plate corona system for various sizes of corona wire, holding all other parameters constant.  $S_x$  is wire-plate spacing,  $S_y$  is wire-to-wire spacing,  $b$  is ion mobility, and  $a$  is corona wire diameter.

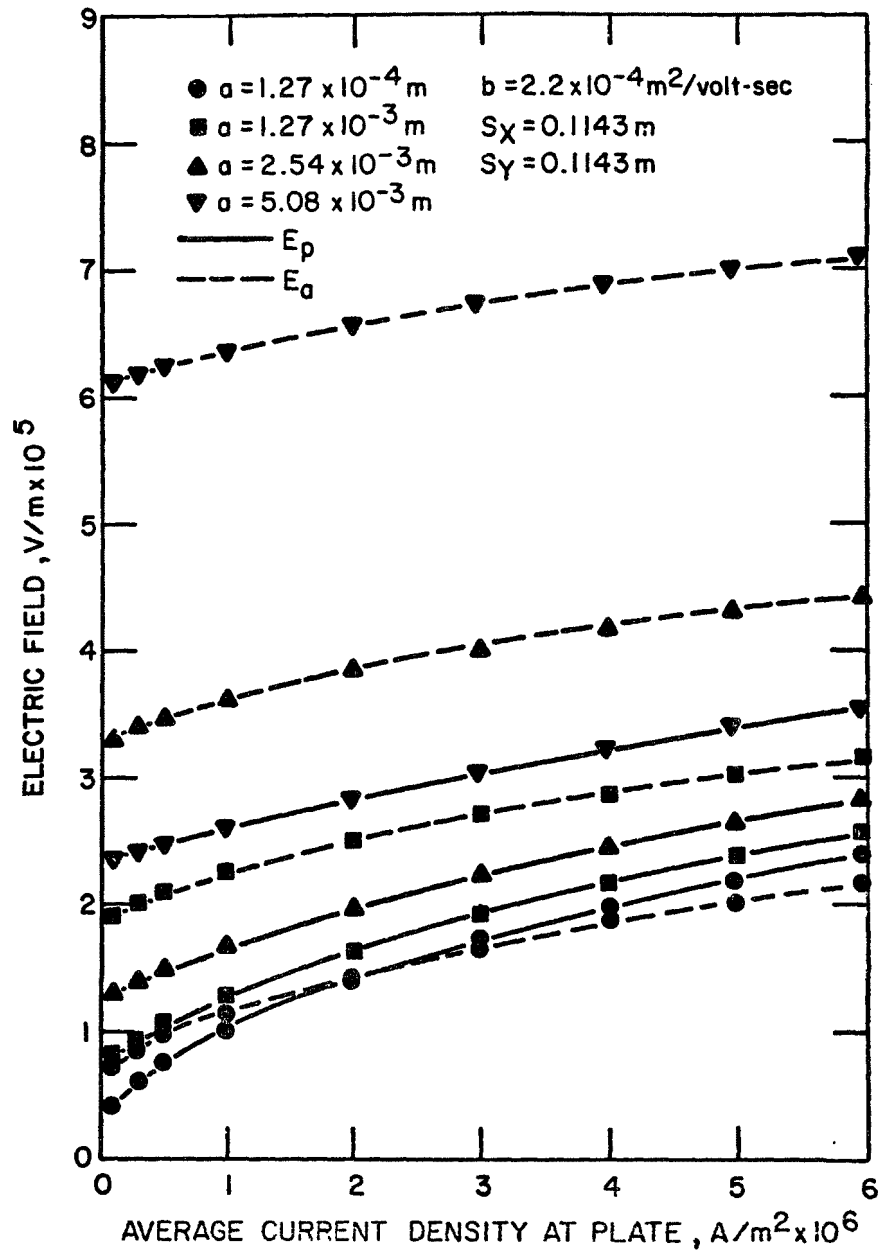


Figure 78. Electric field at the plate electrode,  $E_p$ , and average electric field,  $E_a$  as a function of current density at the plate for various wire sizes in a wire-plate corona system. ( $a$  = wire diameter;  $b$  = ion mobility;  $S_y$  = one half distance between wires;  $S_x$  = wire-plate spacing.)

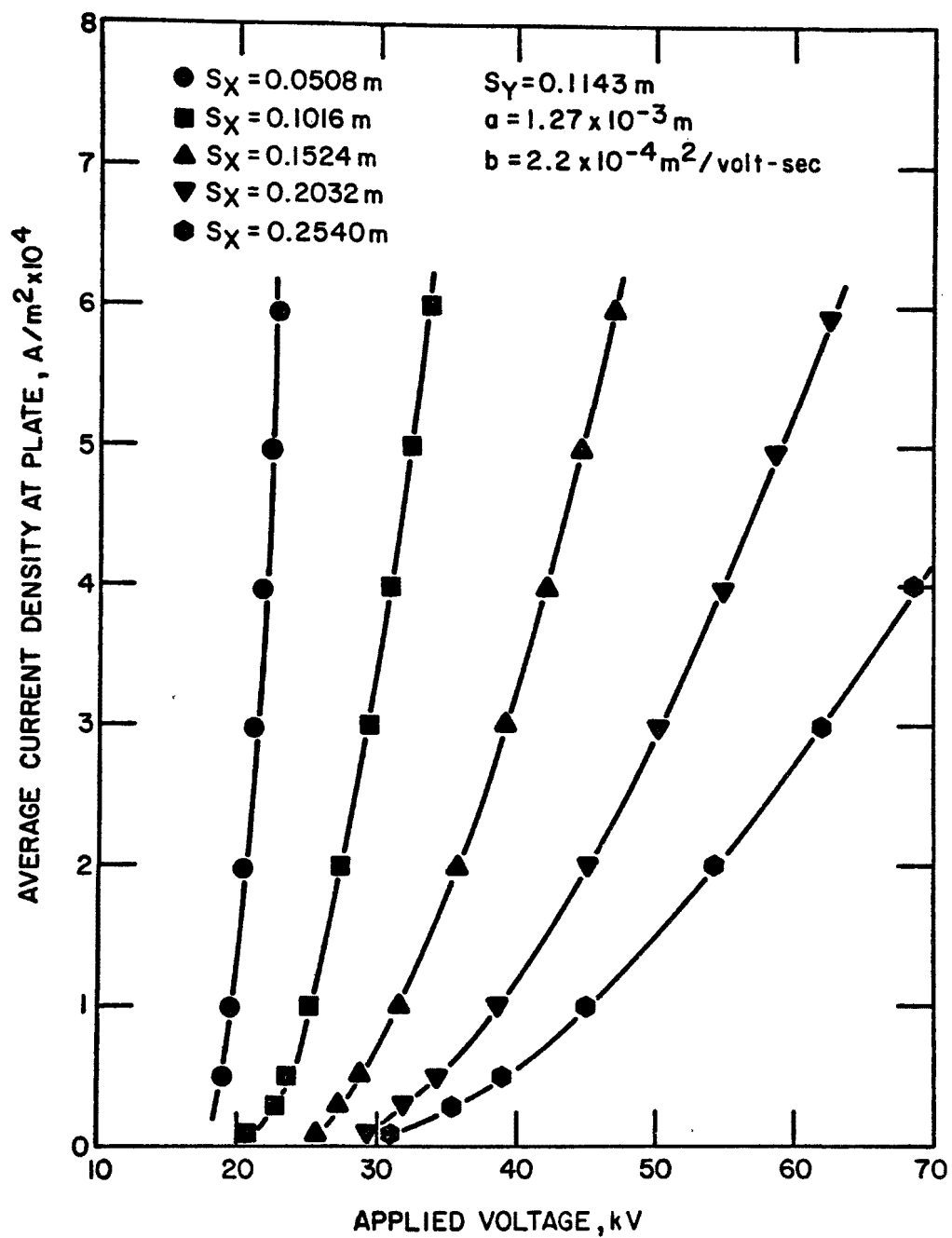


Figure 79. Current-voltage characteristics for a wire-plate corona system for several values of wire-plate separation, holding all other parameters constant.

When back corona occurs, ions of one species are injected at the corona electrode and ions of the opposite type originate at the passive electrode. The overall current increases, but the charging effectiveness is reduced severely by the competing effects of the oppositely charged ions.

The maximum allowable current density at the passive electrode in a corona system depends only upon the resistivity,  $\rho$ , and breakdown strength  $E_b$  of the deposited material:

$$j_{\max} = \frac{E_b}{\rho} ,$$

The breakdown strength is typically of the order of  $10^4$  V/cm. The maximum current density at the plate electrodes is plotted as a function of resistivity for this value of  $E_b$  in Figure 80. Thus for example, if a corona system is operated in the presence of a dust having resistivity of  $10^{10}$  ohm-cm, the current must be limited to a maximum of  $10^3$  nA/cm<sup>2</sup>. All other conditions remaining constant, an increase in particle resistivity requires a decrease in maximum operating current, which, in turn reduces the particle charging effectiveness.

Because the condition for back corona at a given value of current density at the passive electrode depends only upon the resistivity and electric breakdown strength of the accumulated particles, back corona can occur with a very thin layer of high resistivity material on a collecting surface. Efforts to control back corona must, therefore, be directed toward either maintaining the passive electrodes completely free of dust accumulation, or conditioning any collected dust in such a manner that the resistivity is reduced to an acceptable value.

#### Possible Solutions to the High Resistivity Problem

##### a. Mechanical removal of high resistivity particulate

- i. Aerodynamic design. In order to produce effective scouring of the electrode surfaces the gas velocity must be much higher than that which occurs in a conventional precipitator. Thus, the gas would have to be forced through a region of reduced cross sectional area. No data are currently available to indicate how high the velocity must be to produce effective scouring.
- ii. Continuous rapping. Thick accumulations of dust in the precharger can be removed by rapping; however, the adhesive forces on the first few monolayers of dust are extremely strong. Continuous energetic rapping with

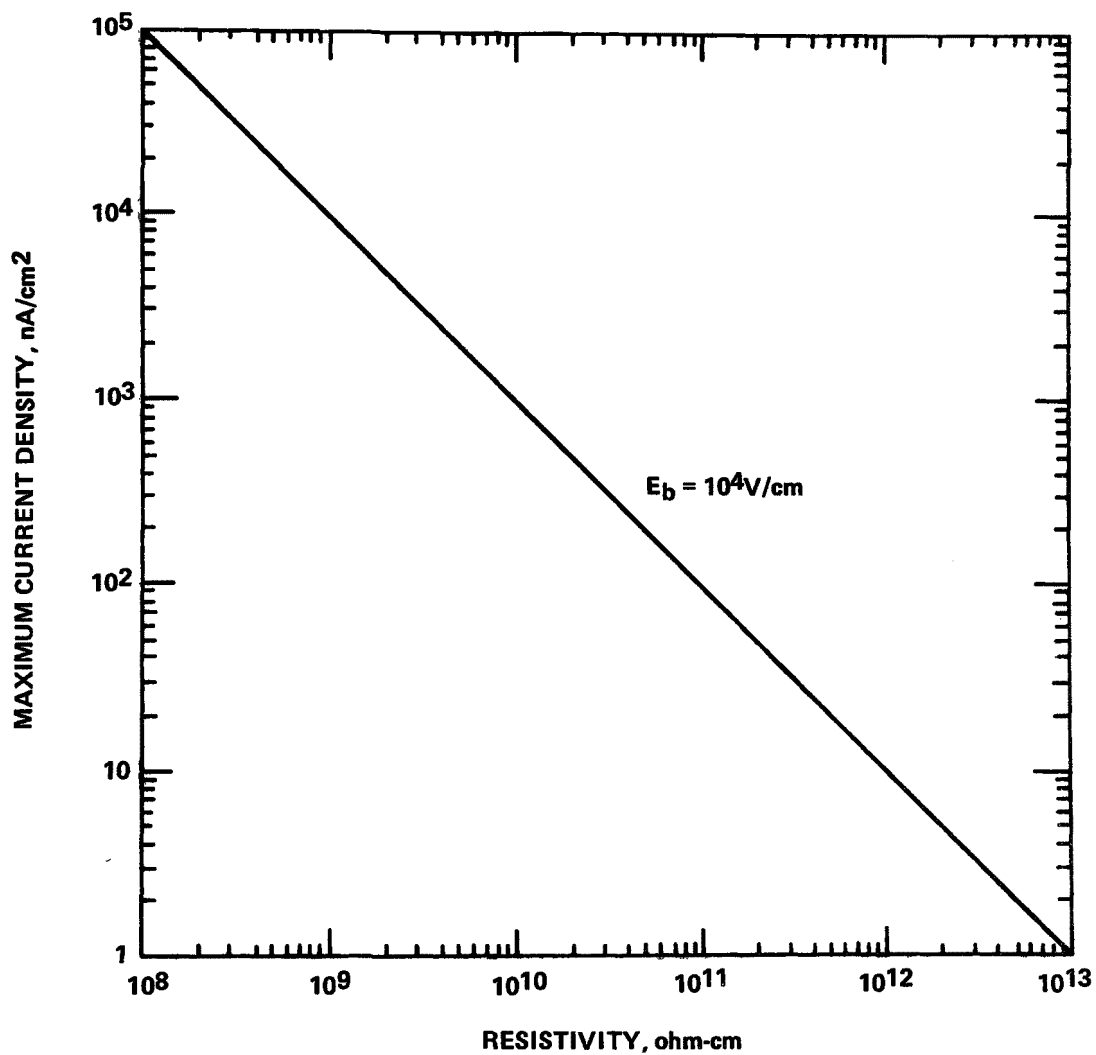


Figure 80. Maximum permissible current density before breakdown as a function of resistivity for an assumed breakdown strength of  $10^4$  V/cm. Back corona and loss of particle charging effectiveness occurs for particle resistivity and corona current density corresponding to points above the diagonal line.

accelerations of the order of several hundred times g would be required to break loose these particles. If the plate is vibrated continuously at frequency f, with amplitude A cm, the peak acceleration is

$$a_{\max} = \frac{4\pi^2 f^2 A}{980} \times g$$

If the plate is made to vibrate in a resonant mode, the driving power would be limited to that required to replace thermal losses. For example, vibration at 100 Hz with an amplitude of 0.1 mm would produce a maximum acceleration of approximately 400 g.

A combination of best aerodynamic design and continuous rapping may serve to keep the precharger electrodes sufficiently clean to avoid back corona, or at least to limit the amount of dust which must be conditioned.

#### b. Steam injection

This method would use low pressure steam forced through a porous electrode to treat and/or remove the deposited high resistivity material. It might also be possible to use a conventional electrode and inject the steam on the upstream side.

- i. Advantages: In many applications (e.g., coal or oil fired boilers) steam is readily available. In any case it is easily generated. Although the principal reason for the steam is to lower the resistivity of the deposited material frequent pulses of increased steam pressure might dislodge at least a large part of the dust and prevent clogging of the pores.
- ii. Possible Disadvantages: There might be a problem in maintaining uniform steam injection through a porous electrode. Localized clogging may become severe, resulting in the build-up of thick patches of dust. Aerodynamic shielding of the passive electrodes might help to alleviate problems of this nature.



### c. Na-glass electrodes

Glass can be fabricated with a large enough concentration of sodium to produce a resistivity  $\sim 10^6$  ohm cm. If a high resistivity glassy particulate layer resides on the surface of such a material in the presence of a large electric field, the  $\text{Na}^+$  ions would tend to be driven into the particles, thus reducing the resistivity of the particulate layer.

A Na-glass electrode could be constructed with an imbedded wire mesh for making contact to ground. In this case, the sodium ions would be depleted gradually, requiring periodic replacement of the electrode.

- i. Advantages: Only a small amount of conditioning agent would be required to provide mobile ions for the deposited particulate matter. It is almost certain that a system of this type could be made to work on some mass loading scale, but the overall ion migration rate into a deposited particulate layer is uncertain.

A large  $\text{Na}^+$  ion density would be available at the glass surface because of the applied field; but in order to produce the desired effect, the ions would have to be transferred very quickly into the particles arriving at the surface.

- ii. Possible Disadvantages: If the necessary reactions proceed too slowly, it may not be possible to accommodate realistic levels of high resistivity mass loading. In addition, a glass electrode is intrinsically somewhat fragile. Rapping to remove any collected material would probably not be possible.

## SPACE CHARGE EFFECTS

### General Nature of the Problem

The presence of charged particles in a corona system reduces the effective mobility of a conducting medium and therefore reduces the current density in the system for a given applied potential. The effect is most pronounced where there exists a large number density of fine particles. The problem is essentially a loading of the corona current by comparatively very massive charge carriers. Ions which become attached to particles no longer move with their original mobility, but travel with the much slower particle drift velocity.

The charging theory does not account for the fact that a fraction of the corona current is carried by ions attached to particles. In most cases the assumption that the particle current is negligibly small compared with the ion current serves as a good approximation. But, if the density of charge attached to the particles is a significant fraction of the total charge density the apparent mobility associated with the corona current is reduced, and the particle charging processes are impeded.

The total current density in the system (neglecting free electron current) is:

$$j = \mu_{eq} NE = \mu_i N_i e E + \sum_p \mu_p N_p n_p e E \quad (20)$$

where  $\mu_p$  = particle mobility,

$\mu_{eq}$  = equivalent mobility of the system,

$\mu_i$  = ion mobility,

$N$  = total charge density,

$N_i$  = ion density,

$N_p$  = density of particles of diameter  $p$ , and

$n_p$  = number of elementary charges per particle of diameter  $p$ .

Now,

$$N = N_i e + \sum_p N_p n_p e$$

and so, solving equation (20) for  $\mu_{eq}$ , we have

$$\mu_{eq} = \mu_i \left[ \frac{1 + \sum_p \frac{\mu_p}{\mu_i} \frac{N_p}{N_i} n_p}{1 + \sum_p \frac{N_p}{N_i} n_p} \right]$$

Consider the case for which  $\sum N_p n_p < 10N_i$ . Since  $\mu_i \gg \mu_p$  the sum in the numerator may be neglected, and hence

$$\mu_{eq} = \mu_i \left[ 1 + \frac{1}{N_i} \sum_p N_p n_p \right]^{-1}.$$

But  $\sum N_p n_p e = Q$ , the total charge on the particulate material in the system, so

$$\mu_{eq} = \mu_i \left[ 1 + \frac{Q}{eN_i} \right]^{-1}$$

In terms of the specific charge  $Q/M$ , where  $M$  is the total mass per unit volume,

$$\mu_{eq} = \mu_i \left[ 1 + M \frac{(Q/M)}{eN_i} \right]^{-1} \quad (21)$$

The ratio  $Q/M$  increases for decreasing particle diameter as shown in Figure 62, Section 5. Thus, the equivalent mobility decreases as the particle size is made smaller, for a given mass loading  $M$ . The effect of changing mobility for a fixed current density and particle size distribution is shown in Figure 81. It is also fairly accurate to say that the maximum current density decreases by the same amount as the equivalent mobility, i.e.,

$$j/j_{max} = \mu_{eq}/\mu_i \quad (22)$$

If, for example, we have a flue gas with  $1.0 \text{ g/m}^3$  of  $0.5 \text{ } \mu\text{m}$  diameter particles where the charging process has produced an average charge/mass ratio of  $5 \times 10^{-5} \text{ coul/g}$ , in a region where the ion density is  $10^{14} \text{ m}^{-3}$  the reduction in current is

$$j/j_{max} = \left[ 1 + M \frac{(Q/M)}{eN_i} \right]^{-1}$$

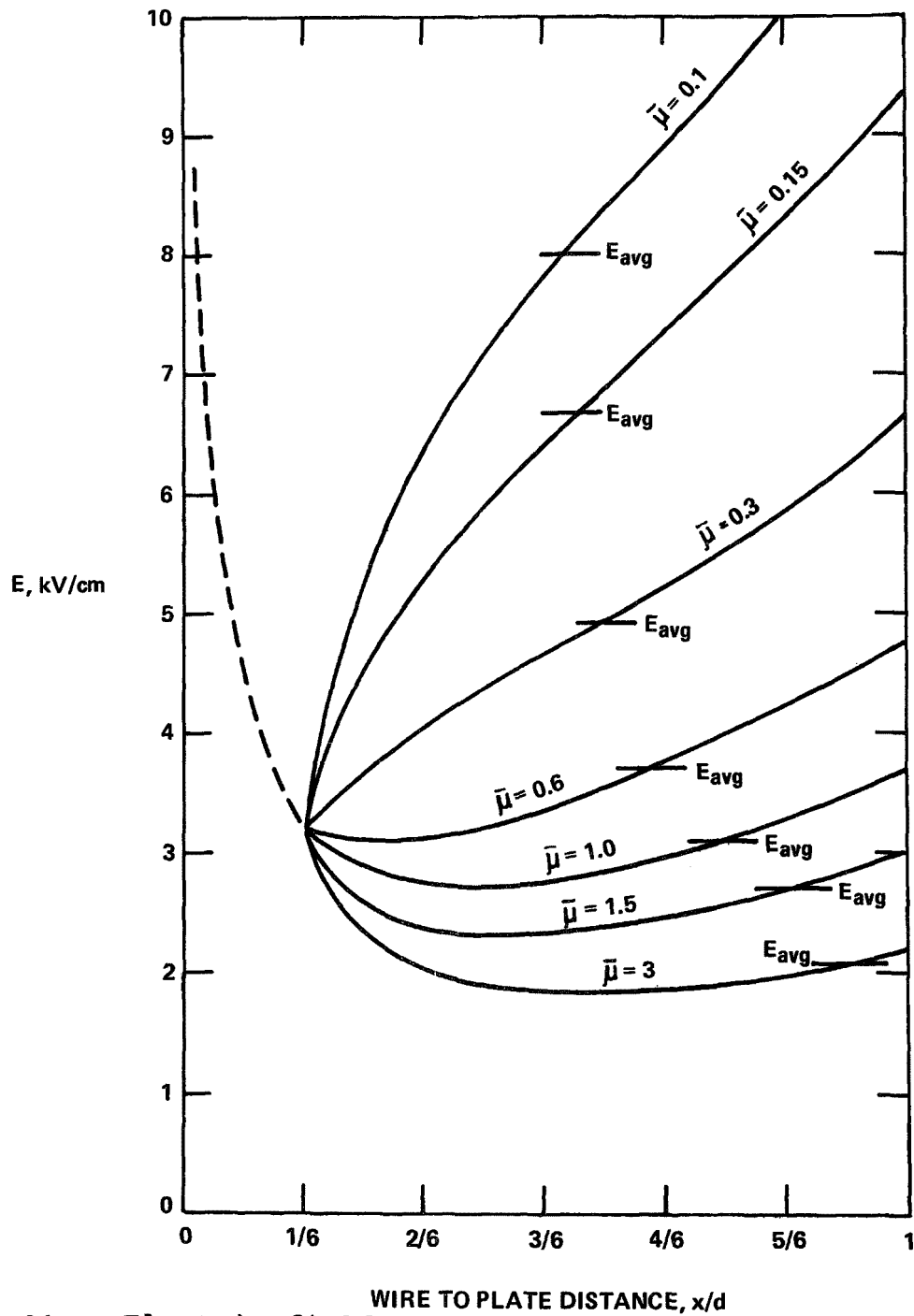


Figure 81. Electric field profile in a duct geometry device for various values of equivalent mobility, while holding the average current density constant at the plate electrode. The parameter  $\bar{\mu}$  is the ratio  $\mu_{eq}/\mu_i$ .

or

$$j/j_{\text{max}} = 0.24 .$$

Clearly, in this case a severe degradation in particle charging performance would result.

### Practical Operating Conditions

The reduction in equivalent mobility of a system containing charged particles depends very strongly upon the fraction of the total charge density which resides on the particles. For a given mass loading the space charge problem is more severe as the particle size is reduced, because the ratio of charge to mass is generally an inverse function of particle diameter. Because of the fundamental nature of the effect it appears that the only way in which it can be minimized is to use a corona electrode geometry which will produce a maximum ion density for a given electric field. This generally requires small wire-plate spacing (see Figures 50 and 79). The numbers shown above were chosen for convenience because they are related to data obtained on a particular pilot scale precharger. They should not be taken as absolute limits because of the dependence on charger geometry and operating conditions.

### GENERAL PRECHARGER DESIGN CONSIDERATIONS

Large values of both electric field strength and ion density are required in order to produce a suitable level of particle charging for electrostatic precipitation. In those cases where high resistivity particles or space charge effects do not present special difficulties, the principal consideration in precharger design is optimization of the electric field profile and current density in the charging region. In the following discussion theoretical calculations of electrical characteristics for various electrode geometries are made and compared, some limited experimental data are presented, and comparative performance estimates are given.

#### Electrode Configurations - Theoretical

A comparison of static electric field profiles was made for several electrode geometries. The spacing between corona electrode and passive electrode was made the same for all cases, and the limiting field at the passive electrode was set at 5 kV/cm for each system. The field profiles for the configurations described in the following are plotted in Figure 82.

- a. Duct geometry. The Cooperman expression was used to provide the field profile for the duct geometry, with wire-plate spacing of 5 cm.

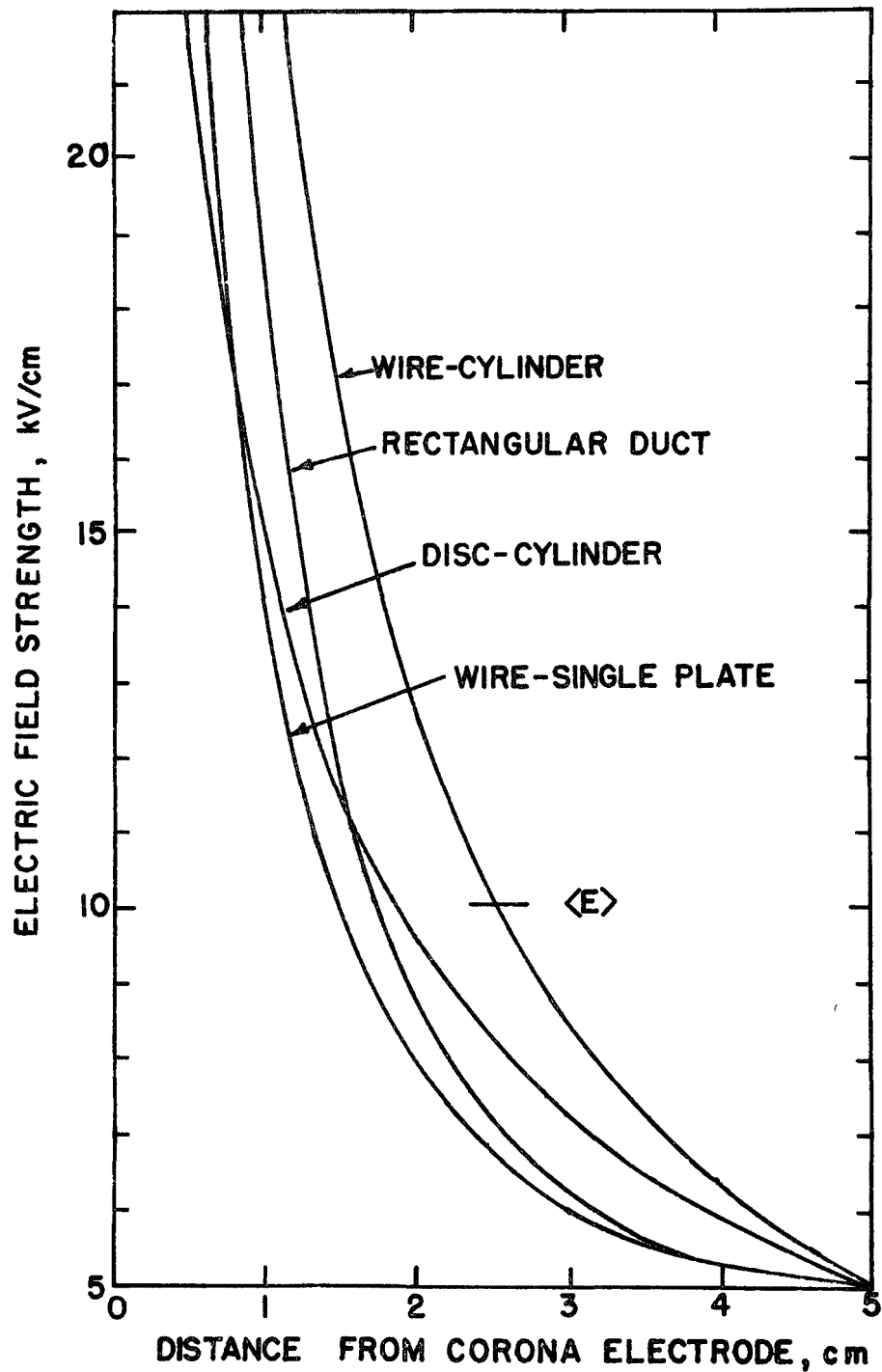


Figure 82. Theoretical electric field profiles for various electrode geometries, all normalized to a field of 5 kV/cm at the passive electrode.

- b. Single plate-wire. Although this geometry has little to recommend it in practice, a field profile is included for the case of a corona wire parallel to a single plate, at a distance of 5 cm. The expression for the field as a function of  $x$ , the distance from the corona wire on a line normal to the plate and passing through the wire is

$$E_{(x)} = \frac{2k_1 d}{x(2d-x)} \quad (23)$$

where  $d$  is the wire-plate spacing, and  $k_1$  is a constant, depending upon the linear charge density of the wire.

- c. Wire-cylinder system. The field as a function of radial distance,  $r$ , from a wire along the axis of a grounded cylinder is

$$E_{(r)} = \frac{k_2}{r}$$

where  $k_2$  is a constant depending upon the boundary conditions. In this case, end effects are ignored. The cylinder radius is 5 cm.

- d. Disc-cylinder geometry. A sharp-edged disc and a grounded cylinder with coincident axes form an electrode system where the field in the annular region between the disc and cylinder as a function of the radial distance,  $x$ , from the edge of the disc is

$$E_{(x)} = k_3 \left\{ (a + x) \left[ 1 - \frac{\ln^2 \frac{b}{a+x}}{\ln^2 \frac{b}{a}} \right]^{\frac{1}{2}} \right\}^{-1}$$

Again,  $k_3$  is a constant depending upon the boundary conditions;  $a$  is the disc radius and  $b$  is the cylinder radius.

The arithmetic average field (i.e., applied voltage divided by electrode spacing) is probably not the best way to compare the above systems for a short precharger section, because in the cylindrical geometries there is a much higher probability that a particle will pass through a low field region near the plate than through a higher field region near the corona electrode. These considerations can be taken into account by defining the mean charging field  $\langle E \rangle$  as

$$\langle E \rangle = \int_R P(s) E(s) ds \quad (24)$$

where  $P(s)$  is probability that a particle will pass through an element of volume  $ds$  where the field is  $E(s)$ . The integral is carried out over the charging region  $A$ , and  $P(s)$  is normalized to unity over  $R$ . The integral depends very strongly, in general, upon the radius of the discharge wire (or radius of curvature of an edge used as a corona electrode). For this reason a more reasonable comparison of  $\langle E \rangle$  can be made by observing the areas under the curves of the products  $P(s)E(s)$  for each of the corona systems, as shown in Figure 83.

These curves are derived directly from the field profiles shown in Figure 82. The probability function  $P(s)$  for both wire-plate geometries is simply a constant. And for the cylindrical systems,

$$P(r) = k_n(r)$$

where  $k_n$  is the normalizing function for the particular system. For example, normalizing  $P(r)$  over an annular region in the disc-cylinder device requires

$$P(r) = \frac{2r}{a^2 + b^2 - \frac{1}{2} d^2} \quad (25)$$

where  $r = x + a$ .

Because of the asymptotic behavior of the curves in Figure 81, estimates of the integrated values  $\langle E \rangle$  are not immediately apparent (area under curves), except in the case of the wire-cylinder system, where, clearly  $\langle E \rangle = 10$  kV/cm. The value of  $\langle E \rangle$  for the rectangular duct geometry is certainly greater than that of the single plate-wire system, but the relative values of other pairs depend upon the point where the maximum equipotential is chosen at the corona electrode. If that point is taken to be at less than approximately  $x = 0.8$  cm, the rectangular duct system has an  $\langle E \rangle$  greater than the disc-cylinder, but less than the wire-cylinder.

The above analysis does not include space charge effects, but may serve at least as a qualitative guide in the investigation of corona system geometries. Variations on the type of corona discharge electrode (i.e., barbed wire or helix) may provide some improvement on any general corona geometry, but they are generally beyond the available theory and must be tested experimentally.



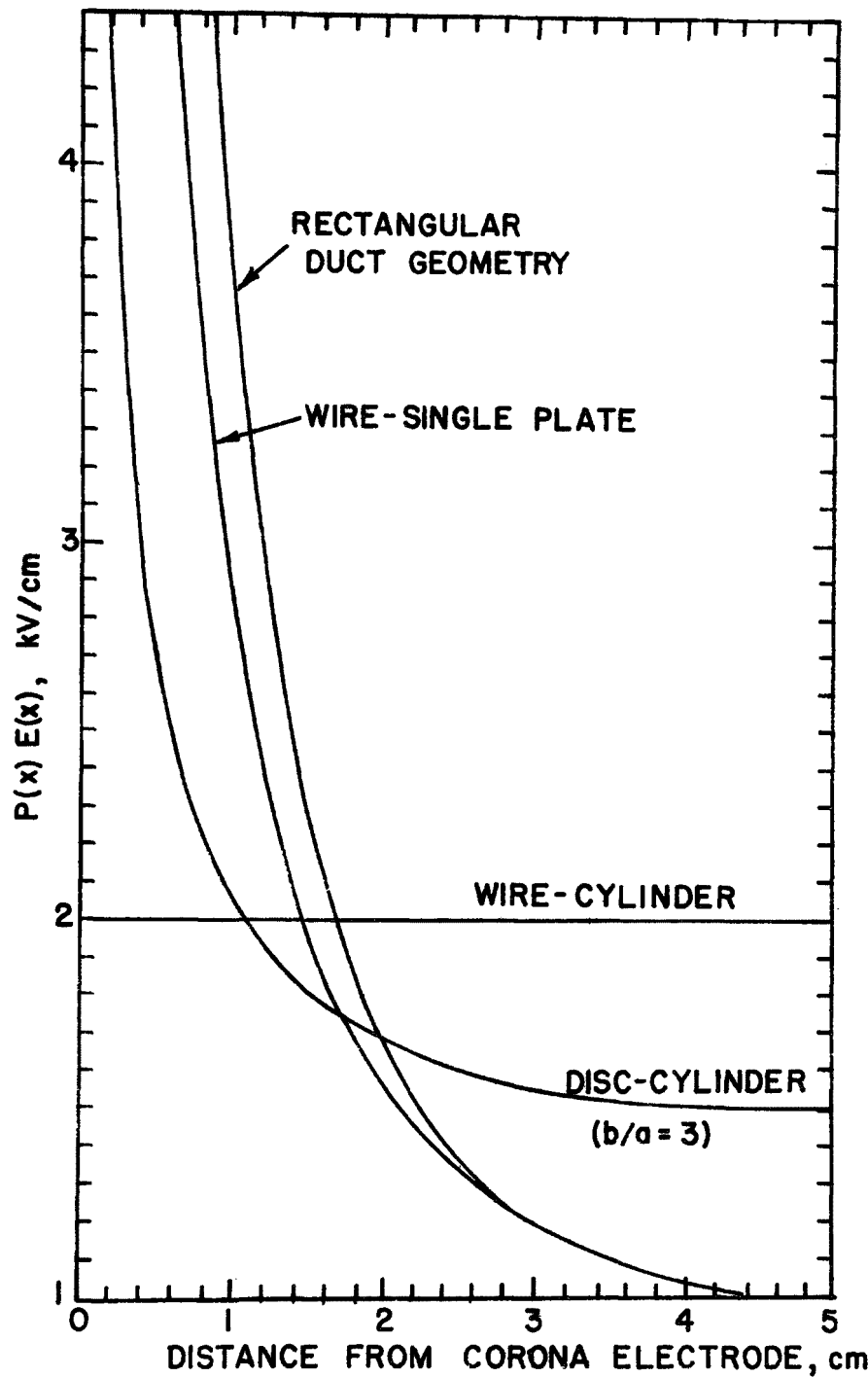


Figure 83. Probability charging field as a function of distance from corona electrode, calculated from the field profiles shown in Figure 106. The area under each curve is the mean charging field  $\langle E \rangle$ .

For a particular current density at the passive electrode, a cylindrical geometry may offer some advantage since the average ion density in the charging region will be higher than that found in a rectangular geometry.

### Electrical Configurations - Experimental

In the preceding section a theoretical comparison of electrical field profiles, neglecting space charge, was presented for several corona electrode systems. A limited experimental study has also been carried out.

A disc with 1.9 inch diameter was mounted centrally inside a 5.5 inch i.d. pipe, 18 inches long. The disc axis was aligned with the axis of the pipe. The disc was approximately 1/32 inch thick and the edge was sharpened. The I-V characteristic for this geometry is shown in Figure 84. (Current density in all cases on this graph is based on the assumption that all of the current is restricted to a strip 1 cm wide on the passive electrode, parallel to the edge of the corona electrode.) For the geometry described above, a maximum of 74 kV was applied before sparking occurred, and a current density of approximately  $7 \times 10^4$  nA/cm<sup>2</sup> was achieved.

A second experiment was carried out using a similar disc, but with a thickness of 0.1 inch, and rounded edge. The maximum voltage before sparking was somewhat lower (65 kV) than that for the sharp-edged disc, and the maximum current density was approximately  $3.5 \times 10^4$  nA/cm<sup>2</sup>.

Two experiments were done using a flat plate 17 inches x 14 inches for the ground electrode. First, a 0.1 inch diameter wire was located approximately 1.9 inch above the plate. In order to minimize field concentrations at the ends of the wire, 1 inch radius bends were made near both ends of the wire, directed away from the plate. The length of the wire between the centers of the bends was approximately 9 inches. The current increased more rapidly with increasing voltage than in the other systems, but the maximum voltage before sparking was only 52 kV, even though the minimum distance between electrodes was the same as for the cylindrical geometry.

Finally, the sharpened edge of a thin (approximately 0.01 inch) plate was used as a corona electrode. The plate was cut so that the edge was the shape of the bent wire electrode described above. The plane of this electrode was mounted perpendicularly to the flat grounded electrode with a 1.9 inch space between the electrode edge and ground plane. As shown in Figure 84, the I-V characteristic for this electrode geometry lies between those found for the disc-cylinder arrangement and the wire-plate electrodes.

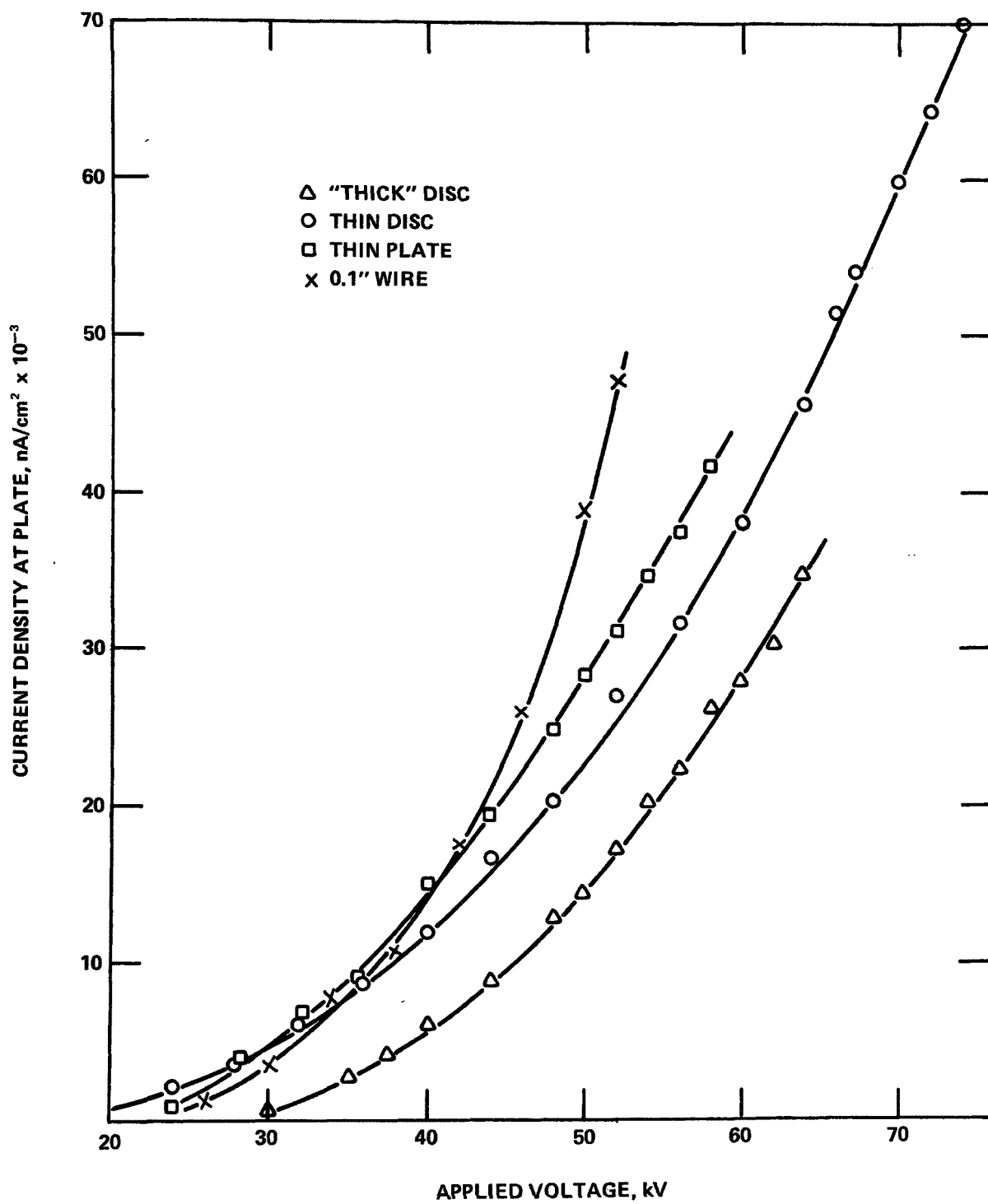


Figure 84. Experimental I-V characteristics for four corona system geometries.

## Optimization of a Plate-Wire-Plate Design

The final geometry of the pilot scale precharger system will depend largely upon the results of laboratory evaluations and careful consideration of cost, ease of fabrication, maintenance, etc. The following analysis is done for a plate-wire-plate system because we have a more complete theory at the moment for that geometry. The foregoing generalized analysis of different geometries indicates that the results predicted for the plate-wire-plate system will be comparable to those predicted for the other systems.

It is assumed in this section that the electrical characteristics are not limited by the resistivity of the dust. This is a necessary assumption because it is clear that the high current densities required for charging particles in a short time or space cannot be sustained if even minute amounts of high resistivity dust remain on the passive electrodes. Thus, the resistivity of troublesome dusts must be modified or the dust removed.

The space charge effect is a more fundamental problem and the electrical design of the Charger-ESP system must be optimized to reduce dust effect if a small size distribution is to be collected effectively. This simply means that the effective mobility (ions and particles) must not fall below some critical value. If this does happen sparking will occur at reduced current densities. In general, for best charging it is desirable to have a high average field and high ion density. For a given  $Nt$  product, it is preferable to have  $N$  large and  $t$  small.

Table 2 shows the predicted performance for several plate-wire-plate chargers which have different wire sizes and plate spacings. The criterion used to generate this table and for comparison of the different geometries is that the field at the plate reach 15 kV/cm. This seems to be a reasonable value to achieve at or near sparkover. One can see from the table that, over the range at parameters shown, the current density and charging field change very little. Of course, for extremely different values this is not true. Table 2, however, covers the range of interest to us. For mechanical strength and stability we would probably choose the larger spacing and wire diameter.

### Estimated Size and Performance

In this analysis we shall assume a value of  $1.0 \times 10^{13}$  sec/m<sup>3</sup> for  $Nt$  in the charger, at an electric field strength of  $1.0 \times 10^6$  V/m.

Figure 14, Section 3 shows the approximate charge that would be acquired by particles of various sizes. Because of the high electric field, charges are much higher than would be expected for normal ESP operation.

TABLE 2. ELECTRICAL OPERATING CHARACTERISTICS FOR SEVERAL PLATE-WIRE-PLATE CHARGER GEOMETRIES

Wire-Plate Spacing (cm)	Wire Diameter (in/mm)			
		0.04/1.02	0.06/1.52	0.08/2.03
3.175	Voltage (V)	38478	41524	43565
	Current Density (nA/cm <sup>2</sup> )	3423	3439	3225
	Electric Field (kV/cm) (ave)	12	13	14
4.064	Voltage (V)	48701	50788	54038
	Current Density (nA/cm <sup>2</sup> )	3399	3225	3225
	Electric Field (kV/cm) (ave)	12	13	13
5.08	Voltage (V)	59313	62467	65901
	Current Density (nA/cm <sup>2</sup> )	3188	3207	3226
	Electric Field (kV/cm) (ave)	12	12	13

For the purposes of this study it is assumed that the downstream collector (ESP) is maximized with regard to the field at the collecting plate and that only enough current is used to charge reentrained dust. A field of 10 kV/cm is assumed in the ESP. Similar calculations were done at a field of 5 kV/cm to simulate a high resistivity dust or other difficult situations.

The basic equation applicable to Charger-ESP system is

$$\text{Efficiency} = 1 - e^{-\frac{q(E_C N_0 t, a)}{6\pi\eta a}} \cdot E_p \cdot \frac{A}{V} \cdot C \quad (26)$$

where  $q(E_C N_0 t, a)$  = the average charge on a particle of radius  $a$  (coulombs),

$E_C$  = the average charging field (V/m),

$N_0$  = the average ion density in the charger ( $\text{m}^{-3}$ ),

$t$  = the average charging time (sec),

$a$  = the particle radius (m),

$\eta$  = the viscosity of the gas (kg/m sec),

$E_p$  = the average electric field at the collecting zone (V/m),

$A$  = the downstream collector area ( $\text{m}^2$ ),

$V$  = the volumetric flow rate ( $\text{m}^3/\text{sec}$ ), and

$C$  = the slip (Cunningham) correction factor.

Table 3 shows charge data taken from Figure 61 and efficiencies and migration velocities calculated for the different particle sizes. The SCA for the downstream ESP was calculated by selecting the efficiency to match that of the full scale ESP on Unit 10 at Gorgas. That ESP has an overall mass efficiency of approximately 99.70%. The theoretical fractional efficiency curves for the Gorgas ESP and the proposed system are shown in Figure 85.

This analysis can be criticized because the calculated migration velocities are so high that the Deutsch equation is no longer valid. On the other hand, the velocity component of the particles toward the collecting plate will be such that calculations of trajectories would also predict very low SCA's.

TABLE 3. CALCULATED CHARGE AND FRACTIONAL EFFICIENCY OF THE PRECHARGER-ESP SYSTEM. THE ESP HAS AN SCA OF 28 ft<sup>2</sup>/1000 ACFM.

<u>Particle Diameter (μm)</u>	<u>Charge (coul.)</u>	<u>Collection Efficiency</u>	<u>Migration Velocity (cm/sec)</u>
0.1	1.44 x 10 <sup>-18</sup>	68	20 cm/sec
0.5	2.2 x 10 <sup>-17</sup>	79	21 cm/sec
1.0	8.6 x 10 <sup>-17</sup>	93%	41 cm/sec
1.5	1.8 x 10 <sup>-16</sup>	96.8	58 cm/sec
2.0	3.2 x 10 <sup>-16</sup>	98.7	77 cm/sec

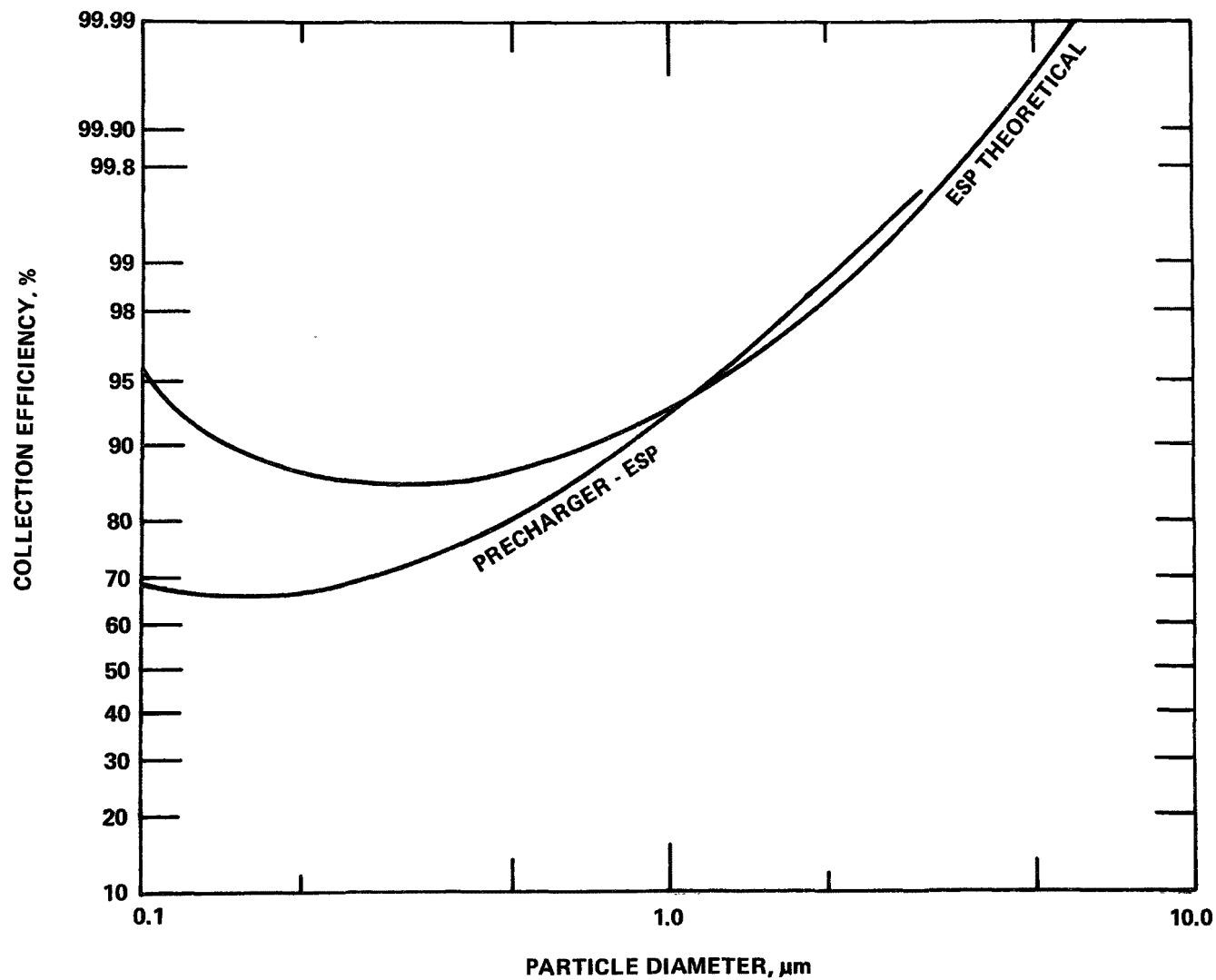


Figure 85. Theoretical collection efficiencies for the Gorgas full-scale precipitator compared to a precharger-E.S.P. system.



The theory, then predicts SCA's of about 1/10 of the value which one would expect for a normal ESP installation. Taken at face value, for example, this means that the Gorgas ESP could be shortened to about 3 ft in length. This is obviously impractical because the ash could not be handled and reentrainment would be a problem.

In summary, if the high current density charger operates as predicted, the size of the downstream collector is determined by mechanical, not electrical, considerations. For costing, we have thus arbitrarily assumed that the dust can be collected and removed, and reentrained dust recollected with a minimum SCA of  $120 \text{ ft}^2/1000 \text{ acfm}$  for new installations and  $240 \text{ ft}^2/1000 \text{ acfm}$  for difficult dust installations, or about a factor of 3 less than a normal ESP.

#### COST ESTIMATES

Since the potential value of an electrostatic collection system employing a precharger will depend to a large extent upon the relative costs of such a system compared with existing technology, we have prepared cost estimates of two different types of precharger-precipitator systems for comparison with conventional electrostatic precipitator installations. The following cases were selected for comparison:

##### Case No.

1. A wire-pipe precharger followed by a modified precipitator with a specific collecting area of  $23.6 \text{ m}^2/\text{m}^3 \text{ sec}$  ( $120 \text{ ft}^2/1000 \text{ cfm}$ ).
2. A wire-pipe precharger followed by a modified precipitator with a specific collecting area of  $47.2 \text{ m}^2/\text{m}^3/\text{sec}$  ( $240 \text{ ft}^2/1000 \text{ cfm}$ ).
3. A wire-plate precharger followed by a modified precipitator with a specific collecting area of  $23.6 \text{ m}^2/\text{m}^3/\text{sec}$  ( $120 \text{ ft}^2/1000 \text{ cfm}$ ).
4. A wire-plate precharger followed by a modified precipitator with a specific collecting area of  $47.2 \text{ m}^2/\text{m}^3/\text{sec}$  ( $240 \text{ ft}^2/1000 \text{ cfm}$ ).
5. A conventional electrostatic precipitator with a specific collecting area of  $59 \text{ m}^2/\text{m}^3/\text{sec}$  ( $300 \text{ ft}^2/1000 \text{ cfm}$ ).
6. A conventional electrostatic precipitator with a specific collecting area of  $118 \text{ m}^2/\text{m}^3/\text{sec}$  ( $600 \text{ ft}^2/1000 \text{ cfm}$ ).

The cost estimates for the precharger assemblies and the conventional precipitators are based on the following assumptions:

1. Flange to flange costs of conventional precipitator without erection =  $\$6.67/\text{ft}^2$  of plate area.
2. Wire-tube precharger array consisting of 4" pipe on 8" centers is estimated to cost  $\$227/\text{ft}^2$  of inlet area. This includes a contingency factor equal to about four times the material and fabrication costs to allow for a means of lowering the resistivity of dust collected in the precharger, removing excessive accumulations, and electrical supplies.
3. Wire-plate precharger consisting of 2" nominal wire-to-plate spacing with diamond section plate assemblies (for stiffness required) 8" long x 4" thick is estimated to cost  $\$80/\text{ft}^2$  of inlet area. This concludes a contingency factor of four as described above.
4. The particulate collection system will collect 99.5% or greater of the mass loading in the flue gas. The precipitator sections consist of conventional plates and relatively large diameter discharge electrodes. For the 120 SCA case, the precipitator is 108 ft wide, 25 ft long, and 15 ft high with 144 gas passages. The plate height is doubled to 30 ft to obtain an SCA of 240.

Cases 1, 3, and 5 are considered to be applicable to dusts in which resistivity does not severely limit conventional precipitator operating conditions, whereas Cases 2, 4, and 6 are considered to be applicable to dust with a resistivity of  $5 \times 10^{10}$  or greater. Tables 4 and 5 give comparisons of cost estimates for the six cases described earlier. The installations with prechargers are estimated to cost approximately 50% to 60% as much as a conventional precipitator under comparable operating conditions based on flange to flange costs with no installation charges included.

Table 6 gives a comparison of projected power requirements for Case 4 and Case 5. This shows that the precharger system does not cause increased power consumption over that experienced with conventional precipitators.

TABLE 4. FLANGE TO FLANGE COST ESTIMATES OF PARTICULATE COLLECTION  
SYSTEMS  
(NO INSTALLATION COSTS INCLUDED)

Case No.	Precharger Type	Collector Specific Collecting Area $\text{m}^2/\text{m}^3/\text{sec}$ $\text{ft}^2/1000 \text{ cfm}$		Total Flange To Flange Cost \$	Precharger Cost \$	Collector Cost \$
1	Wire-pipe	23.6	120	1,088,100	367,740	720,360
2	Wire-pipe	47.2	240	2,176,200	735,480	1,440,720
3	Wire-plate	23.6	120	850,000	129,600	720,360
4	Wire-plate	47.2	240	1,700,000	259,200	1,440,720
5	None	59.1	300	1,800,000	---	1,800,000
6	None	118	600	3,600,000	---	3,600,000

FIGURE 5. ESTIMATED COST BENEFIT RATIOS FOR PRECHARGER COLLECTOR SYSTEMS

<u>Case No. Comparisons</u>	<u>Ratio of Conventional System to Precharger System</u>
5 to 1	1.65
6 to 2	1.65
5 to 3	2.12
6 to 4	2.12

All systems assumed to have collection efficiency of 99.5% or greater on a typical coal-fired power plant fly ash on 900,000 acfm of flue gas.

TABLE 6. COMPARISON OF PRIMARY POWER REQUIREMENTS IN KILOWATTS - 900,000 ACFM

Precharger System			<u>Conventional Precipitator</u>
<u>Precharger</u>	<u>Collector</u>	<u>Total</u>	
408	88	496	520

Assumptions:

1. Geometry of Case 4 used for precharger system. Case 5 used for conventional precipitator.
2. Precharger operating conditions:  $1760 \times 10^{-9}$  amps/cm<sup>2</sup>, 50 kV.
3. Collector operating condition:  $5 \times 10^{-9}$  amps/cm<sup>2</sup>, 57 kV.
4. Conventional precipitator operating conditions:  $30 \times 10^{-9}$  amps/cm<sup>2</sup>, 45 kV.
5. Conversion efficiency of T-R sets = 65%.

## REFERENCES

1. Murphy, A.T., F.T. Adler, and G.W. Penney. A Theoretical Analysis of the Effects of an Electric Field On Charging of Fine Particles. AIEE Trans. 318-326, Sept. 1959.
2. Mirzabekyan, G.Z. Aerosol Charging in a Corona-Discharge Field. In: Strong Electric Fields in Technological Processes (Ion Technology), V.I. Popkov, ed. Energy Publishing House, Moscow, 1968. pp. 20-38.
3. Pauthenier, M.M., and M. Moreau-Hanot. Charging of Spherical Particles in an Ionizing Field. Journal de Physique et le Radium, 7(3):590-613, 1932.
4. White, H.J. Particle Charging in Electrostatic Precipitation. AIEE. 1186-1191, May 1951.
5. Liu, B.Y.H., and H. Yeh. On the Theory of Charging Aerosol Particles in an Electric Field. J. Appl. Phys. 39(3):1396-1402, 1968.
6. McDaniel, E.W. Collision Phenomena in Ionized Gases. John Wiley and Sons, New York, 1964. p. 473.
7. Liu, B.Y.H., K.T. Whitby, and H.H.S. Yu. Diffusion Charging of Aerosol Particles at Low Pressures. J. Appl. Phys. 38(4):1592-1597, 1967.
8. Hewitt, G.W. The Charging of Small Particles for Electrostatic Precipitation. AIEE. 76:300-306, 1957.
9. Bricard, J. Formation and Properties of Neutral Ultrafine Particles and Small Ions Conditioned by Gaseous Impurities of the Air. In: Aerosols and Atmospheric Chemistry, G.M. Hidy, ed. Academic Press, New York, 1972.
10. Loeb, L.B. Electrical Coronas. University of California Press, Berkeley, California, 1965. 694 pp.
11. Berglund, R.N., and B.Y.H. Liu. Generation of Monodisperse Aerosol Standards. Environmental Science and Technology. 7(2):147-152, 1973.
12. Lindblad, N.R., and J.M. Schneider. Production of Uniform-Sized Liquid Droplets. J. Sci. Instr. 42:635-638, 1965.

13. Ström, L. The Generation of Monodisperse Aerosols by Means of a Disintegrated Jet of Liquid. *Rev. Sci. Instr.* 40(6), 1969.
14. Letter, Kodak Chemical Products, Inc. Coatings Chemicals Division, Kingsport, Tennessee.
15. Handbook of Chemistry and Physics, 45th ed. Chemical Rubber Publishing Company, Cleveland, Ohio. D-106, 1966.
16. Bundy, R.H., et al. Styrene: Its Polymers, Copolymers and Derivatives. ACS Monograph Series R.
17. Fuchs, N., I. Petrjanoff, and B. Rotzeig. On the Rate of Charging of Droplets by an Ionic Current. *Transactions, Faraday Society.* 1131-1138, Feb. 1936.
18. Arendt, P., and H. Kallmann. The Mechanism of Charging of Cloud Particles. *Zeitschrift fur Physik.* 35:836-897, 1935.
19. Rohmann, H. Method of Size Measurement for Suspended Particles. *Zeitschrift fur Physik.* 17:253-265, 1923.
20. Ladenburg, R. Research on the Physical Basis of Electrical Gas Purification. *Annalen der Physik.* 4:863-897, 1930.
21. Penney, G.W., and R.D. Lynch. Measurements of Charge Imparted to Fine Particles by a Corona Discharge. *AIEE.* 76:294-299, July 1957.
22. Drozin, V.G., and V.K. LaMer. The Determination of the Particle Size Distribution of Aerosols by Precipitation of Charged Particles. *J. Colloid Science.* 14:74-90, 1959.
23. Liu, B.Y.H., K.T. Whitby, and H.H.S. Yu. On the Charging of Aerosol Particles by Unipolar Ions in the Absence of an Applied Electric Field. *J. Colloid Sci.* 23:367-378, 1967.
24. Cochet, R. Law of Charging of Fine (Submicron) Particles; Theoretical Studies; Recent Controls; Particle Spectra. In: *Colloque International-La Physique des Forces Electrostatiques et leurs Applications.* Centre National de la Recherche Scientifique, Paris, 1961. pp. 331-338.
25. Millikan, R.A. The General Law of Fall of a Small Body Through a Gas and its Bearing upon the Nature of Molecular Reflection From Surfaces. *Phys. Rev.* 22:1-23, 1923.
26. Cochet, R. Theory of Charging of Submicron Particles in Electrically Ionized Fields; Rate of Precipitation of the Particles. *Compt. Rend. Acad. Sci.* 243:243-246, 1956.

27. Cochet, R. and J. Trillat. Charging of Submicron Particles in Electrically Ionized Fields; Measurement of the Rate of Precipitation in a Uniform Electric Field. Compt. Rend. Acad. Sci. 250:2164-2166, 1960.
28. Knudson, E.O. The Distribution of Electrical Charge Among the Particles of an Artificially Charged Aerosol. Ph.D. Thesis, University of Minnesota, Minneapolis, Minnesota, 1971.
29. Smith, W.B., K.M. Cushing and J.D. McCain. Particulate Sizing Techniques for Control Device Evaluation. EPA-650/2-74-102, U.S. Environmental Protection Agency, Research Triangle Park, N.C. July, 1974. p. 83.



## APPENDIX A

### LITERATURE REVIEW - THEORY OF PARTICLE CHARGING

The works summarized and discussed in this section include the principal previous contributions related to the topic of particle charging. This material has provided the background and insight for the theoretical development presented in Section 3 of this report. The range of experimental data in the literature has indicated a need for a comprehensive study of particle charging under various conditions of electric field strengths and ion density for a variety of aerosol materials and sizes.

#### GENERAL REVIEW

M. Pauthenier & M. Moreau-Hanot (1932)<sup>3</sup>

#### Discussion--

A theoretical and experimental study is made to examine particle charging by a cylindrically symmetric electric field for spherical particles down to several microns in diameter. The theory is used to derive a "law" of charging of particles with time and to determine the maximum charge these particles can acquire. Both conducting and insulating particles are considered and thermal charge is considered to be negligible. The theory is tested over a wide range of particle sizes, field strengths and particle materials, with results which indicate the theory is applicable for particles with diameters down to several microns, where the effects of ion diffusion on the maximum charge start to be observed.

#### Basic Equations--

Potential--The cylindrically symmetric electric field is constructed by grounding a conducting cylinder of inner radius  $R_0$  and by placing a fine wire of radius  $r_0$  along its axis at a potential  $V_m$ . Inside the cylinder the density of negative charge  $\rho(r)$  is

$$\rho(r) = i/2\pi r\mu E \quad (27)$$

where  $i$  = ionization current per unit length,

$r$  = radial distance measured from the cylinder,

$\mu$  = ion mobility, and  
 $E$  = electric field strength.

Solving Poisson's equation using (27) as the charge density gives

$$E = - \left[ \frac{2i}{\mu} + \frac{C^2}{r^2} \right]^{\frac{1}{2}} \quad (28)$$

and

$$V(r) = F(r) - F(R_0) \quad (29)$$

for

$$R_0 \geq \text{corona wire diameter,}$$

where

$$F(r) = C \ln r + \left[ C^2 + \frac{2ir^2}{k} \right]^{\frac{1}{2}} - C \ln \left( \left[ C^2 + \frac{2ir^2}{k} \right] + C \right) \quad (30)$$

and  $C$  is determined by the condition that<sup>22</sup>

$$V_m = V(r_0) - V(R_0) \quad (31)$$

In the case where  $i$  is very small, a zero current approximation of  $E$  can be found from (28) which when inserted in (27) gives a low current approximation of  $\rho(r)$ . Integrating Poisson's equation gives the low current results:

$$E = -\frac{C}{r} \left( 1 + \frac{i}{C^2 \mu} r^2 \right), \quad (32)$$

which is a first order expansion of equation (2), and

$$V = C \ln \frac{r}{R_0} + \frac{i}{2C\mu} (r^2 - R_0^2) \quad (33)$$

On the other hand, series expansions of (28) and (30) give the high current results:

$$E = -\sqrt{\frac{2i}{k}} \left[ 1 + \frac{1}{2} \frac{\mu C^2}{2ir^2} - \frac{1}{8} \left( \frac{\mu C^2}{2ir^2} \right)^2 + \dots \right] \quad (34)$$

and

$$V = \Phi(r) - \Phi(r_0) \quad (35)$$

where

$$\Phi(r) = r \sqrt{\frac{2i}{\mu}} \left[ 1 - \frac{1}{2} \frac{\mu C^2}{2ir^2} + \frac{1}{24} \left( \frac{\mu C^2}{2ir^2} \right)^2 + \dots \right] \quad (36)$$

In many instances in (34), the term  $\mu C^2/4ir^2$  is small, so the potential curve is practically linear over most of its length. Thus, the field due to space charge is approximately constant for high currents.

Travel time--In a constant field, an ion of mobility  $\mu$ , travels a distance  $\ell$  in the time

$$t_0 = \frac{\ell^2}{\mu V} \quad (37)$$

where  $V$  is the potential difference between departure and arrival points.

If the field  $E$  varies in the space considered, then the time of travel  $t$  is

$$t = \frac{1}{\mu} \int_0^{\ell} \frac{d\ell}{E} \quad (38)$$

which in every case is higher than  $t_0$  for constant applied voltage. The effect of ionization is to lower this time. The more intense the corona, the closer the value of  $t$  is to  $t_0$ .

The charging of conducting particles--The capture of ions by a particle which already carries a charge of the same sign takes place by two processes:

1. Under the influence of thermal agitation, an ion can acquire sufficient kinetic energy to overcome the Coulomb repulsion of the particle, and be attracted by its image charge. This may be the dominant mechanism for particles whose diameter is less than one micron.
2. In the presence of an applied electric field, ions move along electric field lines and are attracted to their image charges on the particle. For larger particles, which can acquire a larger maximum charge, this is the dominant charging mechanism.

The second case is considered here. A conducting sphere of radius  $a$  and negative charge  $Q$  is placed in an electric field  $E_0$ . Nearby, a negative ion of charge  $e$  is situated. The location of the ion is  $(\theta, a(1+v))$  with respect to the center of the particle.

The uniform field  $E_0$  exerts a force on the ion whose radial component is

$$F_1 = -eE_0 \cos \theta \quad (39)$$

Due to the field  $E_0$ , the charge  $Q$  on the sphere is unequally distributed and gives rise to a second force on the ion whose radial component is

$$F_2 = - \frac{2E_0 e \cos \theta}{(1+v)^3} \quad (40)$$

The charge  $Q$  on the sphere repels the ion with a radial force equal to

$$F_3 = \frac{eQ}{a^2 (1+v)^2} \quad (41)$$

And finally, the ion induces an image charge on the particles which exerts a force of attraction expressed by

$$F_4 = - \frac{e^2}{4a^2 v^2} \frac{2(1+v)^2 - 1}{(1+v)^3 (1+v/2)^2} \quad (42)$$

which for small values of  $v$  reduces to:

$$F_4 \approx -e^2/4a^2 v^2 \quad (43)$$

The ion approaches the sphere if

$$F \equiv F_1 + F_2 + F_3 + F_4 < 0 \quad (44)$$

If  $Q$  is small,  $F$  is negative regardless of the distance  $a(1+v)$ , with the condition that  $\theta$  is smaller than some limit  $\theta_0$ . As the charge  $Q$  increases,  $\theta_0$  decreases and eventually the sphere is completely surrounded by a repulsive zone which the ions cannot penetrate, except when thermal agitation provides them with sufficient kinetic energy.

The equation  $F = 0$  cannot be solved for  $\theta_0$  at  $v = 0$ . However, (18) is always negative if  $Q$  is less than  $3E_0 a^2$ , and in the region where

$$v \ll 1 \quad (45)$$

and

$$\frac{e^2}{4a^2 v^2} \ll 1 \quad (46)$$

concurrently,  $Q = 3E_0 a^2$  leads to a very small value for (44).

Setting

$$Q = 3E_0 a^2 \lambda, \quad (47)$$

where  $\lambda$  is a dimensionless parameter, allows one to rewrite (44) as:

$$F = E_0 \cos \theta \left[ y_1 + (\lambda - 1) y_2 \right] \frac{y_3}{a^2} \quad (48)$$

where  $y_1$ ,  $y_2$ , and  $y_3$  depend only on  $v$ .

A graphical study of (48) shows that the repulsive zone completely envelopes the sphere for values of  $\lambda$  slightly greater than unity. Increasing  $\lambda$  tends to rapidly enlarge the repulsive region.

For spheres with radii larger than ten microns,  $\lambda$  is essentially unity. However, when particle radii are on the order of one micron, then  $\lambda \approx 1.1$ . The conclusion is that at this size that the effects of thermal agitation are being observed.

The law of charging of particles with time--The above discussion shows that thermal agitation has an insignificant influence on the limit charge of a large particle in an ionized field. Therefore, for large particles ( $a \geq 10 \mu$ ) thermal effects cannot be considered as dominating in the evaluation of the time necessary for a particle to acquire a charge. Indeed, a simple calculation shows that even in the region of maximum charge density there are not enough ions to appreciably influence the charging rate of a large particle by diffusional effects alone. The larger part of the charge is formed by ions entrained by the field with a speed of  $\mu E$ .

The charge brought to the particle in time  $dt$  is proportional to the flux  $\Phi$  of radial force  $F$  across a spherical segment limited by the edge of the repulsive zone. We choose a spherical segment very near the particle but far enough away from the surface so that (42) is negligible. Then the limit of integration  $\theta_0$  is defined by

$$\cos \theta_0 = \frac{Q}{3E_0 a^2} = \lambda \quad (49)$$

and

$$\Phi = -e \int_0^{\theta_0} \left( 3E_0 \cos \theta - \frac{Q}{a^2} \right) \cdot 2\pi a^2 \sin \theta d\theta \quad (50)$$

$$= -3\pi E_0 e a^2 (1 - \lambda)^2 \quad (51)$$

The negative charge  $-dQ$  acquired equal to

$$-dQ = -3E_0 a^2 d\lambda \quad (52)$$

and the charge density at a distance  $r$  from the cylinder axis is

$$\rho = \frac{E_0}{4\pi r} \quad (53)$$

So in a time  $dt$ , the negative charge acquired is

$$\frac{E_0}{4\pi r e} \mu \phi dt \quad (54)$$

From which one obtains the differential equation

$$\frac{d\lambda}{(1-\lambda)^2} = \frac{\mu E_0}{4r} dt \quad (55)$$

with solution

$$\lambda = \frac{t}{t+\tau} \quad (56)$$

where

$$\tau = \frac{4r}{\mu E_0} \quad (57)$$

is the time required to reach half the limit charge. We see that (55) does not depend on  $a$ . Therefore, the charging time is independent of particle size.

The charging of dielectric spheres--The charging of dielectric spheres in an electric field proceeds in a manner analogous to that for the conducting case. It is sufficient to replace the induced charge on a conducting particle by the polarization charge of the dielectric. A rigorous treatment would also require modification of (42); but the final results above are essentially independent of this term so it is not included here. Thus, the limit charge is now

$$Q_0 = p E_0 a^2 \quad (58)$$

where

$$p = 1 + \frac{2(k-1)}{(k+2)} \quad (59)$$

and  $k$  is the dielectric constant of the particle.

Application to electrostatic precipitation--When this theory is applied to electrostatic precipitators with a vertical corona wire and planar precipitation electrode, an analysis of particle trajectories to determine collection time and point of impact shows:

- a. For negligible air resistance, i.e., large particles, and with laminar gas flow numerical solutions of the equations of motion show that particles are collected

according to size. The relationship between particle size and collection time is double valued. It is found that at a particular point on the planar electrode collection begins with a certain size particle with both larger and smaller ones being collected at later times.

- b. For very light particles which quickly reach their terminal velocity, the time necessary for precipitation is independent of density and inversely proportional to the radius. Selection according to particle size is very noticeable.

### Experimental Results--

A cylindrically symmetric electric field was generated in a grounded conducting cylinder 30 cm in diameter with an axial wire which could be kept at a desired potential  $V_m$  with respect to ground ( $12 \text{ kV} < V_m < 48 \text{ kV}$ ). The potential was measured at points in the field for weak ( $1.15 \text{ } \mu\text{A}$ ) and stronger ( $13.2 \text{ } \mu\text{A}$ ) ionization currents. In the corona region, the theory developed above was in good agreement with the experimental results.

In order to measure the limit charge for spherical particles moving through the electric field, two procedures are used: first, to measure the limit charge for large particles, conducting and insulating spheres with diameters on the order of 1 mm to 1 cm were dropped from rest through the cylinder. Their acquired charge was measured by discharge through an electrometer. The theory was verified to within an experimental uncertainty of 1 to 2%. Second, small conducting and insulating spheres with diameters on the order of 20  $\mu\text{m}$  to 200  $\mu\text{m}$  were dropped from rest in the field and their trajectories were photographed. These were analyzed for deviation from a theoretically determined trajectory based on the effects of gravity and field charging rate, corrected for viscous forces and initial charge. Once again, the experimental results and theoretical predictions are in good agreement. This second method is called the "method of trajectories". Particles were also collected on the side of the cylinder on wet gelatin plates. This allowed accurate measurements of the number of particles of a particular size which move through a precisely determined vertical distance.

### Conclusions--

The theoretical and experimental results lead to the following conclusions:

- a. For particles with radii larger than several microns, the limit charge acquired is primarily

due to the electric field and is given accurately by the equations developed above.

- b. The law of charging accurately predicts the charging rate for large particles ( $a > 50 \mu$ ), and when trajectories are corrected for viscous effects agreement between theory and experiment can be extended to particles whose radii are on the order of several microns.
- c. The underlying principles of electrostatic precipitation of large particles ( $a > 5 \mu$ ), are adequately explained by the theoretical analysis of particle trajectories in an electric field.

#### Comments and Remarks--

This paper is definitive with regard to field charging phenomena. The authors limit their attention to particles large enough so that no diffusional charging effects need be considered. In some of the numerical analysis fairly crude assumptions are made in order to obtain results but these do not affect the conclusions drawn. The experimental work was carefully done and clearly designed to test the theory.

N. Fuchs, I. Petrjanoff, & B. Rotzeig (1936)<sup>17</sup>

#### Discussion--

An experimental investigation was made into the kinetics of the particle-charging process. Particles ranging from approximately 1.0  $\mu$ m to 6.0  $\mu$ m in diameter were examined. Curves for particle charge as a function of particle size were obtained for different values of ion concentration, electric field strength, ion current density, and time. The data were to be compared with the field-charging equation

$$Q = \left(1 + 2\frac{K-1}{K+2}\right) Ea^2 \left(\frac{\pi\mu Net}{1 + \pi\mu Net}\right) \quad (60)$$

for agreement, where

$Q$  = particle charge,

$K$  = dielectric constant of particles,

$E$  = external field strength,

$a$  = particle radius,



$N$  = ion density,  
 $\mu$  = ion mobility,  
 $e$  = elementary unit of charge, and  
 $t$  = time.

It was suspected that for smaller particles, the agreement between equation (34) and experiment would be less because of the increased influence of ion diffusion and image forces.

In the experiment, uncharged oil mist droplets were charged by passing a narrow air-jet containing the oil mist through a short trajectory along the axis of a wire pipe precipitator near the collecting surface. The oil mist was formed by taking a hot air-stream saturated with oil vapors and mixing it with a cold air-stream. The cloud produced by condensation was then diluted by mixing with clean air in order to obtain a suitable concentration of droplets. By adjusting the hot and cold airstream flows, clouds containing different particle sizes could be generated.

The velocity and width of the aerosol jet were adjusted until a jet was produced that had maximum stability and a width that remained essentially constant over its trajectory. Under these conditions, the linear velocity of the jet was assumed constant. The average velocity of the jet was obtained from the rate of flow of the oil mist before it entered the charging region and the cross-sectional area of the jet. Using the average velocity and the length of the trajectory, the average residence time of the droplets within the charging region could be determined.

The ionic current density intersecting the aerosol jet was calculated from the average current flowing through the inner section of the three-section precipitator. Measurements were made to ensure that the tubes, introduced into the precipitator to produce the jet and carry it off, did not appreciably alter the ionic current density in the region of the jet.

After passing through the charging region, the jet was pulled into an ultramicroscopic cell where both the size and charge of the droplets were determined by the "photographic oscillation method". In this method, the droplets were allowed to fall under the influence of gravity and simultaneously were forced by an alternating electric field to oscillate in a horizontal direction. By photographing the zig-zag paths of the droplets, the size is first determined from the rate of fall and then charge is found from the horizontal velocity.

## Conclusions--

The experimental results were plotted and compared with those predicted by equation (34) with  $j/E$  substituted for  $\mu\text{Ne}$ . The mobility  $\mu$  was taken to be  $1.75 \times 10^{-4} \text{m}^2/\text{V-sec}$  to give best agreement with theory. The electric field strength  $E$  was not measured directly but was determined from

$$E = \sqrt{\frac{4\pi jr}{\mu}} \quad (61)$$

where  $j$  is the current density at the surface of the pipe, and  $r$  is the radius of the pipe.

The mean values of the measured charges lie satisfactorily on the theoretical curves. However, insufficient data were obtained to determine the validity of equation (60) for particles having radii less than one micron.

## Comments and Remarks--

The jet employed in the experiment was greatly affected by the corona discharge and suffered deviation from a straight-line path and dispersion sooner for increasing current density. This limited the measurements to rather low values of external field strength and ion concentration. The deflection and spreading of the jet, due to the charges acquired by the droplets, limited this method of measurement to low values of particle charge. Charge on the droplets up to about 1/3 of the saturation charge could be measured.

H. J. White (1951)<sup>4</sup>

## Discussion--

An account was given of the work done on particle charging up until the time of publication. Existing theories were presented and the pertinent experimental studies discussed briefly. The theories were compared with experiment for agreement. In addition, some previously unpublished results were given.

Studies involving electric charges associated with industrial aerosols yielded the following findings:

- a. The majority of industrial aerosols are charged.
- b. The charge usually is equally distributed between positive and negative charges so that the aerosol as a whole is electrically neutral.

- c. The average particle charge is comparatively small although not negligible.

The above facts indicate clearly that electrostatic precipitation must include particle charging as an inherent part of the process.

The existing theories considered two particle-charging mechanisms to be important in the unipolar corona discharge.

- a. Bombardment of the particles by ions moving in the d-c field.
- b. Attachment of ions to the particles by ion diffusion.

The first mechanism was considered to be of primary importance in electrostatic precipitation and the latter process ordinarily was considered to be important only for particles smaller than about 0.2  $\mu\text{m}$  in diameter.

#### Basic Equations--

The theoretical equations were based on the following assumptions:

- a. The particles were assumed to be spherical.
- b. Particle spacing was assumed large compared to particle diameter.
- c. Ion concentration and electric field in the region of any given particle were assumed uniform.

Charging by ion bombardment--In the ion bombardment process, the ions move along the electric lines of force, strike the particle, and impart charge by attachment. This charge on the particle in turn produces a repulsive force which alters the field configuration and lowers the charging rate by reducing the electric flux entering the particle. Ultimately, sufficient charge is acquired to completely counteract the external field. At this point, the electric flux entering the particle is zero and charging ceases. The charging equation for this process is given by

$$\frac{n}{n_s} = \frac{t}{t + t_0} \quad (62)$$

where

$$n_s = \left(1 + \frac{2K-1}{K+2}\right) \frac{E_0 a^2}{e} \quad (63)$$

and

$$t_0 = \frac{1}{\pi N_0 e \mu} \quad (64)$$

In the equations,

- $n$  = particle charge,
- $n_s$  = saturation charge,
- $t$  = time,
- $t_0$  = particle charging time constant,
- $N_0$  = undisturbed ion concentration,
- $e$  = elementary unit of charge,
- $\mu$  = ion mobility,
- $K$  = dielectric constant of particle,
- $a$  = radius of particle, and
- $E_0$  = external field strength.

Equations (62)-(64) indicate the following features of this type of charging process:

- a. The particle charge  $n$  approaches the saturation value  $n_s$  for large values of  $t$ .
- b. The saturation charge  $n_s$  is directly proportional to both the electric field strength  $E_0$  and to the surface area represented by  $a^2$ .
- c. The charging time constant  $t_0$  is inversely proportional to both ion concentration  $N_0$  and to ion mobility  $\mu$ .

Charging by ion diffusion--Equations based on ion diffusion give reasonable results for particles of 0.1  $\mu\text{m}$  or less in diameter. In this mechanism, the thermal energies of the ions cause them to diffuse through the gas and suffer collisions with molecules and particles. Upon collision with a particle, the ions adhere to the particle due to the attractive electrical

image forces present. The diffusion process will occur in the absence of an external electric field although the presence of an external field will enhance charging. As the particle acquires charge by diffusion, it sets up a repelling field which tends to keep additional charges from reaching the particles. Thus, the charging rate decreases as the particle accumulates charge and ultimately becomes negligible.

Arendt and Kallman<sup>18</sup> made the first significant study of particle charging by diffusion of unipolar ions and derived the equation

$$\frac{dn}{dt} \left( 1 + \frac{a^2 c}{4nKe} \right) = \pi a^2 c N_0 e^{-ne^2/akT} \quad (65)$$

to describe the mechanism, where

$dn/dt$  = charging rate,

$c$  = mean thermal speed of ions,

$k$  = Boltzmann's constant,

$T$  = absolute temperature,

and the other symbols are as defined previously. Equation (65) is long in derivation, valid only for the case where the particle has already acquired appreciable charge, and must be solved numerically.

A simpler derivation and equation is presented which gives essentially the same results as equation (65) and where

$$n = \frac{akT}{e^2} \ln \left( 1 + \frac{\pi ac N_0 e^2 t}{kT} \right) . \quad (66)$$

In equation (66),  $n=0$  at  $t=0$  so that the particle is initially uncharged. From equation (66), it is seen that the particle charge will depend on the thermal energies of the ions, on the particle size, and on the time of exposure.

Comparison of theoretical equations with experiment--Experimental measurements essentially validate the equations presented for ion bombardment and ion diffusion. Experiments by Rohmann,<sup>19</sup> Ladenburg,<sup>20</sup> Pauthenier and Moreau-Hanot,<sup>3</sup> Arendt and Kallman,<sup>18</sup> Fuchs and Petrjanoff,<sup>17</sup> and White can be described reasonably well by one or the other of the charging mechanisms.

## Conclusions--

In general, the particle-charging mechanism is mainly that of field charging for particles larger than about  $0.5\text{ }\mu\text{m}$  in diameter and the ion diffusion process predominates for particles smaller than about  $0.2\text{ }\mu\text{m}$  in diameter. An exact theory should account simultaneously for both charging mechanisms, but this approach leads to mathematical difficulties.

## Comments and Remarks--

The ion diffusion mechanism presented does not account for the effects of the external field, which are appreciable. Diffusion charging can occur simultaneously with field charging, and this is not taken into account.

Gaylord W. Penney & Robert D. Lynch (1957)<sup>21</sup>

## Discussion--

An experimental investigation was made into the charging of fine particles by both positive and negative corona discharge. Experimental results were given for particle charge as a function of particle radius, electric field strength, and time. Particle sizes range from  $0.15\text{ }\mu\text{m}$  to  $0.32\text{ }\mu\text{m}$  in radius. Electric field strengths were varied from 1.2 to 3.8 kV/cm at the collecting surface.

The experimental apparatus and methods can be summarized as follows:

- a. Aerosol Generator and Particle Size Determination - The generator employed could produce a dioctyl phthalate aerosol containing particles largely uniform in size. The particle size was determined by an optical instrument called the "owl." This instrument passes white light through the aerosol and particle size information is inferred from the angular scattering pattern.
- b. Particle Charger and Charge Determination - The particles were charged by a concentric wire and pipe corona discharge in most of the tests. Also, some tests were run with a special particle charger that used the electric field between parallel screens for charging the particle. Results from the tests using the screen charger could be compared with charging theories because both the electric field and ion concentration were essentially uniform over the charging region. The particles were passed through the charging region and the resulting particle charge was determined by two different methods.

- i. Weight Method - The charged aerosol is drawn through a filter and the weight increase is that of the particles. The current collected due to the particles is measured by a galvanometer so that the total charge can be found from the integral of the current over time. From the total weight, total charge, and particle size, the charge per particle can be determined. This method was unfavorable because too long a time was required to collect a weighable number of particles and certain variables could not be kept constant over this period of time.
- ii. Mobility Method - The mobility of the particles is determined by measuring the efficiency when the charged particles are passed through a special parallel-plate precipitator having a uniform electric field between the plates, and designed to minimize turbulence. A linear relation exists between the plate efficiency and the potential between the plates and the mobility is determined from a plot of this relationship. Knowing the mobility and particle size, the charge per particle can be found from Stokes' Law. Data obtained from the weight and mobility methods showed reasonable agreement. The mobility method was preferable since it yielded results more conveniently.

## Conclusions--

The following are some results and conclusions from certain tests.

- a. With positive corona in the cylindrical charger, the particle charge was measured as a function of electric field strength. At a field strength of 4,000 V/cm and  $Nt = 10^8 \text{ sec/cm}^3$ , the measured charge was approximately twice that predicted by theory which neglected field effects. Thus, in this case, the field has a significant effect on the charging process.
- b. With negative corona in the screen charger, the particle charge was measured as a function of electric field strength. At approximately a field strength of 5,400 V/cm and  $Nt = 2.1 \times 10^7 \text{ sec/cm}^3$ , the measured charge was approximately twice that predicted by theory which neglected field effects. Again, field effects are important.
- c. At an electric strength of 1,600 V/cm and  $Nt = 3.3 \times 10^7 \text{ sec/cm}^3$ , both the positive corona in the cylindrical charger and the negative corona in the screen charger give both the same charge. These

results indicate that at low electric fields, the charging by positive and negative corona is approximately the same.

- d. With negative corona in the cylindrical charger, the particle charge was measured as a function of electric field strength. At low voltage, the charge due to negative corona was only a little greater than that given by positive corona. As the voltage was increased, the charge due to negative corona increased much more rapidly than that due to positive corona. At 13 kV the negative charge was 50% higher than the positive charge. This behavior is attributed to the possible presence of free electrons in the negative corona discharge at high voltages.
- e. The charge was measured as a function of  $Nt$  for both positive and negative corona in the cylindrical charger at a potential of 11 kV. Here both experimental charging curves were well above the curve predicted by theory neglecting field effects. Also, the charging due to negative corona was greater and increased more rapidly than that for positive corona. The effects of the electric field and the possible presence of free electrons is reflected in these measurements.

#### Comments and Remarks--

At higher voltages, the tests indicated that charging rates due to positive and negative corona differ quite drastically from one another. This difference is attributed to the presence of free electrons. If free electrons are present in negative corona discharge at high voltages, then charging would be greatly enhanced and theories would have to account for charging by electrons in addition to ions.

Data presented on charging versus time were very limited. One set of data was presented for a particle size of 0.15 micron and electric field strength of 2.65 kV/cm. More experimental data is needed on this type of measurement.

Also, more tests were needed with the screen charger so that the experimental data could be compared with theory.



Discussion--

Experimental results are given on the charging of submicron particles in air as a function of particle size, field strength, ion concentration, and charging time. Data are given on particle mobilities as a function of field strength, charge, and particle size. These data include particle sizes ranging from 0.14  $\mu\text{m}$  to 1.32  $\mu\text{m}$  in diameter and electric field strengths varying from 300 V/cm to 10800 V/cm.

The measurements were made with a system consisting of the following components and capabilities.

- a. Aerosol Generator, "OWL", and Concentration Meter - Cloud-type measurements were possible. The aerosol generator produced liquid, spherical particles of dioctyl phthalate of controllable and very uniform size. The size and concentration of the aerosol particles were measured by light-scattering methods. Particle sizes were measured with an instrument called the "owl", which analyzes the angular intensity of light reflected from the particles. Concentrations were determined by a concentration meter in which light scattered by the particles is focused on a photomultiplier tube.
- b. Particle Charger - The charging device provided independent control of the electric field strength  $E$ , ion concentration  $N$ , and charging time  $t$ .
- c. Mobility Analyzer - Mobilities of the charged particles were obtained by measuring their velocities in an electric field. Data were obtained in order to plot a curve of relative particle concentration versus mobility from which an average mobility is found. The relation between mobility and particle charge is determined by mobility measurements on particles of the same size carrying very few charges. A small amount of charge can be given to the particles by using low values of  $E$ ,  $N$ , and  $t$  in the particle charger.

Conclusions--

The experimental results lead to the following statements.

- a. The most difficult particles to precipitate are those ranging from 0.2  $\mu\text{m}$  to 0.4  $\mu\text{m}$  in diameter.

- b. For each charging field, there is a particle size at which the mobility reaches a minimum.
- c. The additional mobility produced by a charging field is approximately proportional to the strength of the field.
- d. The external electric field is important for all particle sizes.
- e. Charging curves show a greater slope at  $Nt=10^7$  ( $\text{cm}^{-3}$  sec) than theory indicates.
- f. Experimental curves do not flatten off as quickly as theory predicts.
- g. In the absence of an external field, the "classical" diffusion charging theory agrees reasonably well with experiment.
- h. For large particles and high electric field strengths, the "classical" field charging theory is in line with experimental results.

#### Comments and Remarks--

This experimental work was carefully done and covers the broadest range of particle sizes and electric field strengths available in the literature. All results are presented in graphical form. The results predicted by field charging and diffusion charging theories are plotted with the experimental results in certain cases to check for agreement. The charging rates for particles of diameters 0.18 to 0.92  $\mu\text{m}$  are most complete. Still, more experimental charging rates are needed for particles larger than 0.92  $\mu\text{m}$  in diameter.

Vadim G. Drozin & Victor K. La Mer (1959)<sup>22</sup>

#### Discussion--

As part of a method for determining the particle size distribution of aerosols, the particle charging law was determined experimentally by measuring particle charge as a function of particle radius. The data was obtained using monodisperse stearic acid aerosols produced in a La Mer-Sinclair generator. The particle size was determined from the angular position of red bands in the higher order Tyndall spectra. Particle sizes ranging from 0.1  $\mu\text{m}$  to 0.7  $\mu\text{m}$  in radius were examined.

The charging device employed a unipolar corona discharge and satisfied the following conditions:

- a. The losses of particles in the device due to precipitation under the influence of the charging field should be as small as possible.
- b. The particles may obey any charging law except one in which the number of acquired charges is linearly dependent on the radius of the particle. The general form of this dependence is

$$n = kr^{\alpha} , \quad (67)$$

where  $k$  and  $\alpha$  are constants.

- c. All particles of the same size should pick up the same number of charges.

Two methods were investigated for determining the charge acquired by a particle during the charging process.

- a. Individual Particle Observation - The upward and downward velocities of charged particles were measured with a known electric field in a Millikan chamber. If the particle sizes were determined optically, then the particle charge could be determined from the equation

$$neE \pm mg = \frac{6\pi\eta a S}{t_{up}} \quad (68)$$

where  $n$  = particle charge,

$e$  = elementary unit of charge,

$E$  = electric field in Millikan chamber,

$m$  = mass of particle ( $\frac{4}{3} \pi r^3 \rho$ ),

$g$  = acceleration of gravity,

$\eta$  = viscosity of the carrier gas,

$a$  = particle radius,

$S$  = distance particle travels under the influence of  $E$ , and

$t_{up}$  = time it takes the particle to travel the distance  $S$  upward.

As a check on how uniformly the particles were charged in the charging device under given charging conditions,

the particle size and charge were both determined in the Millikan chamber for a small number of particles. Normally, a monodisperse aerosol will have some size distribution and the size of a particular particle may not be exactly that determined from the higher order Tyndall spectra.

The particle radius was determined from the equation

$$a = k \sqrt{\frac{1}{t_{\text{down}}} - \frac{1}{t_{\text{up}}}} \quad , \quad (69)$$

where

$$k = \sqrt{\frac{9\eta S}{4\rho g}} \quad , \quad (70)$$

and  $\rho$  is the density of the particle material,

$t_{\text{down}}$  is the time the particle takes to travel the distance  $S$  in the downward direction, and

$t_{\text{up}}$  is the time the particle takes to travel the same distance  $S$  in the upward direction.

Knowing  $a$ , the particle charge could then be determined using equation (68).

This method had several disadvantages.

- i. The velocity measurements in the Millikan chamber were very tedious.
  - ii. Particles with radii under  $0.3 \mu\text{m}$  were difficult to observe.
  - iii. To establish a charging law, the velocities of many particles of different sizes should be measured and this would be extremely tedious.
- b. Particle Cloud Observation - For very monodisperse and sufficiently uniformly charged aerosol particles, it was much easier to measure the velocity of a moving "front" of the particles. This measurement yielded an average over many particles.

In order to determine the charging law by this method, the following steps were taken.

1. The number concentration  $N$  of monodisperse particles of a given size was determined by filtration of the

particles. A zero-penetration filter was weighed, the aerosol was passed through the filter, and after 15 to 20 minutes of filtration, the filter was weighed.

2. The penetration  $P$  through the charging device was measured by determining the ratio between the number of aerosol particles leaving and entering the charging device as a function of ionic current.
3. The current  $i_p$  caused by total precipitation of charged particles in the precipitator was measured as a function of ionic current.

Using the results of the above three steps, the number of charges  $n$  on a particle of given size could be determined from the equation

$$n = \frac{i_p}{NUPe} , \quad (71)$$

where  $U$  is the rate of aerosol flow.

Then, by following the same procedure on monodisperse aerosols of different particle sizes, the charging law was determined from the curve representing particle charge as a function of particle radius.

## Conclusions--

Experimental curves for particle charge as a function of particle radius were obtained for an aerosol flow rate of 4 l/min with a charging current of 300  $\mu$ A and for an aerosol flow rate of 2 l/min with charging currents of 40  $\mu$ A, 80  $\mu$ A, and 120  $\mu$ A. The charging curves yielded a charging law of the form,  $n = kr^\alpha$ , with  $\alpha$  having a value of approximately 2 for particles of radius greater than 0.2  $\mu$ m. The result that  $n$  is proportional to  $r^2$  is in agreement with the prediction of classical field-charging theory. For particles of radius less than 0.2  $\mu$ m, the exponent  $\alpha$  must be decreased in order to fit experimental data. This indicates that a mechanism other than field-charging is predominant for these particle sizes.

## Comments and Remarks--

This work indicates that experimentally, it is best to measure macroscopic properties of a large number of monodisperse particles rather than the properties of individual particles when studying aerosol particle charging.

Discussion--

A theoretical model is developed based on the concepts of kinetic theory in order to describe the charging of fine particles. The particle is considered to acquire charge primarily due to the thermal motion of ions in the process known as "ion diffusion" charging. It is assumed that "field" charging takes place initially and very quickly the particle reaches a maximum charge due to this mechanism. This maximum charge is then used as the initial charge for calculations in this model. Previous models for "ion diffusion" charging accounted only for electric field effects due to the charge on the particle and neglected any effect due to the external electric field. The model presented accounts for both the field due to the particle and external field. By use of the model, an attempt is made to estimate the effects of the external field under differing conditions. In analyzing the effects of the external field on the random-motion charging process, two possible mechanisms for altering the charging rate are investigated in depth:

- a. An ion moving in the direction of the external field towards a particle will acquire a certain amount of energy due to the field in addition to its thermal energy which will enhance its chances of overcoming the potential field due to the charge already on the particle.
- b. The external electric field will alter the density distribution of ions in the neighborhood of the particle and thus affect the movement of ions towards the particle.

In the mathematical formulation of the charging model, the number of ions that may reach the particle depends on the following factors:

- a. The number of ions in the neighborhood of a point P in space.
- b. The number of ions at point P headed in the correct direction.
- c. The number of ions at point P with sufficient velocity to overcome the repulsive force due to the like-charged particle.
- d. The number of ions at point P that manage to avoid a collision on the way to the particle.
- e. All points P in space.

- f. All areas on the particle that an ion may strike from point P.

#### Basic Equations--

The charging rate for an infinitesimal surface area  $dS$  on the particle is given by

$$\left. \frac{dn}{dt} \right|_{dS} = \frac{dS}{4\pi} \int_0^\infty dr \int_0^{\pi/2} d\theta_r \sin\theta_r \times \int_0^{2\pi} d\phi_r N \cos\theta_r e^{-r/\lambda} \int_{c_m}^\infty \frac{c}{\lambda} f(c) dc \quad (72)$$

where  $n$  = number of electronic charges on particle,  
 $dS$  = infinitesimal area on particle,  $\text{cm}^2$ ,  
 $x_r, y_r, z_r$  = Cartesian co-ordinates with  $dS$  as origin,  $\text{cm}$ ,  
 $r, \theta_r, \phi_r$  = spherical co-ordinates for  $x_r, y_r, z_r$  system,  $\text{cm}$ , radians,  
 $N$  = ion density at point P,  $\text{ions}/\text{cm}^3$ ,  
 $c$  = speed of ion (without regard to direction),  $\text{cm}/\text{sec}$ ,  
 $\lambda$  = mean free path of ions colliding with molecules,  $\text{cm}$ ,  
 $f(c)dc$  = probability that an ion will have a speed between  $c$  and  $c+dc$  after collision,  
 $c_m$  = minimum speed which an ion can have at P and still reach  $dS$ ,  $\text{cm}/\text{sec}$ , and  
 $t$  = time measured from start to charging,  $\text{sec}$ .

Equation (72) accounts for the first five factors (mentioned in the general discussion), which determine the charging rate in this model. The sixth factor is accounted for by integrating over the surface of the particle to find the total charging rate which is given by

$$\frac{dn}{dt} = \int_S \left. \frac{dn}{dt} \right|_S = 2\pi a^2 \int_0^\pi d\theta_E \sin\theta_E \left\{ \frac{1}{dS} \left. \frac{dn}{dt} \right|_{dS} \right\} \quad (73)$$

where  $a$  = particle radius,  $\text{cm}$ ,  
 $x_E, y_E, z_E$  = Cartesian co-ordinates with center of sphere as origin,  $\text{cm}$ , and

$r_E, \theta_E, \phi_E$  = spherical co-ordinates for  $x_E, y_E, z_E$  system,  
radians.

In order to evaluate equation (73), the quantities  $f(c)$  and  $N$  must be known.

Ideally,  $f(c)$  represents the general velocity distribution for ions in an electric field. Once a form is chosen for  $f(c)$ , the integral

$$\int_{c_m}^{\infty} c f(c) dc \quad (74)$$

can be evaluated. It is noted that the minimum speed  $c_m$ , that an ion can have at point P and still reach the surface of the particle is a function of position and a criterion is established for determining  $c_m$  for each point in space.

The ion density  $N$  is a function of position and in general, is a solution to the diffusion equation

$$\nabla^2 N + \nabla \psi \cdot \nabla N = 0 \quad (75)$$

where the dimensionless potential energy function is given by

$$\psi = \frac{ne^2}{kTR} + \frac{eE_0 a}{kT} \left( \frac{R}{a} - \frac{a^2}{R^2} \frac{K-1}{K+2} \right) \quad (76)$$

and

$e$  = electronic charge, statcoulombs,

$k$  = Boltzmann's constant, erg/°K,

$T$  = absolute temperature, °K,

$R$  = distance from center of particle to P, cm,

$E_0$  = uniform external field strength ( $E_0$  parallel to  $z_E$ ), cm,  
and

$K$  = dielectric constant of particle.

The solution to equation (75) is of the form  $e^{-\psi}$  and must satisfy the boundary condition that  $|\psi|$  remain finite as  $R \rightarrow \infty$ .



## Conclusions--

Due to the difficulties involved in solving equation (73), it is not solved rigorously. Insight into the effects of the external electric field is gained by other methods. In order to determine the effect of the external field on the energy of the ion, the dimensionless function

$$g = \psi_0 - \psi \quad (77)$$

is examined for certain simple cases, where  $\psi_0$  is the dimensionless potential energy at the surface of the particle. The effect of the external electric field on the ion density  $N$  is estimated by solving equation (75) using finite difference approximations along special directions in space where solutions could be obtained more easily.

All ions headed towards  $dS$  from points in space such that  $g < 0$  have enough velocity to reach the particle. Only a fraction,  $(1 + g)e^{-g}$ , of the ions headed towards  $dS$  from points in space such that  $g > 0$  have enough velocity to reach the particle. Consideration of the function  $g$  in the case where the ions travel along the direction of the external field shows that  $g = 0$  at some distance  $R_0$  from the particle and all ions a distance of  $R_0$  or greater from the particle will have sufficient velocity to reach the particle. In the absence of an external field, the number of ions reaching  $R_0$  with sufficient velocity to reach the particle is smaller. So in the presence of an external field, more ions arrive at  $R_0$  with sufficient velocity to reach the particle than in the absence of an external field. Even though the external field increases the number of ions arriving at  $R_0$  with sufficient velocity to reach the particle, these ions only have a chance of getting to the particle because of the possibility of suffering a collision along the way. The probability of suffering a collision over the distance  $R_0$  is  $e^{-R_0/\lambda}$ . For a mean free path typical of a molecular ion,  $e^{-R_0/\lambda}$  is very small. Thus, it is seen that the increased energy effect for ions moving in the direction of the field will be small for molecular ions. Also, for ions moving in a direction opposite to the external field  $g$  is always positive and always larger with an external field present than with no external field. Thus, there will be fewer ions capable of reaching the particle from this direction when an external field is present.

Solution of equation (75) using finite difference approximations along special directions shows that the external field has a large effect on the ion density  $N$  at the surface of the particle which would lead to increased charging. The following results are found:

- a. The ion density at the surface of the particle is increased by a large factor over the zero field value where the external field and particle field are directly opposite one another. In addition, the factor by which the ion density increased depends greatly on both the particle charge and the external field.
- b. The ion density at the surface of the particle is decreased by only a small factor from the zero field value where the external field and the particle field are exactly in the same direction.

#### Comments and Remarks--

The model presented here is fundamentally sound and the conclusions drawn concerning the effects of the external field are valid. The difficulty with the model lies in the mathematical complexity in finding the charging rate from equation (73). This difficulty centers around the solution of equation (75) for the ion density  $N$  as a function of position in the existing fields, the many integrations that must be performed in equation (73), and the complex relationships between certain variables in equation (73). Since equation (73) could not be solved rigorously, the theory could not be compared with experiment for agreement except by making rough estimates. These rough estimates showed fair agreement with the limited experimental data of Penney and Lynch. Also, the initial charge used in this theory should be due to both "field" and "diffusion" charging which can occur simultaneously instead of "field" charging alone.

Benjamin Y. H. Liu, Kenneth T. Whitby, & Henry H. S. Yu (1967)<sup>7</sup>

#### Discussion--

An experimental investigation was made into the pure ion diffusion process at various pressures less than one atmosphere. By varying the pressure, the mean free path of the ions could be changed and its effect on the ion diffusion process could be deduced. Theories based on kinetic theory predict that the mean free path will have relatively little effect on the particle charging process, whereas, those based on macroscopic diffusion of ions indicate that it should have a considerable effect.

The experimental data were obtained by exposing a monodisperse aerosol to unipolar ions produced by a high-voltage positive corona discharge and measuring the electrical mobility and charge of the aerosol. The experiment consisted of the following techniques and apparatus:

- a. Aerosol Generation and Sizing - The aerosols used were monodisperse aerosols of di-octyl phthalate (DOP) having diameters of 1.35  $\mu\text{m}$  and 0.65  $\mu\text{m}$ . The aerosols were produced by a generator of the atomization-condensation type and put through a process of charge neutralization. The particle sizes were measured by a calibrated optical particle counter and by direct microscopic sizing of the collected DOP drops.
- b. Aerosol Charger - The aerosol was exposed to positive ions in the charging region which was bounded on one side by a solid electrode and on the other by a screen through which the positive ions produced by the corona discharged flowed. An ac square wave voltage was applied to the solid electrode to minimize the aerosol loss during the charging process.

For a given particle size and pressure, charging due to pure diffusion of ions depends on  $N_0$ , the number concentration of ions in the charging region and  $t$ , the time during which the particles are exposed to ions. The charging time  $t$  was calculated from the aerosol flow rate and the dimensions of the charging region. In order to determine the ion concentration  $N_0$ , in the charging region, a dc voltage was substituted for the ac square-wave voltage and the corresponding dc current,  $I$ , which flowed through the screen into the charging region, was measured. The ion concentration was then calculated using the equation

$$N_0 = I / eE\mu_i A \quad (78)$$

where  $e$  = elementary unit of charge,

$E$  = intensity of charging field,

$\mu_i$  = ion mobility, and

$A$  = area of screen through which ions flow into the charging region.

- c. Measurement of Small Ion Mobility - Since the ion mobility could be greatly affected by trace amounts of unknown impurities, a measurement was made of this quantity. In a small ion mobility analyzer, positive ions produced by the corona wires were made to flow periodically into an ion drift space by a square-wave voltage applied to an electronic shutter. In the ion drift space, a high voltage dc power supply created an electric field and the time it took the ions to travel from

a grounded screen to an ion collecting plate was measured on an oscilloscope screen. The ion mobility was then calculated from the measured ion transit time, the width, and the electric field intensity in the drift space.

- d. Aerosol Mobility Analyzer - The charged aerosol was introduced into the aerosol mobility analyzer in the form of an annular ring around a core of particle-free, clean air and collected at the other end by a filter. A negative voltage was applied to a rod located at the center of the annular ring. The negative voltage was increased in steps and the corresponding current was measured by an electrometer attached to the filter. The electrometer current represented the current due to the charged aerosol collected by the filter and hence, not collected by the center rod. A voltage-current curve was plotted in order to obtain the mobility. Then, the electrical mobility of the aerosol was obtained by using the equation

$$\mu_p = C(q/V) \quad (79)$$

where  $\mu_p$  = electrical mobility of the aerosol,

$q$  = total volumetric rate of flow of air and aerosol in the mobility analyzer,

$V$  = value of the center rod voltage at which the electrometer current is equal to half of its maximum value, and

$C$  = instrument constant depending on the dimensions of the mobility analyzer.

From the measured mobility of the aerosol, the electric charge on the particles was determined from the equation

$$n_p = \frac{3\pi\eta D_p \mu_p}{c} \quad (80)$$

where  $n_p$  = number of elementary units of charge on a particle,

$\eta$  = viscosity of air,

$c$  = Cunningham's correction factor, and

$D_p$  = particle diameter.

## Conclusions--

The experimental results were obtained over a pressure range of 0.0311 to 0.960 atm with a corresponding particle radius to ion mean-free path ratio,  $a/\lambda$ , ranging from 1.0 to 66. The data led to the following results and conclusions.

- a. The ion mobility varies inversely with pressure.
- b. The experimental data could be fitted by the equation

$$n_p/D_0 = 9.0 \ln(1 + 1.02 \times 10^{-5} N_0 t D_p) \quad (81)$$

where  $D_p$  is the particle diameter in micrometers.

- c. The particle charge is independent of the ratio,  $a/\lambda$ , and depends only on the product  $N_0 t$ .
- d. Equation (81) agrees with the classical ion diffusion equation,

$$n_p e^2 / a k t = \ln [1 + (\pi \bar{c}^2 a N_0 t / k t)] \quad , \quad (82)$$

provided the value of  $\bar{c}$ , the mean thermal speed of ions, is taken as  $1.18 \times 10^4$  cm/sec.

- e. The measured ion mobility  $\mu_i$  at atmospheric pressure was  $1.1 \text{ cm}^2/\text{V}\cdot\text{sec}$ .
- f. The values of  $\bar{c}$  and  $\mu_i$  were considerably smaller than the usual values of  $\bar{c} = 4.72 \times 10^4$  cm/sec and  $\mu_i = 1.6 \text{ cm}^2/\text{V}\cdot\text{sec}$  for positive ions produced in a corona discharge. These results suggest a molecular weight for the ions which is on the order of 16 times that of air. Thus, the ions were probably clusters of molecules produced in the corona discharge rather than simple ionized air molecules.

## Comments and Remarks--

The results of this investigation indicate a need to design experiments to identify the ions present in the corona discharge and determine their relative numbers. Mass spectroscopy has been used by other investigators to identify the ions present in the corona discharge. Several different ions were identified and the largest mass found was 200. Liu, et al, suggest a molecular weight for ions of 460 in order to obtain agreement between their experimental data and classical charging by pure ion diffusion.

Since theories based on kinetic theory depend on the mass of the ions, it is necessary to have some average ionic mass representative of that found in the corona discharge.

Benjamin Y. H. Liu, Kenneth T. Whitby, & Henry H. S. Yu (1967)<sup>23</sup>

#### Discussion--

An analysis of the particle charging process in the absence of an applied electric field is presented. An order of magnitude calculation is made in order to show that under practical charging conditions, the charging process for micron and submicron particles cannot be described as a macroscopic diffusion process in which ions are assumed to diffuse continuously in a quasi-steady state toward the particle under the action of a concentration gradient because, in fact, the charging process is essentially discontinuous. A theory is developed based upon the classical kinetic theory of gases and its predictions are compared with available experimental data and other existing theories. This theory predicts that the particle charging rate will be unaffected by the mean free path of the ions.

#### Basic Equations--

For a neutral particle of radius,  $a$ , in a gaseous medium containing  $N_0$  ions/cm<sup>3</sup>, the average time  $t$ , needed for the particle to capture an ion is

$$t_1 = 1/\pi a^2 \bar{c} N_0 \quad , \quad (83)$$

where  $\bar{c}$  is the mean thermal speed of the ions.  
The average diffusion time  $t_2$  is on the order of

$$t_2 = a^2/D \quad , \quad (84)$$

where  $D$  is the diffusion coefficient of the ions. If  $t_1 \ll t_2$ , then many ions will be captured within the time interval  $t_2$  and the charging process may be considered a continuous diffusion process. From equations (83) and (84) and the condition  $t_1 \ll t_2$ , it is found that

$$N_0 \gg \frac{D}{\pi a^4 \bar{c}} \quad . \quad (85)$$

If the diffusion coefficient  $D$  is taken to be

$$D = \frac{3\pi \bar{c} \lambda}{16\sqrt{2}} \quad , \quad (86)$$

where  $\lambda$  is the mean free path of the ions, then equation (85)

requires that

$$N_0 \gg \frac{3\lambda}{16\sqrt{2} a^4} \quad (87)$$

in order that the particle charging process may be considered as a continuous diffusion process. Taking  $a = 1.0\mu$  and  $\lambda = 10^{-6}$  cm,  $N_0$  must be much greater than  $10^9$  ions/cc for the process to be considered as continuous. In practical charging devices, the maximum  $N_0$  is on the order of  $10^8$  ions/cm<sup>3</sup> which is sufficient to produce a continuous charging process.

An alternate approach, based on kinetic theory, is developed in order to describe the particle charging process. The development employs the same line of reasoning as that used by Murphy et al, in an earlier publication and, as before, the charging rate is found to be

$$\frac{dn_p}{dt} = \left( \int_S \int_{r=0}^{\infty} \int_{\theta=0}^{\pi/2} \int_{\phi=0}^{2\pi} \frac{dS \cos \theta}{4\pi r^2} (r^2 \sin \theta dr d\theta d\phi) N \right) \times \left( \int_{c=c_m}^{\infty} \frac{c}{\lambda} f(c) e^{-\lambda/r} dc \right), \quad (88)$$

where

$n_p$  = particle charge,

$t$  = time,

$dS$  = element of surface area on the particle,

$S$  = surface of the particle,

$r, \theta, \phi$  = spherical coordinates of a point P in space with  $dS$  as origin of the coordinate system,

$N$  = ion concentration in the volume  $dV$  at a point P in space,

$c$  = mean thermal speed of the ions,

$c_m$  = minimum speed corresponding to the minimum kinetic energy which an ion must possess to arrive at the surface of the particle from a point P in space,

$f(c)$  = distribution function in terms of ionic speed, and

$\lambda$  = mean free path of ions.

In order to perform the integrations in equation (88), the value of  $c_m$ , the spatial dependence of  $N$ , and the dependence of  $f(c)$  on  $c$  must be known.

The value of  $c_m$  is determined by using the results of classical scattering theory and accounting for the deflection of the ion due to the charge on the particle. An ion has a chance of making a grazing collision with a particle provided that it has a minimum initial speed  $c_m$  which satisfies the condition

$$\sin^2 \theta = 1 - \frac{\gamma}{\xi_n} + \frac{\gamma}{\xi_n} \left( \frac{a}{R} \right) , \quad (89)$$

where

$$\gamma = \frac{n_p e^2}{akT} , \quad \xi_n = \frac{1}{2} \frac{m c_m^2}{kT} , \quad (90)$$

and

$\theta$  = spherical coordinate of a point P in space with dS as origin,

$n_p$  = number of electrons on particle,

$e$  = elementary unit of charge,

$a$  = particle radius,

$k$  = Boltzmann's constant,

$T$  = absolute temperature,

$m$  = ionic mass, and

$R$  = radial distance from the center of the particle to a point P in space.

The local concentration  $N$  of ions at a point P in the vicinity of a charged particle is obtained using the Boltzmann distribution,

$$N = N_0 e^{-\gamma a/R} \quad (91)$$

In using equation (91), it is assumed that the average time interval needed by the particle to capture an ion is long compared to the time needed for the equilibrium distribution of ions to be established around the particle.

Assuming that the presence of the charged particle does not disturb the distribution function  $f(c)$  too greatly, then  $f(c)$



may be taken as the equilibrium distribution function and will be Maxwellian. Then,

$$cf(c)dc = \bar{c} \xi e^{-\xi} d\xi, \quad (92)$$

where

$$\xi = \frac{1}{2} \frac{mc^2}{kT}, \quad (93)$$

and

$$\bar{c} = \frac{2}{\sqrt{\pi}} \left( \frac{2kT}{m} \right)^{1/2}. \quad (94)$$

Due to symmetry considerations, equation (89) can be readily integrated with respect to  $dS$  and  $d\phi$ . The remaining integrals can be written in a simpler form by using relations (90), (91), (92), and defining new variables  $\tau$  and  $x$  given by

$$\tau = \frac{\pi a \bar{c}^2 N_0 t}{kT}; \quad x = \frac{r}{a}. \quad (95)$$

Then, equation (88) can be rewritten in the form

$$\frac{dr}{d\tau} = \frac{a}{\lambda} \int_0^\infty e^{-x(a/\lambda)} dx \int_{\theta=0}^{\pi/2} 2 \sin\theta \cos\theta e^{-\gamma(a/R)} d\theta \times \int_{\xi=\xi_m}^\infty \xi e^{-\xi} d\xi. \quad (96)$$

Since

$$\int_{\xi=\xi_m}^\infty \xi e^{-\xi} d\xi = (1 + \xi_m) e^{-\xi_m} \quad (97)$$

and according to equation (89),

$$\xi_m = \frac{1}{\cos^2 \theta} \gamma \left( 1 - \frac{a}{R} \right), \quad (98)$$

we have

$$\frac{d\gamma}{d\tau} = \frac{a}{\lambda} \int_{x=0}^{\infty} e^{-x(a/\lambda)} dx \int_{\theta=0}^{\pi/2} 2 \sin\theta \cos\theta \times \left[ 1 + \frac{1}{\cos^2\theta} \gamma \left( 1 - \frac{a}{R} \right) \right] \exp \left\{ \left[ -\gamma \frac{a}{R} + \frac{1}{\cos^2\theta} \left( 1 - \frac{a}{R} \right) \right] \right\} d\theta. \quad (99)$$

In equation (98), the ratio  $(a/R)$  is a function of  $\theta$  where it can be shown from geometrical considerations that

$$(R/a)^2 = 1 + x^2 + 2 x \cos \theta. \quad (100)$$

Since the ratio  $(a/R)$  does not vary greatly over the interval of integration, it is replaced by an appropriate mean value  $(a/\bar{R})$  so that the integral over  $\theta$  can be performed in closed form. After integrating equation (99), the charging rate is given by

$$\frac{d\gamma}{d\tau} = e^{-\gamma}. \quad (101)$$

Conclusions--

The charging rate derived by Murphy is

$$\frac{d\gamma}{d\tau} = e^{-\gamma(1 + \delta\gamma)}, \quad (102)$$

where  $\delta$  is a function of the ratio  $a/\lambda$ .

Murphy's equation differs from equation (101) in that the charging rate depends on the mean free path of the ions. Experiments performed by Liu et al, in which charging rates were found for different mean free paths, indicate that equation (101) is valid. In equation (101), the charging rate is independent of the mean free path and this is a consequence of considering the deflection of an ion as it approaches a charged particle. Murphy did not consider the deflection of the ions in his development.

Equation (101) is identical with the classical diffusion equation derived by White. White derived his equation under the assumption that the particle radius is large compared to the mean free path of the ions. This analysis shows that the equation will be valid even when the radius of the particle may not be considered large compared to the mean free path of the ions.

The theory developed shows good agreement with experimental charging curves when the mean thermal speed of the ions is taken

to be  $1.18 \times 10^4$  cm/sec. This is equivalent to an ionic molecular weight of 460.

Theories based upon the microscopic diffusion of ions predict a dependence of the charging rate on the mean free path. The steady-state diffusion equation can not properly describe the particle charging process because of the low concentration of ions present in the charging process and the essentially discontinuous nature of the charging process.

#### Comments and Remarks--

The experimental data is plotted, and it is stated that the classical diffusion equation gives reasonable agreement with the data if the mean thermal speed  $\bar{c}$  is taken to be  $1.18 \times 10^4$  cm/sec. It would be of interest to see the results given by the classical diffusion equation when the usual value of  $4.63 \times 10^4$  cm/sec is used and see how this compares with the experimental data. This would give some idea into how sensitive the diffusion charging process is to the choice of  $\bar{c}$ . If it is highly sensitive to the value of  $\bar{c}$ , then a determination of the ionic masses must be made in order to have a reliable value of  $\bar{c}$  to use in the theories.

Benjamin Y. H. Liu and Hsu-Chi Yeh (1968) <sup>5</sup>

#### Discussion--

An approximate theory is developed in an attempt to describe particle charging over a broad range of particle sizes and applied electric fields. Due to the approximations introduced in the theory, the resulting mathematical equations can be readily solved by numerical methods. The theory is constructed so that it will account for the following experimentally observed facts.

1. For high electric-field intensities and large particles, the field-charging equation

$$n = n_s \pi N_0 e \mu_i t / (\pi N_0 e \mu_i t + 1) \quad (103)$$

is in reasonable agreement with experimental results, where

$n$  = charge on particle, elementary units,

$n_s$  = saturation charge on particle, elementary units,

$N_0$  = concentration of ions at a great distance from particle, ions/cm<sup>3</sup>,

$e$  = elementary unit of charge,  $4.8 \times 10^{-10}$  esu,

$\mu_i$  = electric mobility of ions,  $\text{cm}^2/\text{stat V}\cdot\text{sec}$ ,  
and

$t$  = time, sec.

2. In the absence of an external electric field, the diffusion-charging equation

$$n = (akT/e^2) \ln (1 + \pi e^2 \bar{c} a N_0 t / kT) \quad (104)$$

yields results in line with experimental data, where

$a$  = particle radius, cm,

$k$  = Boltzmann's constant, cgs,

$T$  = absolute temperature, degrees K,  
and

$\bar{c}$  = mean thermal speed of ions, cm/sec.

3. The applied electric field has a large effect on the charging rate for submicron particles.

The theory approaches equation (103) in the limit of large particles and high external fields, reduces to equation (104) with no external field, and allows the external field to have an appreciable effect in charging submicron particles.

The theory divides the charging process into two regimes depending on the amount of charge on the particle. If the charge  $n$  on the particle is less than the saturation charge  $n_s$ , then charging takes place in Regime II. Charging in Regime I is considered as due to both field charging and diffusion occurring simultaneously. Thus, in Regime I the ions are driven onto the particle by the electric field and also reach the particle due to their thermal motion. In Regime II, since no electric field lines can enter the particle, the mechanism by which ions reach the particle is deduced by analyzing their motion along the special direction where the electric field due to the particle and the external electric field are exactly opposite one another. An ion is visualized as drifting towards the particle along the direction of the total electric field until it reaches a certain distance  $r_0$  from the particle where the potential energy is a minimum. From  $r_0$  to the surface of the particle, the ion must move against the total electric field and can accomplish this by means of the diffusion process and a concentration gradient. Thus, diffusion is the sole charging mechanism in Regime II.

## Basic Equations--

The ions experience an electric potential given by

$$V = \frac{ne}{r} + E_0 \cos \theta \left\{ r - (a^3/r^2) \left[ \left( \frac{K-1}{K+2} \right) \right] \right\} \quad (105)$$

where  $E_0$  = the external electric field, and

$K$  = the dielectric constant of the particle.

In Regime I, ions are driven onto the particle along electric field lines between the angles  $\theta = 0$  and  $\theta = \theta_0$ , where  $\theta_0$  is determined from the condition that

$$E_r = \frac{\partial V}{\partial r} \bigg|_{r=a} = 0 \quad (106)$$

The charging rate in Regime I is given by

$$\left( \frac{dn}{dt} \right)_I = \pi e N_0 \mu_i n_s (1 - n/n_s)^2 + \frac{1}{4} N_0 C [2\pi a^2 (1 + n/n_s)] \quad (107)$$

where the first term is the "classical" field-charging rate and the second term is a correction to the charging rate which allows for diffusion of ions to the particle. The factor  $2\pi a^2 (1 + n/n_s)$  is the surface area of the particle containing all electric field lines that leave the particle.

In Regime II, the diffusional charging rate is given by

$$\left( \frac{dn}{dt} \right)_{II} = \left( \frac{1}{4} \bar{N} C \right) (4\pi a^2) \quad (108)$$

where  $\bar{N}$  = the average concentration of ions over the entire particle surface.

In general, the local ion concentration  $N$  must be found by solving the steady state diffusion equation for ions in an electric field given by

$$\nabla^2 N + \nabla(eV/kT) \cdot \nabla N = 0 \quad (109)$$

A solution to equation (109) is constructed and is given by

$$\begin{aligned} \bar{N} &= N_0 && \text{for } r > r_0 \\ N &= N_0 e^{-(e/kT)(V-V_0)} && \text{for } r < r_0, \end{aligned} \quad (110)$$

where  $V_0$  = the electric potential at  $r_0$ .

Solution (110) satisfied the boundary condition that as  $r \rightarrow \infty$ ,  $N \rightarrow N_0$ . To find  $r_0$  along the line  $\theta = 0$ , the condition

$$\left. \frac{\partial V}{\partial r} \right|_{\theta=0} = 0$$

is used so that

$$-(ne/r_0^2) + E_0 \left\{ 1 + 2 \left[ \frac{K-1}{K+2} \right] \left( \frac{a^3}{r_0^3} \right) \right\} = 0 \quad (111)$$

determines  $r_0$ .

The concentration of ions at the particle surface at  $\theta = 0$  is

$$N_a = N_0 e^{-e/kT(V_a - V_0)} = N_0 e^{-e/kT(\Delta V)} \quad (112)$$

where  $V_a$  = the electric potential on the particle's surface at  $\theta = 0$ .

It is argued that the average ion concentration of ions over the entire particle surface should be of the same order of magnitude as  $N_a$  and as a first approximation  $N_a$  is used in place of  $\bar{N}$  in equation (108). Thus, the charging rate in Regime II can be calculated from

$$\left( \frac{dn}{dt} \right)_{II} = \pi a^2 N_0 c e^{-e/kT(\Delta V)} \quad (113)$$

used in conjunction with equations (105) and (111).

## Conclusions--

The predictions of the theory are compared with the experimental particle charging data of Hewitt for particles of radius 0.09  $\mu\text{m}$  to 0.46  $\mu\text{m}$  and with external field strengths ranging from 300 V/cm to 10,800 V/cm. The agreement of the theory with experiment is excellent for the 0.09  $\mu\text{m}$  particle for all electric field intensities available. The agreement of the theory with experiment for the 0.46  $\mu\text{m}$  particle is less desirable and overestimates the charge by about 30% for all electric field intensities. It is concluded that the theory gives a reasonable explanation of the charging process because it agrees fairly well with experiment over a wide range of conditions.

## Comments and Remarks--

The following observations are made concerning the theory.

1. In the physical picture of the theory,  $N=N_0$  for  $r>r_0$  where  $r_0$  corresponds to the radial distance from the particle along  $\theta = 0$  at which the potential is a minimum. Since at  $r_0$ , the electric field due to the particle is exactly equal in magnitude to the external electric field, it appears that the electric field due to the particle will have an appreciable effect on the ion concentration out to a much larger distance than  $r_0$  so that  $N$  is approximately equal to  $N_0$  at some greater distance from the particle than  $r_0$ .
2. In finding the average ion concentration at the particle surface, it is assumed that the average is equal to the concentration of ions at the particle surface at  $\theta = 0$ . This should lead to charging rates that are too large since the concentration of ions at the particle surface will be largest at  $\theta = 0$ . Some type of averaging of the ion concentration over the entire particle surface is needed.
3. The theory agrees well with Hewitt's experimental data for small particles but the agreement appears to worsen as the particle size is increased. Since the largest particle size given in Hewitt's data is  $0.46 \mu\text{m}$ , the theory is untested for particle sizes of one micron and larger.

G. Z. Mirzabekyan (1969)<sup>2</sup>

## Discussion--

Existing theories concerned with particle charging by unipolar ions are discussed and commented upon. The charging process is discussed in light of two possible charging mechanisms, field charging and diffusion charging. The relative effects of the two mechanisms are classified according to the following ranges of particle size:

1. For particles of radius  $\rho > 2-3 \mu\text{m}$ , field charging predominates and the effects of ion diffusion may be neglected.
2. For particles of radius  $0.8 \mu\text{m} \leq \rho < 2 \mu\text{m}$ , field charging and diffusion charging are both important and should be considered simultaneously.

3. For particles of radius  $\rho < 0.08-0.1 \mu\text{m}$ , diffusion charging is the dominant effect and the contribution due to field charging may be disregarded.

A new theory which includes both charging mechanisms is developed based on the general diffusion equation. The results are compared with the best experimental data available and the differences do not exceed 3-8 percent.

#### Basic Equations--

The mechanism of field charging, which is valid for particles of radius  $\rho > 2-3 \mu\text{m}$ , was described by Pauthenier and Moreau-Hanot. The particle charge as a function of time was given by these authors as

$$Q = 4\pi\epsilon_0 (1 + 2\frac{\epsilon-1}{\epsilon+2}) E_0 \rho^2 \frac{\pi\mu en_0 t}{4\pi\epsilon_0 + \pi\mu en_0 t} , \quad (114)$$

where  $Q$  = particle charge,

$\epsilon_0$  = permittivity of free space,

$\epsilon$  = relative dielectric constant of the particle,

$E_0$  = external field strength,

$\rho$  = particle radius,

$\mu$  = ionic mobility,

$e$  = ionic charge,

$n_0$  = undisturbed ion concentration, and

$t$  = time.

The diffusion process, which predominates for particles of radius  $\rho < 0.08-0.1 \mu\text{m}$ , was investigated by several authors, using different methods. Deutsch and Koptsov employed general energetic relationships to describe the process and it is pointed out that this approach produces some error, since the energy of the ions does not remain unchanged after its collisions with air molecules. Fuchs and Arendt, Kallman considered the diffusion of the ions in the electric field of the particle and it is pointed out that this approach is better justified physically. The ion current to the particle was found by solving the diffusion equation in the form

$$4\pi R^2 \left[ D \frac{dn}{dR} - n\mu E_R \right] = \Phi = \text{constant}, \quad (115)$$



where  $R$  = distance from the center of the particle to the point in space under consideration,

$D$  = diffusion coefficient,

$n$  = ion concentration,

$E_R$  = magnitude of the electric field of the particle, which consists of the coulomb repulsion field of the ion and the polarization field of the particle in the field of the ion impinging on it, and

$\Phi$  = ion current to the particle.

The first term on the left-hand side of equation (89) gives the component of the current  $\Phi$  due to the nonuniform distribution of ions around the particle; the second term represents the movement of the ions under the influence of the electric field  $E_R$ .

In order to solve equation (115), it is necessary to impose two boundary conditions. The first condition was

$$\lim_{R \rightarrow \infty} n = n_0 \quad . \quad (116)$$

The second boundary condition employed by Fuchs was

$$\lim_{R \rightarrow \rho} n = 0 \quad . \quad (117)$$

The solution to equation (115), with boundary conditions, (116) and (117) was given by

$$\Phi = \frac{dN}{dt} = 4\pi\rho^2 D \left. \frac{dn}{dR} \right|_{R=\rho} = n_0 \frac{4\pi D}{\int_{\rho}^{\infty} \frac{e^{e\phi/kT}}{R^2} dR} \quad , \quad (118)$$

where  $\phi$  = potential due to the electric field of the particle,

$N$  = number of ions impinging on the particle,

$k$  = Boltzmann's constant, and

$T$  = absolute temperature.

The second boundary condition employed by Arendt gave the ion current at the particle surface as

$$\phi = 4\pi\rho^2 \frac{\langle c \rangle}{4} n_R = \rho + \lambda , \quad (119)$$

where  $\langle c \rangle$  = mean thermal velocity of the ions, and

$\lambda$  = mean free path of the ions.

The solution to (115), with boundary conditions (116) and (119), was given by

$$\phi = \frac{dN}{dt} = 4\pi\rho^2 \frac{\langle c \rangle}{4} n_0 e^{-(\phi\rho + \lambda e)/kT} \times \frac{1}{1 + \frac{\langle c \rangle}{4} \frac{\rho^2}{D} e^{-(\phi\rho + \lambda e)/kT} \int_{\rho+\lambda}^{\infty} \frac{e^{e\phi/kT}}{R^2} dR. \quad (120)$$

The charging curves given by equations (118) and (120) agree well with each other. The agreement is due to the fact that boundary conditions (117) and (119) are approximately equivalent. Equation (118) can be written in final form, neglecting the polarization field, as

$$\frac{\epsilon_0}{eK} \left[ E_i(A) - \ln(A) - 0.5772 \right] = n_0 t , \quad (121)$$

where  $E_i$  is an integral exponential function and

$$A(n_0 t) = \frac{Qe}{4\pi\epsilon_0 \rho kT} . \quad (122)$$

The graph of the function  $A$  can be constructed and then the particle charge can be determined from the relationship

$$Q = 4\pi\epsilon_0 \rho \frac{kT}{e} A(n_0 t) . \quad (123)$$

From equation (123), it is seen that in purely diffusional charging, the particle charge is proportional to the particle radius.

In the transition region where particle radii lie in the range  $0.8 \mu\text{m} < \rho < 2 \mu\text{m}$ , it is necessary to consider simultaneously diffusional and field charging. Kapotev, Murphy, and Cochet proposed models to account for both mechanisms. These models are discussed and their weaknesses are pointed out. It is concluded that a rigorous solution of the problem can be achieved

only by a solution of the of the general diffusion equation in which account is taken of both field and diffusional charging.

A differential equation is developed based on both charging mechanisms. The following assumptions are made in the derivation:

1. The charging process is considered to be quasi-stationary;
2. The effect of the space charge due to the ions on the resultant field near the particle is neglected.

The condition of continuity of the ion current vector  $\vec{v}$  is given by

$$\vec{v} = n\mu\vec{E} - D\nabla n . \quad (124)$$

The first term on the right-hand side of equation (124) is the component of the current produced by movement of ions under the influence of the electric field  $\vec{E}$ , the sum of the external field  $\vec{E}_0$ , the polarization field of the particle in the field  $\vec{E}_0$ , and the coulomb field of the particle; the second term is the component of the current produced by diffusion of the ions under the influence of the concentration of the ions.

Under assumption (1),

$$\nabla \vec{v} = 0 \quad (125)$$

and from the assumption (2),

$$\nabla \vec{E} = 0 . \quad (126)$$

Substituting equation (124) into equation (125 and using (126) gives

$$\nabla n + \frac{\mu}{D} \nabla \phi \cdot \nabla n = 0 . \quad (127)$$

The electric potential  $\phi$  in equation (127) is given by

$$\phi = \frac{Q}{4\pi\epsilon_0 R} + E_0 R \left(1 - \frac{\epsilon-1}{\epsilon+2} \frac{\rho^3}{R^3}\right) \cos\theta. \quad (128)$$

A solution to equation (127) was sought with the boundary conditions

$$\left. \begin{array}{l} \lim_{R \rightarrow \infty} n = n_0 \\ \lim_{R \rightarrow \rho} n = 0 \end{array} \right\} \quad (129)$$

Initially, analytical solutions were investigated but a solution of this type could not be found. Next, numerical solutions were examined. Using the method of finite differences, it was found that a very large number of increments were necessary in order to obtain a system of algebraic differential equations that were solvable.

In order to facilitate the numerical solution of equation (127) on a computer, a change of variable was made by letting

$$U = (n_0 - n)e^{-\mu/2D}(\phi) \quad (130)$$

Using relation (130), equation (127) can be written in terms of the variable U as

$$\nabla U - \frac{1}{4} \left( \frac{\mu}{D} \right)^2 (\nabla \phi)^2 U = 0 \quad (131)$$

The boundary conditions that U must satisfy are

$$\left. \begin{array}{l} \lim_{R \rightarrow \rho} U = n_0 e^{-\mu/2D} \\ \lim_{R \rightarrow \infty} U = 0 \\ \lim_{R \rightarrow \rho} \phi \end{array} \right\} \quad (132)$$

Using spherical coordinates and introducing the variable  $X = \cos \theta$  in equation (131) leads to the equation

$$\frac{\partial}{\partial R} \left\{ R^2 \frac{\partial U}{\partial R} \right\} + \frac{\partial}{\partial X} \left[ (1-X^2) \frac{\partial U}{\partial X} \right] - \left( \frac{1}{2} \frac{\mu}{D} \nabla \phi \right)^2 R^2 U = 0 \quad (133)$$

Equation (133) is solvable, hence the ion current to the particle is determined by

$$\Phi = D \int_{S \text{ particle}} \frac{dn}{dR} \Big|_{R=\rho} dS \quad (134)$$

## Conclusions--

The charging curves obtained using this theory showed the following agreement with existing theories and experimental data:

1. For  $\rho > 1-6 \mu\text{m}$ , the curves practically coincided with those obtained by using Pauthenier's theory.
2. The curves were in agreement with Hewitt's experimental data to within 3-8% and this agreement was over a wide range of particle sizes and electric field strengths.
3. Charging curves were calculated for a wide range of values of  $E_0$  (100-500 kV/m) and  $\rho$  (0.2-2  $\mu\text{m}$ ) and compared with the results obtained by taking the sum of the charge calculated by Pauthenier's field charging (equation (114) and that calculated by Fuch's diffusion charging (equation (123)). The comparison showed that the difference in the curves did not exceed 20%.

The following conclusions were made:

1. The general diffusion equation describes the particle charging process over a wide range of values of  $\rho$  and  $E_0$ .
2. The magnitude of the charge on the particle may be approximately determined as the sum of the charges calculated by the theories of field and diffusion charging.

## Comments and Remarks--

The authors approach of combining field and diffusional charging mechanisms into their formalism is physically sound. Murphy et al, and Liu and Yeh both suggest this approach. Although agreement with Hewitt's data to within 3 to 8 percent is claimed, those results are not shown here. A quantitative evaluation of the theory can only proceed by solving equation (133) for a variety of particle sizes and electric fields. Since, as Mirzabekyan points out, solutions of this equation involve a complicated numerical procedure and unusually long computer running times, his formalism does not seem practical for our purposes.

Arendt and Kallmann (1926)<sup>18</sup>

## Discussion--

The mechanism of diffusional charging of aerosol particles was studied theoretically and experimentally. The particles

ranged in size from 0.5  $\mu\text{m}$  to 2.2  $\mu\text{m}$  diameter. Theoretically, the desired result is to calculate the charge taken up by a particle in a given time and the dependence of this charge on particle radius and ion density in air. To do this, the classical diffusion equation is solved with the assumption of no external field and large initial charge on the particle. Boundary conditions are constructed so that simple forms are obtained for the potential energy  $\phi$  and boundary surface current  $i_0$ . Due to the initial basic assumptions, the charging equation obtained is only valid for large times. The theory is compared with charging measurements made on a Millikan Oil-Drop Apparatus modified to produce large numbers of ions. Individual particles were observed for hours at a time and their accumulated charge was recorded to obtain the charging curves. At high ion densities, spontaneous discharges occurred from the particles, but these discharges did not grossly affect the shape of the charge curve or the limit charge.

#### Basic Equations--

When an uncharged particle of radius  $a$ , is brought into an ionized space, ions will impinge on the particle surface due to thermal motion and the particle will acquire an electric charge. As the charge increases, the ionic current must decrease due to coulomb repulsion and eventually a limit charge is reached. In a calculation to determine an expression for this current, one must account for the separate effects of an external electric field, image forces, ionic diffusion and coulomb repulsion. If the density distribution of ions in the vicinity of the ion can be determined with these effects accounted for, then the charging rate can be determined.

The change in ion density  $f$ , with time is controlled by the general diffusion equation

$$\frac{\partial f}{\partial t} = \nabla \cdot (\mu f \nabla \phi + D \nabla f) \quad (135)$$

where  $\mu$  = ionic mobility,

$D$  = diffusion constant, and

$\phi$  = electric potential energy.

A solution of (135) requires specification of a uniformly constant ion current at  $t=0$ ,  $f$ , at the particle surface,  $f_a$ , and at infinity,  $f_\infty$ .

The following simplifications are introduced:

1. The effect of any external field is neglected.

2. At a distance on the order of a mean free path,  $\lambda$ , from the surface of the particle, the simple diffusion equation fails. Therefore, the assumption is made that for  $a + \lambda \leq r < \infty$  the ion current  $i$  through a surface element  $ds$  given from diffusion theory by

$$i = (\mu E f - D \frac{\partial f}{\partial z}) ds \quad (136)$$

where  $E$  = electric field strength, and

$z$  = normal to  $ds$ .

For  $a \leq r \leq a + \lambda$ , the ion current is given from kinetic theory by

$$i = x c f ds \quad (137)$$

with

$$c = \frac{1}{4} \sqrt{\frac{3kT}{m}} \quad (138)$$

where  $x$  = fraction of ions retained after striking a unit surface of the particle,

$c$  = a constant which comes from kinetic theory and is proportional to the number of ions striking a unit surface of the particle per unit time, here with no field effects considered,

$k$  = Boltzmann's constant,

$T$  = Kelvin temperature of the ions, and

$m$  = mass of the ions.

3. Consider only the case in which the ion current to the particle has decreased so that  $\partial f / \partial t \approx 0$ . Thus, we obtain a "stationary" diffusion equation

$$\nabla \cdot (\mu f \nabla \phi + D \nabla f) = 0 \quad (139)$$

with a boundary condition given by integrating (136) and (137) over a surface area enclosing the particle to obtain the total current to the particle  $i_0$ .

$$i_0 = \int \left[ \mu E_{a+\lambda} f_{a+\lambda}^{-D} \left( \frac{\partial f}{\partial z} \right)_{a+\lambda} \right] ds = \int x c f_a ds \quad (140)$$

where the subscript indicates where the variable is to be evaluated. It is assumed that negligible error is introduced by evaluating the right hand side of (140) at  $a$  instead of  $a+\lambda$ .

Equation (139) is rewritten as

$$D \nabla^2 f + \mu \nabla f \cdot \nabla \phi = 0 \quad (141)$$

where the effect of the ions in the calculation of  $\phi$  is neglected; therefore,  $\nabla^2 \phi = 0$ . Approximating the spherical surface by an infinite plane gives the image contribution to the electrical potential energy of the particle of charge  $ne$ ,

$$\phi = \frac{ne}{r} - \frac{e}{(r-a)} \frac{\epsilon-1}{\epsilon+1} \quad (142)$$

where  $\epsilon$  = dielectric constant of the particle.

Equation (139) is now solved to obtain an expression for  $f$ . This solution contains two arbitrary constants. One is determined from the known ion density at infinity,  $f_\infty$ . The other is expressed with the help of the first part of (140).  $f$  is thus obtained as a function of  $i_0$ . This expression for  $f$  is introduced into the right side of (140) from which  $i_0$  is calculated as a function of  $n$ , the number of ions captured by the particle  $f_\infty$ , and  $a$ . The result is

$$f = C e^{-\phi e/kT} + e^{-\phi e/kT} \int \frac{i_0 e^{\phi e/kT}}{4\pi r^2 \mu kT} dr \quad (143)$$

The calculation of  $i_0$ , the current flowing to the particle follows from (140).

$$i_0 = e \frac{dn}{dt} = 4\pi a x c f_a \quad (144)$$

where



$$f_a = C e^{-\phi_a e/kT} + e^{-\phi_a e/kT} \left\{ \int \frac{e i_0 e^{\phi e/kT}}{4\pi r^2 \mu kT} dr \right\}_a \quad (145)$$

Substituting (142) in (144) and (145) gives an expression which can be integrated with respect to time to obtain the relationship between current and particle charge. When this is done, the effect of the image force is seen to be important only if it is appreciable at a distance of one mean free path,  $\lambda$ , away from the particle. Separate calculations show that the image force is large at  $\lambda/2$ , but small compared to coulomb repulsion at  $\lambda$ ; therefore, all image effects are disregarded. Expressing C through the constant ion density at infinity  $f_\infty$ , one obtains

$$e \frac{dn}{dt} \left( 1 + \frac{xc4\pi a^2}{4\pi n \mu e} \right) = 4\pi a^2 x c f_\infty e^{-ne^2/akT}, \quad (146)$$

which is valid only for n initially larger (at  $t=0$ ).

Equation (146) exhibits the following behavior:

- a. With increasing particle charge, the charging rate decreases rapidly.
- b. The limit charge increases almost linearly with particle radius.
- c. The limit charge grows very slowly with increasing ion density. The limit charge doubles if the ion density increases by one hundred fold.

## Experiments, Results and Conclusions--

The aerosol particles of paraffin oil were studied in a modified Millikan Oil-Drop Apparatus. Aluminum foil coated with varying amounts of Polonium was used to produce ions which were brought into the charging region by the action of an applied electric field. The number of ions per cubic centimeter varied from 515 to 67,000. In the charging region, a separate electric field was used to manipulate the particle under observation and keep it located at roughly the same place for all observations. The growth of charge with time was measured for more than 300 drop-

lets with sizes ranging from 0.5  $\mu\text{m}$  to 2.2  $\mu\text{m}$ . The charging rate was obtained from the slope of the charging curve.

Occasional discharges were obtained at high ion densities. Investigation shows that this is a transient phenomena with no lasting effect on either the limit charge or the charging rate. When a discharge occurs, only several elementary charges are lost and these are replaced rapidly.

The following experimental results are noted:

- a. The limit charge does not noticeably depend on charge polarity.
- b. The limit charge increases almost linearly with particle radius in good agreement with equation (146). This measurement was somewhat difficult because of changing fields and ionization rates, but the overall behavior was clear.
- c. The dependence of limit charge on ion density was again in agreement with equation (146).
- d. Experimental and theoretical agreement on ion density versus particle radius and total charge allow estimation of the fraction of particles adhering after collision,  $x$ . Within experimental uncertainty all the ions adhere.

It is therefore concluded that the theory developed above is sufficient to describe the charging of small particles with time, as well as their limit charge.

The close agreement of theory and experiment indicate that a diffusion-like charging mechanism is probable for particles in the size range investigated.

#### Comments and Remarks--

In order to solve the diffusion equation, a number of simplifying assumptions were made. The net effect of these assumptions is to limit the applicability of the results to diffusional or thermal charging; i.e., charging in the absence of an applied field.

The experiments are described in detail and the discontinuous nature of the diffusional charging process is clearly demonstrated. The agreement between theory and experiment is good enough to verify the validity of the "classical" diffusional charging equation. Although a broad range of ion densities was

used in the experiments, the values were far lower than ordinarily encountered in conventional electrostatic precipitators.

Robert Cochet (1961)<sup>24</sup>

#### Discussion--

A correction is made to the classical law of field charging, due to Pauthenier and Moreau-Hanot.<sup>3</sup> The nature of this correction is to extend field charging equations to particles of submicron size. To test the corrected theory, small shellac particles with radii from 0.02  $\mu\text{m}$  to 0.5  $\mu\text{m}$  were precipitated in a planar precipitator. The relationship of particle size to precipitation rate was measured and was found to be adequately described by the corrected theory.

#### Basic Equations--

It is assumed that an exact solution to the problem of charging micron and submicron sized particles which takes into account both field and diffusional effects is impossible to obtain, and that despite thermal motion of the ions, it is almost always the ion flow due to the electric field which controls the charging mechanism for electrostatic precipitator applications. Therefore, the author's approach to this problem is to introduce a correction to the classical field charging theory as developed by Pauthenier and others. This correction combines both the charging due to thermal agitation of the ions and the electric field into a single generalized law of charging.

From classical field charging theory, the number  $n$  of charges captured in a time  $t$  by a spherical particle of radius  $a$  in an electric field of strength  $E_0$  is

$$n = \frac{pE_0a^2}{e} \frac{t}{t+\theta} \quad (147)$$

with

$$p = 1 + 2 \frac{(\epsilon - \epsilon')}{\epsilon + 2\epsilon'} \quad (148)$$

and

$$\theta = \frac{1}{\pi\mu N_0 e} \quad (149)$$

where  $\epsilon$  and  $\epsilon'$  are the dielectric constants of the particle and the surrounding medium respectively,  $\mu$  is the ionic mobility, and  $N_0 e$  is the charge density.

These formulas are valid in air at STP for  $a > 1 \mu\text{m}$ . When  $a < 1 \mu\text{m}$ , the capture of ions by the particle is enhanced by the image force and thermal diffusion. Previous authors have usually accounted for one effect or another but not both.

The ions are imagined to be entrained in a cylindrical volume so that all ions which pass within one ionic mean free path,  $\lambda_i$  of the particle are captured. This is a reasonable assumption because the image force is not small in this region.

The region in which ions may be captured is defined by the condition that at the boundary  $\rho = a + \lambda_i$ , the radial component of the electric field is zero.

The ion flow is thus:

$$\frac{dn}{dt} = N_0 \mu \pi \frac{(\alpha E_0 a^2 - ne)^2}{\alpha E_0 a^2} \quad (150)$$

where

$$\alpha = \left(1 + \frac{\lambda_i}{a}\right)^2 + \frac{2}{1 + \lambda_i/a} \frac{\epsilon - \epsilon'}{\epsilon + 2\epsilon'} \quad (151)$$

If  $E_0$ ,  $N_0$ , and  $\mu$  are constant along the particle trajectory, then integration of (150) yields  $n$  as a function of time:

$$n = \frac{\alpha E_0 a^2}{e} \frac{t}{t + \theta} \quad (152)$$

giving a limit charge

$$Q_0 = \alpha E_0 a^2 \quad (153)$$

when  $\lambda_i/a$  is small,  $\alpha$  approaches  $p$  and the classical field charging analogs of equations (152) and (153) are regained.

If the charge on a particle is known, then the precipitation rate  $\omega$  of the particle in an electric field  $E$  can be calculated by the use of Stokes' Law as corrected by Millikan.<sup>25</sup>

$$\omega = \left[ \left(1 + \frac{\lambda_g}{a}\right)^2 + \frac{2}{(1 + \lambda_g/a)} \left(\frac{\epsilon - \epsilon'}{\epsilon + 2\epsilon'}\right) \right] \left(1 + A' \frac{\lambda_g}{a}\right) \frac{E_0 E a}{6\pi\eta} \quad (154)$$

where  $A'$  = Millikan correction coefficient,

$\lambda_g$  = mean free path of the surrounding gas molecules, and

$\eta$  = the absolute viscosity of the surrounding medium.

Curves of  $\omega$  versus  $a$  exhibit minima such as that found by Pauthenier.

#### Experimental Results and Conclusions--

An aerosol made of shellac particles was entrained in an electric field  $E_0$ , and exposed to positive ions for varying lengths of time. After charging, the particles were passed through a parallel plate capacitor where the field  $E_0$  was maintained. The capacitor thus acted as a precipitator for these particles. An experimental study was made using an electron microscope to study the particles' size as a function of the position where they were precipitated on the capacitor/precipitator plate.

As Pauthenier had seen earlier, the size spectrum of precipitated particles is not single valued. At the beginning of the deposit, one finds both large ( $a=0.5 \mu\text{m}$ ) and small ( $a=0.05 \mu\text{m}$ ) particles and at the end, only very small ( $a=0.01 \mu\text{m}$ ) particles.

In addition to parallel plate capacitors, cylindrical capacitors were also used for precipitating the shellac aerosol. Essentially the same particle size spectrum was observed here as was seen above. The principal difference was that initially particles of all sizes were observed. At the end, only spheres with  $a \approx 0.01 \mu\text{m}$  were seen. In the cylindrical capacitor, the ionization current from the axial electrode produces flow turbulence in the aerosol. Thus, one might expect some mixing of particle sizes with this device.

It is observed that in equation (154), taking  $\lambda_i = \lambda_g$  does not give a high enough precipitation rate. However, by taking  $\lambda_i = \sqrt{2} \lambda_g$ , good agreement is found between theory and experiment. The author therefore concludes that the correction to the classical theory made here is sufficient to extend the theory to submicron sized particle charging.

#### Comments and Remarks--

This paper is a combination of two earlier papers,<sup>26,27</sup> by the same author. The idea of extending the particle radius by one mean free path in the field charging equation was first suggested here, and does lead to better agreement with experiment.

The experiments confirm the existence of a minimum in the mobility of charged particles according to size as previously observed by Pauthenier. For satisfactory agreement between theory and experiment, the ionic mean free path is treated as an adjustable parameter. No justification is given for the value finally used; i.e.,  $\lambda_i = \sqrt{2} \lambda_g$ .

## APPENDIX B

### LITERATURE REVIEW - PARTICLE CHARGING DATA

The literature was reviewed for information pertinent to experimental charging studies. Four papers<sup>8,27,17,21</sup> contain experimental results and/or techniques which were of use in validating our experimental results. Table 7 summarizes the available experimental data.

Cochet<sup>27</sup> presents curves for the speed of precipitation versus particle radius. Using the relationship between electrical mobility and the speed of precipitation, it is possible to obtain the electrical mobility as a function of particle size. This was done and the results are plotted in Figure 86. Cochet used a shellac aerosol having a dielectric constant of 3.2 (as measured by Pauthenier.<sup>4</sup>)

Fuchs et al<sup>17</sup> determined the charge on mineral oil droplets as a function of their size for a given  $Nt$  and electric field strength. Figures 87, 88, and 89 give his results. There is a large amount of scatter in these data but the dearth of experimental information with the charging conditions specified makes these figures worth noting. Knudsen<sup>28</sup> has observed that the scatter in some early experimental data may be introduced by the charging device used. This may also be the case here.

Hewitt<sup>8</sup> has performed an exhaustive experimental charging study, and the majority of the experimental information presented in this section has been drawn from his paper. Figures 90 through 98 give the pertinent results. Figure 92 is not a reproduction of any of Hewitt's graphs but is plotted so that some of the results obtained by Hewitt may be compared with other results from Penny and Lynch.<sup>21</sup> Figure 98 does not strictly pertain to aerosol particle charging but gives information on the performance of Hewitt's Mobility Analyzer. Since the SRI Mobility Analyzer is patterned after Hewitt's device, Hewitt's data has been used for characterizing the performance of the SRI Mobility Analyzer.

Penney and Lynch<sup>21</sup> made a charging study which was contemporary with Hewitt. The same type of aerosol was used and there is enough overlap in the data so that some comparisons can be made. Figures 99 through 102 give these authors' results. Note that both positive and negative corona charging has been used. Figures 100 and 101 show the effect of changing the potential on the corona wires while particle size and air flow are held constant. Thus, the particle charge is found for a particular value of  $E$  and  $Nt$ .

TABLE 7. SUMMARY OF THE PUBLISHED EXPERIMENTAL DATA ON PARTICLE CHARGING

Author	Aerosol	K	Corona	d, diameter ( $\mu\text{m}$ )	$\mu$ , mobility ( $\text{m}^2/\text{V sec}$ )	E field (V/m)	Nt ( $\text{Sec}/\text{m}^3$ )	Remarks
Cochet	Shellac	3.2	Positive	Variable	Variable	$5.0 \times 10^5$ $1.5 \times 10^5$	$8.0 \times 10^{11}$ $3.2 \times 10^{12}$	$\mu$ vs. d
Fuchs et al	Mineral Oil	2.56	Negative	Variable	-	$5.56 \times 10^4$ $7.32 \times 10^4$ $9.40 \times 10^4$	$3.27 \times 10^{11}$ $4.64 \times 10^{11}$ $5.10 \times 10^{11}$	charge vs. d
Hewitt	DOP	5.1	Positive	Variable	Variable	$1.08 \times 10^6$ $7.2 \times 10^5$ $3.6 \times 10^5$ $6.0 \times 10^4$	$1.0 \times 10^{13}$	$\mu$ vs. d
Hewitt	DOP	5.1	Positive	1.20 0.84 0.60 0.36 0.28 0.14	Variable	Variable	$1.0 \times 10^{13}$	$\mu$ vs. E
Hewitt	DOP	5.1	Positive	Variable	-	$1.08 \times 10^6$ $3.6 \times 10^5$ $6.0 \times 10^4$	$1.0 \times 10^{13}$	charge vs. d
Hewitt	DOP	5.1	Positive	0.18	-	$1.08 \times 10^6$ $3.6 \times 10^5$ $3.0 \times 10^4$	Variable	charge vs. Nt
Hewitt	DOP	5.1	Positive	0.28	-	$9.0 \times 10^5$ $3.6 \times 10^5$ $3.0 \times 10^4$	Variable	charge vs. Nt
Hewitt	DOP	5.1	Positive	0.28		Variable	$5.0 \times 10^{13}$ $4.0 \times 10^{13}$ $3.0 \times 10^{13}$ $2.0 \times 10^{13}$	charge vs. E
Hewitt	DOP	5.1	Positive	0.56	-	$3.6 \times 10^5$	Variable	charge vs. Nt
Hewitt	DOP	5.1	Positive	0.92	-	$9.0 \times 10^5$ $3.6 \times 10^5$ $6.0 \times 10^4$	Variable	charge vs. Nt
Hewitt	DOP	5.1	Positive	0.28	-	$3.6 \times 10^5$	Variable	Spread in analyzer curve vs. Nt
Penney & Lynch	DOP	5.1	Positive	Variable	-	$2.3 \times 10^5$	$6.4 \times 10^{13}$	charge vs. d
Penney & Lynch	DOP	5.1	Positive	0.30	-	Variable	Variable	charge, Nt vs. d
Penney & Lynch	DOP	5.1	Negative	0.30	-	Variable	Variable	charge, Nt vs. d
Penney & Lynch	DOP	5.1	Negative Positive	0.30	-	$2.7 \times 10^5$	Variable	charge vs. Nt

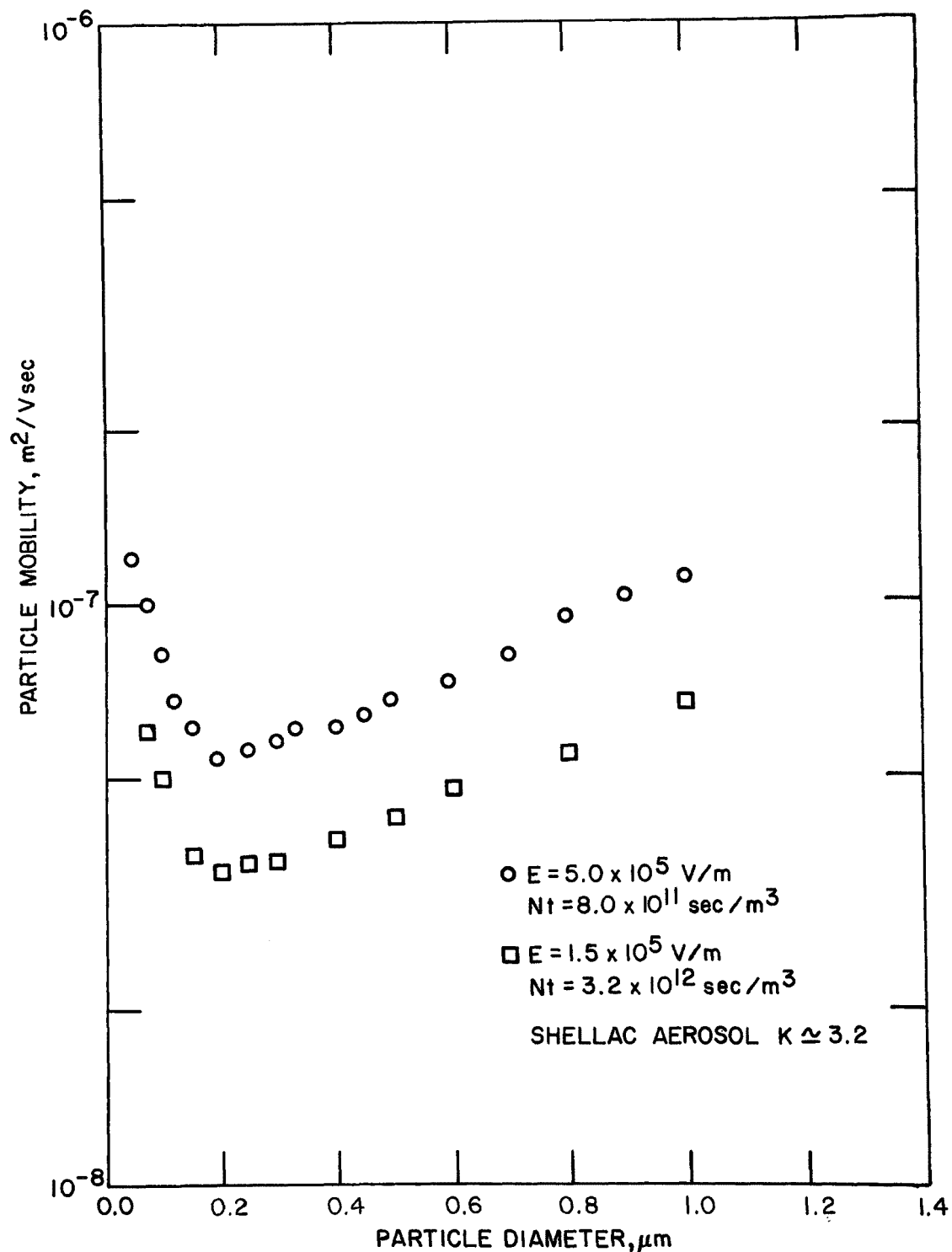


Figure 86. Particle mobility as a function of diameter for shellac aerosol particles charged in a positive ion field (after Cochet and Trillat<sup>18</sup>).  $K$  is the dielectric constant of the aerosol.



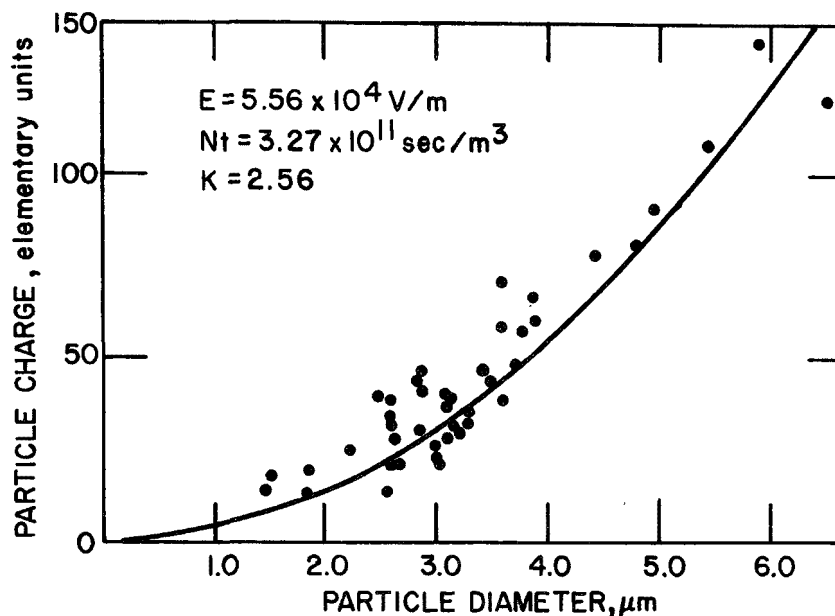


Figure 87. Charge per particle for a mineral oil aerosol charged in a negative ion field (after Fuchs et al<sup>2</sup>).  $Nt = 3.27 \times 10^{11} \text{ sec/m}^3$ .  $K$  is the aerosol dielectric constant.

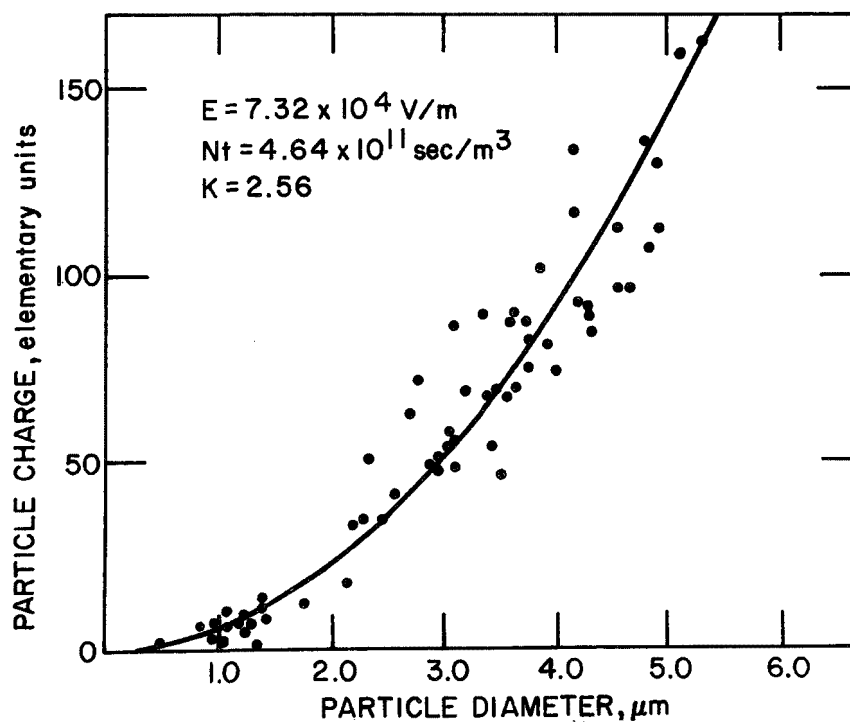


Figure 88. Charge per particle for a mineral oil aerosol charged in a negative ion field (after Fuchs et al<sup>2</sup>).  $Nt = 4.64 \times 10^{11} \text{ sec/m}^3$ .  $K$  is the aerosol dielectric con-

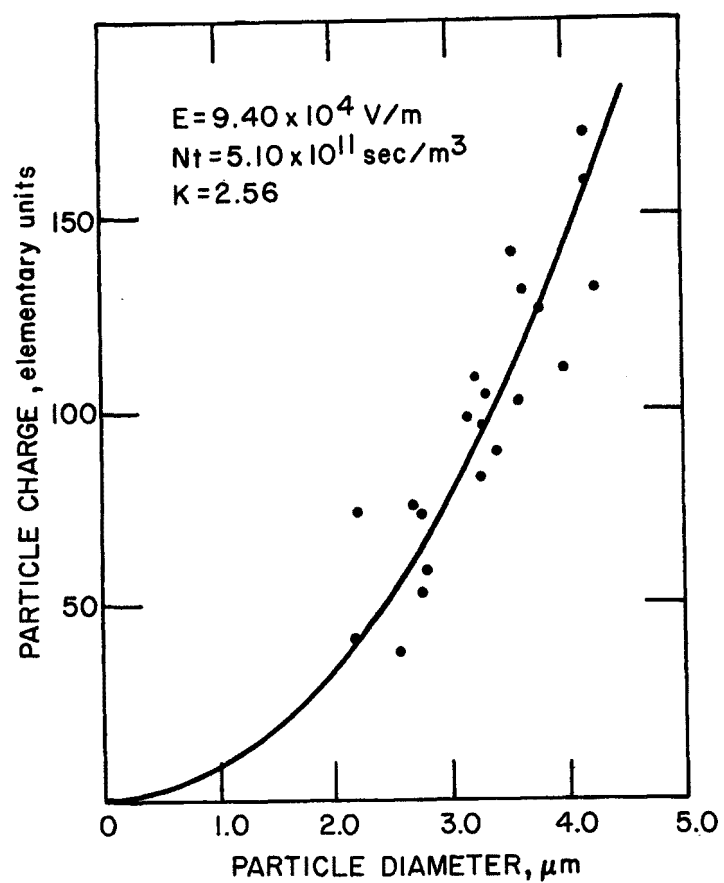


Figure 89. Charge per particle for a mineral oil aerosol charged by negative ions (after Fuchs et al<sup>2</sup>).  $Nt = 5.10 \times 10^{11} \text{ sec/m}^3$ .  $K$  is the aerosol dielectric constant.

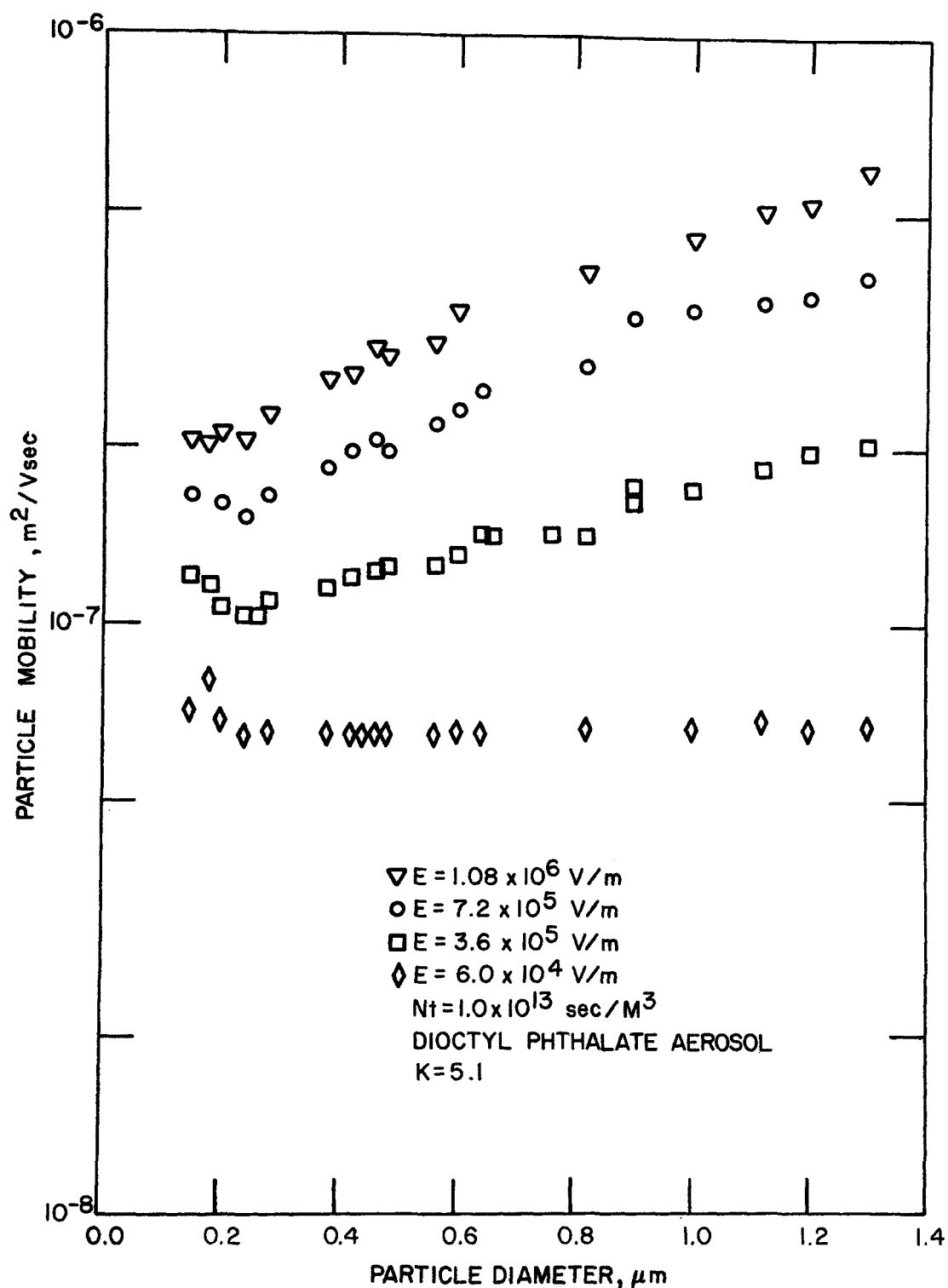


Figure 90. Electrical mobility of dioctyl phthalate droplets as a function of particle diameter (after Hewitt<sup>8</sup>). Positive corona charging.  $K$  is the aerosol dielectric constant.

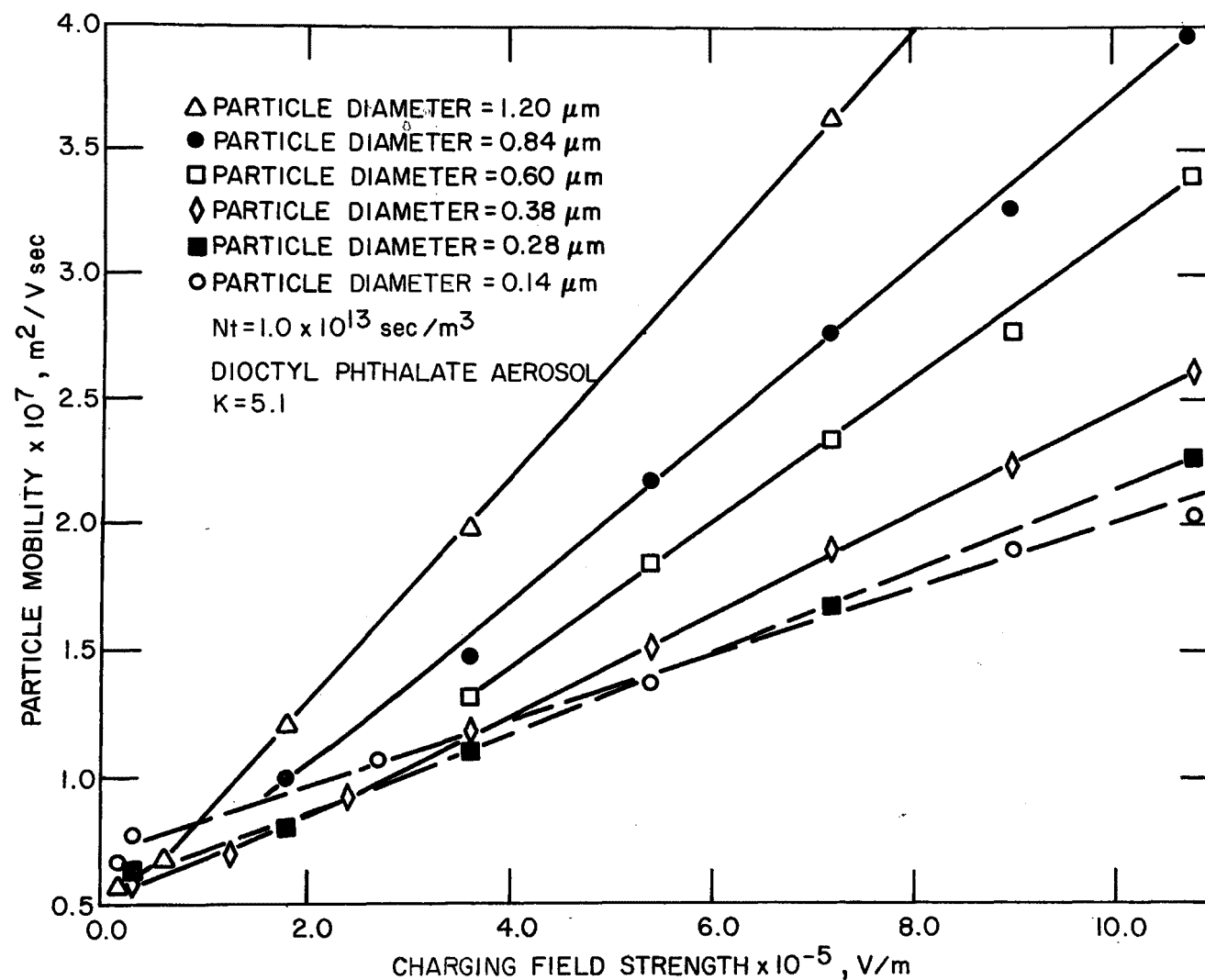


Figure 91. Particle mobility as a function of charging field strength for a dioctyl phthalate aerosol under positive corona charging (after Hewitt<sup>8</sup>).  $K$  is the aerosol dielectric constant.

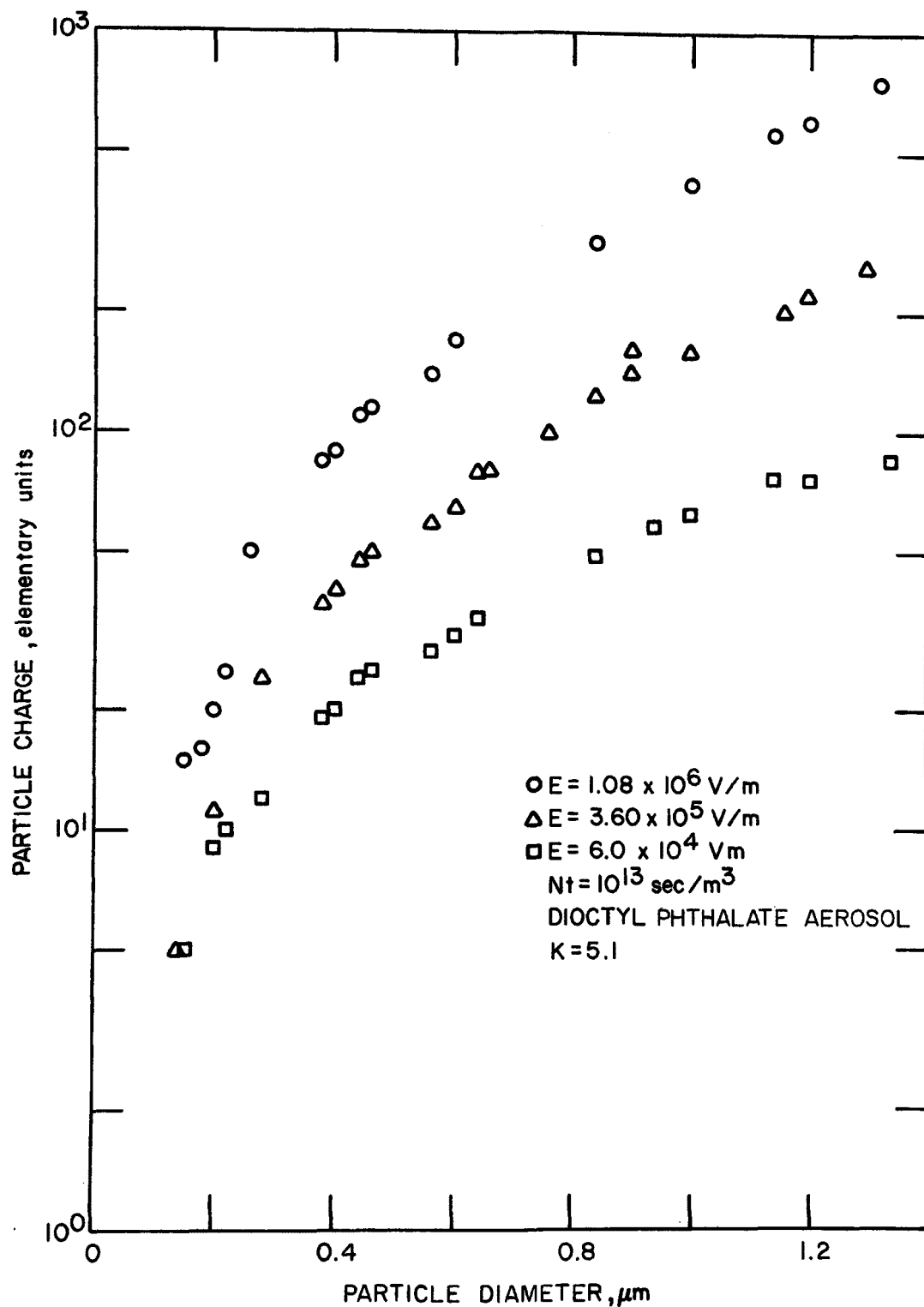


Figure 92. Charge per particle as a function of particle diameter for a dioctyl phthalate aerosol under positive corona charging (after Hewitt<sup>8</sup>).  $K$  is the aerosol dielectric constant.

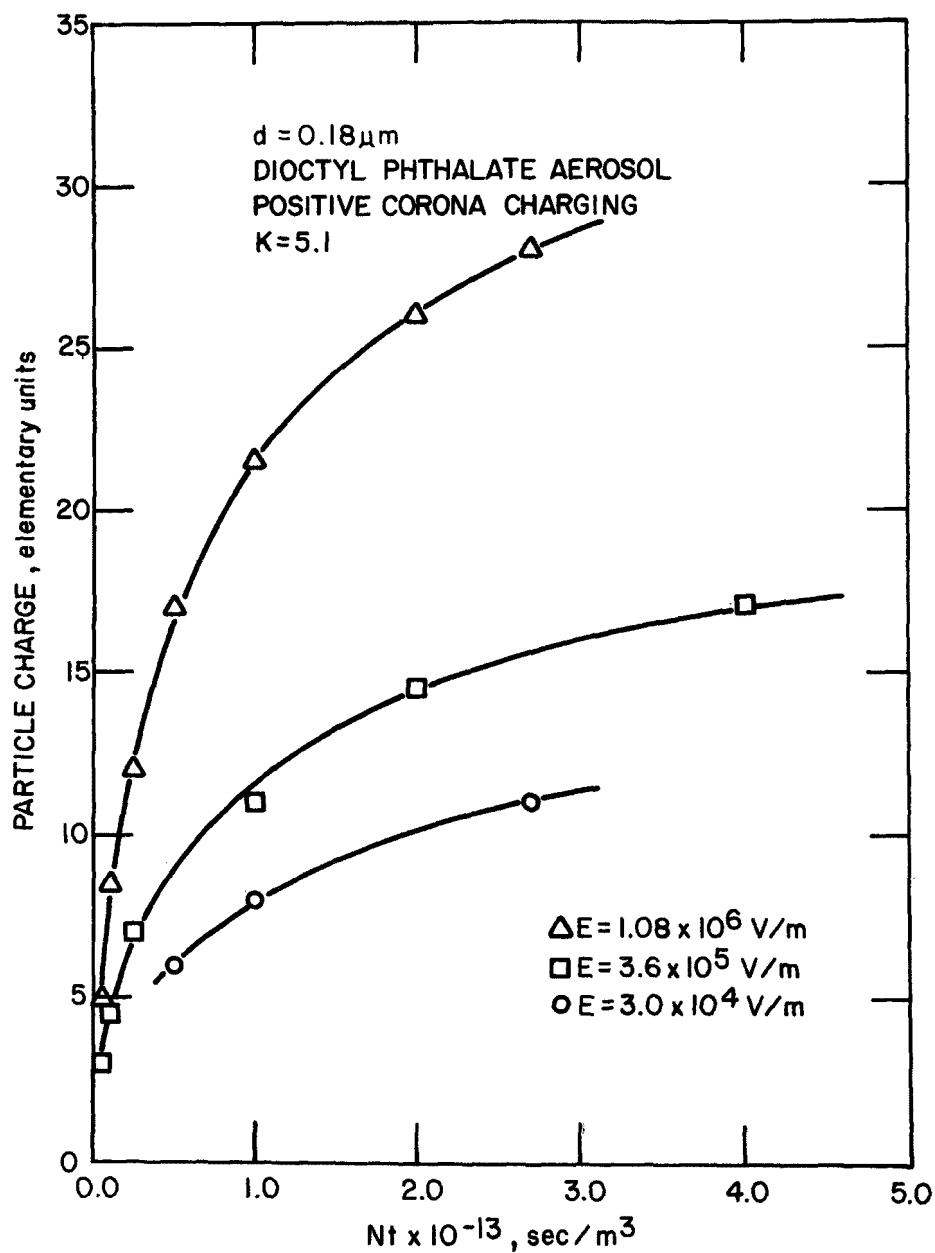


Figure 93. Charge per particle as a function of ion density-residence time product,  $Nt$  in a positive corona (after Hewitt<sup>8</sup>) for  $0.18 \mu\text{m}$  diameter dioctyl phthalate particles.  $K$  is the aerosol dielectric constant.

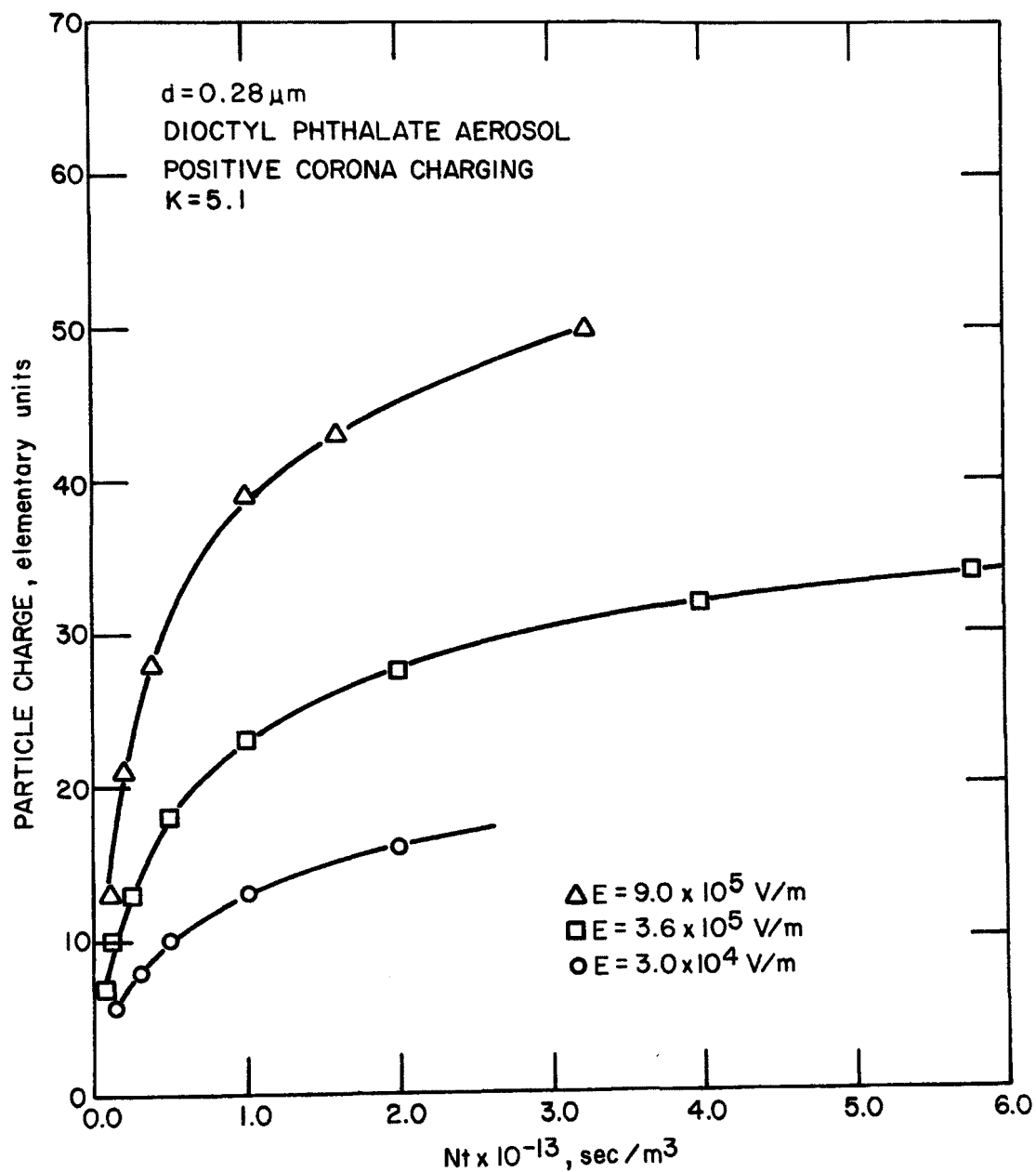


Figure 94. Charge per particle as a function of ion density-residence time product,  $Nt$  in a positive corona for  $0.28 \mu\text{m}$  diameter dioctyl phthalate particles (after Hewitt<sup>8</sup>).  $K$  is the aerosol dielectric constant.

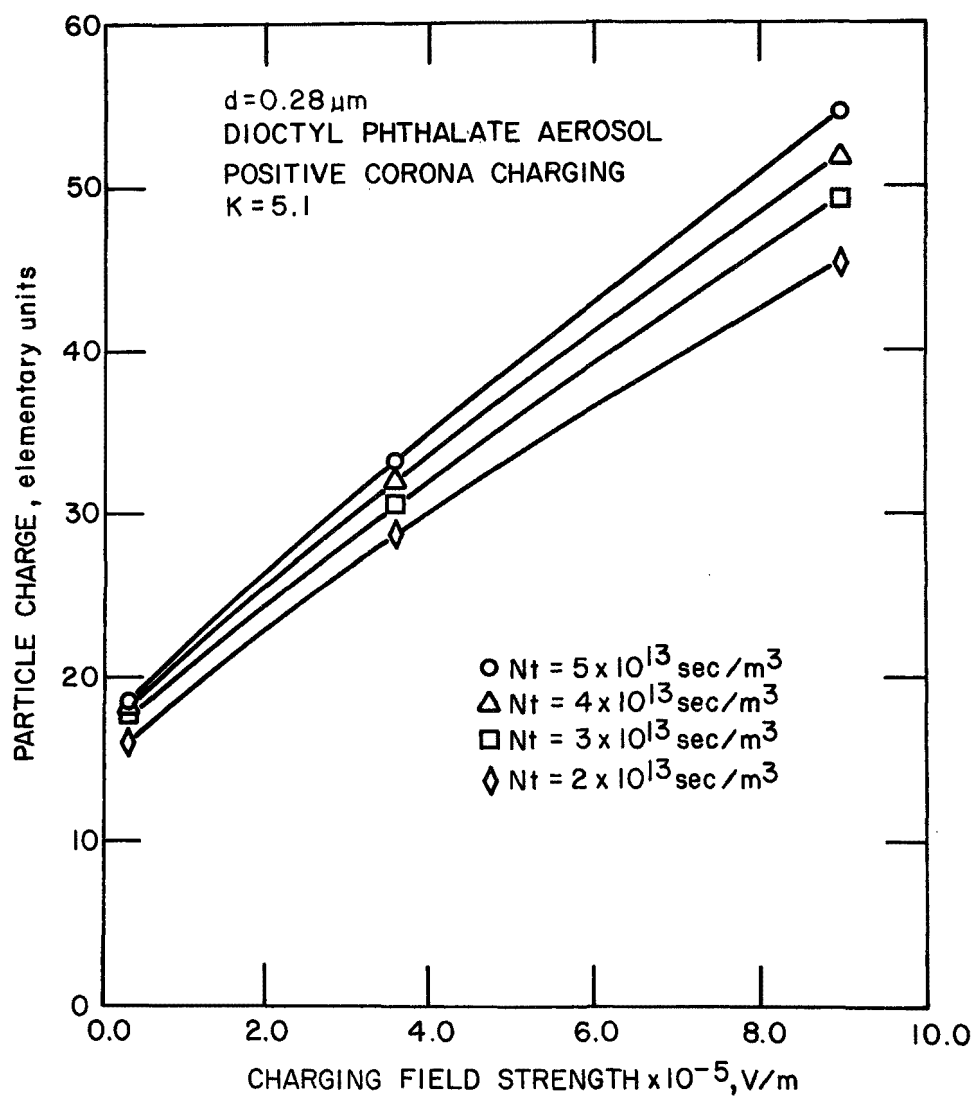


Figure 95. Particle charge as a function of charging field strength for  $0.28 \mu\text{m}$  diameter dioctyl phthalate particles (after Hewitt<sup>8</sup>).  $K$  is the aerosol dielectric constant.



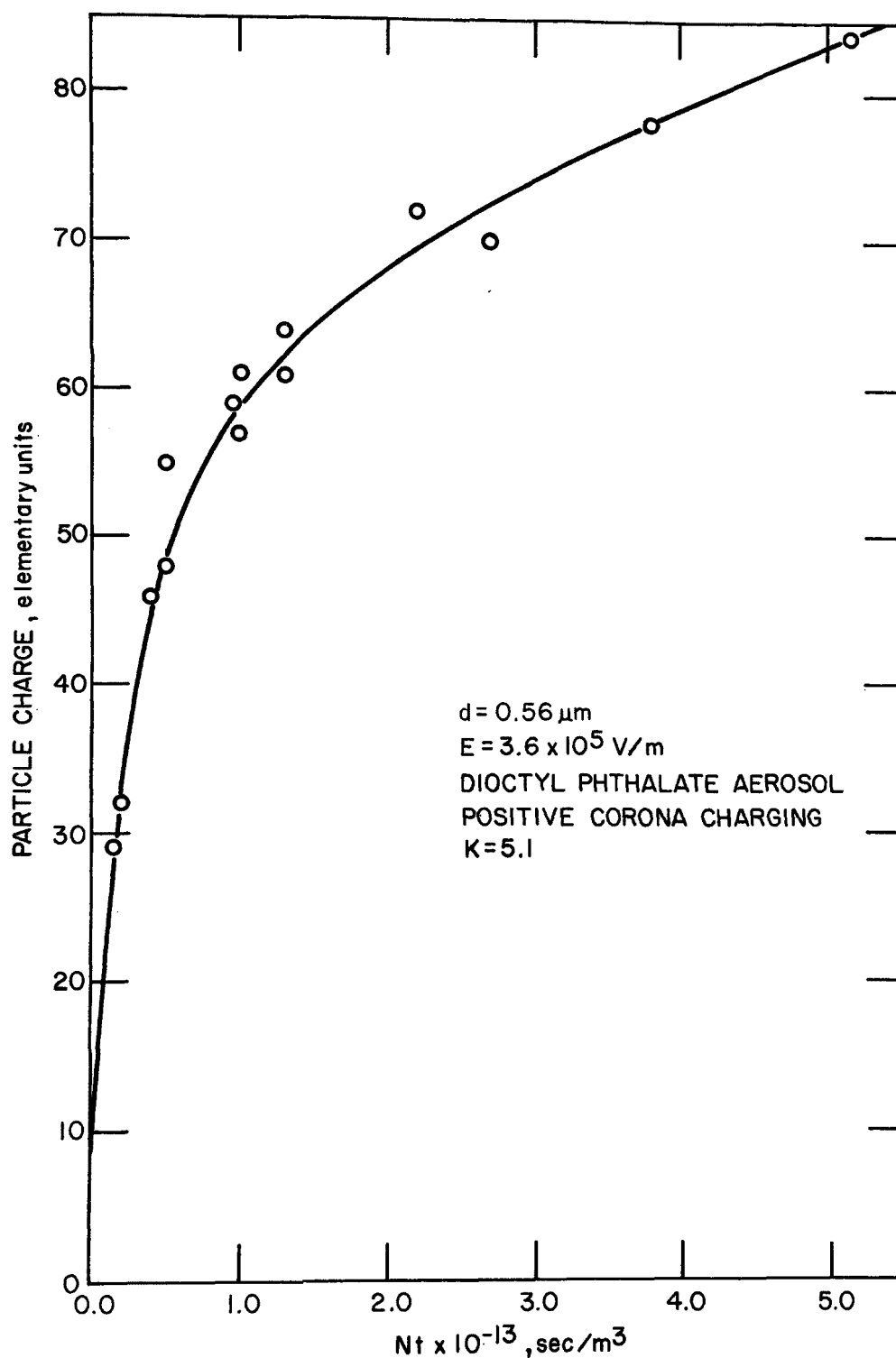


Figure 96. Particle charge as a function of ion density-residence time product for  $0.56 \mu\text{m}$  diameter dioctyl phthalate particles (after Hewitt<sup>8</sup>).  $K$  is the aerosol dielectric constant.

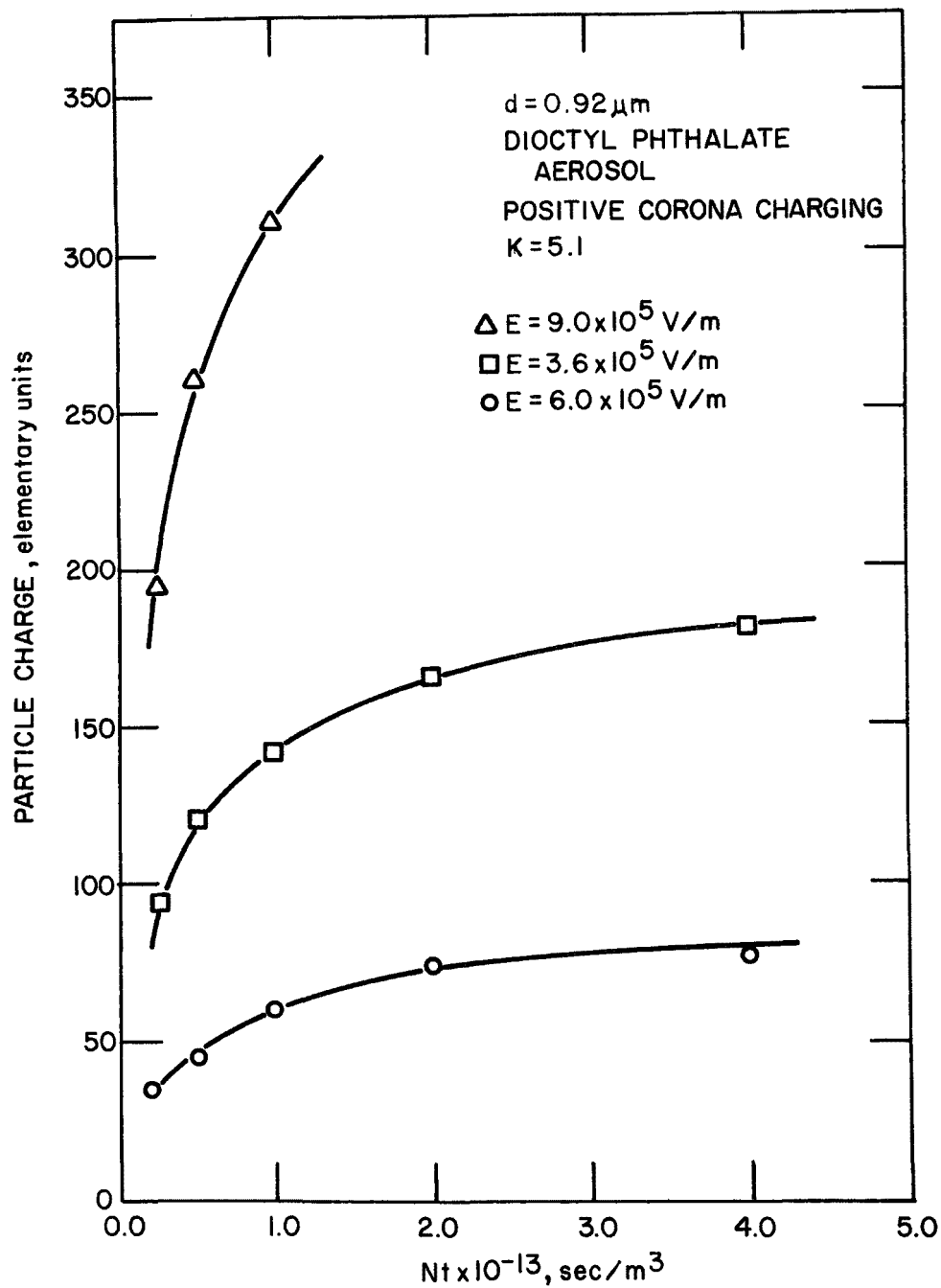


Figure 97. Particle charge as a function of ion density-residence time product for  $0.92 \mu\text{m}$  diameter dioctyl phthalate aerosol particles (after Hewitt<sup>8</sup>).  $K$  is the aerosol dielectric constant.

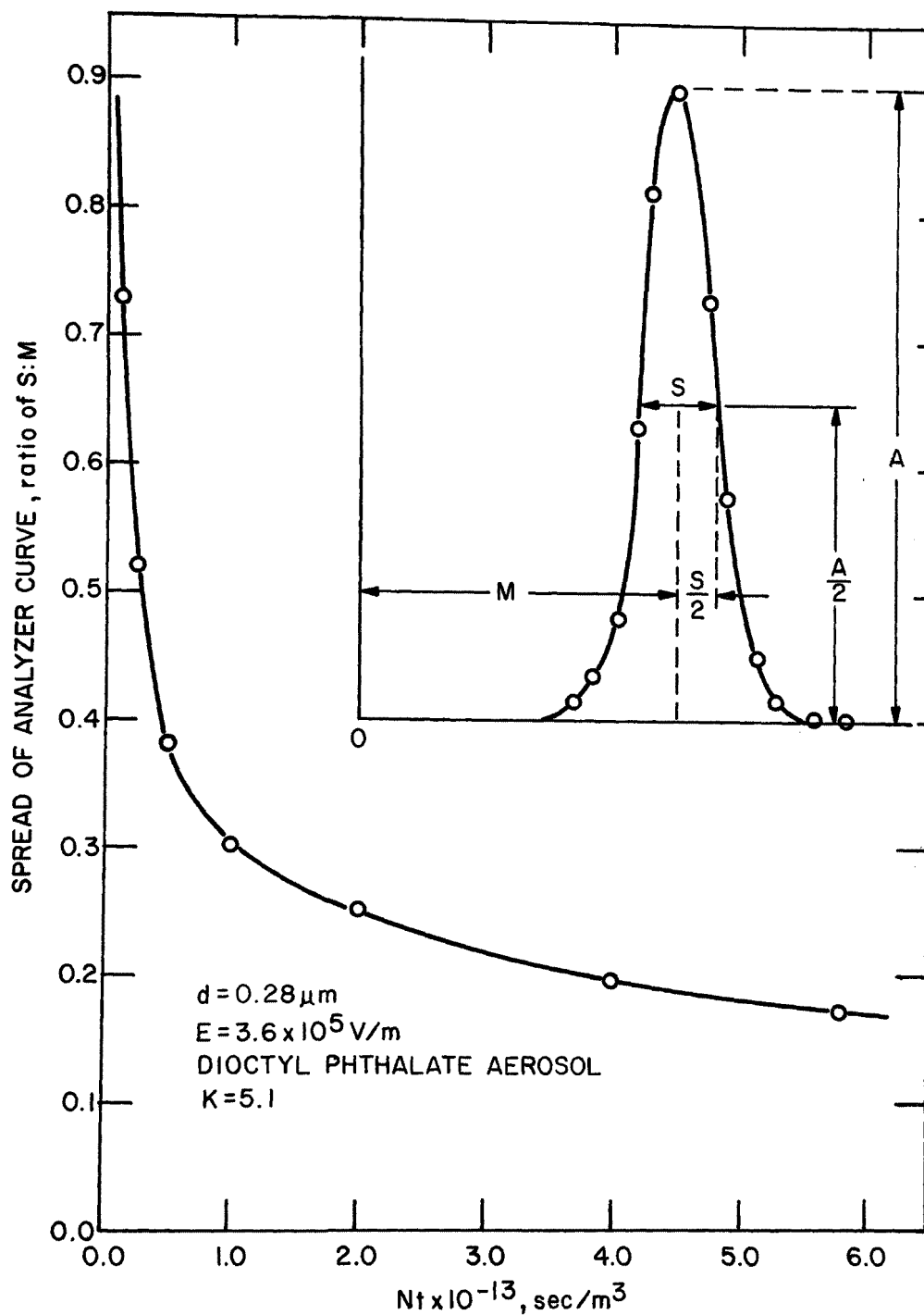


Figure 98. The spread of the mobility analyzer response curve for fixed values of  $Nt$ , particle size and charging field strength (after Hewitt<sup>8</sup>).

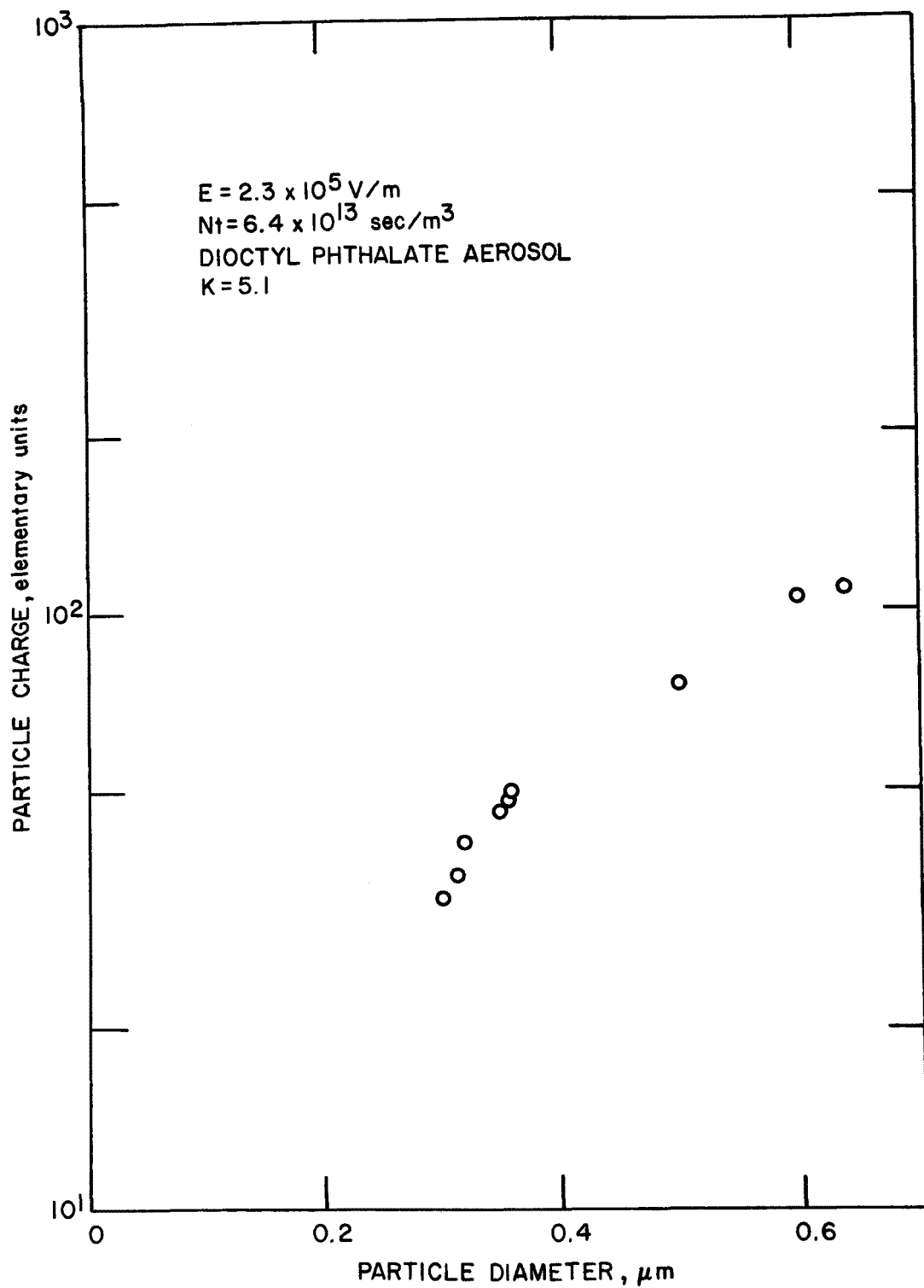


Figure 99. Particle charge as a function of particle diameter for a dioctyl phthalate aerosol (after Penney and Lynch<sup>7</sup>).  $K$  is the aerosol dielectric constant.

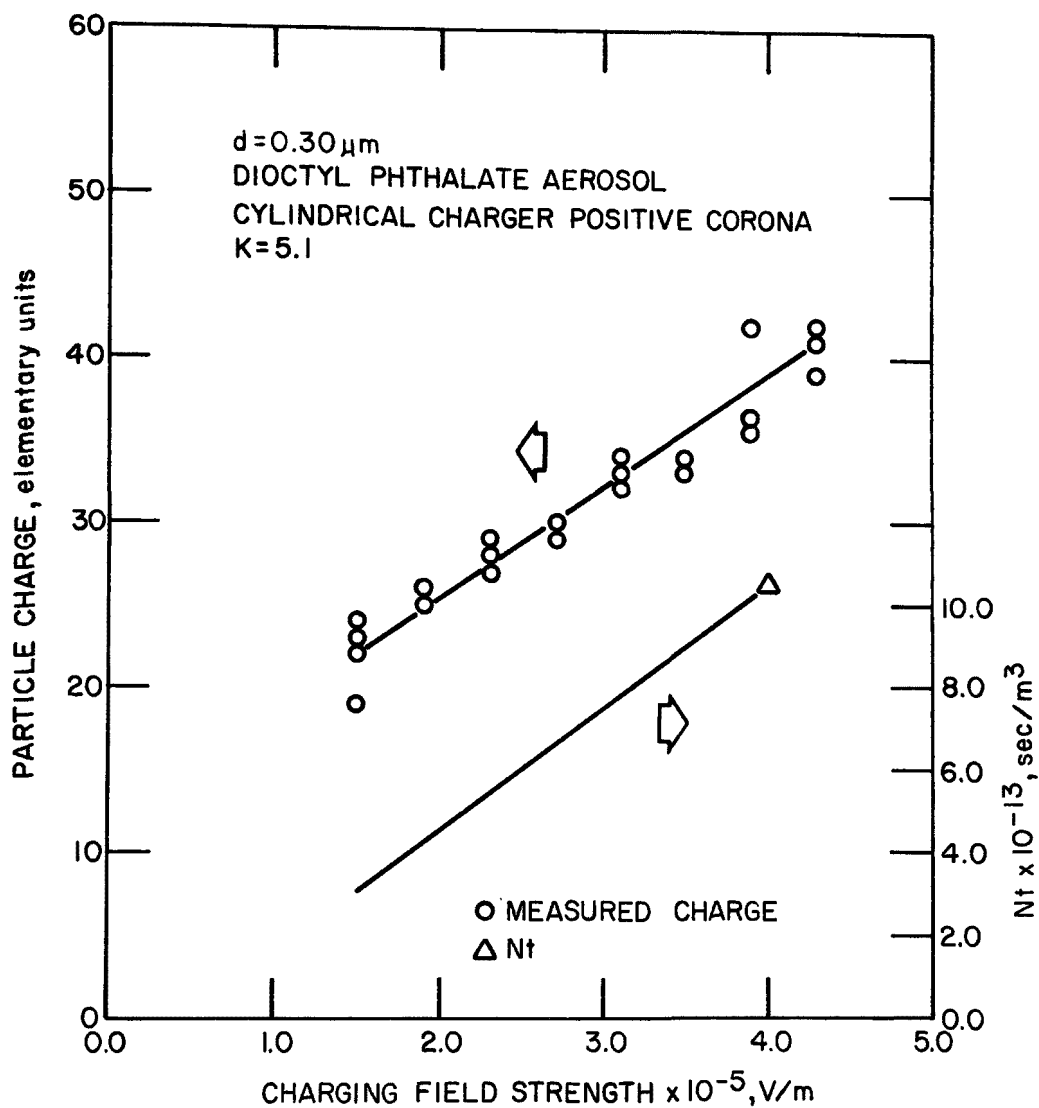


Figure 100. Particle charge as a function of charging field strength for  $0.30 \mu\text{m}$  diameter dioctyl phthalate particles in a positive corona (after Penney and Lynch<sup>7</sup>).  $K$  is the aerosol dielectric constant.

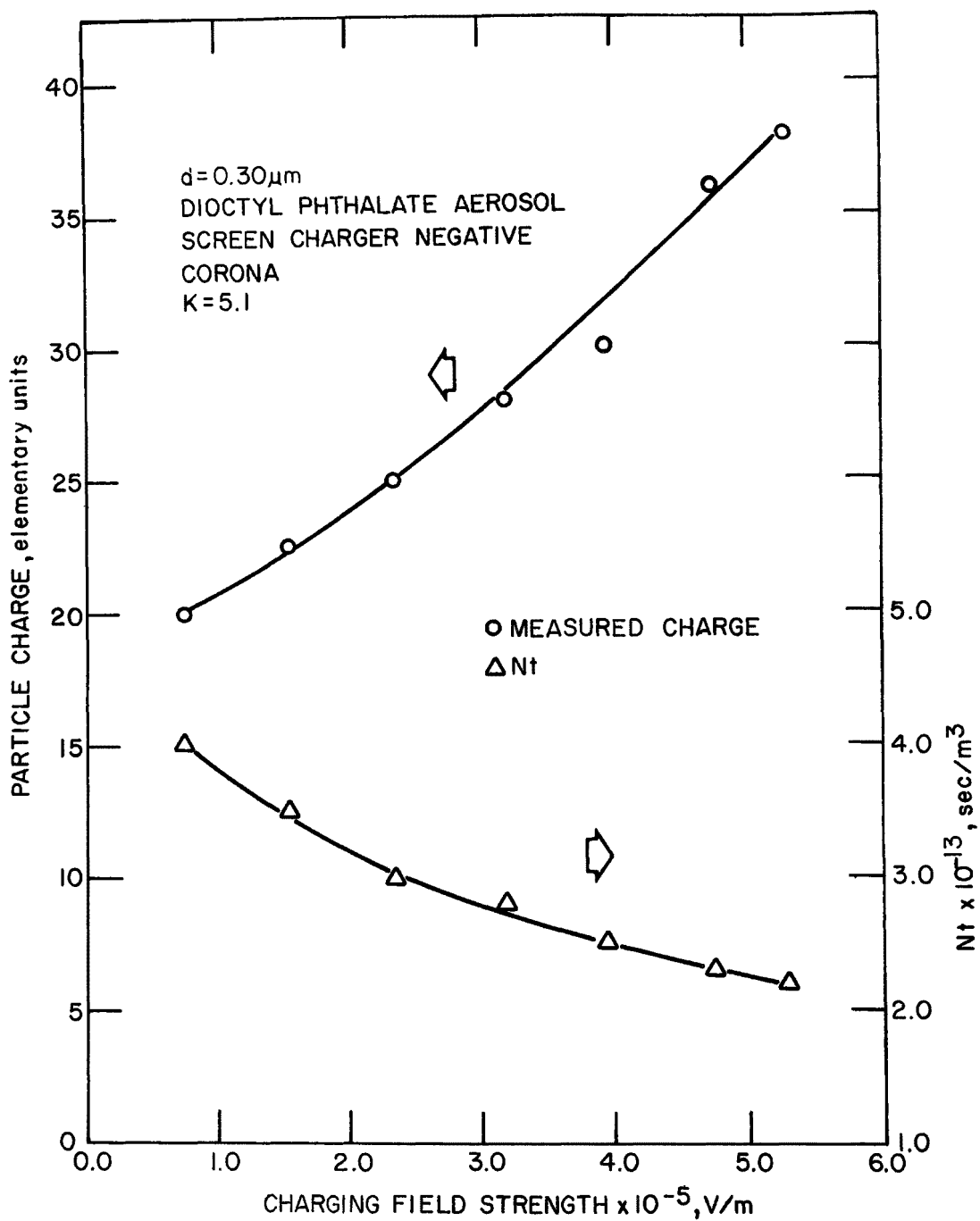


Figure 101. Particle charge as a function of charging field strength and ion density-time product for a  $0.30 \mu\text{m}$  diameter dioctyl phthalate aerosol in a negative ion field (after Penney and Lynch<sup>7</sup>).  $K$  is the aerosol dielectric constant.

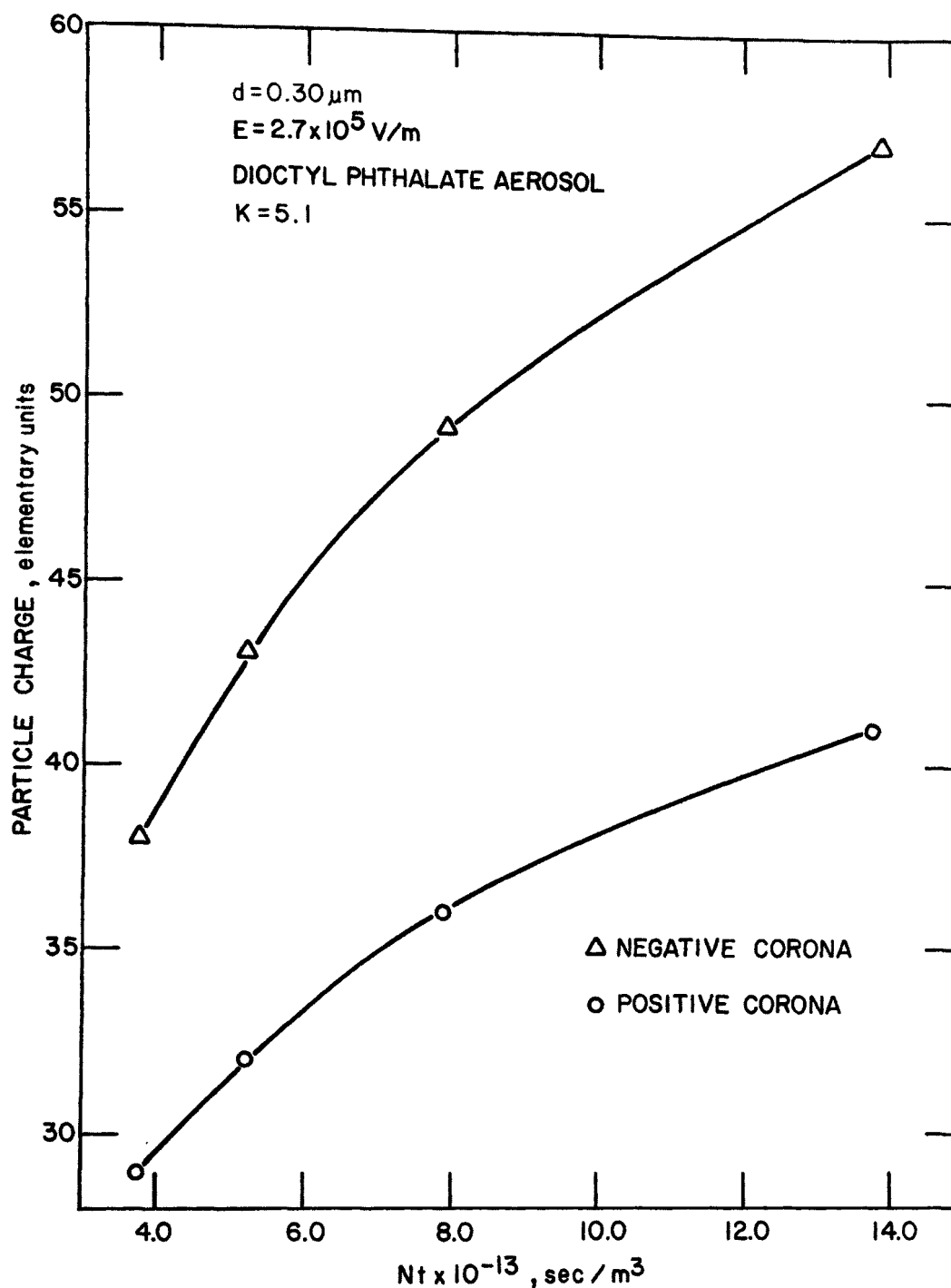


Figure 102. Comparison of particle charging for negative and positive corona acting on  $0.30 \mu\text{m}$  diameter dioctyl phthalate particles (after Penney and Lynch<sup>7</sup>).  $K$  is the aerosol dielectric constant.

Figures 101 and 102 for a field strength of  $2.7 \times 10^5$  V/m and positive corona charging, allow one to compare, with some extrapolation, the charges acquired for different  $Nt$  values for DOP droplets of approximately the same size. Table 8 shows that the agreement between Hewitt, Penney and Lynch over a range of  $Nt$  values is quite good.



TABLE 8. COMPARISON OF EXPERIMENTAL DATA  
Number of Elementary Charges as a Function of Nt

Nt (sec/m <sup>3</sup> )	Hewitt <sup>8</sup> (d=0.28 μm)	Penney & Lynch <sup>22</sup> (d=0.30 μm)
2. x 10 <sup>13</sup>	25.5 elementary charge units	25.0 elementary charge units
3. x 10 <sup>13</sup>	27.0	27.2
4. x 10 <sup>13</sup>	28.5	29.5
5. x 10 <sup>13</sup>	29.5	31.5

DOP Aerosol, E = 2.7 x 10<sup>5</sup> V/m, positive corona charging.

## APPENDIX C

### PARTICLE CHARGING PROGRAMS FOR PORTABLE CALCULATORS

An approximate calculation of the total charge accumulated by an aerosol particle of radius  $a$  in an electric field  $E$ , where there exists a unipolar ion density  $N$ , may be derived from the sum of diffusion charging and field charging effects:

$$n_p = (n_p)_{\text{field}} + (n_p)_{\text{diff}}$$

where

$$(n_p)_{\text{field}} = \frac{4\pi\epsilon_0 a^2 E}{e} \left[ 1 + 2 \left( \frac{k-1}{k+2} \right) \right] \frac{t}{t + t_0} ,$$

and

$$(n_p)_{\text{diff}} = \frac{4\pi\epsilon_0 a K T}{e^2} \ln \left( \frac{a e^2 v N t}{4\epsilon_0 K T} + 1 \right) .$$

In these expressions

- $t$  = particle residence time (sec),
- $t_0 = 4\epsilon_0 / Ne\mu$ ,
- $k$  = particle dielectric constant,
- $e$  = electron charge (coul),
- $\epsilon_0$  = permittivity of free space (fd/m),
- $\mu$  = ion mobility ( $\text{m}^2/\text{V}\cdot\text{sec}$ ),
- $T$  = temperature ( $^{\circ}\text{K}$ ),
- $K$  = Boltzmann's constant ( $\text{j}/^{\circ}\text{K}$ ), and
- $v$  = mean thermal ion speed (m/sec).

The sum of  $(n_p)_{\text{field}}$  and  $(n_p)_{\text{diff}}$  may therefore be written

$$n_p = \pi a C_1 \left\{ \frac{\mu a E N t}{\mu N t + C_1} \left[ 1 + 2 \left( \frac{k-1}{k+2} \right) \right] + C_2 T \ln \left( \frac{a v N t}{C_1 C_2 T} + 1 \right) \right\} \quad (155)$$

where

$$C_1 = \frac{4\epsilon_0}{e}$$

and

$$C_2 = \frac{K}{e}$$

Program listings for the Hewlett-Packard model HP-65 and the Texas Instruments model SR-52 programmable pocket calculators are included in this Appendix. Each of these programs will carry out a calculation for  $n_p$  in accordance with the above expression.

# HP-65 Program

## User Instructions

STEP	INSTRUCTIONS	INPUT DATA/UNITS	KEYS		OUTPUT DATA/UNITS
1	Clear programs (W/PRGM mode)		<input type="text" value="f"/>	<input type="text" value="PRGM"/>	
2	Enter card (RUN mode)		<input type="text"/>	<input type="text"/>	
3	Enter particle diameter	$\mu\text{m}$	<input type="text" value="STO"/>	<input type="text" value="1"/>	
4	Enter Nt product	$\text{sec}/\text{m}^3$	<input type="text" value="STO"/>	<input type="text" value="2"/>	
5	Enter average electric field	$\text{V}/\text{m}$	<input type="text" value="STO"/>	<input type="text" value="3"/>	
6	Enter temperature	$^{\circ}\text{K}$	<input type="text" value="STO"/>	<input type="text" value="4"/>	
7	Enter relative dielectric constant, particle		<input type="text" value="STO"/>	<input type="text" value="5"/>	
8	Enter ion mean thermal speed	$\text{m}/\text{sec}$	<input type="text" value="STO"/>	<input type="text" value="6"/>	
9	Press A		<input type="text"/>	<input type="text" value="A"/>	
10	Read particle charge	$n_p$	<input type="text"/>	<input type="text"/>	electronic charges
			<input type="text"/>	<input type="text"/>	
	To rerun for different charging conditions it is necessary to enter in the appropriate registers only the changed parameters, and then press key A, as in the following example where only the particle diameter and the temperature are changed:		<input type="text"/>	<input type="text"/>	
			<input type="text"/>	<input type="text"/>	
			<input type="text"/>	<input type="text"/>	
			<input type="text"/>	<input type="text"/>	
			<input type="text"/>	<input type="text"/>	
1 ex	Enter new particle diameter	$\mu\text{m}$	<input type="text" value="STO"/>	<input type="text" value="1"/>	
2 ex	Enter new temperature	$^{\circ}\text{K}$	<input type="text" value="STO"/>	<input type="text" value="4"/>	
3 ex	Press A		<input type="text"/>	<input type="text" value="A"/>	
4 ex	Read charge		<input type="text"/>	<input type="text"/>	electronic charges

# Example

Store the following parameters as indicated in the instructions:

$d = 2a = 1.0 \text{ } \mu\text{m}$   
 $Nt = 1.0 \times 10^{13} \text{ sec/m}^3$   
 $E = 6.0 \times 10^4 \text{ V/m}$   
 $T = 295 \text{ K}$   
 $k = 5.0$   
 $v = 500 \text{ m/sec}$

Initiate program, key A to find  $n_p = 74.5$  elementary charges

## Program Listing

CODE	KEYS
23	LBL
11	A
34 01	RCL 1
05	5
43	EEX
42	CHS
07	7
71	x
33 01	STO 1
34 06	RCL 6
71	x
34 02	RCL 2
71	x
34 04	RCL 4
81	÷
01	1
09	9
00	0
05	5
02	2
33 07	STO 7
81	÷
01	1
61	+
31	f
07	ln
34 04	RCL 4
71	x

CODE	KEYS
34 07	RCL 7
71	x
33 07	STO 7
03	3
05	5
07	7
01	1
34 02	RCL 2
81	÷
04	4
83	.
05	5
02	2
03	3
43	EEX
42	CHS
09	9
61	+
35	g
04	1/x
34 03	RCL 3
71	x
34 01	RCL 1
71	x
33 08	STO 8
34 05	RCL 5
01	1

CODE	KEYS
51	-
34 05	RCL 5
02	2
61	+
81	÷
02	2
71	x
01	1
61	+
34 08	RCL 8
71	x
34 07	RCL 7
61	+
35	g
02	$\pi$
71	x
34 01	RCL 1
71	x
33 07	STO 7
34 01	RCL 1
02	2
43	EEX
06	6
71	x
33 01	STO 1
34 07	RCL 7
24	RTN

R <sub>1</sub>	d	R <sub>4</sub>	T	R <sub>7</sub>
R <sub>2</sub>	Nt	R <sub>5</sub>	k	R <sub>8</sub>
R <sub>3</sub>	E	R <sub>6</sub>	v	R <sub>9</sub>

## SR-52 Program

Two different programming formats are in general use in portable calculators. The "reverse polish" format, employed in Hewlett-Packard systems, was used in the above development. A calculation for  $n_p$ , based on Equation 155 is presented on the following pages in the algebraic format used in the Texas Instruments SR-52 calculator.

### User Instructions

STEP		ENTER	PRESS		DISPLAY
1	Store particle diameter	$d, \mu\text{m}$	A		$d, \mu\text{m}$
2	Store $Nt$	$Nt, \text{sec}/\text{m}^3$	B		$Nt, \text{sec}/\text{m}^3$
3	Store electric field strength	$E, \text{V}/\text{m}$	C		$E, \text{V}/\text{m}$
4	Store Temperature	$T, ^\circ\text{K}$	D		$T, ^\circ\text{K}$
5	Store ion speed	$v, \text{m}/\text{sec}$	E		$v, \text{m}/\text{sec}$
6	Store dielectric constant	K	2nd	A	K
7	Store ion mobility	$\mu, \text{m}^2/\text{Vsec}$	2nd	B	$\mu, \text{m}^2/\text{Vsec}$
8	Calculate particle charge		2nd	C	$n_p$
	For new parameters, repeat only those steps of 1 through 7 for which a change is required, then go to step 8.				

The previously mentioned example may be used to test this program. A complete program listing follows:

LOC	CODE	KEY
000	46	LBL
	18	C'
	43	RCL
	00	0
	01	1
005	55	÷
	02	2
	52	EE
	06	6
	95	=
010	42	STO
	00	0
	08	8
	65	x
	59	$\pi$
015	65	x
	02	2
	93	.
	02	2
	02	2
020	04	4
	52	EE
	08	8
	42	STO
	00	0
025	09	9
	65	x
	53	(
	19	D'
	85	+
030	10	E'
	54	)
	95	=

LOC	CODE	KEY
035	81	HLT
	46	LBL
	19	D'
	53	(
	53	(
040	53	(
	43	RCL
	00	0
	07	7
	65	x
045	43	RCL
	00	0
	08	8
	65	x
	43	RCL
050	00	0
	02	2
	65	x
	43	RCL
	00	0
055	03	3
	54	)
	55	+
	53	(
	53	(
060	43	RCL
	00	0
	07	7
	65	x
	43	RCL
065	00	0
	02	2
	85	+

(continued)

LOC	CODE	KEY
070	43	RCL
	00	0
	09	9
	54	)
	54	)
	54	)
075	65	x
	53	(
	01	1
	85	+
	02	2
	65	x
080	53	(
	53	(
	43	RCL
	00	0
	06	6
	75	-
085	01	1
	54	)
	55	+
	53	(
	43	RCL
	00	0
090	06	6
	85	+
	02	2
	54	)
	54	)
	54	)
095	56	RTN
	46	LBL

LOC	CODE	KEY
100	10	E'
	53	(
	08	8
	93	.
	06	6
	07	7
105	01	1
	52	EE
	94	+/-
	05	5
	42	STO
	01	1
110	00	0
	65	x
	43	RCL
	00	0
	04	4
	65	x
115	53	(
	53	(
	43	RCL
	00	0
	08	8
	65	x
120	43	RCL
	00	0
	05	5
	65	x
	43	RCL
	00	0
125	02	2
	55	÷
	53	(
	53	(
	53	(
	53	(
130	53	(
	53	(
	53	(
	53	(
	53	(
	53	(

(continued)

LOC	CODE	KEY
135	43	RCL
	00	0
	09	9
	65	x
	43	RCL
140	01	1
	00	0
	65	x
	43	RCL
	00	0
145	04	4
	54	)
	54	)
	85	+
	01	1
150	54	)
	23	ln
	54	)
	56	RTN
	46	LBL
155	11	A
	42	STO
	00	0
	01	1
	56	RTN
160	46	LBL
	12	B
	42	STO
	00	0
	02	2
	56	RTN
	46	LBL
	13	C

LOC	CODE	KEY
165	42	STO
	00	0
	03	3
	56	RTN
	46	LBL
170	14	D
	42	STO
	00	0
	04	4
	56	RTN
175	46	LBL
	15	E
	42	STO
	00	0
	05	5
180	56	RTN
	46	LBL
	16	A'
	42	STO
	00	0
185	06	6
	56	RTN
	46	LBL
	17	B'
	42	STO
190	00	0
	07	7
	56	RTN

### Comparison With Other Particle Charging Calculations

The calculator program results, derived from Equation 155, provide a good approximation, in most cases, to the computer results obtained from the more complete charging theory described in Section 3 of this report. In Figure 103 there is presented a set of curves representing simple diffusion charging theory, simple field charging, the sum of diffusion and field charging (Equation 155), and the S.R.I theory, all calculated from the same charging data.



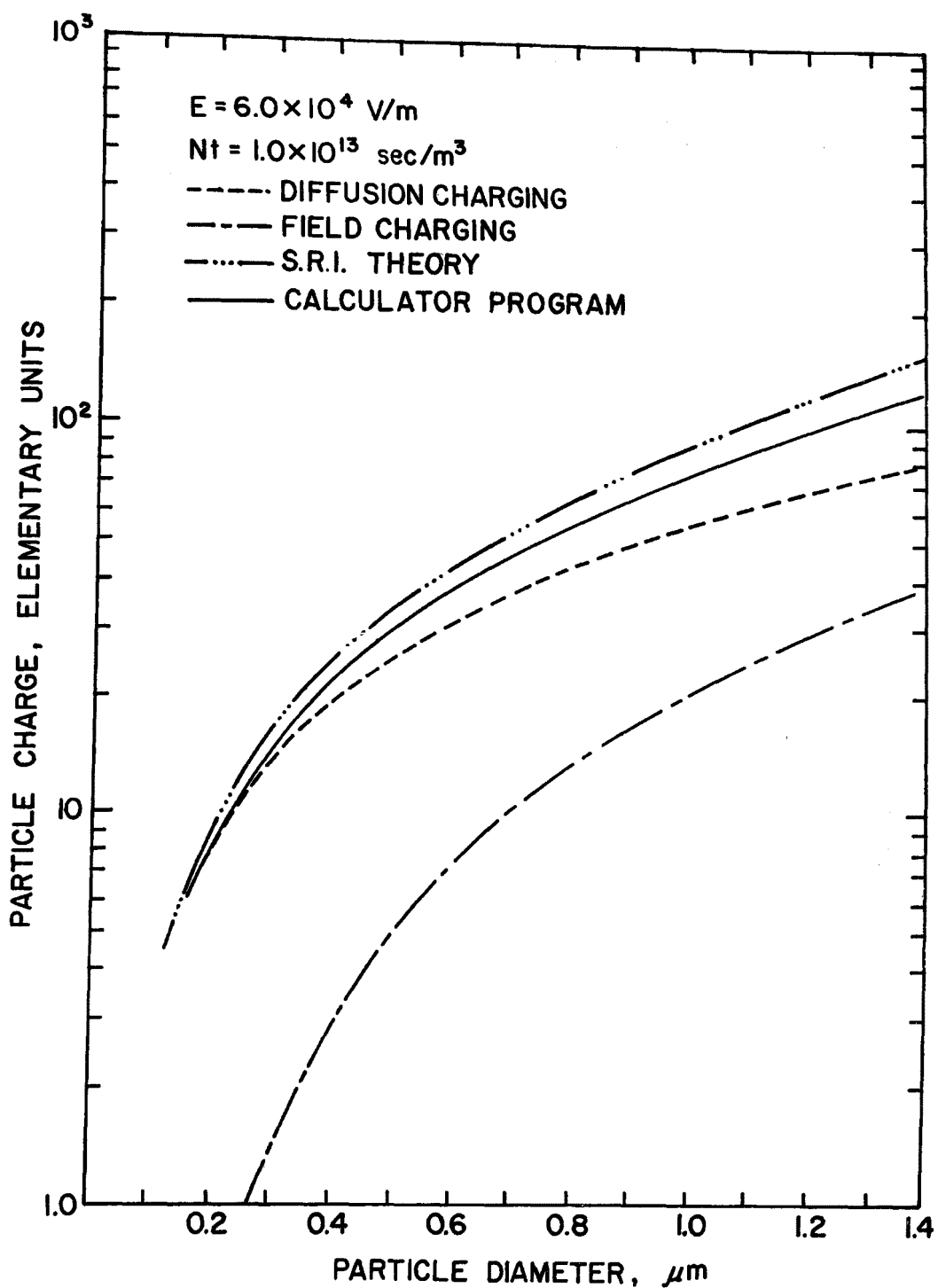


Figure 103. Average charge per particle as a function of particle diameter. The curve derived from the calculator program is the simple sum of the field charging and diffusion charging results.

TECHNICAL REPORT DATA (Please read instructions on the reverse before completing)		
1. REPORT NO. EPA-600/2-77-173	2.	3. RECIPIENT'S ACCESSION NO.
4. TITLE AND SUBTITLE Fine Particle Charging Development	5. REPORT DATE August 1977	6. PERFORMING ORGANIZATION CODE
7. AUTHOR(S) D. H. Pontius, L. G. Felix, J. R. McDonald, and W. B. Smith	8. PERFORMING ORGANIZATION REPORT NO. SORI-EAS-77-039 Project No. 3345F	
9. PERFORMING ORGANIZATION NAME AND ADDRESS Southern Research Institute 2000 Ninth Avenue, South Birmingham, Alabama 35205	10. PROGRAM ELEMENT NO. LAB012; ROAP 21ADL-036	11. CONTRACT/GRANT NO. 68-02-1490
12. SPONSORING AGENCY NAME AND ADDRESS EPA, Office of Research and Development Industrial Environmental Research Laboratory Research Triangle Park, NC 27711	13. TYPE OF REPORT AND PERIOD COVERED Final; 7/74-2/77	14. SPONSORING AGENCY CODE EPA/600/13
15. SUPPLEMENTARY NOTES IERL-RTP project officer for this report is Leslie E. Sparks, Mail Drop 61, 919/541-2925.		
16. ABSTRACT The report gives results of theoretical and experimental investigations into the charging of fine particles by unipolar ions in an electric field, and evaluation of a specially designed small pilot-scale (600-1000 acfm) precharging device. Following an extensive review of the literature, a new theory was developed, predicting statistically the average charge per particle in a large collection of particles. The electrical mobility of particles charged under controlled conditions of ion density, charging time, electric field strength, and ion polarity was measured to determine the average charge per particle for comparison with the theory. Agreement between experimental results and theory was generally within 20%. The precharger evaluation, based on direct particle charge measurements and the effects on performance of a pilot-scale electrostatic precipitator of conventional design located downstream from the precharger, indicated that effective particle charging was achieved in accordance with the theoretical predictions. Particle migration velocities in the precipitator, with the precharger on, were up to 60% greater than with the precharger off.		
17. KEY WORDS AND DOCUMENT ANALYSIS		
a. DESCRIPTORS	b. IDENTIFIERS/OPEN ENDED TERMS	c. COSATI Field/Group
Air Pollution Dust Electrostatics Charged Particles Charging Electrostatic Precipitators	Air Pollution Control Stationary Sources Particulate Particle Charging Precharging Unipolar Ions	13B 11G 20C 20H
18. DISTRIBUTION STATEMENT Unlimited	19. SECURITY CLASS (This Report) Unclassified 20. SECURITY CLASS (This page) Unclassified	21. NO. OF PAGES 240 22. PRICE